Massive black holes beyond the Eddington limit

Warren Massonneau

▶ **To cite this version:**

Warren Massonneau. Massive black holes beyond the Eddington limit. Astrophysics [astro-ph]. Sorbonne Université, 2022. English. NNT : 2022SORUS410 . tel-03977150

HAL Id: tel-03977150
https://theses.hal.science/tel-03977150v1

Submitted on 7 Feb 2023

HAL is a multi-disciplinary open access archive for the deposit and dissemination of scientific research documents, whether they are published or not. The documents may come from teaching and research institutions in France or abroad, or from public or private research centers.

L'archive ouverte pluridisciplinaire **HAL**, est destinée au dépôt et à la diffusion de documents scientifiques de niveau recherche, publiés ou non, émanant des établissements d'enseignement et de recherche français ou étrangers, des laboratoires publics ou privés.

THÈSE DE DOCTORAT
DE SORBONNE UNIVERSITÉ

SPÉCIALITÉ ASTROPHYSIQUE
ECOLE DOCTORALE N°127 - ASTRONOMIE ET ASTROPHYSIQUE D'ÎLE-DE-FRANCE

Massive black holes beyond the Eddington Limit

Auteur:
Warren MASSONNEAU

Superviseurs:
Marta VOLONTERI
Yohan DUBOIS

JURY

Benoit SEMELIN	Président	Professeur
Luca CIOTTI	Rapporteur	Professeur
Sadegh KHOCHFAR	Rapporteur	Professeur
Raffaella SCHNEIDER	Examinatrice	Professeure
Michaela HIRSCHMANN	Examinatrice	Professeure adjointe
Marta VOLONTERI	Directrice de thèse	Directrice de recherche
Yohan DUBOIS	Invité	Chargé de recherche
Ricarda BECKMANN	Invitée	Docteure

Cette thèse est soutenue le ***6 Décembre 2022*** *en vue de l'obtention du grade de Docteur en Astrophysique*

réalisée à

Institut d'Astrophysique de Paris

"Science sans conscience n'est que ruine de l'âme."

Rabelais, 1532

Abstract

Massive black holes beyond the Eddington Limit

by Warren MASSONNEAU

Decades of surveying the sky have lead to the conclusion that in the center of most galaxies lies a massive compact object of 10^6 to $10^{10}\,M_\odot$ known as a supermassive black hole (SMBH). Several relations connecting SMBHs and their host properties have been derived and it is now commonly accepted that galaxies and SMBHs co-evolve. For instance, SMBHs are able to grow with the gas that galaxies funnel towards them and can efficiently convert parts of this accreted gas into radiation, winds and jets. The effect that the energy injection through these phenomena has on the galaxy is usually referred to as *feedback*. SMBHs that accrete and produce radiation through their accretion discs are called active galactic nuclei, and the most luminous among them, which can shine significantly more brightly than their host galaxies, are called quasars. Some of these quasars are detected within 1 Gyr after the Big Bang, and their SMBHs have masses $\gtrsim 10^9\,M_\odot$. This implies that these compact objects must have grown extremely fast, or have grown from very massive seeds. This is one of the major unsolved problems in extragalactic astrophysics, where a standard Eddington-limited accretion scenario cannot explain the observed population of high-redshift quasars.

A number of different scenarios have been put forward to explain the presence of these SMBHs and the one considered in this thesis invokes accretion *beyond the Eddington limit*. Super-Eddington accretion has been discussed both from a theoretical point of view and an observational perspective. This regime is characterized by very high accretion rates, which, if able to feed the SMBHs for sufficiently long times, would allow for a faster growth compared to "standard" assumptions. Accretion at such high rates may have consequences on the amount of energy released in the surroundings of the compact object, thus impacting the environment the SMBH is embedded in. This could lead to halting the growth of SMBHs altogether, thus having the opposite effect from the one desired.

The idealised simulations presented in this thesis are meant to provide a better understanding of the impact that super-Eddington accretion has on BH growth. By adding a BH to the center of an emergent galaxy embedded in an isolated dark matter halo, we have been able to conduct a survey on the parameter dependence regarding BH growth. We have investigated the overall impact on the gas inflows and outflows, varying the feedback efficiencies and modes of injection in the super-Eddington regime. These simulations showed that, under the assumptions explored in this thesis, super-Eddington feedback efficiently and rapidly shuts off further super-Eddington episodes. Our findings also suggested that with the right combination of BH spin and super-Eddington feedback strength, there may be a window for mildly super-Eddington mass evolution. A subsequent study of BH spin evolution during super-Eddington phases coupled with sub-Eddington episodes, revealed that BHs with low spin magnitude may undergo efficient super-Eddington growth for a short period of time, before inevitably spinning-up and ceasing critical accretion altogether.

Résumé

Trous noirs massifs au-delà de la Limite d'Eddington

par Warren MASSONNEAU

Des décennies d'observations du ciel ont conduit à la conclusion qu'au centre de la plupart des galaxies se trouvait un object compact massif de 10^6 à $10^{10}\,M_\odot$ connu sous le nom de trou noir supermassif (TNSM). Plusieurs relations associant TNSMs et propriétés de leurs hôtes ont été établies et il est désormais communément admis que les galaxies et TNSMs évoluent ensemble. Par exemple, les TNSMs peuvent croître à l'aide du gaz fourni par les galaxies, et sont capables de convertir efficacement une partie de ce gaz accrété sous forme de rayonnement, de vents et de jets. L'injection d'énergie par ces mécanismes a un certain effet sur la galaxie, généralement appelé *rétroaction*. Les TNSMs qui accrètent et produisent des rayonnements par le biais de leurs disques d'accrétion sont appelés noyaux actifs de galaxie, et les plus lumineux d'entre eux, qui peuvent briller beaucoup plus que leur galaxie hôte, sont appelés quasars. Certains de ces quasars sont détectés moins de 1 Gyr après le Big Bang, et leurs TNSMs ont une masse $\gtrsim 10^9\,M_\odot$. Cela implique que ces objets compacts ont dû croître extrêmement rapidement ou à partir de graines très massives. Il s'agit de l'un des principaux problèmes non résolus en astrophysique, où un scénario d'accrétion standard limité par Eddington ne peut expliquer la population de quasars observée à haut redshift.

Un certain nombre de scénarios différents ont été proposés pour expliquer la présence de ces TNSMs et celui considéré dans cette thèse invoque l'accrétion *au-delà de la limite d'Eddington*. L'accrétion super-Eddington a été discutée à la fois d'un point de vue théorique et observationnel. Ce régime est caractérisé par des taux d'accrétion très élevés qui, s'ils sont capables d'alimenter les TNSMs pendant des temps suffisamment longs, permettraient une croissance plus rapide par rapport aux hypothèses "standard". L'accrétion à des taux aussi élevés peut avoir des conséquences sur la quantité d'énergie libérée dans les alentours de l'objet compact, impactant ainsi l'environnement dans lequel le TNSM se trouve. Cela pourrait conduire à un arrêt total de la croissance des TNSMs, ayant ainsi l'effet inverse de celui recherché.

Les simulations idéalisées présentées dans cette thèse ont pour but de fournir une meilleure compréhension de l'impact de l'accrétion super-Eddington sur la croissance des TNs. En ajoutant un TN au centre d'une galaxie émergente au sein d'un halo isolé de matière noire, nous avons pu mener une étude sur la dépendance des paramètres concernant la croissance du TN. Nous avons étudié l'impact global sur les flux de gaz entrants et sortants, en faisant varier les efficacités de rétroaction et les modes d'injection dans le régime super-Eddington. Selon les hypothèses explorées dans cette thèse, ces simulations ont montré que la rétroaction super-Eddington empêche efficacement et rapidement d'autres épisodes super-Eddington. Nos résultats suggèrent également qu'avec la bonne combinaison de spin du TN et de rétroaction super-Eddington, il peut y avoir une possibilité pour une croissance légèrement au-delà de la limite. Une étude ultérieure de l'évolution du spin du TN pendant les phases super-Eddington couplées à des épisodes sous-Eddington, a révélé que les TNs en rotation lente peuvent obtenir une croissance super-Eddington efficace pendant une courte durée, avant d'inévitablement accélérer leur rotation et cesser d'accréter à super-Eddington.

Contents

List of Figures

List of Tables

To my grandparents

Chapter 1

Introduction

The discovery around year 2000 (Fan et al. 2000) of quasars powered by supermassive black holes with mass $> 10^9\,M_\odot$ at $z > 6$, when the Universe was less than a billion years old, requires understanding the rapid growth of such black holes in the early stages of the Universe. There is still no clear consensus related to their origin, and we explore in this thesis one of the proposed scenarios to explain their assembly: breaking the Eddington limit. First and foremost, some context needs to be established to better understand this intriguing puzzle.

After a brief introduction to the historical discoveries that led to the modern view of the nature of our Universe (Section 1.1), we introduce the formation and evolution of galaxies (Section 1.2), as well as their residents, the massive black holes (Section 1.3). Since both are already in place less than a billion years after the Big Bang (Section 1.4), we explore the possibility of accretion beyond the Eddington limit to explain their rapid growth, by reviewing observations and theory behind this principle (Section 1.5). Finally, we describe the main questions that are investigated in this thesis.

1.1 A short history of the Universe

The Universe has fascinated humans for millennia, which led to many observational discoveries and a better understanding of the physics underlying the Cosmos. We now know that our own galaxy, the Milky Way, is one amongst billions in the Universe. Looking back at how astronomy developed this concept over time one can see how scientists and philosophers struggled with comprehending the nature of galaxies, and as a consequence the enormity of our Universe. In Ancient Greece, Democritus proposed, along the development of the atomic theory of the Universe, that the *bright band in the sky*, *i.e.* the Milky Way, was composed of distant stars. This idea was eclipsed by the perspective of the Universe advanced by Aristotle, who thought that the Milky Way was a contact point in the Earth atmosphere between terrestrial and celestial spheres. Almost two millennia later, Galilei (1610) demonstrated in his *Siderus Nuncius* that in fact the Milky Way was a massive gathering of individual faint stars. During the second half of the 18$^{\text{th}}$ century, Wright (1750) speculated that the "many cloudy spots" in the sky were distant galaxies, leading philosopher Kant (1755) to famously name these *island Universes*. During the same period of time, observations from Messier (1781) were compiled in a catalog of more than 100 of the brightest nebulae at the time, which were followed a century later by observations from Herschel (1864) with over 5000 objects. Even while documenting all of these nebulae it remained unclear as to exactly what they were. This stimulated a so called *great debate* between Shapley and Curtis in the early 20$^{\text{th}}$ century,

as two visions of what these objects were arose. This debate was resolved by astronomer Hubble (1925) with the discoveries of cepheids in the Andromeda galaxy and concluded that the Milky Way was just one of many galaxies, which came to be the dominant scientific perspective.

Back in 1913, Slipher (1913) provided the first empirical basis of an expanding Universe, as he discovered that distant galaxies are redshifted when he measured high Doppler shifts, thus relating redshift to recessing velocities. Based on this finding, Hubble (1929) concluded that the Universe was expanding. This idea was also supported theoretically a few years earlier by Friedmann (1922) and Lemaître (1927) using the mathematical framework of the newly formed general relativity (GR; Einstein 1916).

In the mid-20$^{\text{th}}$ century, with an increasing number of radio telescopes built around the globe, hundreds of radio sources were detected and listed in famous catalogues (*e.g.* 3C catalogue Bennett 1962, Matthews & Sandage 1963). During the same period, Schmidt (1963) discovered the first radio quasar, which had a nuclear region 100 times brighter than the luminous galaxies identified with radio sources up until this point. The construction of these telescopes also indirectly led to the discovery of the cosmological microwave background (CMB; Penzias & Wilson 1965), a remnant radiation from the early stages of the Universe, predicted by Alpher, Herman and Gamow (the "$\alpha\beta\gamma$" paper Alpher et al. 1948).

From this point on, tools used for astronomy were increasing in numbers, which subsequently resulted in a boom of breakthroughs. From the 1960s to the 1980s, theories regarding the beginning of the Universe flourished, as the idea of an expanding Universe from a hotter and denser initial state made sense with the nature of the CMB. Guth (1981), Starobinsky (1982) and Linde (1982) pioneered the theory of cosmic inflation, a period of accelerated expansion. This solved several issues of cosmology, such as the isotropic distribution of matter, the uniform radiation of the CMB as well as the flatness of the Universe. From the end of the 20$^{\text{th}}$ century until today, many different telescopes surveyed the Cosmos, both on Earth and in space. Thanks to measurements of the CMB by the *Planck* satellite (Planck Collaboration et al. 2020), we now know with great precision what the Universe is made out of:

- $\Omega_{\text{m}} = 0.315 \pm 0.007$, the matter density parameter taking into account both baryonic ($\Omega_{\text{b}} = 0.048 \pm 0.001$) and dark ($\Omega_{\text{c}} = 0.265 \pm 0.008$) matters;
- $\Omega_{\text{r}} \simeq 10^{-5}$, the relativistic matter density parameter;
- $\Omega_{\Lambda} = 0.685 \pm 0.007$, the dark energy density parameter;
- $\Omega_{\text{K}} = 0.0007 \pm 0.0019$, the curvature of the Universe;

Using the Λ-Cold Dark Matter (ΛCDM) model as the standard modern cosmological model, gives us a good idea of the different phases of evolution of the Universe (listed below in a chronological order):

- Big Bang (t = 0 s): singularity of infinite density and temperature, *i.e.* the beginning of the Universe;
- Inflation (t = 10^{-36} to 10^{-33} s): brief period of accelerated expansion, generating quantum fluctuations, which become the seeds for the growth of structures in the Universe;

- Recombination ($t \simeq 370\,\mathrm{kyr}$): as the Universe is expanding, it cools down to 3000 K, where the formation of neutral hydrogen is energetically favored. Photon decoupling also occurred during this period: once photons decoupled from matter, they constitute what is observed today as the CMB;
- Dark Ages ($t \simeq 370\,\mathrm{kyr}$ to 150 Myr): during this period, the Universe continues to cool down. Gas flows into halos of dark matter that form from overdensities, and as this gas cools and collapses it generates light-producing structures such as stars and galaxies;
- Reionization (t = 150 Myr to 1 Gyr) & Formation and Evolution of Galaxies ($t \gtrsim 150\,\mathrm{Myr}$): despite a continuous expansion of the Universe, matter continues to draw together under the influence of gravity. The first generation of stars starts to form and along with successive generations of stars born in the first galaxies, radiation able to re-ionize neutral hydrogen is produced. Pockets of ionized plasma, *i.e.* HII regions, expand individually until they intersect and fully ionize the Universe.

1.2 Galaxy formation & evolution

Galaxies are gravitationally bound objects mainly composed of dark matter (DM), gas, dust and stars, and act as hosts for massive central compact objects known as supermassive black holes (see Section 1.3.1 for a definition). In the Milky Way, the bulge, a bound stellar structure at the center of the galaxy composed of the oldest stars, is surrounded by a stellar disc which is estimated to extend all the way up to a few tens of kpc ($1\,\mathrm{pc} = 3.09 \times 10^{16}\,\mathrm{m}$). Extending all the way up to a few hundred of kpc is a DM halo which surrounds the galaxy. Not all galaxies resemble ours, as we know of several millions with vast ranges of sizes, masses, morphologies and luminosities. Providing physically motivated models to understand how galaxies form and evolve, and make predictions on unknown properties of their population, has been the goal of galaxy evolution studies.

1.2.1 The emergence of the first stars & galaxies

The small density fluctuations appearing at the end of the period of inflation, act as the seeds of gravitational collapse. These perturbations grow with time, as the small over-dense regions which collapse first, naturally increase the gravitational contrast between them and under-dense regions. Imprints of these perturbations nowadays form a complex DM structure known as the *cosmic web*, which is composed of dense clusters connected by filaments and otherwise near-empty void regions. These filaments feed the formation and growth of bound and virialised structures, the DM halos (White & Rees 1978). As both baryonic and dark matters are coupled via gravity, gas follows DM into the halos, creating gaseous halos. This mass assembly process takes a long time. As there are no metals (*i.e.* any other element besides H and He) in the early Universe, effective cooling processes only occur for molecular and atomic hydrogen if the virial temperature is below or above 10^4 K respectively (*e.g.* Abel 1995, Haiman et al. 2000). In the knots of the cosmic web, the density of ordinary and dark matter continues to increase and certain regions start to fragment as they exceed the local Jeans (1928) length $\lambda_\mathrm{J} \propto T^{1/2}\rho^{-1/2}$. Further cooling and fragmentation leads to the formation of dense molecular clouds, the birthplace of stars.

Population III (hereafter PopIII) stars are the first generation of stars to form. They are necessarily metal-free (Kashlinsky & Rees 1983, McDowell 1986) and are expected to form in 10^5 to $10^6\,M_\odot$ DM "minihalos" (Haiman et al. 1996, Tegmark et al. 1997). Their initial mass function (IMF; Salpeter 1955, Kroupa 2001, Chabrier 2003) has not been measured because these metal-poor stars have only existed in the earliest times, further than modern observations have managed to achieve. It is believed that the IMF of PopIII stars is *top-heavy*, with the production of a large number of unusually massive stars (with mass ranges of $10 \lesssim M_{\rm PopIII}/M_\odot \lesssim 10^3$) in comparison to later generations (*e.g.* Schwarzschild & Spitzer 1953, Schneider et al. 2002, 2006a, Sokasian et al. 2004, Marks et al. 2012). Inefficient cooling at this time along with high gas temperatures preventing fragmentation to smaller masses, are expected to lead to these massive stars. Observations of high-redshift galaxies have struggled to detect strong signatures of PopIII stars, as they have a short lifespan due to being massive stars, and are therefore limited to existing at very high redshifts (see Bromm 2013 for a review); although some models predict that clumps of metal-free gas may lead to the formation of PopIII stars even at $z \sim 3$ (Liu & Bromm 2020).

Early metal-enrichment from winds and supernovae (SNe) explosions at the death of PopIII stars can have negative and positive impact on the fate of interstellar medium (ISM). It can be negative, as both the radiative heating from UV photons and shock waves from the SN may eject significant amounts of gas from the minihalo, which may not have a deep enough potential well to retain the gas, thus limiting the available material to form stars. On the other hand, early metal-enrichment leads to more efficient cooling via metal line transitions (*e.g.* Choi & Nagamine 2009, Smith et al. 2009), enhancing the star formation rate. These newly formed stars will undergo similar processes at their death, thus creating a cycle that regulates the lifetime and the evolution of galaxies. As gas continues to fragment and form the next generations of stars, the basic processes of galaxy evolution are in place.

1.2.2 Galaxy evolution

From dwarf galaxies with stellar masses as low as $M_* \sim 10^9\,M_\odot$, to massive ones with $M_* > 10^{12}\,M_\odot$, galaxies are varied systems with a wide range of morphologies and luminosities. The main shapes of a galaxy (known as *galaxy types*) have been labelled in the early 1930s, with a famous classification diagram known as the "Hubble tuning fork" (Hubble 1926). Based on this classification, galaxies are divided in three main categories: spirals (or disc galaxies), lenticulars and ellipticals (or bulge galaxies), as well as irregular and peculiar galaxies. A majority of galaxies found in the local Universe at redshift $z < 0.03$ are spirals ($\sim$ 72 per cent, Hammer et al. 2005). At the same redshift, the fraction of lenticulars and ellipticals is $\sim$ 18 per cent while $\sim$ 10 per cent of galaxies have peculiar morphologies. However, the Universe was (and is) in constant evolution. The Hubble sequence evolves with redshift, with more than 50 per cent of the total galaxies found at $0.4 < z < 0.8$ being peculiar (Delgado-Serrano et al. 2010). Explaining the origin of the diverse population of galaxies all coming from simple initial conditions remains challenging.

Observations of galaxies led to the discovery of scaling relationships, correlating their global properties. For example, disc galaxies, which are rotation dominated, follow the Tully-Fisher relation (Tully & Fisher 1977) linking the galaxy luminosity with its maximum rotational velocity; whilst bulge ones are dispersion dominated and follow the Faber-Jackson

relation (Faber & Jackson 1976) linking the galaxy luminosity with the velocity dispersion σ of the stars in its bulge. Other studies show that there is a strong trend between the star formation activity of galaxies and their colours, such that "bluer" galaxies are predominantly star forming, while "redder" ones are more quiescent, with their old stellar population (*e.g.* Kauffmann et al. 2003, Blanton & Moustakas 2009).

Galaxies have also been found to have different formation histories: as in disc galaxies, metal rich young stars are found near the edge of the galactic disc and the central "pseudo-bulge" is filled with older stars (*e.g.* Bell & de Jong 2000, MacArthur et al. 2004, Sánchez-Blázquez et al. 2014); whereas bulge galaxies tend to have a more homogeneous stellar population. Various theories attempt to explain these differences. For instance, disc galaxies are thought to experience strong SN feedback early on, heating and ejecting gas at high-redshift (*e.g.* Weil et al. 1998). Some studies predict that this ejected gas would flow in the halo, cool down and later be slowly re-accreted by the disc, where it would feed continuous star formation (*e.g.* Fall 1979, Oppenheimer & Davé 2008, Brook et al. 2012, 2014, Übler et al. 2014, Christensen et al. 2016).

On the other hand, for bulge galaxies, their stellar population are thought to grow early on in deep potential wells. The stellar feedback is comparably weak and may lead to the formation of massive and compact systems (*e.g.* Khochfar & Silk 2006, Naab et al. 2007, Galametz et al. 2009, Feldmann et al. 2010, Rodriguez-Gomez et al. 2016). It is proposed that despite the deceleration of star formation after the cosmic peak at $z \sim 2$, they are able to increase their stellar mass thanks to mergers of smaller galaxies, resulting in dispersion dominated galaxies (*e.g.* Toomre 1977, Barnes 1988, Hernquist 1992, Naab et al. 1999, Hopkins et al. 2010, Oser et al. 2010, Ceverino et al. 2015).

Galaxies are not evolving in isolation: during their lifetime, they experience a variety of interactions. They are shaped by mergers, minor or major (*e.g.* Bournaud et al. 2005, Ferreras et al. 2009, Lotz et al. 2010, McLure et al. 2013), wet or dry (*e.g.* Lin et al. 2008, Khochfar & Silk 2009), via tidal stripping and harassment during close encounters (*e.g.* Gunn & Gott 1972, McCarthy et al. 2008). They group in clusters, colossal structures which are the largest gravitationally bound structures in the Universe, and the environment in which they evolve can further impact the morphology and other properties of galaxies (*e.g.* Hirschmann et al. 2014b).

As galaxy studies have been expanded over the last decades, measurements of the stellar mass function (*e.g.* Bell et al. 2003, Pérez-González et al. 2008, Ilbert et al. 2010, Muzzin et al. 2013) have been used as key observables of a population of galaxies. The stellar mass function (SMF) describes the number density of galaxies as a function of their stellar masses. Separating the SMF between quiescent and star-forming galaxies, observations have shown that galaxies of different types have distinct SMFs and the most massive galaxies are generally the quiescent ones (*e.g.* Bernardi et al. 2010, Ilbert et al. 2013, Tomczak et al. 2014, Davidzon et al. 2017, McLeod et al. 2021). It is also shown that their abundance rises with time, compared to star-forming galaxies which are thus thought to be progenitors of the quiescent ones (*e.g.* van Dokkum & Franx 2001, Kaviraj et al. 2009).

However, regardless of the redshift, the characteristic SMF found from observations (see

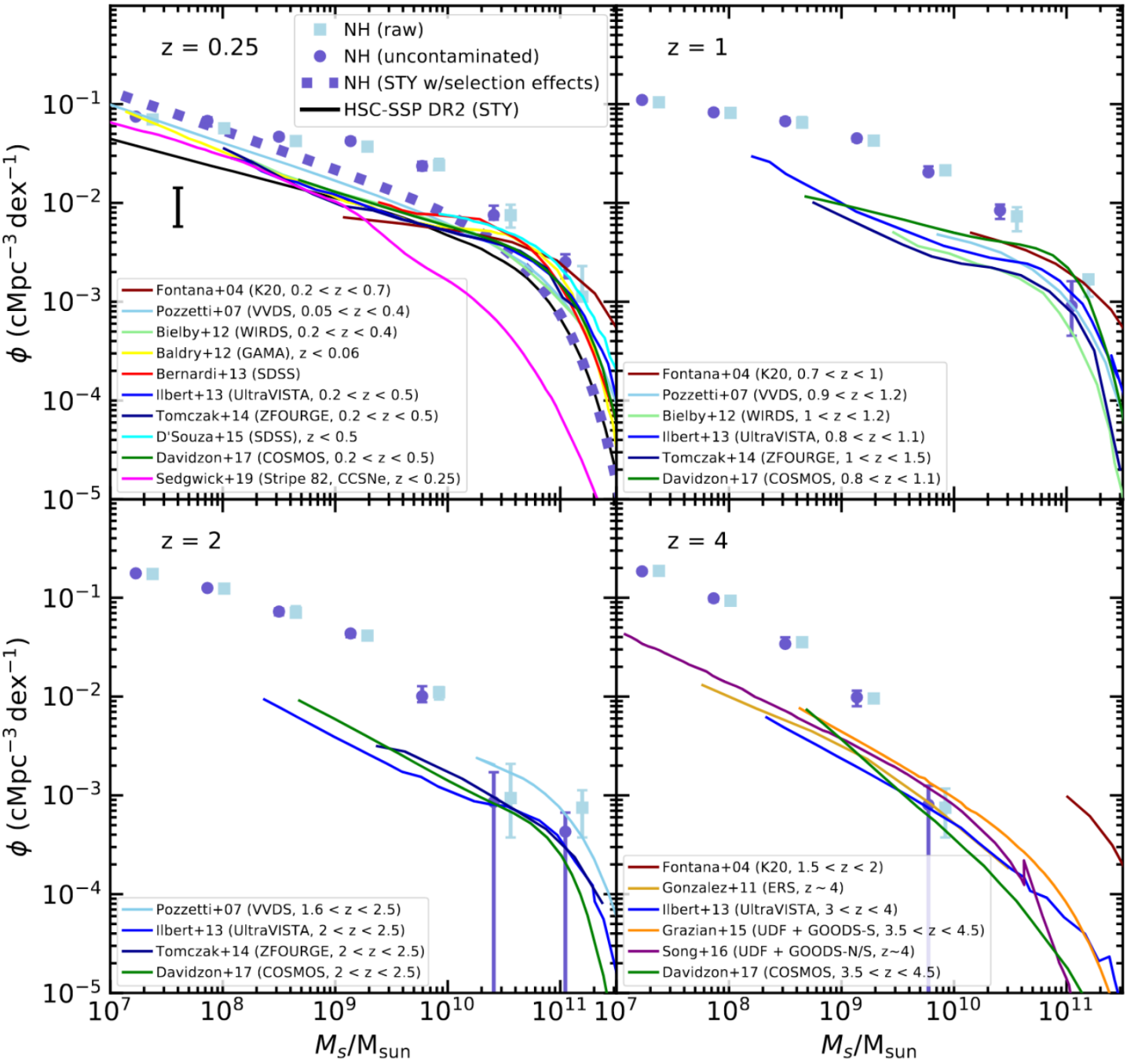

FIGURE 1.1: Stellar mass function at different redshifts in the `NewHorizon` simulation (coloured markers and thick purple line) from Dubois et al. (2021) accompanied by additional mass functions from literature (thin coloured lines).

the thin coloured lines in Fig. 1.1) is not well reproduced using the ΛCDM model if one assumes a constant mass ratio between galaxies and DM halos: theory predicts far more galaxies on both the low- and high-mass ends. In other words, models studying galaxy evolution find that both DM halos and galaxies retain too many baryons, producing too many stars. This is known as the "overcooling" problem (White & Rees 1978). Efficient mechanisms able to expel gas, such as powerful galactic-scale outflows of gas from galaxies are needed to explain the discrepancy. Stars and supermassive black holes are the two sources thought to be able to produce these large-scale outflows, or galactic winds. Galactic winds are a ubiquitous feature for both morphological types and at any range of redshift (*e.g.* Veilleux et al. 2005, Heckman & Thompson 2017, Zhang 2018).

At the low-mass end of the SMF ($M_* \lesssim 10^{10}\,\mathrm{M}_\odot$), SN outflows are expected to be able to push the excess baryons out of the galaxies and prevent star formation (*e.g.* Dekel & Silk 1986, Benson et al. 2003, Hirschmann et al. 2013, 2016, Hopkins et al. 2014). However, when examining the most massive galaxies ($M_* \gtrsim 10^{12}\,\mathrm{M}_\odot$), this quenching process are not be only described by the stellar feedback, as the SN winds may not be strong enough to eject the baryons. SNe are not able to eject gas at large scales due to the much stronger gravitational potential that these galaxies possess, meaning that their velocity is less than the escape velocity of the massive galaxies (*e.g.* Springel et al. 2005, Dubois & Teyssier 2008). Only powerful outflows launched by supermassive black holes (which are found in massive galaxies, see Section 1.3.1) are thought to be strong enough to decrease the ability of the most massive galaxies to form stars (*e.g.* Silk & Rees 1998, King 2003, Rafferty et al. 2006, Fabian 2012). "Active galactic nuclei" (AGN) regulating star formation in their host galaxies have been explored and reproduced[1] in state-of-the-art cosmological simulations (*e.g.* Dubois et al. 2014a, Hirschmann et al. 2014a, Vogelsberger et al. 2014, Schaye et al. 2015, Pillepich et al. 2018, Davé et al. 2019; also see "NH" in Fig. 1.1 from Dubois et al. 2021). These AGN outflows and their modeling are further described in Sections 1.3.2 and 2.3.7 respectively.

As we have seen, galaxies are not evolving in isolation and even without such interactions, their evolution is also believed to be driven by internal processes such as feedback from stars and supermassive black holes (*e.g.* Ciotti et al. 1991, Ciotti & Ostriker 1997, 2001, 2007, Springel et al. 2005, Bower et al. 2006, Croton et al. 2006), as well as magnetic fields (*e.g.* Jansson & Farrar 2012, Beck 2015) and cosmic rays (*e.g.* Breitschwerdt et al. 1991, Bykov et al. 2018, Dashyan & Dubois 2020). This brief overview of the current knowledge related to galaxy evolution is used to provide context for the work on supermassive black holes, before delving deeper into our current field of supermassive black holes and their origin. The reader is referred to thorough reviews on the subject, such as Benson (2010), Buta (2013), Conselice (2014), Somerville & Davé (2015), and Naab & Ostriker (2017).

1.3 Supermassive black holes through cosmic times

Black holes come in different mass categories, which are divided in three sub-groups: stellar mass black holes with $M_{\mathrm{BH}} \lesssim 10^3\,\mathrm{M}_\odot$, intermediate mass black holes with $10^3\,\mathrm{M}_\odot < M_{\mathrm{BH}} \lesssim 10^6\,\mathrm{M}_\odot$, and supermassive ones with $M_{\mathrm{BH}} \gtrsim 10^6\,\mathrm{M}_\odot$, the latter being the object of study of this thesis. These supermassive black holes are believed to be present in most galaxies,

[1] There are still some discrepancies between observations and simulations in the low- and high-mass galaxies.

including our own. They have been found to be key components to galaxies. However, discoveries of luminous high-redshift quasars at the beginning of this millenium (Fan et al. 2000, 2001, 2003, 2006) showed that these supermassive black holes were already in place at the end of the reionization era.

1.3.1 Supermassive black holes in local galaxies

It took more than half a century to prove observationally the existence of black holes (BHs), predicted theoretically by GR (Schwarzschild 1916)[2]. They have been reported in a variety of contexts and over a large range of masses. The first stellar mass BH was detected in Cygnus X-1 (Bolton 1972, Webster & Murdin 1972), a rapidly variable X-ray source, which confirmed theoretical work from decades prior. Supermassive BHs (SMBHs) in galaxies have been hinted to since the early 1940s by Seyfert (1943), with the observations of spiral galaxies with unusually bright point-like nuclei, which were confirmed 50 years later (Miyoshi et al. 1995). Furthermore, radio sources such as M87 and Cygnus A, have giant radio lobes with bright optical narrow jets, which suggested that the radio emission is due to relativistic particles, ejected from the central regions of the galaxies, where the SMBH is located.

Similarly to stellar mass BHs found in X-ray binaries, SMBHs are surrounded by an accretion disc that forms due to the infalling material that slowly spirals onto the compact object (see Abramowicz & Fragile 2013 for a review). Dense and fast moving clouds ($> 10^3$ km s^{-1}) are found close to the accretion disc and form the broad-line region (BLR). On scales similar to those of the accretion disc and BLR, dusty material, sometimes referred to as a dusty torus, can lead to significant obscuration if observed at certain angles (Antonucci 1993, Urry 2003, Tadhunter 2008, Beckmann & Shrader 2012). On larger scales (of the order of hundreds of pc to kpc), gas clouds of lower density and significantly smaller orbital speeds ($\sim 10^2$ km s^{-1}) compared to the BLR provide the ground for emission of narrow forbidden and permitted lines. These clouds are generically referred to as the narrow-line region (NLR).

Whilst the first discoveries of SMBHs were through AGN, several techniques of observation have been since developed. Since BHs in isolation do not emit light, their detection must rely on their interaction with matter, gas is the case of AGN, but also interaction with other objects or by lensing radiation from intervening light sources (Paczynski 1986). Regarding SMBHs, a selection of techniques have been developed over the past decades. They include the proper-motion measurements from the gravitational influence on the orbits of stars near the SMBH (Eckart & Genzel 1997, Ghez et al. 2005, GRAVITY Collaboration et al. 2018, 2020), micro-lensing (*e.g.* Irwin et al. 1989, Richards et al. 2004, Chartas et al. 2009, Sluse et al. 2011, 2012), emission from infalling material and from the accretion disc (*e.g.* Reynolds & Nowak 2003, Reynolds 2021, Hu et al. 2008, Agís-González et al. 2014), and the pinnacle of detection being the direct image of the shadow of a SMBH (Event Horizon Telescope Collaboration et al. 2019, 2022).

There has also been impressive progress in measuring $M_{\rm BH}$, in quiescent and active galaxies. If the motion of stars orbiting near the SMBH can be accurately measured, it is possible to measure the mass of the central SMBH. The most evident mass measurement with this technique is Sgr A*, the SMBH of our galaxy, which has been estimated this way to have

[2]We note that if the mass of a compact object (such as a white dwarf) is greater than the Chandrasekhar limit (Chandrasekhar 1931), it will become a BH.

$M_{\rm BH} \simeq 4 \times 10^6\,{\rm M}_\odot$ (*e.g.* Ghez et al. 2003, Schödel et al. 2003). As it is not feasible to resolve single stars, a similar method involving stellar dynamics is used for other galaxies than the Milky Way. Direct stellar dynamical measurements (*e.g.* van der Marel 1994, Gebhardt et al. 2003, Davies et al. 2006, Onken et al. 2007, Gebhardt et al. 2011) use the spectrum of the nucleus, from which the gravitational potential of the galaxy can be modelled and the SMBH mass estimated, as the presence or absence of the SMBH affects motion of stars. Stellar dynamical measurement usually target galaxies with quiescent SMBHs, to prevent luminosity contamination from AGNs (which would render such measurements difficult).

Gas orbiting the compact object can also be used to estimate the SMBH mass. For example, molecular hydrogen emission lines have been used to study gas dynamics and adding constraints on the SMBH mass (*e.g.* Davies et al. 2004a,b, Hicks & Malkan 2008, Scharwächter et al. 2013, den Brok et al. 2015). This method is mainly used for low-luminosity AGNs, as radiation forces close to the central SMBH may be affecting the dynamics of the line emitting gas (see D'Onofrio et al. 2021 and references therein).

Water masers can also be used as a tracer for the central potential (*e.g.* Miyoshi et al. 1995, Rodriguez et al. 2006, Kuo et al. 2011). They correspond to dense molecular clouds in which gas is excited by the X-rays from the actual accretion disc of the central SMBH. The excited molecules then radiate maser radiation at radio frequencies, which can be studied using radio interferometry with excellent spatial resolution. Unfortunately, water masers require very favorable inclination, making them very difficult to detect.

If a galaxy hosts a very bright AGN, the stellar kinematics in the central region may be very difficult to observe and the techniques described above cannot be used. SMBHs masses in bright sources can be estimated via their BLR, although uncertainties of the mass estimate are larger than via direct dynamical measurements. BLRs are used to estimate the mass of SMBHs in AGN under the assumption that the gas is in rotation and that the motion of the emitting clouds is dominated by the gravitational field of the central object:

$$M_{\rm BH} = \frac{V_{\rm vir}^2 R_{\rm BLR}}{G} = \frac{f W^2 R_{\rm BLR}}{G} \tag{1.1}$$

The width of the broad line W is used as an indicator of the virial velocity $V_{\rm vir}$, with the introduction of a virial coefficient f (or geometrical factor). One of the most commonly used methods which provides an estimate of the typical size of the BLR $R_{\rm BLR}$ is reverbation mapping (*e.g.* Blandford & McKee 1982, Peterson 1993, Peterson et al. 2004). By mapping the lagged response from broad emission line to continuum variations, one can in principle reconstruct the kinematics and structure of the BLR, and thus estimate $R_{\rm BLR}$.

Another method referred to as an extension of the reverbation mapping technique is the single-epoch virial mass estimator. It uses one of the findings of reverbation mapping measurements, which is a tight correlation between the BLR size and the continuum luminosity, dubbed the BLR size-luminosity relationship (*e.g.* Kaspi et al. 2000, Bentz et al. 2009). Using this relation, one can estimate the size of the BLR from the measured quasar luminosity, and by combining it with the line width W, one can estimate the SMBH mass (*e.g.* Vestergaard

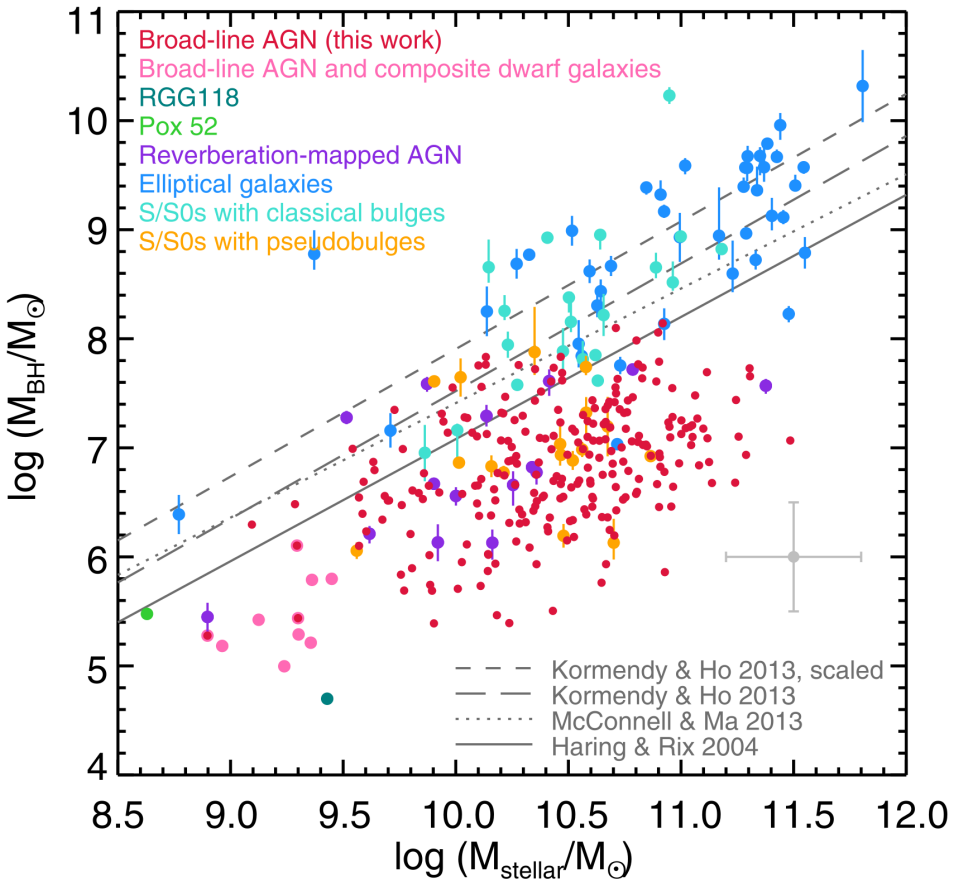

FIGURE 1.2: Relation between $M_{\rm BH}$ and M_* of local host galaxies (Reines & Volonteri 2015). Coloured points show the observational data and scaling relations are shown with the lines.

2002, Vestergaard & Osmer 2009, Shen 2013):

$$\log\left(\frac{M_{\rm BH}}{\rm M_\odot}\right) = a_1 + b_1 \log\left(\frac{L}{10^{44}\,\rm erg\,s^{-1}}\right) + c_1 \log\left(\frac{W}{\rm km\,s^{-1}}\right) \tag{1.2}$$

with a_1, b_1 and c_1 coefficients calibrated against reverbation mapped AGNs.

Finally, the latest method which led to the measurement of two SMBHs masses is the direct observation of the shadow of the compact object (Event Horizon Telescope Collaboration et al. 2019, 2022). With this novel technique, the diameter of the emission ring and the distance of the compact object are required to measure the SMBH mass. This procedure uses very demanding radio interferometric methods, meaning that its use is likely limited to the closest SMBHs.

Once a relatively large sample of SMBH masses has been assembled, it became possible to examine their relation to the host galaxies, and this led to the discovery of correlations with properties of the host galaxies. Kormendy & Richstone (1995) and Magorrian et al. (1998) were amongst the first to notice that SMBHs masses correlate with the luminosity of the bulge component of the stellar distribution. The existence of the $M_{\rm BH} - M_{\rm bulge}$ relationship has been confirmed thanks to further detections of SMBHs. However, it is difficult to rely on decomposing the luminosities of bulge and disc components at high redshift, owing to lack of spatial resolution and sensitivity. Investigating the relationship between $M_{\rm BH}$ and the

total stellar mass M_*, Reines & Volonteri (2015) compiled a large sample of nearby ($z \sim 0$) SMBHs in Fig. 1.2, showing a correlation between stellar and SMBH masses. An even tighter relationship connects the SMBH mass and the velocity dispersion $M_{\rm BH} - \sigma$. These scaling relations, as a whole, suggest a link between SMBH accretion and the star formation history of the host galaxy (*e.g.* Gebhardt et al. 2000, Tremaine et al. 2002, Marconi & Hunt 2003, Haiman 2004, McConnell & Ma 2013). Further support for this link came from the discovery that the cosmic density of the SMBH accretion and of the star formation follow a similar trend over cosmic time (Marconi et al. 2004, Merloni 2004, Shankar et al. 2009). Finally, discoveries in recent years were able to link SMBH masses with the total number of globular clusters in galaxies, showing that the most compact objects at galaxy centers correlate with one of the outermost galaxy components (Burkert & Tremaine 2010, Harris & Harris 2011, Kormendy & Ho 2013).

These observations strongly suggest that the growth of a SMBH is tightly correlated to that of its host galaxy. While the growth of SMBHs might not be entirely understood, they can have significant impact on the formation and evolution of their host, by means of several feedback mechanisms, which is discussed in the next Section.

1.3.2 AGN feedback mechanisms

When gas is accreted onto a BH, a fraction of rest-mass accreted energy is released back to the host galaxy. This process can impact the inflow of material and is expected to impact both star formation and SMBH accretion. AGN feedback can be negative, when it heats and pushes some gas out of the galaxy, thus reducing the existing gas supply and prevent star formation (*e.g.* Silk & Rees 1998, Crenshaw et al. 2003, Nesvadba et al. 2007, Alexander et al. 2010, Morganti et al. 2013). It is also negative when it can reach the circum-galactic medium, by suppressing the cooling flows, thus quenching star formation (*e.g.* Peterson et al. 2003, Brüggen et al. 2005, Dunn et al. 2005, McNamara & Nulsen 2007). Conversely AGN feedback may be positive, as it can trigger star formation, by compression of molecular clouds in the galactic disc (*e.g.* Begelman & Cioffi 1989, Rees 1989, Silk 2005, 2013, Santini et al. 2012, Gaibler et al. 2012, Bieri et al. 2015, 2016) or directly in the outflowing gas (Ishibashi & Fabian 2012). Negative and positive feedback are not necessarily contradictory as AGN activity may both quench and induce star formation in different parts of the host galaxy and on different timescales (*e.g.* De Young 1989, Imanishi et al. 2011, Silk 2013, Zinn et al. 2013, Zubovas et al. 2013, Carniani et al. 2016). Two major modes of AGN feedback, which vary by the nature of the outflows they produce, have been identified (*e.g.* Cole et al. 2000, Benson et al. 2003, Begelman 2004, Bower et al. 2006, Ciotti & Ostriker 2007, Fabian 2012, King & Pounds 2015).

The first is the radiative mode, known as "quasar" mode. This mode operates when the SMBH accretes at a significant fraction ($\gtrsim$ 1 per cent) of the Eddington rate (*e.g.* Heckman & Best 2014, see Section 1.4.1 for a definition) and is believed to proceed via geometrically thin and optically thick accretion disc (Shakura & Sunyaev 1973, see Section 1.5.2 for more details). This form of feedback may have been the most effective when galaxies were most gas rich, *i.e.* at high redshift. Radiation-based feedback can be generated by the extreme luminosities than can be produced by the accretion disc. One scenario (*e.g.* Silk & Rees 1998, Haehnelt et al. 1998) suggested that the radiation would drive a wind which would deposit

energy into the SMBH surroundings, thus heating the gas. Besides radiative heating, momentum driven mechanisms have also been proposed to push cold gas out of the galaxy (King 2003). For example, radiation pressure acting on electrons and on dust via scattering processes (*e.g.* Murray et al. 2005, Fabian 2012, Bieri et al. 2017). An alternative possibility may be that the AGN could power winds which would cover a wide range of velocities, thus being able to drive out significant gas mass (*e.g.* Tremonti et al. 2007, Moe et al. 2009, Feruglio et al. 2010, Fiore et al. 2017). Semi-analytical (*e.g.* Bower et al. 2006, Croton et al. 2006, 2016, Somerville et al. 2008) and numerical simulations (*e.g.* Di Matteo et al. 2008, Booth & Schaye 2009, Ostriker et al. 2010, Dubois et al. 2012b, Hirschmann et al. 2012, Brennan et al. 2018, Choi et al. 2018) have also found relative success in implementing this mechanism and reproducing observations of the global galaxy population.

The second mode is the kinetic mode, known as "radio" mode or maintenance mode. This mode proceeds in the core of massive galaxy halos, with typical signatures being the inflated cavities found at the cores of clusters (*e.g.* Fabian et al. 2006, Forman et al. 2007, Olivares et al. 2019). This mode is believed to be powered by jets and is therefore often associated to lower Eddington rates in comparison to the radiative mode, in analogy with the states of X-ray binaries (Merloni et al. 2003, Falcke et al. 2004). These powerful outflows emerge with relativistic velocities out of their galactic nuclei and exist on a wide range of scales from $\lesssim 1\,\mathrm{AU}$ to $\gtrsim 1\,\mathrm{Mpc}$, as they may travel outside the galaxy whilst staying collimated and terminate in strong, hot spot shocks (*e.g.* Marscher et al. 2008, Asada & Nakamura 2012, Doeleman et al. 2012, Ackermann et al. 2015). Jet production has been linked to extraction of the rotational energy from a spinning BH (Blandford & Znajek 1977), and/or if the accretion disc is strongly magnetised and removes magnetically the angular momentum from the disc (Blandford & Payne 1982). A further ingredient is believed to be the presence of a geometrically thick discs, and this provides the link to the Eddington ratio mentioned above. At accretion rates of the order of a few per cent of the Eddington rate, accretion discs are believed to transition from a thin disc (at high accretion rates) to a thick disc (at low accretion rates). Whilst numerical simulations modeling these jets have been able to reproduce the inflated cavities (*e.g.* Omma et al. 2004, Heinz et al. 2006, Cattaneo & Teyssier 2007, Dubois et al. 2010, Guo & Mathews 2010, Gaspari et al. 2011, Beckmann et al. 2019), the physics behind the creation of these jets is still an area of ongoing research, and efforts towards understanding their formation and how they remain collimated are developed (*e.g.* Tchekhovskoy et al. 2011, McKinney et al. 2012, King & Pounds 2015, Potter & Cotter 2015, Liska et al. 2018, Chatterjee et al. 2019, Lucchini et al. 2021; also see Blandford et al. 2019 for a review on jets).

The AGN feedback occuring at very high Eddington rates (above the Eddington limit) will be discussed in detail in Section 1.5.2. Finally, there are additional plausible mechanisms through which AGN can deposit energy in their surroundings, like magnetohydrodynamical (MHD) winds and cosmic rays (*e.g.* Ehlert et al. 2018, Beckmann et al. 2022b).

1.3.3 High-redshift quasars

Bright high-redshift quasars ($z \gtrsim 6$; less than a billion years after the Big Bang) are difficult to find, as they are rare which requires the need to survey large fractions of the sky. The Sloan Digital Sky Survey (SDSS) was the first survey that allowed to graze the $z \gtrsim 6$ quasar

population (Fan et al. 2000). In the last two decades, the search of luminous quasars continued, with the Canada-France High-Redshift Quasar Survey (CFHQS; Willott et al. 2007, 2009, 2010), the Panoramic Survey Telescope And Rapid Response System (Pan-STARRS; Bañados et al. 2016, Chambers et al. 2016, Tang et al. 2017), and the Dark Energy camera Legacy Survey (DELS; Reed et al. 2017, Wang et al. 2018, 2019, Yang et al. 2019).

Due to sensitivity limits, the $z \gtrsim 6$ quasars observed are all very luminous, shining close to the Eddington limit. They are likely only representative of a small portion of all quasars that can be found in the high-redshift Universe. To have a better understanding of the formation and evolution of these quasars and their SMBHs, it is crucial to find less luminous quasars at $z \gtrsim 6$, which would be equivalent low-redshift "ordinary" quasars. Surveys such as the Subaru High-z Exploration of Low-Luminosity Quasars (SHELLQ; Kashikawa et al. 2015, Matsuoka et al. 2016, 2018, 2019a,b) have been able to detect over 70 quasars in the past few years, starting to populate the lower-end of the quasar luminosity function.

Many of the highest redshift quasars have also been discovered combining multiple surveys, with the United Kingdom Infrared Telescope (UKIRT) and Deep Sky Surveys (UKIDSS; Lawrence et al. 2007, Mortlock et al. 2011), the VISTA Kilo-degree Infrared Galaxy (VIKING) Survey (Edge et al. 2013, Venemans et al. 2013) and the VLT Survey Telescope - ATLAS (VST-ATLAS; Carnall et al. 2015, Chehade et al. 2018) to name a few. There is now close to 300 quasars detected at $z > 6$ (Bosman 2022) and with the launch of the James Webb Space Telescope (JWST) in 2021, already probing ultra-high-redshift galaxies ($z \gtrsim 9$) within the epoch of Reionization (Adams et al. 2022, Atek et al. 2022), as well as the advent of Euclid and the Nancy Grace Roman Space Telescope surveying the infrared, more quasars at $z > 7$ will be discovered in the near future.

One of the most remarkable features of these high-redshift quasars is the massive SMBHs that they host. The most massive SMBH found at $z \gtrsim 6$ is a $\sim 1.2 \times 10^{10}\,\mathrm{M}_\odot$ BH at $z = 6.30$ (Wu et al. 2015). This monster is not alone, as the most distant quasar from which a SMBH mass could be estimated is J0313-1806 and is found at $z = 7.62$ ($\sim 700\,\mathrm{Myr}$ after the Big Bang) and hosts a SMBH of $(1.6 \pm 0.4) \times 10^9\,\mathrm{M}_\odot$ (Wang et al. 2021). Out of all the SMBHs discovered in the low-luminosity end (from the SHELLQ survey), the SMBHs have an estimated mass $M_{\mathrm{BH}} \gtrsim 10^7\,\mathrm{M}_\odot$ (see Fig. 2 from Inayoshi et al. 2020). These masses are already similar to the SMBHs found in the local Universe, after 13 Gyr of growth (see Section 1.3.1 and Fig. 1.2).

Since the first stars (PopIII) are believed to be formed at $z \simeq 30$ (Baraffe et al. 2001) when the Universe was $\sim 100\,\mathrm{Myr}$ old, it leaves less than 900 Myr for a SMBH to form and have grown from a stellar mass BH (the progenitor is commonly referred to as "seed"). The formation and rapid growth of these compact objects at such an early stage of the Universe are one of the most important puzzles faced by modern astrophysics. In the next Sections, we will investigate theoretical expectations on the assembly of SMBHs within 1 Gyr after the Big Bang and how some of them may have grown very efficiently up to $> 10^9\,\mathrm{M}_\odot$.

1.4 A timescale problem with its solutions

Explaining the very short amount of time for small BHs to become supermassive, is one of the many challenges astrophysicists face nowadays. This question was already in place after

the discovery of quasars at $4 < z < 5$ (Turner 1991), but the realization that SMBHs were already very massive at $z \gtrsim 6$ made it significantly more intriguing (Haiman & Loeb 2001). How can BHs grow of several orders of magnitude within 1 Gyr? In this Section, we discuss the assembly of massive BHs with the different scenarios proposed to explain their growth.

1.4.1 BH growth via gas accretion

An important growth channel for SMBHs is via accretion of gas (besides merger events, see Section 1.4.4 for discussion). We have discussed in Section 1.3.1 that material falling into the deep gravitational potential well of BHs results in a fraction of the gravitational binding energy radiated away. The efficiency of matter-to-radiation conversion of BHs, for radiatively efficient sources (thin discs) is related to the BH spin and varies from about 4 to almost 40 per cent, depending if the accretion disc is in co/counter rotation with the BH (Novikov & Thorne 1973, Shapiro & Teukolsky 1983)[3]. This is more than an order of magnitude larger than the maximum efficiency of nuclear fusion reaction. A typical value used in the literature is 10 per cent, which corresponds to an average spin value of 0.7. Therefore, for some infalling gas, the bolometric luminosity of the BH can be expressed as:

$$L = \epsilon_{\rm r} \dot{M}_{\rm acc} c^2 \,, \tag{1.3}$$

with $\epsilon_{\rm r}$ the radiative efficiency, $\dot{M}_{\rm acc}$ the accretion rate and c the speed of light. The mass that is not radiated away is what actually contributes to the BH growth:

$$\dot{M}_{\rm BH} = (1 - \epsilon_{\rm r}) \dot{M}_{\rm acc} \,. \tag{1.4}$$

An approximation for an upper limit of $\dot{M}_{\rm acc}$ onto a BH comes from a simple spherical model. We assume that we have a massive object of mass $M_{\rm BH}$, surrounded by a gas shell of radius r. The BH accretes some gas from this shell, and a portion of it will be radiated away, as expressed in Eq. 1.3, thus impacting the inflowing material. There is a luminosity limit, the Eddington luminosity $L_{\rm Edd}$, at which the (outwards directed) radiation pressure balances the (inwards directed) force of gravity. Above this limit, a wind is formed and matter is pushed away from the BH; while at the limit, the gas is held in a hydrostatic equilibrium. Within the spherical geometry, one can write the force of gravity as:

$$F_{\rm grav} = \frac{G M_{\rm BH} m_{\rm p}}{r^2} \,, \tag{1.5}$$

where G is the gravitational constant and $m_{\rm p}$ the proton mass. Similarly, the radiative pressure force can be expressed as:

$$F_{\rm rad} = \frac{\sigma_{\rm T} L}{4\pi r^2 c} \,, \tag{1.6}$$

[3]The gravitational accretion efficiency can be more than one order of magnitude larger than p-p nuclear efficiency, with for example the nuclear fusion reaction inside the Sun at ∼0.7 per cent, *i.e.* two orders of magnitude lower than the typical radiative efficiency of a BH.

with σ_T the Thomson cross-section. The equilibrium of the forces $F_{grav} = F_{rad}$ gives $L = L_{Edd}$ (Eddington 1921) which is defined as:

$$L_{Edd} \equiv \frac{4\pi G m_p c M_{BH}}{\sigma_T} \simeq 1.3 \times 10^{47} \left(\frac{M_{BH}}{10^9\,M_\odot} \right) \mathrm{erg\,s^{-1}}\,, \tag{1.7}$$

that can in turn be written in terms of maximum accretion rate *assuming spherical symmetry* $\dot{M}_{Edd}$,

$$\dot{M}_{Edd} = \frac{L_{Edd}}{\epsilon_r c^2}\,. \tag{1.8}$$

This corresponds to the maximum accretion rate onto the BH under the assumptions that most of the gas in the ISM is ionised hydrogen and that radiation is emitted isotropically. The value of the radiative efficiency may vary (see Section 1.5.2), but for the rest of this discussion we set $\epsilon_r = 0.1$. Therefore, while the general expression follows Eq. 1.8, we shall define for the rest of this thesis, unless otherwise noted:

$$\dot{M}_{Edd} \equiv \frac{L_{Edd}}{0.1 c^2}\,. \tag{1.9}$$

We define the ratio of the bolometric luminosity-to-Eddington, known as the Eddington fraction f_{Edd}, as:

$$f_{Edd} \equiv \frac{L}{L_{Edd}}. \tag{1.10}$$

Whilst the luminosity is an outcome of accretion, we use this parameter to determine how efficiently a BH is accreting.

Under the assumption that SMBHs are assembled by the accretion of gas, combining Eqs. 1.7 to 1.10 in Eq. 1.4, one finds:

$$\dot{M}_{BH} = \left(\frac{1-\epsilon_r}{\epsilon_r} \right) f_{Edd} \frac{M_{BH}}{t_{Edd}}\,, \tag{1.11}$$

with $t_{Edd} \equiv M_{BH} c^2 / L_{Edd} = 0.45\,\mathrm{Gyr}$, the Eddington timescale. After integrating, one obtains:

$$M_{BH}(t) = M_{BH}(t=0) \exp\left(\frac{t}{\tau_{Edd}} \right)\,, \tag{1.12}$$

$$\tau_{Edd} = t_{Edd} \left(\frac{\epsilon_r}{1-\epsilon_r} \right) f_{Edd}^{-1}\,, \tag{1.13}$$

with the seed mass $M_{BH}(t=0)$ and the e-folding timescale τ_{Edd}. With the fiducial value of $\epsilon_r = 0.1$, there are only two variables that can be used to determine the mass of a BH at a given time: the seed mass $M_{BH}(t=0)$ and the Eddington fraction f_{Edd}. As shown in Fig. 1.3, to explain the massive SMBHs at $z \gtrsim 6$, one requires stellar mass BHs accreting constantly at the Eddington limit at very high redshifts, or very massive BHs accreting at relatively low per cent of the Eddington limit. We also note that decreasing the radiative efficiency has been hailed as a possible option (King & Pringle 2006).

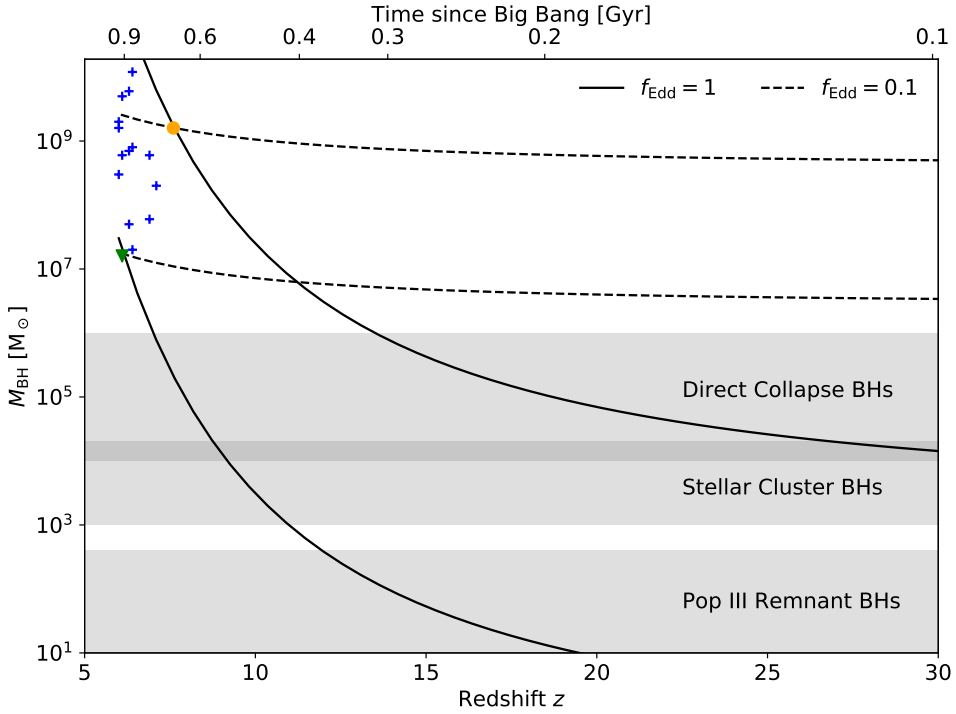

FIGURE 1.3: Theoretical growth of $z \gtrsim 6$ SMBHs. Coloured markers show a sample of SMBHs observed at $z \gtrsim 6$. Dark lines show theoretical growth of two SMBHs (orange circle and green triangle), at a fixed $\epsilon_{\rm r} = 0.1$ and constant growth ($f_{\rm Edd} = 0.1$ in dashed and $f_{\rm Edd} = 1$ in solid). Shaded areas represent the different theoretical seed formation channels detailed in Section 1.4.2.

1.4.2 SMBH seeds at high-redshifts

Over the years, several formation channels have been suggested for the progenitors of SMBHs and three stand out as the most popular ones: PopIII remnants, dense stellar clusters and direct collapse. The formation processes require different initial conditions, leading to a different seed mass distribution ranging typically from 10 to $10^6\,M_\odot$.

Heavy seeds

We start with the most massive case, the "direct collapse" model. The formation of "massive" seeds gives them a decent head start to reach $\gtrsim 10^9\,M_\odot$. This scenario is popular as it predicts the formation of 10^4 to $10^6\,M_\odot$ BH seeds (*e.g.* Rees 1984, Bromm & Loeb 2003, Shang et al. 2010, Johnson et al. 2011, Agarwal et al. 2012, 2016a,b, 2017, Latif et al. 2013, 2014, 2016b, Latif et al. 2018, 2020, Whalen et al. 2020), thus easing the constraints on seed masses required to explain the $z \sim 6$ SMBHs population. The term "direct collapse" can be misleading because forming such BHs still requires an intermediate stage of a stellar structure (supermassive, see *e.g.* Shibata & Shapiro 2002, Inayoshi et al. 2014, Inayoshi & Haiman 2014; or "quasistar", see *e.g.* Begelman et al. 2006, Begelman 2010, Volonteri & Begelman 2010).

Gas needs to collapse in a single massive object, uninterrupted by fragmentation, meaning that gas needs to be dust and metal poor (*e.g.* Regan et al. 2020), so that cooling processes do not occur. Moreover, a key requirement for the formation of such BH seeds is the very high accretion rates exceeding $0.01\,M_\odot\,{\rm yr}^{-1}$, in order to sustain the stellar structure (*e.g.* Omukai & Palla 2003). Such accretion rates are expected to negate the ionizing radiation

from the star itself, leading to its collapse in a BH via the general relativistic instability (*e.g.* Sakurai et al. 2016a). Such conditions are suggested to be found in atomic cooling halos (*e.g.* Oh & Haiman 2002, Bromm & Loeb 2003), structures more massive than minihalos (10^7 to $10^8\,M_\odot$) with virial temperatures $\gtrsim 10^4$ K.

In order to prevent the gas from cooling and inhibit star formation, a strong Lyman Werner flux of photons that photo-dissociates molecular hydrogen is needed (*e.g.* Omukai 2001). Knowing the threshold above which photo-dissociation becomes effective allows one to estimate of the number of atomic cooling halos that massive seeds can form (*e.g.* Dijkstra et al. 2008, Agarwal et al. 2012), although several authors discuss that this threshold may not be unique (*e.g.* Agarwal & Khochfar 2015, Agarwal et al. 2016b). Other models also suggest that these atomic cooling halos can be exposed to the high Lyman Werner radiation from newly ($\lesssim$ several Myr) formed stars a nearby subhalo: the so-called "synchronized pair of halos" scenario (see Visbal et al. 2014 and references therein).

Having an atomic cooling halo is not always needed, as recent work from Latif et al. (2022) shows that turbulent cold flows prevent star formation until a certain mass threshold is reached, forming a massive stellar structure without the need of atomic cooling. Chon & Omukai (2020) have also shown that a heavy seed can still form in halos slightly enriched, where fragmentation has started, as the metal poor gas feeds the growing stellar structure. Runaway collisions in a stellar cluster may also provide enough material to create a sufficiently massive stellar structure, by preventing its contraction (Tagawa et al. 2020, Das et al. 2021). Other possible mechanisms able to form very massive seeds have been suggested, such as "merger-driven direct collapse" (see Mayer & Bonoli 2019 and references therein), where multiple massive gas-rich galaxies merge, leading to extremely rapid inflow rates $\gtrsim 10^3\,M_\odot\,\mathrm{yr}^{-1}$ and creating (with or without a stellar structure stage) a very massive seed.

Due to the strict environmental conditions enumerated earlier (no efficient cooling mechanisms, strong Lyman Werner radiation, large and continuous inflow rates), the formation of heavy seeds is predicted to be quite rare (*e.g.* Dijkstra et al. 2008, Agarwal et al. 2012, 2014, Habouzit et al. 2016, Valiante et al. 2016). However, due to the difficulties to constrain the formation mechanisms of heavy seeds, their number density is still uncertain.

Medium seeds

In the early Universe, fragmentation may occur in environments with densities of the order of $10^9\,\mathrm{amu\,cm}^{-3}$ (*e.g.* Clark et al. 2011, Greif et al. 2011, 2012, Smith et al. 2012), but can also be helped with traces of dust grains (*e.g.* Schneider et al. 2003, Schneider et al. 2006b, 2012, Omukai et al. 2008, Dopcke et al. 2011, 2013, Klessen et al. 2012, Bovino et al. 2016). These provide ideal conditions for the formation of very dense clusters, which have a typical mass of $\sim 10^5\,M_\odot$ and $\sim$ pc radii (Volonteri 2010). A large fraction of them will collapse on timescales shorter than the lifetime of massive stars; consequently, runaway collisions amongst the stellar population lead to the formation of a massive BH seed of 10^3 to $10^4\,M_\odot$ (*e.g.* Omukai et al. 2008, Devecchi & Volonteri 2009, Lupi et al. 2014, Katz et al. 2015, Yajima & Khochfar 2016).

In the scenario where the core collapse happens on timescales longer than the lifetime of stars, the stellar cluster will be left with stellar mass BHs that can undergo runaway growth into a 10^3 to $10^4\,M_\odot$ BH, via tidal interactions (*e.g.* Stone et al. 2017, Sakurai et al. 2019).

Another possibility may be that the stellar mass BHs merge as they sink via dynamical friction towards the center of the collapsing cluster, producing a seed in the similar mass range (Giersz et al. 2015). However, gravitational recoil from merging the BH binaries could eventually lead to the expulsion of the merged BHs, unless the escape velocity of the stellar cluster is sufficiently high to retain the kicked BH, potentially generating multiple merging episodes and leading to significant mass growth (Antonini et al. 2019).

Light seeds

Finally, as introduced in Section 1.2.1, the first generation of stars (PopIII) formed from metal-free gas could leave remnants[4] of up to $\sim 10^2\,\mathrm{M}_\odot$ (*e.g.* Madau & Rees 2001, Volonteri et al. 2003, Johnson & Bromm 2007, Turk et al. 2009, Jeon et al. 2012, Smith et al. 2018). This scenario provides small BH seeds in comparison to the other formation channels, meaning that their accretion rates will be small in comparison (see Eq. 1.9). However, since they are believed to form at the end of the Dark Ages, they have more time to accrete. Such stellar remnants are also expected to form far more frequently than more massive ones from the "direct collapse" model for example (*e.g.* Sassano et al. 2022). If a small fraction of PopIII remnants are able to maintain accretion rates close to the Eddington limit for their entire growth until $z \sim 6$, they would grow by a factor $\sim 10^6$, thus explaining *some* of the population of high-redshift quasars (see Fig. 1.3).

Due to the radiation of PopIII stars, it has been suggested that they heat the minihalo they form in and eject the ionized gas (*e.g.* Whalen et al. 2004, Johnson & Bromm 2007). Furthermore, at their death, their SN explosions may also evacuate the gas, owing to the shallow gravitational potential of the minihalo (*e.g.* Whalen et al. 2008, Ritter et al. 2012). Accretion onto the stellar remnant is therefore likely not to be in a high density environment. Even in the scenario where the PopIII radiation or SN explosion were not able to starve the newly formed remnant, the feedback produced by the accreting BH could be enough to evacuate its surroundings (*e.g.* Alvarez et al. 2009, Jeon et al. 2012). It could also simply wander owing to erratic motion outside of dense regions meaning that the BH growth would remain inefficient (Smith et al. 2018). Nonetheless, rare massive ($M_\mathrm{h} \gtrsim 10^8\,\mathrm{M}_\odot$) halos could fulfill the conditions for sustained Eddington accretion (Tanaka 2014).

The $z \sim 6$ SMBH progenitors are characterised by different formation mechanisms which are not mutually exclusive, and a variety of seeds that could form in the Universe (Volonteri & Begelman 2010, Sassano et al. 2022, Spinoso et al. 2022). In the next Section, we explore the questions related to the availability of gas to feed continuously these seeds.

1.4.3 Gas inflows feeding the seed

Regardless of the seeding mechanisms in play at high-redshift, we must discuss the availability of gas to sustain high accretion rates on the BH seed. To study this question, very large-scale ($> 100\,\mathrm{Mpc}$) cosmological simulations are often invoked, due to the statistically significant number of massive ($\gtrsim 10^{12}\,\mathrm{M}_\odot$) halos that they can produce. Such simulations provide necessary information related to the large scale inflows of gas, that can potentially sustain high accretion rates all the way down to the seed.

[4] As long as their stellar masses are outside of the pair instability mass range, *i.e.* $140 - 260\,\mathrm{M}_\odot$ (Fraley 1968).

At large scales, cold filamentary streams connected to the cosmic web can survive powerful outflows from AGN. For example, Di Matteo et al. (2012) and Khandai et al. (2012) have found that the most massive BHs in their most massive halos were continuously fed via cold filamentary infall, despite AGN feedback, and were able to reach several $10^9\,M_\odot$ at $z \simeq 6$. Dubois et al. (2012a) have shown that, cold flows were directly responsible for maintaining sufficiently large amounts of gas in the bulge, allowing the BH to accrete at its maximum rate. For instance, in the absence of feedback, gas fell nearly radially to feed the center of the galaxy, and once filaments gained angular momentum, they contributed to the formation of proto-galactic discs (Pichon et al. 2011), which gave rise to the formation of a gravitationally unstable disc component surrounding the bulge of the galaxy. This caused disc instabilities and clump migration, bringing large quantities of gas towards the bulge (Bournaud et al. 2011).

On smaller scales, the dynamics of accreting gas is influenced by gravity from the compact object, at the so-called Bondi radius (Bondi 1952). Gas is captured in the gravitational sphere of influence of the BH and is assumed to flow inwards at supersonic velocities. This accretion rate is supposed to be in general an upper limit on the accretion rate as it assumes free-fall of the gas from the Bondi radius, but inflows can be heavily influenced by feedback mechanisms (see Section 1.3.2) or rotation. For instance, continuous accretion at Eddington levels is challenging to sustain, as feedback from gas accretion onto the BH seed can severely affect gas inflows and prevent efficient BH growth (*e.g.* Johnson & Bromm 2007, Alvarez et al. 2009, Milosavljević et al. 2009, Dubois et al. 2013). It is also interesting to note that even in the absence of such mechanisms, if the gas is very cold (therefore, for a given $M_{\rm BH}$, the Bondi radius and accretion rates are high), gas may be susceptible to gravitational perturbations (Hopkins & Quataert 2010).

Accretion of cold and turbulent gas, in the so-called "chaotic" (or incoherent) accretion, provides an alternative growth mechanism for SMBHs (e.g. King et al. 2005, 2008, Zhang & Lu 2019, Zhang et al. 2020, Zubovas & King 2021). In this scenario, the gas flows from random directions towards the BH, keeping the BH spin magnitude low. This keeps radiative efficiencies low, providing more efficient growth.

As discussed above, inflows of cold gas can stream all the way down to the seed. With efficient feeding, BH seeds could grow very rapidly if the accretion rates are not capped by the Eddington limit (*e.g.* Haiman 2004, Shapiro 2005, Volonteri & Rees 2005, Volonteri et al. 2015). Analytical models have shown that a PopIII remnant seed could grow from $10^2\,M_\odot$ to a few $10^9\,M_\odot$ within 1 Gyr (Madau et al. 2014), thanks to reduced radiative efficiency. Similarly, if the PopIII remnants are embedded in very dense environments (Lupi et al. 2016) or in dense stellar clusters (Alexander & Natarajan 2014), they can achieve brief and recurring periods of super-critical (*i.e.* super-Eddington) accretion and grow into $\gtrsim 10^4\,M_\odot$ BHs in a few 10^6 to 10^7 yr. Furthermore, super-Eddington accretion can contribute significantly to the seed growth, all the way up until $z \sim 6$ (Pezzulli et al. 2016), and even when feedback mechanisms associated with the critical accretion are present, super-Eddington growth of the first SMBHs from light BH seeds can be explained if the inflowing gas has low angular momentum (Pezzulli et al. 2017). Finally, super-Eddington accretion is not limited to PopIII remnants, as (*e.g.*) Pacucci & Ferrara (2015) discussed the growth of $M_{\rm BH} = 10^5\,M_\odot$ seeds growing efficiently at super-Eddington rates. A discussion related to the super-Eddington

regime is devoted to Section 1.5.

1.4.4 The role of BH-BH mergers

As mentioned in Section 1.4.1, another growth channel for SMBHs is via BH-BH mergers. During the process of galaxy mergers, the two SMBHs can also merge and contribute to the growth of the remnant SMBH if their coalescence is shorter than the Hubble time (*e.g.* Volonteri et al. 2003, Sesana et al. 2007, Valiante et al. 2021). During the galaxy merger, dynamical friction (Chandrasekhar 1943) against stars, DM and gas can lead to the dragging of the two SMBHs towards the center of the new galaxy, thus reducing their separations from kpc-scales down to pc-scale distances and forming a binary system (*e.g.* Begelman et al. 1980, Callegari et al. 2011, Capelo et al. 2015). The emission of gravitational waves only becomes efficient when the separation is below the milliparsec-scale, leading to the eventual coalescence. This "final parsec problem" (Milosavljević & Merritt 2003) has been studied for decades and different processes have been suggested to happen from pc- to millipc-scales, such as scattering with stars (*e.g.* Quinlan 1996, Khan et al. 2012) or interactions with another incoming BH (see Bonetti et al. 2018 and references therein) or with a circumbinary disc (*e.g.* Dotti et al. 2007, Goicovic et al. 2017).

Growth via mergers has been expected to play a major role in the formation of SMBHs at high-redshift (*e.g.* Petri et al. 2012, Valiante et al. 2016, Dayal et al. 2019). BH-BH mergers, by themselves, cannot explain the formation of $z \gtrsim 6$ SMBHs, as high accretion rates are still required, almost independently of the initial seed mass (*e.g.* Sesana et al. 2007, Tanaka & Haiman 2009). This is partially due to the gravitational recoil that the merged BH seeds are assumed to experience, due to the emission of gravitational waves. The remnant BH has a typical recoil velocity of a few $100\,\mathrm{km\,s^{-1}}$ depending on the spin and mass configuration before merging occurs (Campanelli et al. 2007, Herrmann et al. 2007), which can be high compared to the escape velocity of the halo at very high-redshift. This could lead to the ejection of the BH from its halo, therefore unable to accrete at high rates, thus slowing its growth (Haiman 2004). Whilst this is a pessimistic scenario for merger-driven BH growth, Volonteri & Rees (2006) have suggested that, if the BH grows more massive before experiencing its first merger, then the kick velocity from the recoil will be significantly lower (down to a few $\mathrm{km\,s^{-1}}$), leading to the possibility of explaining the $z \sim 6$ SMBHs. In addition, recent work from Pfister et al. (2019) show that if the mass of the BH in the satellite galaxy is $M_{\mathrm{BH}} < 10^4\,\mathrm{M_\odot}$, they are unlikely to contribute to the merging population, as the sinking process via dynamical friction to the center of the main galaxy would take too long.

Overall, a merger-driven growth at high-redshift is feasible but does not solve by itself the timescale issues discussed in Section 1.4.1. Gas accretion is still required to explain the population of high-redshift SMBHs. A combination of different seeding channels and growth mechanisms may be in play in the high-redshift Universe. As one pathway may be more prevalent than an other, depending on the local environment conditions, we explore in the next Section the possibility of accreting more than the Eddington limit.

1.5 The super-Eddington regime

There are several theoretical models that have been developed to form SMBHs starting from various seed sizes. We have seen that if BHs accreted continuously at the maximum accretion rate set by the Eddington limit, a massive seed is required at very early times to explain the most massive SMBHs detected. However, this calculation not only assumes that the Eddington limit sets a hard limit to the maximum a BH can accrete in a given time, but also supposes that the luminosity of the compact object grows proportionally to the accretion rate. This latter point is a reasonable assumption if the BH accretion rate is well below the limit, as the effects of radiative forces on the accreting material are relatively small or can be ignored (this shall be covered in Section 1.5.2). One can view the Eddington limit as an estimate to when radiative pressure forces (along with other effects) start to affect the accretion flow. In this Section, we detail some observations of sources that seem to break the Eddington limit and discuss the characteristics of this regime.

1.5.1 Observational evidence of super-Eddington sources

Concerning AGNs, SMBHs accreting above the Eddington limit are found at all redshifts (see Fig. 3 of Yang et al. 2021[5] which compares $f_{\rm Edd}$ for both low- and high-redshift quasars). As pointed out by Pognan et al. (2020), who generated super-Eddington accretion disc spectral energy distributions mimicking the photon-trapping effects (see Section 1.5.2 for a definition), there may be a hidden population of super-Eddington accreting AGNs that have been missed by optical quasar surveys such as SDSS. A subclass of AGNs that are candidates to host these SMBHs are narrow-line Seyfert-1 galaxies (*e.g.* Boroson & Green 1992, Mineshige et al. 2000, Wang & Netzer 2003, Collin & Kawaguchi 2004, Du et al. 2014, 2018, Jin et al. 2017, Yao et al. 2021). These galaxies are characterised by their "narrow" broad lines (in their BLR). On average, they have very strong FeII emission and weak [OIII] lines (see Komossa 2008 for a review). Furthermore, it was found that they all have steep soft X-ray excess (Boller et al. 1996), which corresponds to the emission super-Eddington accretion discs are predicted to have in some models (Kawaguchi 2003, Collin & Kawaguchi 2004).

Other sources have been observed and estimated to be accreting at rates above the limit. For instance, transient systems such as tidal disruption events (TDEs) exceed the Eddington luminosity over short timescales (a few days to years) (*e.g.* Hills 1975, Burrows et al. 2011, Cenko et al. 2012, Guillochon & Ramirez-Ruiz 2015, Lin et al. 2017, 2022, Angus et al. 2022). TDEs happen when a star is subject to tidal forces after it passes sufficiently close to a BH that tidal forces are stronger than the self-gravity of the star, disrupting its envelope. A fraction of the star forms an accretion disc around the BH and produces flares with a well-defined time-evolution. The super-Eddington nature found in some TDEs comes from the highly luminous observed X-ray/soft gamma-ray emission ($L_{\rm X} \simeq 100 L_{\rm Edd}$) that is believed to be produced by a relativistic collimated magnetised jet with low opening angles (*e.g.* Giannios

[5]We note that an interesting feature of high-redshift quasars is that the estimated Eddington ratios are high on average (*e.g.* Kurk et al. 2007, Jiang et al. 2007, Willott et al. 2010, Schindler et al. 2020, Yang et al. 2020, Wang et al. 2021), close to (or greater than) unity. As mentioned in Section 1.3.3, the question of whether the high Eddington ratios of these high-redshift quasars are intrinsic or affected by selection effects is still debated, since high-redshift surveys probe the relatively luminous end of the distribution.

& Metzger 2011, Zauderer et al. 2011, 2013, Berger et al. 2012, Metzger et al. 2012, Wiersema et al. 2012, Tchekhovskoy et al. 2014).

In the outskirts of galaxies, extremely bright (10^{39} to $10^{41}\,\mathrm{erg\,s^{-1}}$) systems named ultra luminous X-ray (ULXs) sources can be found (Makishima et al. 2000, see also Kaaret et al. 2017 for a review). A neutron star of $2\,\mathrm{M_\odot}$ in a binary system has an Eddington limit of $\sim 2\times10^{38}\,\mathrm{erg\,s^{-1}}$. This means that, in order not to violate the classical limit, astronomers believed that the first detections of ULXs had a very massive compact object: an intermediate mass BH accreting at sub-Eddington rates (Colbert & Mushotzky 1999). While some ULXs are good intermediate mass BHs candidates (especially the brightest ones with $> 10^{41}\,\mathrm{erg\,s^{-1}}$, see Barrows et al. 2019 and references therein) accreting at sub-Eddington rates, analysis of other ULXs spectra favours smaller compact objects accreting at critical rates in a binary system with a donor star (*e.g.* King et al. 2001, Winter et al. 2006, Poutanen et al. 2007, Gúrpide et al. 2021). An indirect clue for super-Eddington accretion comes from the presence of bubbles or cavities of ionised gas around some ULXs (*e.g.* Pakull & Mirioni 2002, Grisé et al. 2012, Berghea et al. 2020, Soria et al. 2021), indicating strong jetted outflows. Furthermore, the detection of a pulsation provides more direct evidence that some systems host an accreting neutron star (*e.g.* Bachetti et al. 2014, Bachetti et al. 2021, Israel et al. 2017a, Israel et al. 2017b, Quintin et al. 2021), a compact object which mass cannot exceed a few $\mathrm{M_\odot}$ and can also display relativistic outflows (*e.g.* Migliari & Fender 2006, Coriat et al. 2019), reaching luminosities far above the classical limit for a neutron star.

The most famous example of a super-Eddington accretor is found in our Galaxy: SS433 (*e.g.* Stephenson & Sanduleak 1977, Margon et al. 1984, Okuda 2002, Fabrika 2004). This high-mass X-ray binary system hosts a compact object which nature remains unknown, although the presence of a BH is suggested (Goranskij 2011, Han & Li 2020, Cherepashchuk 2021), and a secondary giant star of a few $\mathrm{M_\odot}$. Despite lower luminosities than ULXs found outside of the Milky Way, this microquasar also produces precessing jets with mass outflow rates ~ 300 times the Eddington limit (Fuchs et al. 2006), thus suggesting super-critical accretion (King 2002). In comparison to transient events such as TDEs, systems like SS433 and ULXs can have sustained high luminosities for several years, making them one of the best laboratories to explore super-Eddington accretion in the local Universe.

1.5.2 Characteristics of the critical regime

From thin disc to slim disc

Over the last decades, several theoretical models have been developed to understand how the accretion flows behave around compact objects such as BHs. We start this discussion with the most understood state of accretion: the standard, geometrically *thin disc*, also referred to as "thermal" state (Novikov & Thorne 1973, Shakura & Sunyaev 1973). This disc structure occurs between about 1 per cent to the Eddington luminosity (*i.e.* $0.01 < f_{\mathrm{Edd}} \leq 1$). The accretion disc is supported by gas and radiation pressures, which balances the vertical force of gravity. As the gas rotates on keplerian orbits, it gradually loses angular momentum due to viscosity, moving very slowly closer to the BH, one keplerian orbit after the other. It is believed that these discs are viscous due to magnetorotational instabilities (MRI; Balbus & Hawley 1991). Such discs have high optical depths $\tau \gg 1$, making them optically thick,

meaning that the gas on each orbit radiates as a blackbody, at their own temperatures. It takes significantly longer for the gas in the disc to reach the BH than to radiate viscously-generated energy, meaning that all the emission is radiated locally, where it is produced. This makes such discs radiatively-efficient. The disc is therefore cool and geometrically thin, typically with low disc scale height, *i.e.* $h/r \ll 1$.

Once the thin disc theory was established, it was commonly understood that these discs could break the Eddington limit. It is now also widely accepted that the classical limit can be exceeded in disc accretion because of the separation of the directions of the gas inflow and of the radiation output. In their seminal paper, Shakura & Sunyaev (1973) predicted that the excess energy when breaking the Eddington limit goes into powering outflows. For instance, the inner regions, which are the most energetic, would produce a radiatively driven outflow inside the so-called spherization radius $r_{\rm sp}$. The disc is still radiatively efficient, and in the inner regions radiation inflates the disc which becomes geometrically thick, *i.e.* $h/r \gg 1$; while the outer regions remain thin even if the accretion rates are super-critical. This spherization radius, where the accretion luminosity first reaches the Eddington limit, corresponds to the distance where the thickness of the disc becomes of the order of the distance from the BH:

$$r_{\rm sp} = \frac{9}{4}\dot{m} r_{\rm Sch} \,, \tag{1.14}$$

where $\dot{m} \equiv \dot{M}_{\rm acc}/\dot{M}_{\rm Edd}$ is the normalised accretion rate and $r_{\rm Sch}$ is the Schwarzschild radius. Shakura & Sunyaev (1973) find that the luminosity of the radiatively driven outflows exceeds the Eddington limit logarithmically as $L_{\rm Edd} \times \ln \dot{m}$, meaning the total luminosity of the disc in the super-Eddington regime is:

$$L = L_{\rm Edd}(1 + \ln \dot{m}) \,. \tag{1.15}$$

This picture does not take into account an important effect. Since the properties of the disc changes within the inner regions and thickens (both optically and geometrically), photons now have to undergo multiple scatterings before reaching the disc surface. Therefore, advection, another mechanism of cooling which corresponds to the transport of radiation along r, will affect the local radiation for each radius in the inner regions. This means that photons do not have enough time to diffuse vertically before they are dragged radially inwards by the inflowing gas. This "photon-trapping" effect (Katz 1977, Begelman 1978) indicates that most of the photons are locked up inside the accretion flow and end up advected with the accretion flow and captured by the BH, with only a small fraction escaping, *i.e.* the disc is radiatively-inefficient. The trapping radius $r_{\rm trap}$ inside which the photon-trapping effect is significant is given by (*e.g.* Kato et al. 2008) :

$$r_{\rm trap} = \frac{3h}{2r}\dot{m} r_{\rm Sch} \,. \tag{1.16}$$

This also implies that luminosity does no longer increase linearly with the accretion rate, but instead increases logarithmically. Abramowicz et al. (1988) constructed for the first time an accretion disc model for the super-Eddington regime including photon-trapping effects:

the so-called *slim disc*. It has since been done using a fully relativistic treatment by Beloborodov (1998).

As discussed above, both ways of understanding the structure of the accretion flows lead to the same conclusion: the luminosity follows a logarithmic law when $\dot{m} > 1$. Furthermore, these effects shown in Eqs. 1.14 & 1.16 become physically relevant when these radii are outside of $r_{\rm Sch}$, *i.e.* for $\dot{m} \gtrsim 0.1$. In the first case, the excess of radiation triggers winds and radiatively driven outflows, whilst in the second case, the excess of radiation is lost to advection towards the BH.

Photon-trapping effect in numerical simulations

Over the years, radiation hydrodynamical (RHD) simulations studied the high accretion flows and agree on finding photon-trapping effects above the Eddington limit. As shown by Fig. 1.4 which compiles theoretical (semi-analytical and numerical) results for radiative luminosity against the BH accretion rate, there is a discrepancy regarding how (in)efficient the photon-trapping effect is. For instance, 3D radiation MHD (RMHD) simulations (Jiang et al. 2014; shown with the pink squares) have shown that vertical advection caused by magnetic-buoyancy can reduce the effects of photon trapping around BHs in the super-Eddington regime. Some studies (Sądowski et al. 2015, Jiang et al. 2019) have also explored the very high accretion rates ($\dot{m} \gg 1$). In the general relativity RMHD (GRRMHD) setting, Sądowski et al. (2015) find very low radiative efficiencies ($\epsilon_{\rm r} \simeq 0.01$) in the "hyper-Eddington" regime ($\dot{m} \simeq 3000$) for a BH close to maximally spinning ($a = 0.9$). In their models, they emulate the magnetic dynamo operating in magnetized accretion discs and find that the luminosity is as high as $\sim 100 L_{\rm Edd}$, significantly above the analytical results in this regime. This shows that magnetic fields in the super-critical regime may play a key role at preventing radiatively-inefficient flows, since these effects are not taken into account in the analytical models (from Madau et al. 2014 in dashed orange and Watarai et al. 2000 in red solid lines). Finally, there are differences between numerical simulations. They come from the use of different numerical algorithms for radiative transfer (besides differences in magnetic field, geometry and size of the computational domain), which are more or less accurate and lead to different results, notably the flux-limited diffusion (*e.g.* Ohsuga et al. 2005, Kitaki et al. 2021b) and M1 closure (*e.g.* Sądowski et al. 2015).

Super-Eddington outflows

The super-Eddington regime not only features thermal emission (due to being optically thick), but also relativistic jets and winds, from its thick geometry. Discs which are geometrically thick tend to produce jets as evidenced by observations of AGNs and BH binaries. Several observational examples were given in Section 1.5.1 which had these relativistic outflows. On the numerical end, simulations of super-critical accretion are relatively new. This field was initiated with seminal works by Ohsuga et al. (2005, 2009), Ohsuga & Mineshige (2007), and Ohsuga & Mineshige (2011) who performed RHD simulations. Recent work from the same group with Kitaki et al. (2021b) and Yoshioka et al. (2022) find that the mass loaded in the outflows above the disc suface is smaller than the mass accreted by the BH, as a consequence of "failed outflows". These are outflows which leave the disc surface at

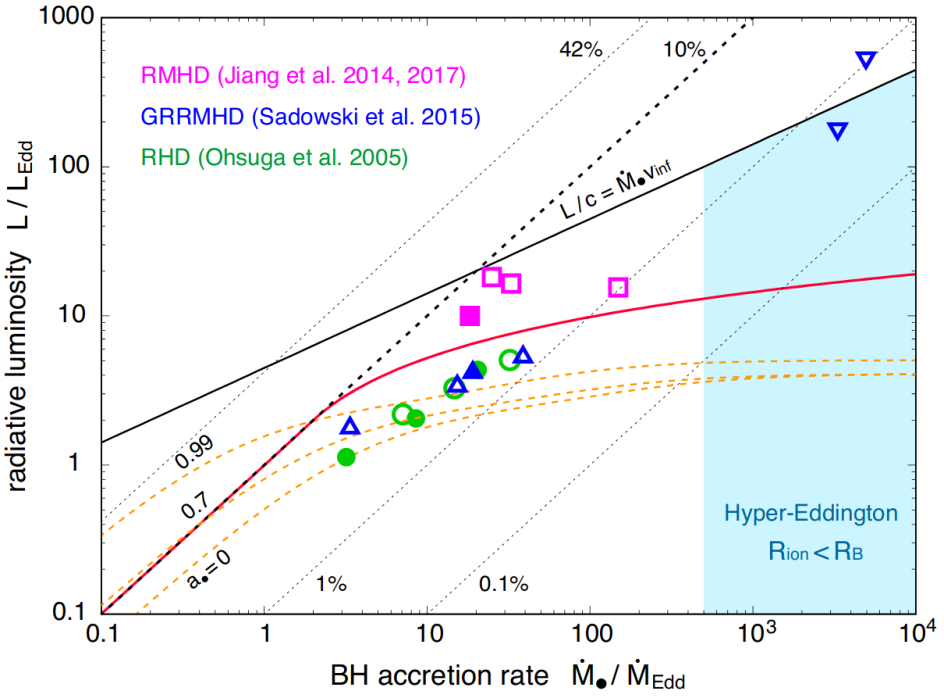

FIGURE 1.4: Summary of theoretical (analytical and numerical) results for the radiative luminosity vs the accretion rate of the BH, showing photon-trapping effects at super-critical rates. Analytical models are shown in solid red (Watarai et al. 2000) and dashed orange (Madau et al. 2014). Simulations are shown with the different markers. Figure from Inayoshi et al. (2020).

smaller radii but eventually fall back to the disc at large radii. Furthermore, they do not find a "puffed-up", *i.e.* geometrically thick, disc structure below the trapping radius. They also conclude that this lack of structure may also be responsible for the lower outflow rates they find. In parallel with these works, Hu et al. (2022a) performed very similar simulations and obtained significantly larger outflow rates. They believe this difference owes to the assumption of equatorial symmetry that the former simulations assume, which is known to suppress the convective motion of the gas and produces less outflows in the polar region (Li et al. 2013); as well as the larger viscosity parameter which is known to reduce the convection and decrease the outflow rates (*e.g.* Inayoshi et al. 2018).

The inclusion of GR in simulations was made a few years after the seminal works discussed before. It was McKinney et al. (2014, 2015), Sądowski et al. (2014), and Sądowski & Narayan (2015) who studied the polar outflows including GR, and performed some of the first simulations including jets with the accretion disc resolved. In their simulations, the magnetic field was in a magnetically arrested disc (MAD) state. In such a configuration, these accretion discs accumulate large-scale magnetic flux on the BH, until this flux becomes so strong that it chokes gas infall. The excess magnetic field leaves and pushes parts of the disc away: the accretion flow enters a MAD state. Sądowski et al. (2016) find that the properties of the flow of energy in the super-Eddington regime when a BH is rotating, can be considered as the superposition of the disc component (with an efficiency similar to the one found in thin discs), and the jet contribution coming from the Blandford-Znajek process (Blandford & Znajek 1977). Interestingly, they note that the power of the jets may overwhelm (in magnitude) the radiative outflows from the disc, but if the confinement provided by the geometrically thick disc is strong enough, these jets are likely to stay collimated.

All these works agree qualitatively on the main features of super-Eddington accretion, that super-Eddington accretion is possible, that these flows are optically and geometrically thick, and that they are characterized by strong polar outflows and significant winds. Other numerical works modelling the accretion disc near the BH find that if gas inflows are funneled in the equatorial plane with the radiation and outflows escaping out from the poles, then the accretion disc is stable despite important outflows, and super-Eddington accretion can be sustained (*e.g.* Inayoshi et al. 2016, Sakurai et al. 2016b, Sugimura et al. 2017, Takeo et al. 2018, 2020, Toyouchi et al. 2019, 2021). However, it is worth noting that these simulations have explored the properties of the accretion flows close to the BH, on small scales (typically sub-pc but sometimes all the way down to the accretion disc). One of the conditions of their studies is the imposed mass inflow from the outer boundary. The existence of outflows launched from rapidly accreting BHs is ubiquitous and can potentially affect the inflow of material from larger scales.

Outflows on large scales and impact on BH growth

Bridging the gap between BH accretion and galactic scales is essential to study the accretion physics far from the central object, and the impact that super-Eddington feedback may have on inflowing gas and growth overall. To this end, Botella et al. (2022) investigated larger scale nested simulations, from $r_{\rm Sch}$ all the way up to $\sim 10^6\,{\rm r_{Sch}}$ ($\sim 10^{-4}\,{\rm pc}$), where they separated the computation domain into several regions and treated the dynamics of accretion and feedback crossing those regions in a self-consistent way. They find that outflows on larger scales entrain ~ 60 per cent of the inflowing mass, larger than Kitaki et al. (2021b) but less than Hu et al. (2022a).

Inayoshi et al. (2022a) performed RHD simulations of a proto-galactic nucleus and investigated the growth of $10^5\,{\rm M_\odot}$ seed BHs during early bulge formation. Their resolution ranged from 10^{-1} to $10^2\,{\rm pc}$ and find that massive seeds were able to grow consistently, with little interruption, at hyper-Eddington rates, as anisotropic outflows were not affecting inflows. They confirm results from Takeo et al. (2020), who performed RHD simulations combining radiative and mechanical feedback and who found that gas in the polar region was completely evacuated, but gas inflows from the equatorial region maintained super-Eddington accretion rates. The outflows were able to pierce through the gas distribution without disrupting it.

Conversely, Regan et al. (2019) investigated how super-Eddington bipolar jet outflows affect gas inflows in an atomic cooling halo in a cosmological setting. They were able to reach resolutions down to the BH gravitational sphere of influence and found that jets almost entirely shut down the inflow of gas towards the BH on small scales ($\simeq 0.1\,{\rm pc}$) and were not able to break out of the halo. The effective accretion rate averaged over the simulation duration was found to be ~ 4 orders of magnitude below the Eddington limit, thus suggesting that BHs are not able to grow effectively above the limit with strong jetted outflows. The discrepancy between these results may be linked to the gas geometry, however it is unclear if the axisymmetric disc configuration in Takeo et al. (2020) can be achieved assuming the turbulent nature of high-redshift galaxies.

An isolated galaxy has also been studied by Sassano et al. (2022), in the context of the growth of a $10^3\,{\rm M_\odot}$ BH seed in a gas-rich proto-galaxy at $z = 15$. They include different

sub-grid models for the super-Eddington regime (the slim disc model with the radiative efficiency following Madau et al. 2014 and the "Jiang" model following Jiang et al. 2014, 2019 results) with a thermal feedback deposition of energy, and find that, in all their simulations, BHs are not growing owing to SN feedback shortly after 1 Myr of evolution. They notice that the regulation is faster for BHs with higher radiative efficiencies in the super-Eddington regime, and that the super-Eddington phase does not last more than 0.1 Myr. For the few BHs that reach $10^4\,M_\odot$, they extrapolate the final mass those BHs would have by $z \sim 6$, and find that they would fall short of the high-redshift population by ~ 3 orders of magnitude.

Zhu et al. (2022) performed zoom-in simulations on a $z \sim 6$ massive DM halo, to explore the formation of the high-redshift quasars, assuming super-Eddington accretion in a cosmological context. They tested various BH seeding scenarios (from 10 to $10^6\,M_\odot$) associated with various accretion/feedback prescriptions, including thin and slim accretion discs. They find that seeds with $M_{\rm BH} \lesssim 10^3\,M_\odot$ fail to grow to $10^8\,M_\odot$ SMBHs by $z \sim 6$, as a consequence of strong negative feedback from critical accretion, which in turn drastically reduces the accretion rates. Heavier seeds ($M_{\rm BH} \gtrsim 10^4\,M_\odot$) are able to reach rapidly 10^8 to $10^9\,M_\odot$ by $z \sim 6$, provided that the accretion is maintained near Eddington for $\gtrsim 40$ per cent of the time.

Finally, Hu et al. (2022a), who performed a series of long-term RHD simulations for super-Eddington accreting flows onto a BH, proposed a subgrid feedback model associated with outflows, which can be applied to large-scale cosmological simulations. In Hu et al. (2022b), they incorporate these results and investigate the assembly of the first massive BHs using a Monte Carlo merger tree model. Contrary to the previous results discussed above, they find that with their prescription, even stellar-mass seeds at $z \sim 30$ can grow to become SMBHs by $z \sim 6$, even in the presence of moderate outflows that would reduce the BH feeding rate. The presence of strong outflows appear to substantially reduce the SMBH mass achievable from PopIII stars, but does not seem to impact strongly the growth of heavier seeds. They also note that the massive SMBHs that form up to $z \sim 6$ in their work tend to be overmassive relative to their host galaxies.

The questions related to the impact the super-Eddington regime has on the material available for accretion, the BH growth rates and on the scales which may impact these processes are still debated to this day. From the different studies discussed in this Section, the effect of super-Eddington feedback appears to be mild when the outflow is assumed to be a wind, and strong when the outflow is assumed to be a jet. Nonetheless, it remains crucial to understand the connection between the inflowing material found at large scales and the sustainability of super-Eddington accretion. This question is at the core of this thesis and is developed in the next Section.

1.6 Organisation of the thesis

The present Chapter gave an introduction on the properties of galaxies and the supermassive black hole that they host. We have described their formation, growth, and their co-evolution throughout cosmic times, regulated by means of feedback mechanisms. We have focused the discussion on the super-Eddington regime which can be used to explain the $z \gtrsim 6$ population of supermassive black holes, and described the characteristics of this state of accretion.

Different studies discussed in this Chapter showed that despite being radiatively-inefficient, super-critical accretion may be accompanied (if not dominated) by powerful jetted outflows, which added to the radiation can have significant impact on black hole growth. Several questions related to the black hole growth assuming this state of accretion arise: Is the super-Eddington feedback strong enough to prevent black holes from growing? Is it possible to have efficient super-Eddington growth? If so, what are the conditions related to such growth? What is the global impact that this feedback has on the gas close and far from the black hole accretion region? In this thesis, to better assess the impact that super-Eddington accretion and feedback processes have on the growth of black holes in a realistic galaxy environment, we have performed numerical simulations using the code `Ramses` (Teyssier 2002) with the inclusion of the super-Eddington regime.

Chapter 2 gives an overview of the numerical tool that was used in this thesis. We describe the code `Ramses`, a grid-based hydro solver with adaptive mesh refinement, along with our implementation of the super-Eddington regime. In this Chapter, we investigate the correct implementation of the regime using an isothermal sphere setup, and study the impact that resolution has on the growth of the compact object. We also implement a refinement criterion for the super-Eddington feedback and investigate its use for more realistic simulations.

In Chapter 3, we explore whether a black hole can sustain super-Eddington accretion when both wind and mechanical feedback work together. We study the impact that this critical regime has on black hole growth and on the gas properties of the host galaxy, from star-forming clouds to galactic scales. We perform several simulations of an individual galaxy in an isolated dark matter halo. We add a black hole to the center of the emergent galaxy and conduct a survey on the parameter dependence regarding black hole growth and overall impact on the gas inflows and outflows, varying the feedback efficiencies and modes of injection in the super-Eddington regime.

In Chapter 4, we investigate for the first time the spin evolution of a black hole undergoing both super- and sub-Eddington accretion in idealised hydrodynamical simulations of isolated galaxies, using the suite of initial conditions from Chapter 3. By extending the BH spin model from Dubois et al. (2021) in `Ramses` to the super-Eddington regime, we explore the different phases of spin evolution when super-Eddington accretion is involved, as well as its impact on black hole growth. We attempt to describe explicitly the evolution in order to predict the final value of the black hole spin after a given mass is accreted.

Chapter 5 concludes all the studies made in this thesis.

Chapter 2

The Ramses code

In order to understand the evolution of the Universe, one cannot rely on an analytic analysis of the problem. The complex mystery that revolves around the origin of the first SMBHs and how their host galaxy evolves can be broken down into a set of distinct processes (gravity, hydrodynamics, star formation, cooling, feedbacks). Blending these laws together in a computer gives rise to a simulation of the Universe. There are many codes developed independently capable to do such simulations, and Ramses (Teyssier 2002) is one of them. In this Chapter, we describe the concept of grid based numerical simulations and the methods implemented in Ramses to solve the different processes described above. We then describe the implementation of the super-Eddington routines and discuss a test case scenario: the isothermal sphere.

It is important to note that this Chapter is not meant to be used as a user guide of the Ramses code[1], as we shall only describe the numerical methods relevant for this thesis.

2.1 Structure

The aim of a simulation is to model complex physical processes given a set of initial conditions with the help of a numerical tool. This tool must therefore "understand" the system of equations governing the Universe. There are essentially two ways of *discretising* the equations of hydrodynamics. One approach is to follow the properties of the fluid dynamics with *particle* elements: a lagrangian description. These particles follow the natural evolution of the fluid, so that the density at each point can be determined with the number of particles present locally. A smoothing function is associated to each particle, corresponding to the probability function to find a fluid element near the particle. Furthermore, the spatial resolution "element" of this method is given by the characteristic scale of the smoothing function, named smoothing length. For these reasons, the approach is named *Smoothed Particle Hydrodynamics* (SPH) and has been used to study galaxy evolution in codes like Gadget (Springel et al. 2021: for the latest version) and Gasoline (Wadsley et al. 2017: for the latest version).

The second approach, which is used in Ramses, corresponds to a eulerian viewpoint. If the volume studied is instead discretised in a number of cubic *cells*, which form a grid, then the evolution of the properties of the fluid can be described at any point in time, anywhere in the grid. Each cell holds information related to the properties of the fluid, and by communicating with the neighbouring cells, the properties of the fluid can evolve. Precisely solving the differential equations depends significantly on the size of the cells, which determines the

[1] https://bytebucket.org/rteyssie/ramses/wiki/ramses_ug.pdf

spatial resolution of the grid. In the astrophysical context, particularly for the formation of large-scale structures in cosmology, the use of a regular evenly spaced grid is not adapted to describing simulations with a high contrast in density. For instance, to observe structures, it is necessary to have a very high resolution to follow the collapse of the gas or describe correctly the shocks in the fluid. This approach is therefore numerically expensive, but to overcome these limitations, Berger & Oliger (1984) introduced the idea of having an *adaptive* mesh, to have a higher resolution near the elements of interest (for example, where the fluid undergoes shocks). This is called the *Adaptive Mesh Refinement* (AMR) approach. Similar to the SPH approach, many codes besides `Ramses` have emerged over the years, like `Flash` (Fryxell et al. 2000: for its original version) and `Enzo` (Brummel-Smith et al. 2019: for the latest version).

In `Ramses`, the grid is refined cell by cell, and uses an *octree* structure. At the base level, called l_{min}, the entire simulation box is refined uniformly. As is discussed below, cells can be split (resp. unsplit) into more (resp. fewer) cells (by multiples of 8), at a refinement level $l+1$ (resp. $l-1$) if certain refinement criteria are fulfilled (resp. unfulfilled). This process happens until no more refinement criteria are met, or that the user-defined maximum refinement level l_{max} is reached. The cells which have finished their refinement are referred to as "leaf cells", and make up the grid which covers the simulation box.

Refinement criteria are often hard coded in `Ramses`, but custom ones can be defined for specific context. In this thesis, we have used four refinement criteria, starting with a quasi-lagrangian approach. It resolves cells based on the local density such that the total mass, *i.e.* for baryonic mass: gas+stars and BHs, enclosed in a grid cell is roughly the same on each refinement level. If the total mass is greater than (usually) 8 times this threshold mass, refinement proceeds. With this way, a stellar structure can be resolved even in environments with low gas density. Commonly used in conjunction with the quasi-lagrangian refinement criterion is the Jeans length criterion. In order to resolve the collapse length scale at all times, any cell smaller than a quarter of the Jeans length is refined. The other two refinement criteria will be introduced in Sections 2.3.5 and 2.4.3.

In order for simulations to evolve, a timestep has to be set. To make sure we follow the evolution correctly, no particle can cross more than a cell per timestep, the Courant condition[2] must be respected, and the free-fall time of the gas must not be exceeded during the timestep. The minimum timestep of a given level is imposed to all cells in that level, to guarantee the Courant condition in all cells of that level. Timesteps can be *adaptive*: a refinement level l will have one timestep when $l+1$ will have two, etc. This method of *sub-cycling*, which reduces numerical costs, is shown in Fig. 2.1 (from Rosdahl et al. 2013).

Even with the AMR in place with the timestep sub-cycling, simulations are still expensive, as computers can only do a fixed amount of operations every second. `Ramses` is parallelised to overcome this issue, using `MPI` libraries. The domain is decomposed into different sub-volumes, so that each processor has a smaller amount of operations to do. They handle their own physics, particles, refinement, etc., as well as a passive copy of the adjacent cells from their neighbouring processor ("ghost" cells), in order to compute the fluxes in the cells edging their sub-domain.

[2]No gas, particle or sound wave can cross more than a cell each timestep.

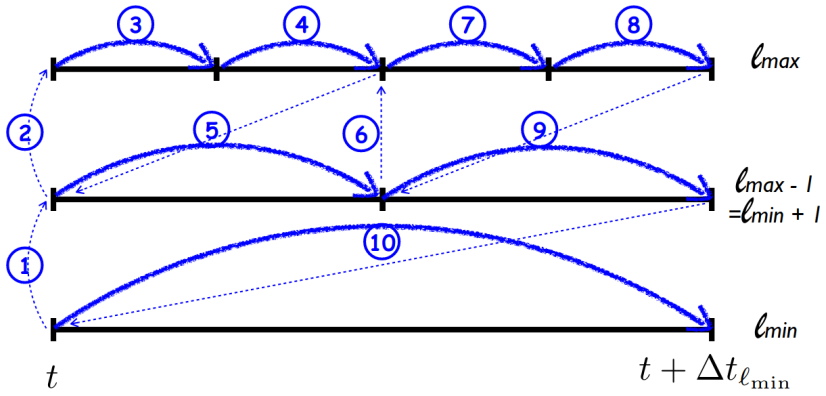

FIGURE 2.1: Hierarchy of the timesteps in Ramses (from Rosdahl et al. 2013). Evolution follows from the highest level $l_{\rm max}$ to the lowest $l_{\rm min}$.

2.2 Gas and particles

Gas, DM and stars are the main ingredients used to form galaxies. To model processes that occur during their birth and evolution, it is necessary to follow the dynamics of these accordingly. We start with the gas, which follows the Euler equations, describing the conservation of mass, momentum and energy[3]:

$$\frac{\partial \rho}{\partial t} + \nabla\cdot(\rho \mathbf{v}) = 0\,, \tag{2.1}$$

$$\frac{\partial \rho \mathbf{v}}{\partial t} + \nabla\cdot(\rho \mathbf{v}\otimes\mathbf{v} + P\mathbb{1}) = -\rho\nabla\Phi\,, \tag{2.2}$$

$$\frac{\partial E}{\partial t} + \nabla\cdot((E+P)\mathbf{v}) = -\rho\mathbf{v}\cdot\nabla\Phi\,, \tag{2.3}$$

where $\mathbf{v}$ is the velocity vector, E is the total energy, ρ is the density and P is the pressure. One needs to add a *closure* equation, so that this system of equations has a unique solution. This is done with the addition of the equation of state of the gas (assumed to be ideal and non relativistic), which follows:

$$P = (\gamma-1)(E - \frac{1}{2}\rho|\mathbf{v}|^2)\,, \tag{2.4}$$

where γ is the adiabatic index. The distribution of gas in Ramses is discretised on the grid, and each cell the density, momentum and total energy at all times. Those conserved quantities are updated over a given timestep by the fluxes evaluated at the cell boundaries. Each boundary corresponds to a Riemann problem, that is solved in Ramses using a second-order Godunov (1962) scheme. Numerically, different approximate Riemann solvers can be used, with the most accurate (while retaining computational efficiency) one used: the Harten-Lax-van Leer-Contact solver (for a review on different solvers, see Toro 1999). We note that in Chapter 3, we will mention the use of another solver, named Lax-Friedrichs solver, with the reasons of its use discussed later. A total variation diminishing scheme linearly interpolates the conserved quantities at cell interface, with a Min-Mod slope limiter in order to obtain

[3]The addition of cooling/heating terms to the conservation of energy is discussed in Section 2.3.1.

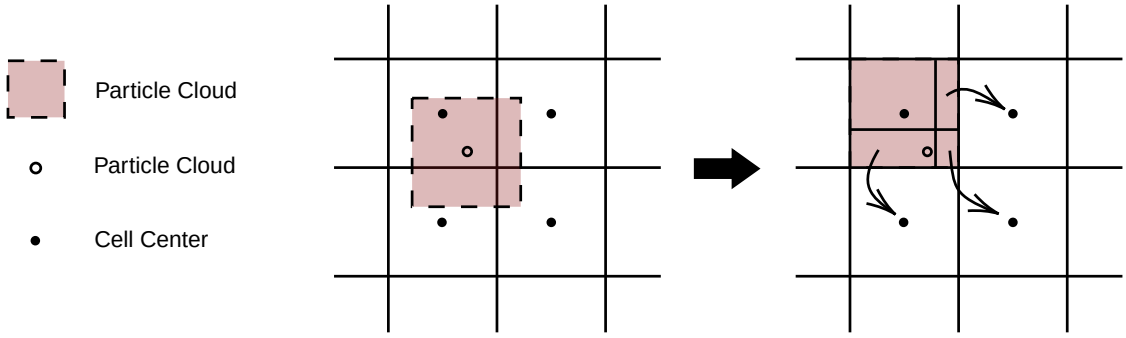

FIGURE 2.2: Principle of the CIC interpolation scheme. A cubic cloud surrounds the particle, and the mass is distributed to the neighbouring cells, proportionally to the cloud volume overlapping them.

second-order accuracy of the Godunov scheme and guarantee stability (*i.e.* non-oscillatory behavior).

In Ramses, DM and stars (see Section 2.3.2) can be described as "collision-less" particles, meaning they only interact via gravity. The equations of motions for each individual particle follow:

$$\frac{d^2\mathbf{x}}{dt^2} = -\nabla\Phi \,, \tag{2.5}$$

with $\mathbf{x}$ is the trajectory of the particle and Φ the gravitational potential. This potential can be obtained through the Poisson equation:

$$\Delta\Phi = 4\pi G\rho_{\rm tot} \,, \tag{2.6}$$

with G the gravitational constant and $\rho_{\rm tot}$ the total density (gas, stars, DM, BHs). Ramses uses a multi-grid approach (Guillet & Teyssier 2011) for coarse grids and follow a conjuguate gradient solver to compute the potential Φ in Eq. 2.5. The code also updates the velocity and position of particles each timestep with a leapfrog algorithm. Particles can be distributed anywhere onto the grid (not just at the cell centers), therefore, the mass of particles needs to be spread out onto the cells they overlap with. Ramses uses the Cloud In Cell (CIC) technique, which splits the particle mass between the cells around it, according to the volume the cloud occupies in each cell (see Fig. 2.2).

2.3 Adding more physics to the mix: the subgrid approach

The equations and solvers described in the previous Section are only able to tell how gas and particles generally move in the simulation box. However, processes that are important to galaxy formation and evolution (such as feedbacks, cooling, formation of stars, etc.) cannot be modeled using only gravity or hydrodynamics. They are important processes that occur at very small scales, and very often below the resolution of the smallest cell Δx found in the box. For this reason, codes like Ramses have to rely on "subgrid physics". These processes are understood and relevant physics, but because they cannot be self-consistently resolved, these codes have to find a way to include them. We detail here several of the subgrid physics included in Ramses.

2.3.1 Cooling and heating

There are many processes (Bremsstrahlung, collisional excitation or ionisation, recombination) which lead to radiative cooling, corresponding to the process of gas losing energy and decreasing its temperature. Depending on the chemical composition (*i.e.* metallicity Z) of the gas and on its temperature T, the cooling is more or less efficient. Furthermore, the abundance of metals varies with redshift. This information is given in so-called "cooling functions" which are modeled with the cooling curves from Sutherland & Dopita (1993) (for $T > 10^4$ K) and Rosen & Bregman (1995) (for $10\,\mathrm{K} < T < 10^4$ K) in Ramses. Finally, at $z \simeq 10$, a heating process occurs: reionization (see Section 1.1). To mimic its impact, Ramses adds this uniform ultraviolet background, computed following Haardt & Madau (1996).

2.3.2 Stars: formation

Stars have radii as large as $\sim 10^{-8}$ pc, several orders of magnitude below the resolution of the simulations performed in this thesis. Being far off resolving single stars, they are implemented as particles[4] (similar to DM in Section 2.2) of mass $m_* \gtrsim 10^3\,\mathrm{M}_\odot$, which represents a stellar population. Each particle has a defined IMF (say Chabrier (2003)) with low and high mass cutoffs ($0.1\,\mathrm{M}_\odot$ and $100\,\mathrm{M}_\odot$ respectively for the Chabrier IMF).

As gas collapses under its own gravity, it can form stars. The Kennicutt-Schmidt law (Schmidt 1959, Kennicutt 1998) finds a correlation between the star formation rate (SFR) surface Σ_{SFR} and the gas surface density Σ_{gas}. To be more specific, Schmidt (1959) expressed the SFR (per units volume) as:

$$\dot{\rho}_{\mathrm{SFR}} = \epsilon_* \frac{\rho_{\mathrm{gas}}}{t_{\mathrm{ff}}}, \tag{2.7}$$

$$t_{\mathrm{ff}} = \sqrt{\frac{3\pi}{32\rho_{\mathrm{gas}} G}}, \tag{2.8}$$

with ρ_{gas} the gas density, t_{ff} the free-fall time and ϵ_* the star formation efficiency. If the gas density exceeds a user-defined density threshold n_{SF}, stars will form following Eq. 2.7. Star particles are generated using a Poisson distribution (Rasera & Teyssier 2006), with a stellar mass resolution set by the numerical resolution Δx and the density threshold n_{SF}.

Usually, the star formation efficiency is constant ($\epsilon_* \sim 0.01$) and has been calibrated to recover observations. However, since star formation occurs in regions which are gravitationally bound with respect to turbulence, a theory of a gravo-turbulence driven star formation efficiency can be built. This led to developments of more sophisticated models (Krumholz & McKee 2005, Hennebelle & Chabrier 2011, Padoan & Nordlund 2011, Federrath & Klessen 2012). The model adopted in this thesis is from Federrath & Klessen (2012)[5] and has been used in recent simulations (Kimm et al. 2017, Trebitsch et al. 2017, 2021, Dubois et al. 2021).

[4] This holds true for stellar particles, as their collisional cross section is almost negligible.
[5] It follows approaches from Hennebelle & Chabrier (2011) and Padoan & Nordlund (2011).

It follows:

$$\epsilon_* = \frac{1}{4\phi_t} \exp\left(\frac{3}{8}\sigma_s^2\right) \left[1 + \mathrm{erf}\left(\frac{\sigma_s^2 - s_{crit}}{\sqrt{2\sigma_s^2}}\right)\right] , \tag{2.9}$$

$$\sigma_s = \ln(1 + b^2\mathcal{M}^2) , \tag{2.10}$$

$$s_{crit} = \ln\left(\frac{0.067}{\theta^2}\alpha_{vir}\mathcal{M}^2\right) , \tag{2.11}$$

with $\mathcal{M} \equiv u_{rms}/c_s$ the cloud turbulent Mach number, u_{rms} the root mean squared velocity in the cell, c_s the local sound speed and α_{vir} the virial parameter. Other parameters, such as $\phi_t = 0.57^{-1}$, $\theta = 0.33$ and $b = 0.4$ are empirical parameters in the model determined by the best-fit values in Federrath & Klessen (2012). This prescription has the advantage to not be strongly dependent on the gas density threshold chosen. For instance, in regions which are gravitationally bound ($\alpha_{vir} < 1$) and highly turbulent ($\mathcal{M} > 1$), the efficiency can be high; whereas in marginally bound regions, the efficiency can drop to very low values. Furthermore, this allows for clumpier star formation, which is in better agreement with the multitude of star forming clouds that are observed in galaxies.

2.3.3 Stars: feedback

The Type II SN explosions are the most powerful SNe, releasing a total energy of 10^{51} erg and they can affect the entire galaxy, ejecting and heating gas, releasing metals etc. This feedback process has two distinct phases (Chevalier 1974, Cioffi et al. 1988, Blondin et al. 1998): 1) The Sedov phase, during which the explosion expands adiabatically. Cooling is not yet efficient, and energy is conserved. The Sedov solution is used to estimate the fraction of kinetic and thermal energy deposited. 2) Once radiative losses become significant, a dense shell forms behind the radiative shock. The SN enters its snow-plow phase, in which only momentum is conserved. In Ramses, the mass ejected corresponds to a fraction η_{SN} of the stellar particle, with η_{SN} the mass fraction of stars ending up as type II SN. The mass lost is also removed from the mass of the stellar particle.

There has been many updates to Ramses related to how the energy should be deposited, whether it should be modelled with thermal or kinetic energy. The work in this thesis employs the mechanical SN feedback scheme (Kimm & Cen 2014, Kimm et al. 2015). This model explores in which phase the SN explosion is by computing the mass swept up by the SN. For instance, if it is still in the energy-conserving phase, the energy is deposited directly into the gas, as the expansion of the explosion is naturally occuring. On the other hand, in the momentum-conserving phase, the model gives the momentum expected during this phase if the mass of the neighbouring cells exceeds a certain value. This prevents artificial cooling due to the finite resolution, which would drastically underestimate the feedback energy and momentum, and could suppress the expansion of the SN bubble. A randomly selected stellar particle is chosen to undergo SN feedback following a Poisson distribution. In terms of metallicity, at the time of explosion, newly processed metals are deposited in the neighbouring cells. The mass ratio of the newly formed metals over the total ejecta, known as the metal yield, is a user-defined parameter. Finally, we note that there is a delay between the formation of the stellar particle and the SN explosion (*i.e.* the stellar lifetime), which varies

with the mass of the stellar progenitor and varies from a few Myr to 50 Myr (from the most massive to the least massive stars).

2.3.4 Black holes: formation and dynamics

First of all, BHs are modelled as "sink" particles (Krumholz et al. 2004), *i.e.* they are massive particles that move over the grid (just as other kinds of particles, see Section 2.2) and remove a portion of gas, via accretion processes. There are several ways of forming BHs in Ramses. In its simplest form, which was the one used in this thesis, the initial BH mass, position, velocity and angular momentum can be specified as part of the input parameters at the moment one begins (or restarts) the simulation. This cannot be applied when running cosmological simulations, as one needs to find BH formation sites which are physically relevant. For instance, if a cell has 1) gas and stellar densities greater than the threshold for star formation, 2) a stellar velocity dispersion greater than a velocity threshold (set to $20\,\mathrm{km\,s^{-1}}$) and 3) the lack of any other BH within a certain distance from the cell (typically 50 kpc to avoid multiple BHs in galaxies), then a BH will form in this cell. The seed mass in this scenario is chosen to be $10^4\,\mathrm{M_\odot}$ or $10^5\,\mathrm{M_\odot}$.

Numerical shot noise (induced by discrete sampling of mass and gravitational acceleration onto the grid) can cause spurious motions due to finite resolution, in addition to physically-driven perturbations of BH dynamics (interaction with clumps of gas or stars, perturbation by mergers, etc.). To prevent this, an explicit drag force mimicking dynamical friction effects is added to the code (Ostriker 1999). A density-dependant boosting factor $\alpha = \max(\rho_{\mathrm{gas}}/\rho_\alpha, 1)$ (ρ_α is a free parameter) is included in the dynamical friction expression, as gaseous regions around the BHs can sometimes be unresolved (Booth & Schaye 2009), therefore underestimating the resulting drag force. In addition to gas dynamical friction, a stellar dynamical friction is employed, which has the benefit of helping the BH particles stay bound within the galaxy (Pfister et al. 2019).

2.3.5 Black holes: growth

Before discussing the growth of BHs, we introduce the third refinement criterion (see Section 2.1) which is used in our recent simulations. Whenever a BH is formed, we enforce the maximum spatial resolution (*i.e.* at the maximum level of refinement l_{max}) within $4\Delta x$ of the BH, regardless of the gas density present, as it improves the accuracy of BH motion and accretion physics (Lupi et al. 2015). Moreover, surrounding the BH are found 2109 mass-less "cloud particles", uniformly distributed in a sphere of radius $4\Delta x$ and evenly spaced every $0.5\Delta x$. These *test particles* are used to compute accurately the accretion rate on the BH. Any mass removed from the grid during the accretion phase will go directly onto the sink particle, updating its mass every timestep. Finally, the approach chosen to use the cloud particles for accretion follows the Nearest Grid Point (NGP), instead of the CIC interpolation scheme.

There are two ways which can lead to an increase of the BH mass: accretion and merging. In this thesis, only accretion has been studied, however, BHs are allowed to merge in Ramses. For instance, if two BHs get closer than $4\Delta x$ and when the relative velocity of the pair of BHs is smaller than the escape velocity of the binary, then merging occurs. We note that this

approach is vastly different to "instantaneous merging" using halo finders (*e.g.* Davé et al. 2019), as it can take several Myr to Gyr to have BHs coalesce (*e.g.* Pfister et al. 2019).

As already discussed in Section 1.4, a certain mass $\dot{M}_{\rm acc}$ falls onto the BH and a fraction $\epsilon_{\rm r}$ gets radiated away, leaving the growth rate given by Eq. 1.4. $\dot{M}_{\rm acc}$ in Ramses follows the Bondi-Hoyle-Lyttleton (BHL) formalism (Hoyle & Lyttleton 1939, Bondi 1952), written as:

$$\dot{M}_{\rm BHL} = \frac{4\pi G^2 M_{\rm BH}^2 \bar{\rho}_{\rm gas}}{(\bar{c}_{\rm s}^2 + \bar{v}_{\rm rel}^2)^{3/2}}\,, \tag{2.12}$$

where the averaged density $\bar{\rho}_{\rm gas}$, sound speed $\bar{c}_{\rm s}$ and relative velocity between the BH and the gas $\bar{v}_{\rm rel}$ are computed over a sphere of radius of $4\Delta x$ with contributions from each cell weighted by $w \propto \exp\left(-r^2/r_{\rm K}^2\right)$ (Krumholz et al. 2004). The kernel radius $r_{\rm K}$ depends on whether the BHL radius $r_{\rm BHL} = GM_{\rm BH}/(c_{\rm s}^2 + v_{\rm rel}^2)$ is resolved or not, where $c_{\rm s}$ and $\rm v_{rel}$ are the sound speed and relative velocity in the cell where the sink particle lies. It is defined as follows:

$$r_K = \begin{cases} \Delta x/4 & r_{\rm BHL} < \Delta x/4\,, \\ r_{\rm BHL} & \Delta x/4 \leq r_{\rm BHL} \leq 2\Delta x\,, \\ 2\Delta x & r_{\rm BHL} > 2\Delta x\,. \end{cases} \tag{2.13}$$

The boosting factor α discussed in Section 2.3.4 can be applied to $\dot{M}_{\rm BHL}$, although in this thesis we set $\alpha = 1$.

In the *unchanged* version of Ramses, the accretion rate is capped at the Eddington limit (Eq. 1.9). Finally, in order to prevent having cells completely depleted of gas by repeated episodes of accretion, a safety check allows for accretion of only up to 25 per cent of the total mass available in each cell at each timestep of size Δt, *i.e.* $\dot{M}_{\rm floor} = 0.25\rho_{\rm gas}\Delta x^3/\Delta t$. The accretion rate at a given timestep therefore follows:

$$\dot{M}_{\rm acc} = \min(\dot{M}_{\rm BHL}, \dot{M}_{\rm Edd}, \dot{M}_{\rm floor}) \tag{2.14}$$

with the kernel from Eq. 2.13 applied for all cells within $4\Delta x$ of the BH.

2.3.6 Black holes: spin

A spinning BH of mass $M_{\rm BH}$ has an angular momentum $J_{\rm BH}$ which is usually defined by its dimensionless spin parameter $a = J_{\rm BH}c/(GM_{\rm BH})$ and is described by the Kerr metric (Kerr 1963). For the rest of the thesis, we will use the terminology that a prograde (*i.e.* in co-rotation with the gas) BH has $a > 0$ and a retrograde (*i.e.* in counter-rotation with the gas) one has $a < 0$. In Ramses, the evolution of a is done on the fly in the simulation, with the update of the spin after every merger event, as well as every accretion episode. We note however that it is possible to prevent the spin from updating during the accretion phases, by fixing its spin magnitude and direction, if the user desires to investigate a specific situation.

BH spins can change via gas accretion. For high accretion rates ($0.01 < f_{\rm Edd} \leq 1$), Ramses follows the analytical calculation from Bardeen (1970):

$$a_{\rm fin} = \frac{\sqrt{r_{\rm ISCO,ini}}}{3}\frac{M_{\rm BH,ini}}{M_{\rm BH,fin}}\left[4 - \sqrt{3r_{\rm ISCO,ini}\left(\frac{M_{\rm BH,ini}}{M_{\rm BH,fin}}\right)^2 - 2}\right] \text{ for } \frac{M_{\rm BH,fin}}{M_{\rm BH,ini}} < \sqrt{r_{\rm ISCO,ini}}\,, \quad (2.15)$$
$$= 1 \text{ otherwise.}$$

"ini" (and "fin") are the initial (final) value of the quantity measured before (after) accretion respectively. $r_{\rm ISCO}$ corresponds to the innermost stable circular orbit (ISCO; Bardeen 1970), i.e.

$$r_{\rm ISCO}(a) = \frac{GM_{\rm BH}}{c^2}\left(3 + Z_2 \mp \sqrt{(3-Z_1)(3+Z_1+2Z_2)}\right)\,, \quad (2.16)$$

where the $\mp$ sign corresponds to respectively the positive ($-$) and negative ($+$) values of the BH spin, and

$$Z_1 = 1 + (1-a^2)^{1/3} \times \left((1+a)^{1/3} + (1-a)^{1/3}\right)\,, \quad (2.17)$$

$$Z_2 = \sqrt{(3a^2 + Z_1^2)}\,. \quad (2.18)$$

This spin update is correct when the BH and angular momentum from the accreted material are perfectly aligned, however generally spin misalignment occurs. In the latter case, the Lense-Thirring effect (Bardeen & Petterson 1975) causes the accretion disc to precess about the spin axis of the BH. Disc warping can also happen if viscosities are high enough in the accretion disc (*e.g.* Bardeen & Petterson 1975, Fanidakis et al. 2011, Dotti et al. 2013). As a result of these processes, BH and accretion disc will be aligned or anti-aligned, which is calculated with an alignment criterion (King et al. 2005). After determining the alignment, Ramses updates the spin according to the mass gained by the BH $\Delta M_{\rm gr}$ during the timestep, following Eq. 2.15.

In Ramses it is assumed that for lower accretion rates ($f_{\rm Edd} \leq 0.01$), jets (see Section 2.3.7 for their modelling) are powered by energy extraction from the Blandford & Znajek (1977) mechanism and that the BH spin magnitude can only decrease. However, there is no analytical formula which gives the final spin value $a_{\rm fin}$ after the accretion phase in this regime. The spin variation rate, or *spin-up rate*, for this accretion regime is still investigated (*e.g.* McKinney et al. 2012, Tchekhovskoy et al. 2012, Narayan et al. 2022). Dubois et al. (2021) fit the spin-up parameter s found in McKinney et al. (2012) for all values of the spin parameter:

$$s = 0.97 - 12.00a - 4.04a^2 + 5.81a^3 + 2.50a^4\,. \quad (2.19)$$

Following Shapiro (2005), s can be defined as:

$$s \equiv \frac{da}{dt}\frac{M_{\rm BH}}{\dot{M}_{\rm acc}} = \frac{da}{d\ln M_{\rm BH}}(1-\epsilon_{\rm r})\,. \quad (2.20)$$

A numerical integration of Eq. 2.20 with Eq. 2.19 is performed in the code and the spin magnitude and orientation are then updated similarly to the high accretion rates case.

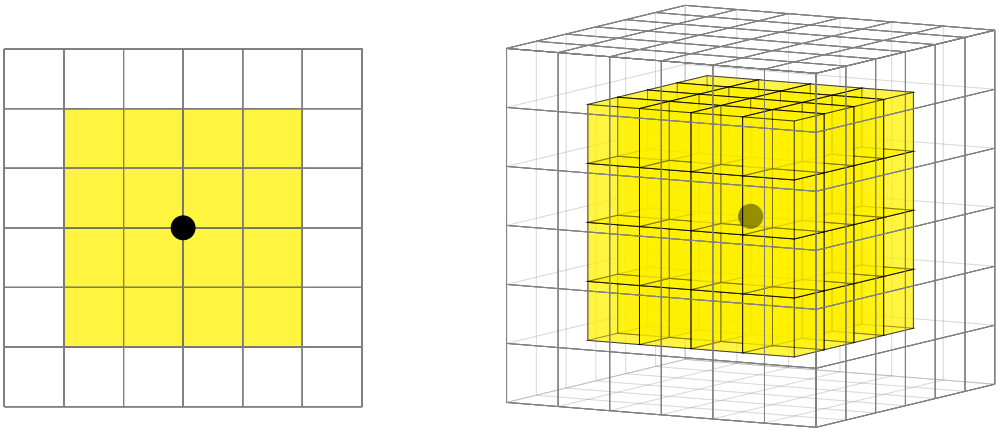

FIGURE 2.3: 2D (left) and 3D (right) schematic representations of the kinetic feedback injection in cells around the BH in Ramses. A BH (black circle) is placed in the center of the $6 \times 6 \times 6$ grid. In this case, $r_{\rm jet} = 2\Delta x$.

Regardless of the accretion regime, a maximum of $a = 0.998$ is set in Ramses, due to the capture by the central BH of radiated photons emitted from the accretion disc (Thorne 1974). Finally, despite not being studied in this thesis, the coalescence of BHs in Ramses updates the spin of the BH remnant following analytical fits from Rezzolla et al. (2008) (for details of the implementation, see Dubois et al. 2014a).

2.3.7 Black holes: feedback

AGN outflows are challenging to include in numerical simulations, as they originate on scales far below the resolution limit. As discussed in Section 1.3.2, these feedbacks are modelled in two different ways depending on their Eddington ratios $f_{\rm Edd}$ (Dubois et al. 2012b).

For low ratios, *i.e.* $f_{\rm Edd} \leq 0.01$, BHs provide a "radio mode" modelled by a kinetic feedback implementation, releasing mass, momentum and energy into the gas surrounding the BHs. These quantities are spread over a cylindrical region of injection of diameter and height equal to $2r_{\rm jet}$ (see Fig. 2.3). This user-defined parameter is in units of the resolution Δx. The jet axis is aligned with the BH spin axis, with no opening angles. The energy, mass and momentum are subject to a kernel when deposited within the cylinder:

$$\psi(r) = \frac{1}{2\pi r_{\rm jet}} \exp\left(-\frac{r^2}{2r_{\rm jet}^2}\right) \tag{2.21}$$

with $r \leq r_{\rm jet}$ the radial distance of the cell within the cylinder. In this thesis, to calculate the energy injected as kinetic energy in all the cells within the cylinder, we follow Sądowski et al. (2016), which gives a total jet feedback of:

$$\dot{E}_{\rm jet} = \eta_{\rm jet} \dot{M}_{\rm BH} c^2 \,, \tag{2.22}$$

where $\eta_{\rm jet} = 1.3 a^2 f_{\rm MAD}^2$ is the efficiency factor of the kinetic feedback for a magnetically arrested disc (MAD) taken from Tchekhovskoy (2015), and $0 \leq f_{\rm MAD} \leq 1$ represents the fraction of MAD strength (magnetic field saturation). As jets traverse the interstellar medium

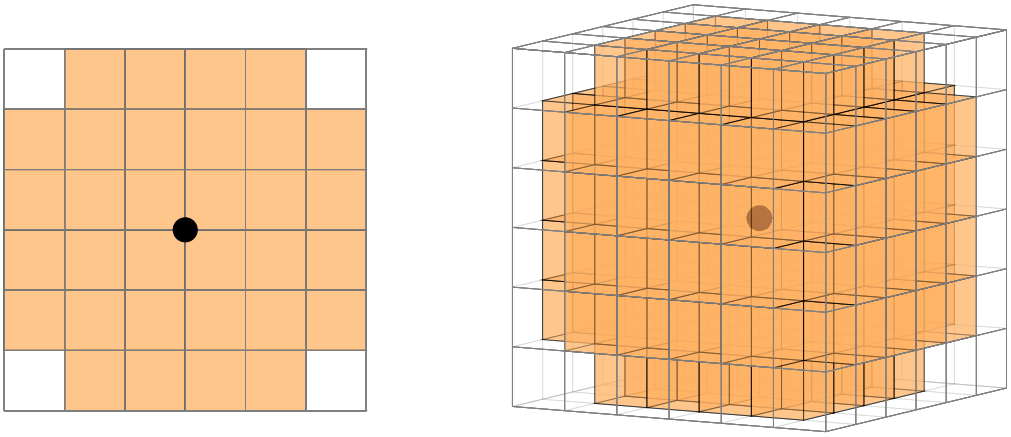

FIGURE 2.4: Same as Fig. 2.3, but for the thermal feedback. In this case, $r_{\rm thm} = 3\Delta x$.

and dense clouds, they entrain mass and slow down: the mass that loads the jet, changes its velocity such as its value at the lowest scale resolved is lower than that at the unresolved launching scale (that of the accretion disc). The mass-loading factor $\beta_{\rm jet}$ is expressed as the ratio between the mass ejection rate $\dot{M}_{\rm jet}$ in the jet and the growth rate of the BH, i.e. $\beta_{\rm jet} \equiv \dot{M}_{\rm jet}/\dot{M}_{\rm BH}$. Assuming that the jet energy is simply the kinetic energy of the jet at injection, *i.e.* $\dot{E}_{\rm jet} = 0.5\dot{M}_{\rm jet}v_{\rm jet}^2$, one can write the mass-loading factor as:

$$\beta_{\rm jet} = 2\eta_{\rm jet}\left(\frac{v_{\rm jet}}{c}\right)^{-2} . \tag{2.23}$$

This mass loaded is transferred from the BH surroundings, with the same weighting applied in Section 2.3.5 with the cloud particles, and redistributed to all enclosed cells within the cylinder. We note that, in this thesis, we studied the impact of $\beta_{\rm jet}$ and $\eta_{\rm jet}$, so $v_{\rm jet}$ is fixed in Eq. 2.23. This helps keeping the timestep of the simulation affordable, as jets could end up being launched at $v_{\rm jet} \sim c$ if not fixed. Unless specified otherwise in this thesis, we set $v_{\rm jet} = 0.1c$.

The modelling in Ramses for higher accretion rates, with $0.01 < f_{\rm Edd} \leq 1$ is different. It represents the "quasar mode", a heating mode where energy is deposited through thermal energy. A bubble of radius $r_{\rm thm}$ represents the region of energy deposition around the BH (see Fig. 2.4). This user-defined parameter is also expressed in units of Δx. The total energy deposited in the cells contained within the spherical region is thus:

$$\dot{E}_{\rm thm} = \eta_{\rm thm}\dot{M}_{\rm BH}c^2 . \tag{2.24}$$

The efficiency factor $\eta_{\rm thm}$ for this regime corresponds to the thermal wind efficiency of the accretion disc. Following Sądowski et al. (2016), the spin-dependent thermal wind efficiency can be written as $\eta_{\rm thm} = \eta_{\rm d\to thm} \times \eta_{\rm ISCO}$, with

$$\eta_{\rm ISCO} = 1 - \sqrt{1 - \frac{2}{3r_{\rm ISCO}(a)}} , \tag{2.25}$$

where $\eta_{\mathrm{d}\to\mathrm{thm}}$ is the fraction of energy released from the disc coupled to the gas within r_{thm}, depending on how well the energy from the accretion disc can be absorbed by the surrounding gas. $\eta_{\mathrm{d}\to\mathrm{thm}} = 0.15$ has been calibrated to reproduce the BH-galaxy scaling relations (Kormendy & Ho 2013).

2.4 The super-Eddington regime: what changes?

2.4.1 Super-Eddington: BH growth

The first addition to have accretion beyond the Eddington limit is to remove said limit. With this first implementation, we allow BHs to have accretion rates such that:

$$\dot{M}_{\mathrm{acc}} = \min(\dot{M}_{\mathrm{BHL}}, \dot{M}_{\mathrm{floor}}) \tag{2.26}$$

The principle stays the same, with the accretion routines described in Section 2.3.5. However, as was discussed in Section 1.5, the photon-trapping effect must be taken into account in our simulations. We opt to use results from Madau et al. (2014), who themselves fitted numerical results from Sądowski (2009), to compute such effect in Ramses. For instance, to calculate the Eddington ratio, we use the following equation:

$$f_{\mathrm{Edd}} = A(a)\left[\frac{0.985}{1.6\dot{M}_{\mathrm{Edd}}/\dot{M}_{\mathrm{acc}} + B(a)} + \frac{0.015}{1.6\dot{M}_{\mathrm{Edd}}/\dot{M}_{\mathrm{acc}} + C(a)}\right], \tag{2.27}$$

with spin-dependent functions A, B and C as:

$$A(a) = (0.9663 - 0.9292a)^{-0.5639}, \tag{2.28}$$
$$B(a) = (4.627 - 4.445a)^{-0.5524}, \tag{2.29}$$
$$C(a) = (827.3 - 718.1a)^{-0.7060}. \tag{2.30}$$

We recall that the radiative efficiency plays a role in the calculation of the growth rate of the BH (*i.e.* $\dot{M}_{\mathrm{BH}} = (1-\epsilon_{\mathrm{r}})\dot{M}_{\mathrm{acc}}$) and is affected by photon-trapping effects at super-Eddington accretion rates. Employing the fits from Madau et al. (2014) in Eq. 2.27, we modify the radiative efficiency:

$$\epsilon_{\mathrm{r}} = 0.1 f_{\mathrm{Edd}} \frac{\dot{M}_{\mathrm{Edd}}}{\dot{M}_{\mathrm{acc}}}. \tag{2.31}$$

This ensures that, in the sub-Eddington scenario where $f_{\mathrm{Edd}} \simeq \dot{M}_{\mathrm{acc}}/\dot{M}_{\mathrm{Edd}}$, we find the typical radiative efficiencies from Novikov & Thorne (1973); whereas for super-Eddington cases, where $f_{\mathrm{Edd}} \ll \dot{M}_{\mathrm{acc}}/\dot{M}_{\mathrm{Edd}}$, photon-trapping is taken into account.

2.4.2 Super-Eddington: BH spin

As will be discussed extensively in Chapter 4, there is little work done for the computation of the spin-up rate in the super-Eddington regime. Because of the jetted outflows, we assume that the MAD state obtained by McKinney et al. (2012) for sub-Eddington thick accretion discs can be extended to the super-Eddington regime. The geometry of the two discs are

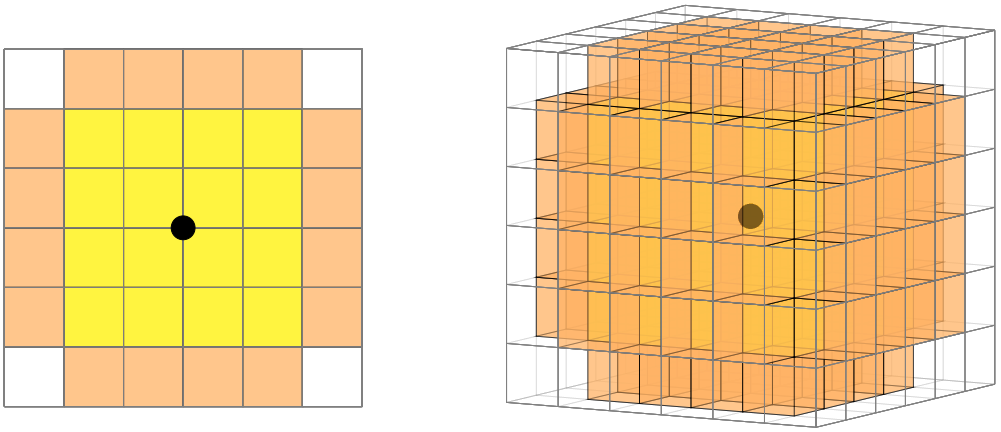

FIGURE 2.5: Same as Fig. 2.3, but for the super-Eddington feedback. For this type of feedback, both $r_{\rm jet}$ and $r_{\rm thm}$ are needed. Here, $r_{\rm jet} = 2\Delta x$ and $r_{\rm thm} = 3\Delta x$.

similar, *i.e.* being thick, however, their radiative efficiencies may differ significantly. It remains to be tested through dedicated GRMHD simulations whether the spin-up rates in the super-Eddington regime is significantly different from the classical thick disc state. The process of updating the spin in the Ramses routines does not change from what is described in Section 2.3.6, we simply use Eq. 2.19 for accretion rates above the limit.

2.4.3 Super-Eddington: BH feedback

To model the super-Eddington feedback in Ramses, energy is injected as both thermal and kinetic energy, as shown in the schematic representation in Fig. 2.5. The total AGN feedback injected in the super-Eddington regime is based off Sądowski et al. (2016), and reads as follows:

$$\dot{E}_{\rm sEdd} = \dot{E}_{\rm jet} + \dot{E}_{\rm thm} = (\eta_{\rm jet} + 0.5\eta_{\rm thm})\dot{M}_{\rm BH}c^2. \tag{2.32}$$

The kinetic feedback is computed in a similar fashion than the one described in Section 2.3.7, within the same radius $r_{\rm jet}$ used for the radio mode. The thermal energy is also deposited within a sphere of radius $r_{\rm thm}$. However, the type of feedback varies the gas temperature in different ways: for instance, kinetic feedback impacts *indirectly* the gas temperature, through the injection of momentum and total energy; whereas thermal feedback changes *directly* the gas temperature, by depositing only energy directly in the cells. To ensure that the feedback is well-separated, we opt to use different values for $r_{\rm jet}$ and $r_{\rm thm}$. In the simulations performed in this thesis, AGN feedback happens on scales below Δx, therefore a small region of injection must be chosen. Dubois et al. (2012b) show that large jet sizes $r_{\rm jet}$ lead to BH masses unrealistic when compared to observations. In addition, they find that increasing $r_{\rm thm}$ would effectively lead to a weaker impact on self-regulating the growth of BHs, thus concluding that the size of injection must be close to Δx. However, to prevent having numerical issues, we found that we cannot use a single cell for feedback injection. Therefore, unless otherwise specified, we set $r_{\rm jet} = 2\Delta x$ and $r_{\rm thm} = 3\Delta x$ as shown in Fig. 2.5.

In order to keep track of the super-Eddington feedback, we add a passive scalar as a hydro variable for the kinetic part of the super-Eddington feedback, which is introduced in Section 2.5.3. A passive scalar is used to easily track a certain quantity. For instance, in our

case, we can follow how far the jets of the super-Eddington feedback travel in the simulation box, the quantity of gas affected by the outflows, etc. Passive scalars are injected in the cells of the feedback injection region with a density $\rho_{\rm scalar}$ equal to that of the gas present in each cell $\rho_{\rm gas}$. They are passive, as they do not affect the flow and hydrodynamics, these scalars are only advected with the flow and mark regions affected by the super-Eddington feedback. To keep track of the most recent outflows, the scalar disappears after a certain time, following an exponential decay. This is used in simulations in Chapter 3, where we find that the decay time best suited for our simulations is $t_{\rm decay} = 3\,{\rm Myr}$.

Another use for the passive scalars is as refinement criteria (see Section 2.1). As we want to follow the AGN bubbles from super-Eddington feedback, we refine the regions which are affected by this feedback using the passive scalars. For instance in this thesis, cells are allowed to be refined if the scalar against gas ratio $\rho_{\rm scalar}/\rho_{\rm gas} > 0.01$ and the gradient of the scalar from one cell to another exceeds 5 per cent. Furthermore, regions with the latest super-Eddington feedback event dating longer than the decay time can eventually de-refine, and therefore not be computationally expensive, as it avoids to have a large fraction of the box refined at all times.

2.5 A small cloud of gas to test super-Eddington

The long-term aim of this thesis is to investigate the role that super-Eddington feedback plays in the evolution of SMBHs over long periods of time. To do so, we need to first understand what role local gas properties play in the efficiency and duration of super-Eddington feedback. In this first study, we investigate super-Eddington accretion on a SMBH at the center of a small cloud of gas, of a given mass and uniform temperature. In this cloud, there is no star formation, no DM, just gas. We model this scenario with an isothermal sphere (Binney & Tremaine 2008). While an isothermal sphere is typically referring to a hydrostatic solution, we investigate a sphere larger than its Jeans length (see below for a definition), thus collapsing sphere. We do not allow the gas to cool or heat up from the collapse of the sphere. This very idealised test case allows to confirm the correct implementation of the model, as well as assessing the behaviour of BH growth with accretion and feedback beyond the Eddington limit. In this Section, we will start by looking for suitable initial conditions for the isothermal sphere, in order to have accretion above the limit. We will then discuss the impact of resolution, one of many parameters that can be changed in this setup, and its role in conjunction with the super-Eddington feedback.

2.5.1 Initial conditions

Physical parameters: density, temperature and BH mass

In order to have high accretion rates, the gas needs to be cold and dense, as given by Eq. 2.12. It also needs to be provided constantly to the BH, to maximise the chances to have super-Eddington episodes. The choice of a collapsing isothermal sphere fulfills these conditions: we can tweak the initial density and temperature of the sphere easily, and the collapse of the sphere will supply the BH (located at the center of the sphere) with the gas needed to have

critical accretion episodes. The density profile $\rho(r)$ of the sphere is given by:

$$\rho(r) = \rho_R \frac{R^2}{r^2} \tag{2.33}$$

with ρ_R the density at the outer radius $r = R$. We note that this profile has a singularity at $r = 0$. In Ramses, distances are calculated from the center of each cell. To prevent singularities, one can shift the center of the sphere in the initial conditions, or add a smoothing parameter to slightly modify the density profile. In our case, we shift the center of the isothermal sphere to the corner of a cell. From this profile follows that the mass of the sphere M_{sph}, its free-fall time t_{ff} and binding energy U_{sph} are respectively:

$$M_{sph} = \int_0^R 4\pi r^2 \rho(r) dr = 4\pi R^3 \rho_R \,, \tag{2.34}$$

$$t_{ff} = \sqrt{\frac{\pi}{32 G \rho_R}} \,, \tag{2.35}$$

$$U_{sph} = \frac{G M_{sph}^2}{R} = (4\pi)^2 G \rho_R^2 R^5 \,. \tag{2.36}$$

Choosing the parameters to make sure that accretion beyond the Eddington limit is feasible is tricky. For example, if the gas is too cold and dense, its free-fall time t_{ff} may be of the order of a few timesteps, meaning the study of super-Eddington will be short lived. On the other hand, to have a longer free-fall time, one could decrease the density; but if ρ_R is too small, M_{sph} will also be small and may not provide enough gas for the BH to accrete at super-Eddington rates. Finally, if the BH is not massive enough, its feedback (which is proportional to M_{BH}^2 if $\dot{M}_{BHL}$ is accreted) will not be able to counter the collapse of the sphere, and the simulation will end with all the mass at the center of the sphere. For this first study, we chose to model a gas cloud of $M_{sph} = 2 \times 10^6\,M_\odot$ and radius $R = 10\,\mathrm{pc}$ (therefore $\rho_R = 6.5 \times 10^3\,\mathrm{amu\,cm^{-3}}$). With these parameters, the free-fall time of the sphere at $r = R$ is $t_{ff} \simeq 370\,\mathrm{kyr}$.

As discussed in Section 1.2.1, the Jeans length λ_J is the parameter which will tell whether or not a cloud of gas will collapse:

$$\lambda_J = \sqrt{\frac{\pi \gamma k_B T}{32 G \rho_R m_p}} \,, \tag{2.37}$$

with k_B the Boltzmann constant, T the temperature of the cloud and $\gamma = 1$ the adiabatic index in the isothermal case. As long as gas is cold and dense enough in our setup, a sphere of a given radius will gravitationally collapse, providing enough gas for super-Eddington accretion on a BH placed in the center of the sphere. In our case, this provides an upper limit to the temperature $T \lesssim 10^5\,\mathrm{K}$, above which the cloud will not collapse under its own gravity. A good balance between T and M_{BH} must be found to study the super-Eddington regime.

Numerical parameter: refinement level

In addition to these two physical parameters, the maximum refinement level $l_{\max}$ of the simulation box must also be studied. The simulation box for the isothermal sphere has a size of $4R$, allowing to cover super-Eddington outflows when they expand out of the isothermal sphere. The maximum level of refinement is linked to the resolution of the simulation, as the smallest cells have a resolution which follows:

$$\Delta x = \frac{4R}{2^{l_{\max}}}\,. \tag{2.38}$$

In a uniform box, the higher the refinement, the higher the density at the center of the sphere, *i.e.* where the BH is located, making it easier to accrete at high accretion rates (see Eq. 2.12). In the case where adaptive refinement is involved, refinement criteria will be triggered to increase the resolution of the box in the center of the sphere, owing to the density increasing. The BH will also force the resolution to be at the maximum within $4\Delta x$ (see Section 2.3.5). All in all, the maximum refinement will be an important parameter that will be discussed in Section 2.5.2.

Super-Eddington accretion rates

The final point to choose the set of initial conditions is to make sure that the BH can experience at least one super-Eddington episode. We are therefore trying to set the initial conditions in order to have super-Eddington accretion as soon as the BH is placed in the sphere. As discussed before, we compute the accretion rates of the BH in Ramses, following Eq. 2.26. We must therefore determine their values before launching the simulations.

Starting with $\dot{M}_{\rm BHL}$, one can calculate it for a given configuration of $M_{\rm BH}$, $l_{\max}$ and T. To simplify the problem, we fix the BH at the center of the sphere throughout the entirety of the simulation, meaning its velocity is set to 0. As the cloud has not started to collapse at the start of the simulation, the relative velocity $\bar{v}_{\rm rel}$ in $\dot{M}_{\rm BHL}$ is also 0.

We also calculate $\dot{M}_{\rm floor}$, which is the maximum accretion rate possible at a given timestep Δt. Since we model episodes of super-Eddington feedback with relativistic outflows, their high velocities will likely drive the computation of the timesteps. We therefore can calculate a lower estimate for what the first timestep should be: $\Delta t = \mathcal{C}\Delta x / v_{\rm jet}$ (we recall that $v_{\rm jet} = 0.1c$ and $\mathcal{C} = 0.8$ is the Courant factor).

Finally, due to this choice of Δt for the calculation of $\dot{M}_{\rm floor}$, we may have very small timesteps for very high resolution simulations. We limit the exploration of parameters to the maximum refinement levels ranging from $7 < l_{\max} < 11$, which gives $10\,{\rm yr} \gtrsim \Delta t \gtrsim 0.5\,{\rm yr}$. The timesteps are short enough to witness the propagation of the jets with a reasonable computational time, as the free-fall time of the sphere $t_{\rm ff} \sim 370\,{\rm kyr} \gg \Delta t$.

Parameters choices

In Appendix A, we detail the procedure that leads to the following choices. Here, we summarize the physical and numerical parameters that are chosen to perform the simulations. The sphere has a radius $R = 10\,{\rm pc}$ and a mass $M_{\rm sph} = 2 \times 10^6\,{\rm M}_\odot$. Its temperature is set to

$T = 10^5\,\mathrm{K}$, close to the upper limit given by the Jeans length (Eq. 2.37). We choose to add a $M_{\mathrm{BH}} = 10^4\,\mathrm{M}_\odot$ BH in the center of the isothermal sphere.

This choice of T and M_{BH} allows to find suitable conditions such that the sphere is not blown off by the strong super-Eddington feedback (which would happen if the gas was colder). On the other hand, choosing a less massive BH would lead to a complete collapse of the sphere with likely no visible AGN feedback. Furthermore, any refinement level from $7 < l_{\mathrm{max}} < 11$ provides accretion rates ranging from $10^2\,\dot{\mathrm{M}}_{\mathrm{Edd}} \lesssim \dot{M}_{\mathrm{acc}} \lesssim 10^4\,\dot{\mathrm{M}}_{\mathrm{Edd}}$ and feedback energies varying from $U_{\mathrm{sph}} \lesssim E_{\mathrm{sEdd}} \lesssim 10\,\mathrm{U}_{\mathrm{sph}}$. This allows the study of the effect of resolution on BH accretion and different feedback powers. Finally, it is possible to investigate the impact of the resolution on resolving r_{BHL}, as one can write (assuming $\bar{v}_{\mathrm{rel}} = 0$):

$$r_{\mathrm{BHL}} = 5 \times 10^{-2} \left(\frac{M_{\mathrm{BH}}}{10^4\,\mathrm{M}_\odot}\right) \left(\frac{T}{10^5\,\mathrm{K}}\right)^{-1} \mathrm{pc}. \tag{2.39}$$

For low refinement levels such as $l_{\mathrm{max}} = 7$, $\Delta x = 0.32\,\mathrm{pc} > r_{\mathrm{BHL}}$; for the intermediate level $l_{\mathrm{max}} = 9$, $\Delta x = 8 \times 10^{-2}\,\mathrm{pc} \sim r_{\mathrm{BHL}}$; and for the highest refinement level $l_{\mathrm{max}} = 11$, we have $\Delta x = 2 \times 10^{-2}\,\mathrm{pc} < r_{\mathrm{BHL}}$. In the next Section, we perform the simulations of this setup and investigate the impact of resolution.

2.5.2 BH growth and r_{BHL}

Now that the parameters determining the initial conditions of the isothermal sphere are chosen, we perform a series of hydrodynamical simulations with Ramses. The simulations are performed in a box of size 40 pc with a root grid of 128^3 (*i.e.* $l_{\mathrm{min}} = 7$) and is then adaptively refined to a maximum level l_{max}. In these simulations, we include three of the four refinement criteria described in the previous Sections, with the exception of the passive scalar criterion (see Section 2.4.3). The isothermal sphere is embedded in a low density ($\rho_{\mathrm{out}} \equiv \rho(r > R) = 0.01\rho_{\mathrm{R}}$) and high temperature ($T_{\mathrm{out}} = 100T$) medium which does not affect the collapse of the isothermal sphere.

We recall that for the entire duration of the simulation, the BH will be at rest in the center of the sphere. The $10^4\,\mathrm{M}_\odot$ BH has a fixed spin along an axis of the box, with an unchanging magnitude of $|a| = 0.7$ despite accretion episodes. The MADness fraction of the accretion disc is set to $f_{\mathrm{MAD}} = 0.5$, which gives a super-Eddington feedback primarily composed of a powerful jet, as in this configuration, $\dot{E}_{\mathrm{jet}} \simeq 20\dot{E}_{\mathrm{thm}}$. In this Section, we analyse the consequences of super-Eddington accretion coupled with its feedback on BH growth and the evolution of the BHL radius r_{BHL}. A set of three simulations are performed, each varying with increasing resolution: $l_{\mathrm{max}} = 7 \Leftrightarrow \Delta x = 0.32\,\mathrm{pc}$, $l_{\mathrm{max}} = 9 \Leftrightarrow \Delta x = 8 \times 10^{-2}\,\mathrm{pc}$ and $l_{\mathrm{max}} = 11 \Leftrightarrow \Delta x = 2 \times 10^{-2}\,\mathrm{pc}$. We note that in this idealised setup, no gas cooling is permitted, which keeps the inflowing gas at a given temperature as long as it is unaffected by feedback events from the BH (as will be later discussed).

A self-regulated growth

We compare the BH mass evolution until the free-fall time of the sphere $t_{\mathrm{ff}} = 370\,\mathrm{kyr}$ for the simulations with $l_{\mathrm{max}} = 7$ (solid green), $l_{\mathrm{max}} = 9$ (solid red) and $l_{\mathrm{max}} = 11$ (solid blue)

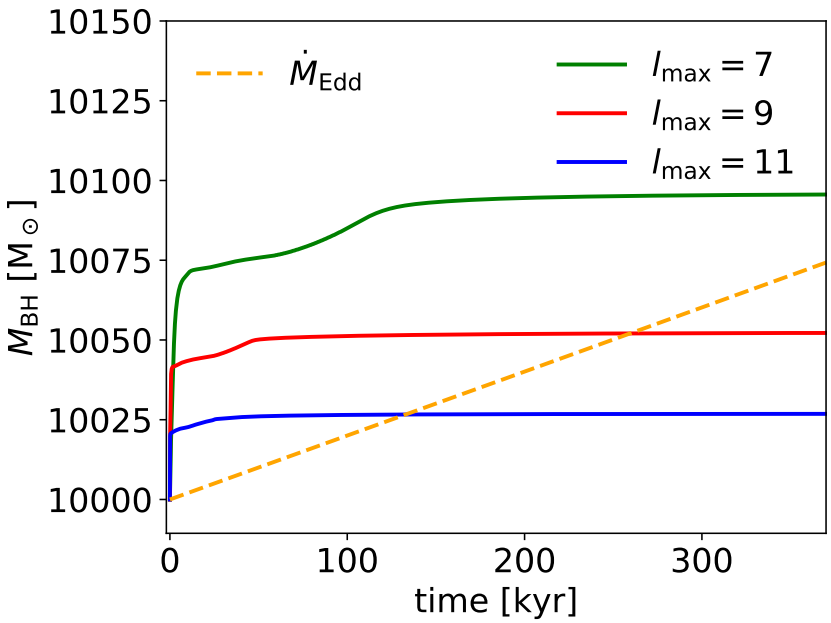

FIGURE 2.6: Evolution of the BH mass M_{BH} for the $l_{max} = 7$ (solid green), $l_{max} = 9$ (solid red) and $l_{max} = 11$ (solid blue) simulations. In dashed orange is also added the expected evolution of a $M_{BH} = 10^4\,M_\odot$ BH if it accreted constantly at the Eddington limit. All three BHs have their growth above the Eddington limit for a few 100 kyr (depending on the simulation), as they are quickly self-regulated by their feedback.

in Fig. 2.6. We add in dashed orange $\dot{M}_{Edd}$, to compare with a theoretical growth at the Eddington limit. Despite the large amount of gas infalling onto the BH, all of them are only able to increase their mass by a small amount: the BHs increased their mass by a factor of 0.2 per cent for the highest resolution case ($l_{max} = 11$), and up to $\sim$ 1 per cent in the least resolved simulation ($l_{max} = 7$). Their growth are overall above the Eddington limit, but they are not able to sustain super-Eddington accretion rates for a long period of time. In fact, their growth completely stops after $\lesssim$ 100 kyr, due to self-regulation from their own feedback. We find that all the BHs in this setup grow at the BHL rate $\dot{M}_{BHL}$, meaning that the mass accreted depends on the BH mass M_{BH}, the average density (temperature) in the $4\Delta x$ surrounding the BH, $\bar{\rho}_{gas}$ ($\bar{T}$). As discussed previously, the BH mass does not significantly change, meaning that a combination of a decreasing density and increasing temperature can explain the decrease in accretion. This possibility is further explored in the next paragraphs.

We also note a difference in terms of growth, which is related to the evolution of the Eddington fraction f_{Edd} of the three simulations in the top left panel of Fig. 2.7. In this panel, only the first 120 kyr of the simulation are shown, and the simulations are represented with the same colour code as Fig. 2.6. A dashed gray line shows $f_{Edd} = 1$. All BHs start super-Eddington and after a certain period of time depending on the resolution of the box, they accrete at sub-Eddington rates, without going back to super-Eddington accretion consistently. In this idealised setup, the time for the transition from super- to sub-Eddington accretion in the $l_{max} = 7$ case is $\sim$ 100 kyr, about twice as long as for $l_{max} = 9$ (*i.e.* $\sim$ 50 kyr) and 5 times longer than $l_{max} = 11$ (*i.e.* $\sim$ 20 kyr). This can be explained when looking at the gas properties near the BH, as they correspond to the BH accretion region and are affected by feedback. We show in the right panels of Fig. 2.7 the evolution of $\bar{\rho}_{gas}$ (top) and $\bar{T}$ (bottom) during the same period of time. Starting with $\bar{\rho}_{gas}$, we notice a strong decrease from

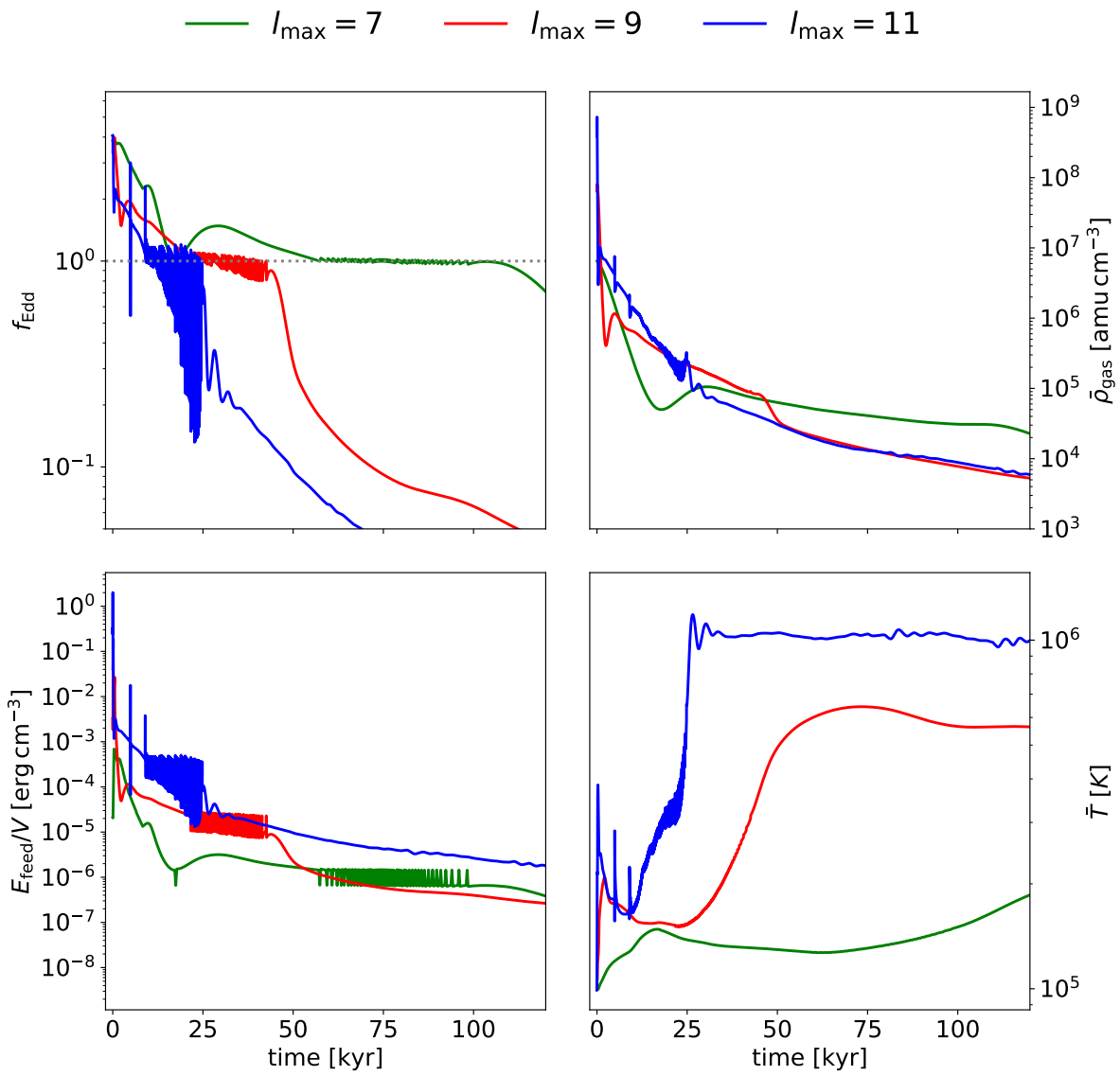

FIGURE 2.7: *Top left:* Eddington ratio f_{Edd} for the $l_{max} = 7$ (solid green), $l_{max} = 9$ (solid red) and $l_{max} = 11$ (solid blue) simulations. The transition from super- to sub-Eddington accretion at $f_{Edd} = 1$ is represented by a dashed gray line. The BHs do not go sub-Eddington at the same time. *Bottom left:* AGN feedback energy per unit volume deposited in the BH surroundings. BHs in more resolved simulations have on average larger feedback per unit volume during super- and sub-Eddington phases. *Top right:* Average gas density $\bar{\rho}_{gas}$ for each simulation. *Bottom right:* Average gas temperature $\bar{T}$ for each simulation.

the initial high gas densities available for accretion. Despite the collapse of the isothermal sphere, it only takes ~ 40 kyr for the average densities to vary little between one simulation to another, reaching $\lesssim 10^5$ amu cm^{-3}. In parallel, the average temperature $\bar{T}$ increases in all three cases, either very slightly (in the $l_{\rm max} = 7$ simulation), or by an order of magnitude (in the other two cases) over the 120 kyr.

The AGN feedback during the super-Eddington phases is responsible for these gas density and temperature variations. The powerful outflows displace a large quantity of gas outside of the BH accretion region, which reduces the available material for accretion, but also heat up the surroundings, meaning that $\dot{M}_{\rm BHL}$ inevitably decreases. Combining the reduction in gas density with the rise in temperature leads to smaller accretion rates, becoming closer to $\dot{M}_{\rm Edd}$ and thus leading to the transition from super- to sub-Eddington accretion. The transition does not happen at the same time in all three simulations because of the temperature differences. These differences are due to the smaller accretion regions the feedback has to heat up in the more resolved boxes. We found that the feedback energy per unit volume is significantly higher for more resolved simulations (which have higher initial accretion rates, due to the more refined and denser accretion region) when comparing the super-Eddington phases of each simulation, as shown in the bottom left panel of Fig. 2.7.

We also notice the temperature plateaus after the transition between super- and sub-Eddington, which is indicative of the change of feedback power. We recall that in the super-Eddington regime, both kinetic and thermal feedback are in play. In our case, the kinetic outflows are ~ 20 times more powerful than the thermal ones. When transitioning to the sub-Eddington "quasar mode", the energy deposited is entirely thermal. The energy deposited in the surroundings in this accretion regime is not high enough to heat up the BH surroundings to even higher temperatures, and since no cooling occurs in these simulations, gas stays at the same temperature.

Finally, we note that the jets are relatively inefficient at blowing out the whole sphere. Since jets are piercing through the sphere in the same direction at all times, the regulation is poor as gas continues to flow on the perpendicular plane of the jets, which allows for the BH to continue its accretion. In a scenario where the jets regularly changed orientation, it would make them work at regulating the infall of gas (*e.g.* Gaspari et al. 2013, Beckmann et al. 2019).

The evolution of $r_{\rm BHL}$

Another purpose of this choice of initial conditions is to study the BHL radius $r_{\rm BHL}$ and its evolution. We show in Fig. 2.8 its evolution over 60 Myr for the three simulations from top to bottom: $l_{\rm max} = 7$, $l_{\rm max} = 9$ and $l_{\rm max} = 11$. We add the maximum resolution at the level $l_{\rm max}$ for each simulation in solid gray, in order to compare more easily the resolution of $r_{\rm BHL}$ throughout time. The trend is clear with our simulations, which shows that $r_{\rm BHL}$ falls generally below the maximum resolution allowed for each simulation, even if it initially starts resolved (*e.g.* $l_{\rm max} = 11$). As discussed in the previous paragraphs, since the BHs only grow by $\lesssim 1$ per cent of their initial mass, this factor does not impact positively the evolution of $r_{\rm BHL}$. On the other hand, the AGN feedback which heats up the BH surroundings, increases the sound speed of the gas and therefore reduces $r_{\rm BHL}$. Since the temperature changes are

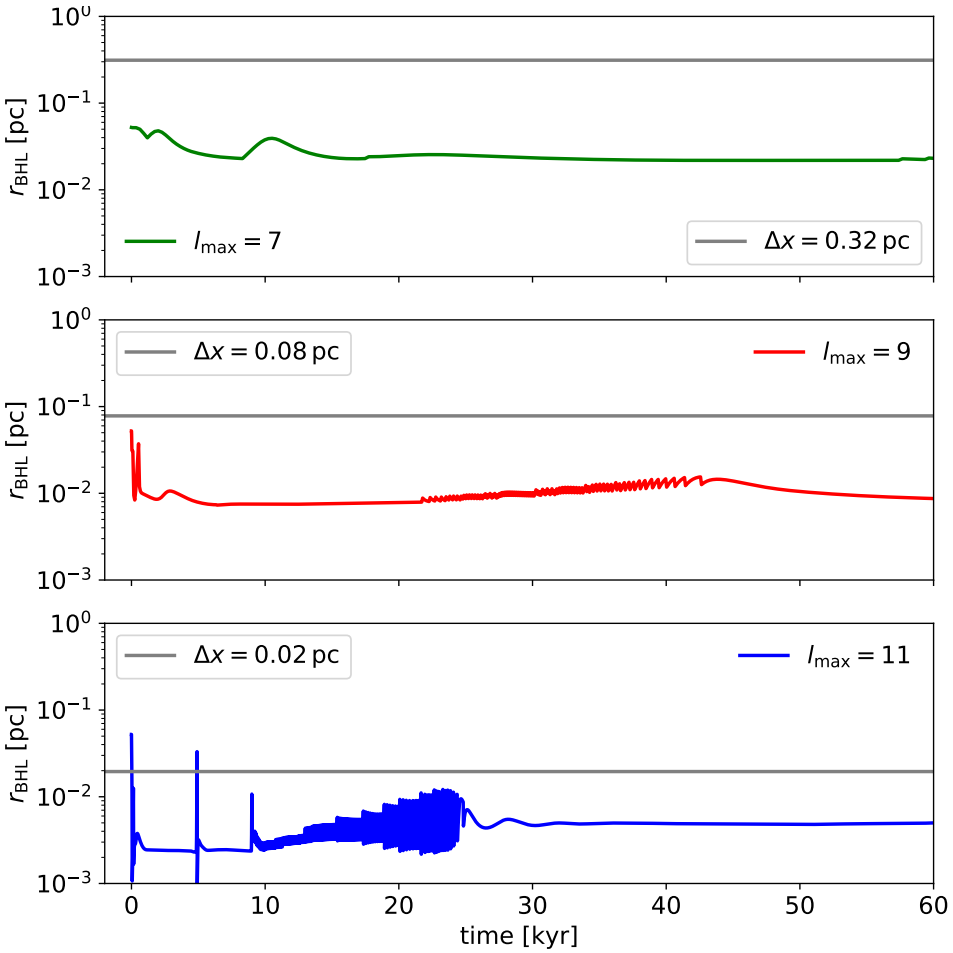

FIGURE 2.8: Evolution of the BHL radius $r_{\rm BHL}$ for the $l_{\rm max} = 7$ (solid green), $l_{\rm max} = 9$ (solid red) and $l_{\rm max} = 11$ (solid blue) simulations. In solid gray is also added the maximal resolution for each simulation. None of the simulations resolve $r_{\rm BHL}$ after the simulation starts, owing initially to the super-Eddington feedback and later on to the lingering quasar feedback.

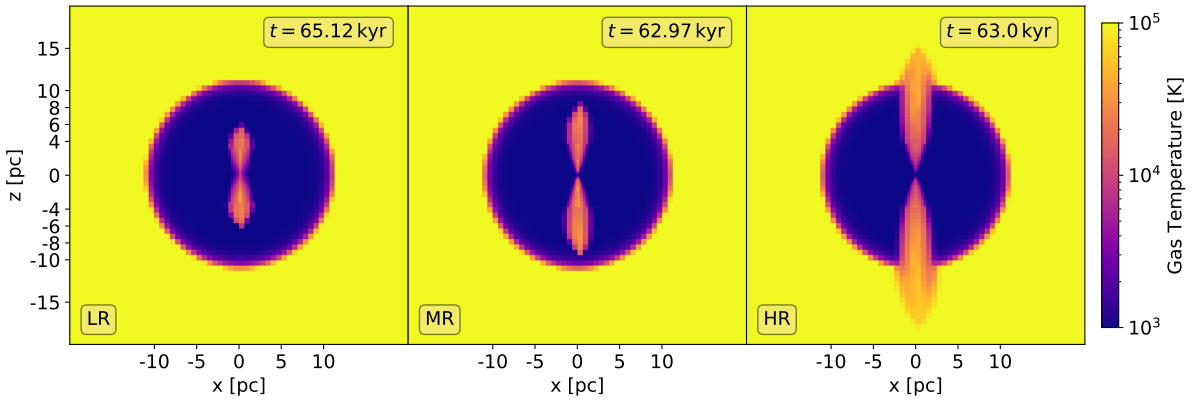

FIGURE 2.9: *Left to right:* Slice of temperature maps of the 'LR', 'MR' and 'HR' simulations at $t \simeq 63\,\mathrm{kyr}$. The jet increases the gas temperature as it expands. Different jet lengths are caused by the different resolution of the simulations.

not significant in the $l_{\mathrm{max}} = 7$ simulation (see Fig. 2.8), r_{BHL} stays relatively constant; however the higher temperatures found near the BH in more resolved simulations lead to a sharp drop of $\sim$ an order of magnitude for r_{BHL}.

Summary of this study

In this Section, we started to quantify the role of super-Eddington feedback in BH evolution using idealised, isolated collapsing clouds. We have seen that super-Eddington feedback in this very idealised setup allows for a short period of continuous growth above the Eddington limit ($\lesssim 100\,\mathrm{kyr}$) but inevitably leads to accretion below the Eddington limit. During this work, we noticed that changing the resolution created a significant difference in long-term accretion duty-cycle and injected energy. BHs were able to reach a higher mass in less resolved simulations, due to lower gas temperatures from the feedback events. This had a significant impact on the duration of the super-Eddington phases, which lead to the differences found in the final BH mass.

Despite accreting at critical rates, BHs stop their growth early on, as their powerful AGN feedbacks eject some inflowing mass outside of their accretion region and increase the temperature of their surroundings. The thermal feedback is weak in comparison to the jets and the former does not seem to play a large role in the regulation of the growth, contrary to the later. We have also investigated the evolution of the BHL radius r_{BHL} and found that it is not resolved during phases of super-Eddington accretion in all three simulations performed, and remains unresolved afterwards. This is once again owing to the AGN feedback, which is the object of the study of the next Section.

2.5.3 The super-Eddington jets

In this Section, we investigate a set of new simulations with only kinetic energy injection and study the impact of the resolution on jets and their effects. The motivation for this study is that with the choices made for super-Eddington feedback in this setup, the BH deposits significantly less thermal energy than kinetic one during the super-Eddington feedback phases. Understanding feedback processes when accretion is involved is complex. For the following

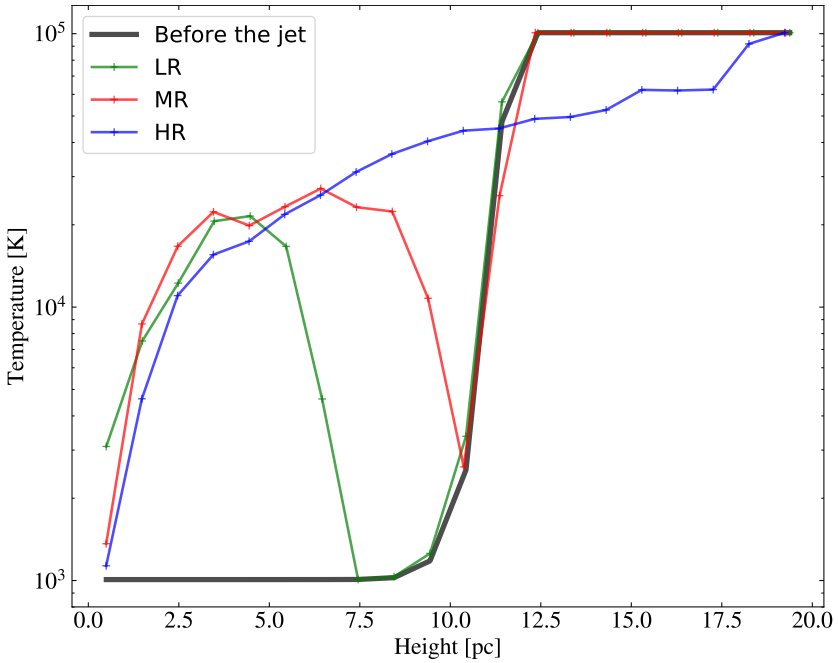

FIGURE 2.10: Gas temperature along a cylinder centered on the BH, before (solid black) and 30 kyr after (coloured lines) the injection of the jet. The presence of the jet is visible with the increase in temperature in the three simulations. This temperature increase is similar in the three cases. However the jet length varies with the resolution: the higher the level of refinement, the longer the jet.

set of simulations, we turned accretion off and injected feedback manually (at a given time with a given energy). In the second part of this Section we introduce the passive scalar for the super-Eddington jets used for the rest of the thesis work.

Impact of the resolution on the jets

In order to reduce the impact of the resolution on the initial launching region of the jets, we modify the density profile of the isothermal sphere. A softening factor χ is added, to flatten $\rho(r)$ as follows:

$$\rho(r) \propto (r^2 + 2^{l_{\rm max}-5}\chi^2)^{-1} \,. \tag{2.40}$$

This allows one to have the same central core for each level of refinement, based on $l_{\rm max} = 5$. This choice was made since the resolution at $l_{\rm max} = 5$ corresponds to 1.25 pc, which is, for $l_{\rm max} = 7$ the size of the BH accretion region. So each simulation will now have a uniform density up to $r = 1.25$ pc. We note that the total mass of the sphere diminishes slightly. We recall that the "singular" isothermal sphere has an outer radius $R = 10$ pc and a sphere mass of $M_{\rm sph} = 2 \times 10^6\,{\rm M}_\odot$. With the new central core, the mass of the sphere is $M_{\rm sph} = 1.8 \times 10^6\,{\rm M}_\odot$ for the same outer radius.

We also set a lower temperature than the previous simulations shown in Section 2.5.2, to allow for a more visible propagation of the jet outflow. The sphere temperature is set to $T = 10^3$ K and we perform simulations with the same resolutions studied before, *i.e.* $l_{\rm max} = 7$, $l_{\rm max} = 9$ and $l_{\rm max} = 11$; namely 'LR', 'MR' and 'HR' respectively.

In each simulation, we model the injection of the kinetic jet as a single burst of energy, at $t = 30$ kyr. The total energy deposited during this burst is equivalent to $20\,{\rm U}_{\rm sph}$. This

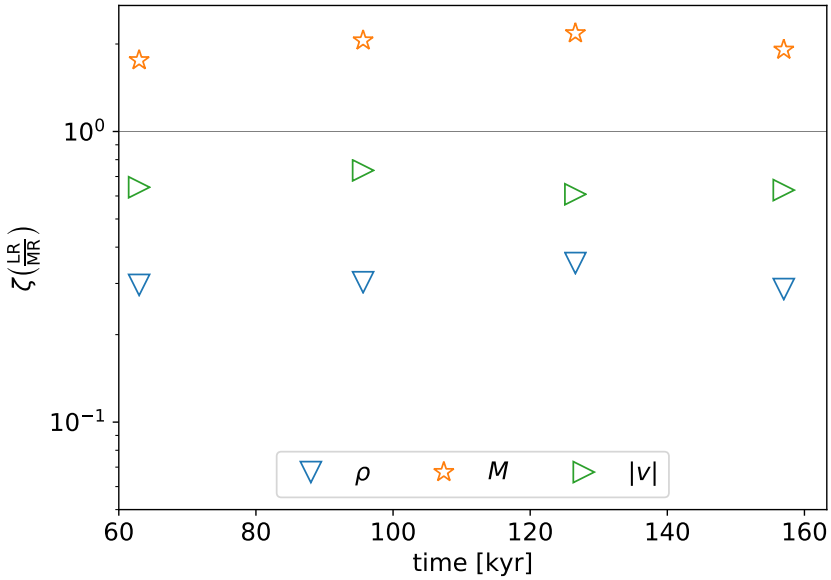

FIGURE 2.11: Ratio of the gas density ρ (blue down triangle), volume V (orange left triangle), mass M (green star) and velocity magnitude $|v|$ (red right triangle) measured in the 'LR' simulation over the same quantity in simulation 'MR'.

allows for the jet to be visible and pierce through the dense sphere in all three simulations. In Fig. 2.9, we plot slice of temperature maps of the isothermal sphere at $t \simeq 63$ kyr for the three simulations. By inspecting visually these simulations, it is clear that jets are able to travel further in the more resolved simulations.

This is confirmed when investigating the temperature of the gas inside the jet, in Fig. 2.10. We set up a cylinder centered on the BH of height z equal to 40 pc (20 pc above and 20 pc below the BH) and radius 0.5 pc and parallel with the outflow. We show in solid black, the gas temperature before the jet is launched, which is indicative of the isothermal profile of the sphere. We recall that the isothermal sphere has an outer radius $R = 10$ pc meaning that the temperature within 10 pc is set to $T = 10^3$ K and outside of the isothermal sphere, $T_{\rm out} = 100T = 10^5$ K. The coloured curves represent the state of the gas for the different simulations at $t \simeq 63$ kyr, *i.e.* the time shown in Fig. 2.9. The jet is clearly present as the coloured curves do not follow the black line. The gas affected by the jet has the same temperature along the axis of the jet regardless of the simulation. For example, 5 pc away from the BH, the gas has a temperature of $\sim 2 \times 10^4$ K in all three simulations. However, the distance traveled by the jet significantly varies: in 'LR', the jet reaches ~ 7 pc in 30 kyr, while in 'MR', it reaches ~ 10 pc in the same amount of time. In the case of the highest resolution, *i.e.* for 'HR', it extends all the way up to the edge of the simulation box, ~ 20 pc away from the BH.

We delve deeper by investigating the properties of the gas along this jet, such as density, mass swept by the outflow and the jet velocity. We need a way to identify the gas cells affected by the feedback. In this idealized set-up one could consider using temperature as a good tracer to indicate the presence of our jet, but in more realistic simulations where gas cooling and other types of feedback are at play this would not be a good choice. We therefore use the passive scalar introduced in Section 2.4.3 as a mean of tracking the outflow in order to study its properties.

We compare in Fig. 2.11, the gas density ρ (blue down triangle), mass M (orange star) and

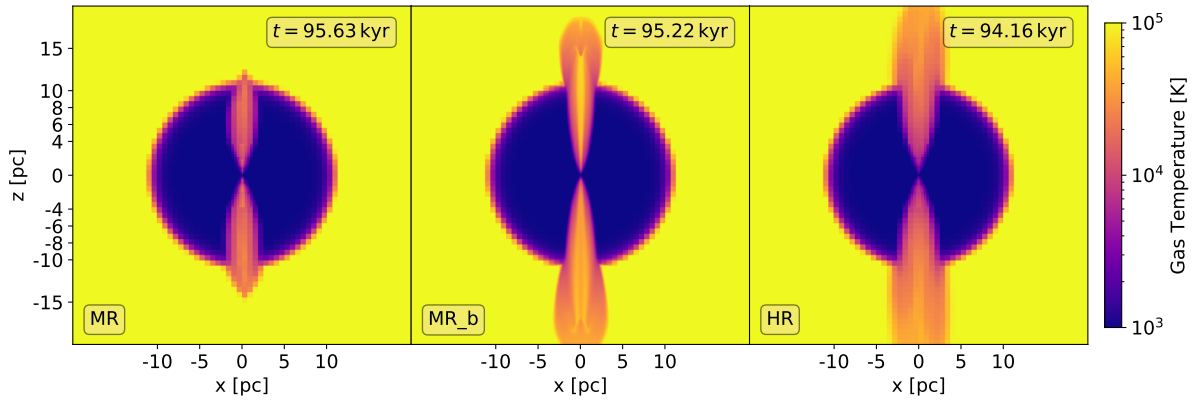

FIGURE 2.12: *Left to right:* Slice of temperature maps of the 'MR', 'MR_b' and 'HR' simulations at $t \simeq 95\,\mathrm{kyr}$. The gas temperature is shown and the jet increases the gas temperature as it expands. The jet structure is better defined when resolved with the passive scalar, which also allows for higher temperatures in the center of the jet.

velocity magnitude $|v|$ (green right triangle) of the cells impacted by the jet in simulations 'LR' and 'MR'. ζ represents the ratio of the quantity (velocity magnitude, density or mass) measured in the 'LR' simulation over the same quantity in simulation 'MR'. Concerning the density, increasing the resolution leads to a higher density that the jet sweeps. Since jets in more resolved simulations travel further, they are able to affect more cells which increases the total gas density swept in the outflow. We also find that the jet affects roughly the same mass when comparing different resolution levels. We confirm that the jet is slightly faster in more resolved simulations, as was already indicated in Fig. 2.10, since the jet travels further in 'MR' than 'LR' in the same amount of time. This is caused by the larger amount of dilution of momentum in the cells that interact with the jet in the less resolved simulation. One can also view this with the following argument: let us consider a constant jet power P_{jet}. The energy flux going through a section of area A of the nozzle of the jet goes as $\rho|v|A \simeq P_{\mathrm{jet}}$. Immediately, we see that $|v| \propto 1/A$, explaining why the better resolved, jets should also be faster.

Refining the jets

As we have seen, resolution plays a crucial role in the way jetted outflows travel throughout the collapsing sphere, and can also impact severely BH growth in the super-Eddington regime (see Section 2.5.2). To better assess the impact of jets, it requires higher resolution. However, increasing the resolution of numerical simulations also increases the cost of computational time. One of the possibilities to have the most resolved jets whilst not drastically increasing the computational time is to only refine the regions of interest. For our final investigation, we therefore use the passive scalar and refine all cells which have a scalar to gas ratio greater than 10^{-10} to the maximum level of refinement of the box. This simulation is performed with $l_{\mathrm{max}} = 9$ and name it 'MR_b'.

We show in Fig. 2.12 similar slice maps as in Fig. 2.9 but between the 'MR', 'MR_b' and 'HR' simulations. The funnel and nozzle are very well defined when the jet is refined with a cocoon that englobes them. Comparing with an unrefined jet, these structures are mixed with the gas and form "one big cocoon". We also note that the length of the jet seems on

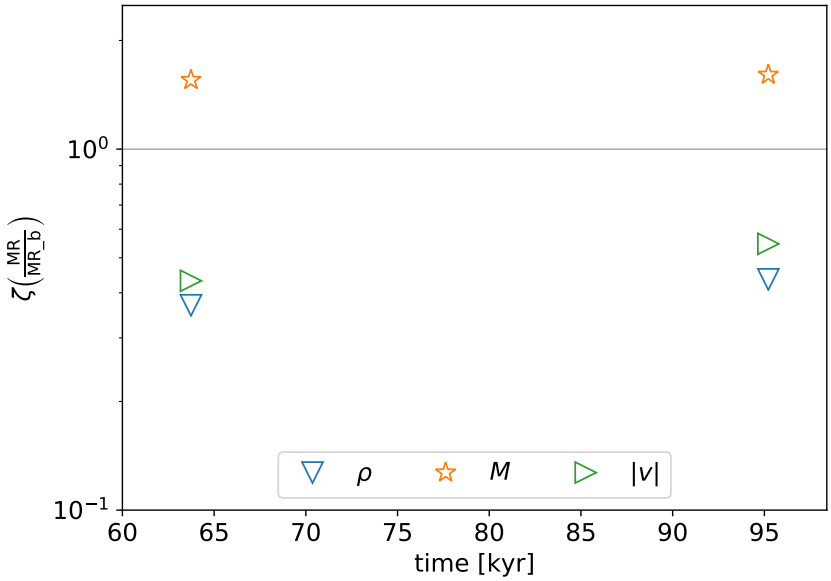

FIGURE 2.13: Ratio of the gas density ρ (blue down triangle), volume V (orange left triangle), mass M (green star) and velocity magnitude $|v|$ (red right triangle) measured in the 'MR' simulation over the same quantity in simulation 'MR_b'.

par with the 'HR' simulation shown on the right panel. The resolved region carries gas with higher temperature, as the funnel is less subject to mixing with the cold gas outside the jet. It is also clear that a refined jet goes significantly faster and is able to travel significantly further than in the unrefined simulation. In fact, when comparing in Fig. 2.13 the velocity magnitude of cells impacted by the jet between 'MR' and 'MR_b', the results show that the jet seem to be twice as fast when resolved. One can view this with the same argument as before ($|v| \propto 1/A$), simply in this case thinner, *i.e.* better resolved, jets should also be faster. Finally, we note that in our idealised setup, the jets carry away the same amount of mass whether refined or not.

Summary of this study

In this Section, we have studied the impact of the refinement on the propagation of the jets in the super-Eddington regime. We find that jets are faster, longer the higher the resolution, but that they drive away the same amount of mass regardless of the resolution studied here. They do not perturb drastically the accretion flow of the black hole for higher resolution levels as the sphere is still collapsing. Refining the jets with the passive scalar allows them to propagate even further, with a more defined funnel and nozzle, that can be visually seen in Fig. 2.12. Thanks to this study, we were able to understand better the role of jetted feedback in this very controlled and idealised experiment. Applying the lessons learnt here to a less idealised accretion driven simulation will allow a better interpretation of the results on how black holes grow in an environment affected by feedback. In the next Chapter, we aim to study the evolution of a BH in a more realistic, yet idealised setting, using the jetted prescription described in this Section.

Chapter 3

How the super-Eddington regime regulates black hole growth in high-redshift galaxies

Super-Eddington accretion is one scenario that may explain the rapid assembly of $\sim 10^9\,M_\odot$ SMBHs within the first billion year of the Universe. This critical regime is associated with radiatively inefficient accretion and accompanied by powerful outflows in the form of winds and jets. In Chapter 2, we investigated super-Eddington accretion and feedback mechanisms using very idealised, isolated collapsing clouds with different ratios of cloud and SMBH properties. During this work, we noticed that changing the resolution created significant differences in BH accretion and injected energy. After analysing the behaviour of jets in this cloud of gas, we had a better understanding of how resolution could affect our results and decided to investigate the super-Eddington regime in a more realistic environment. In this Chapter, we study the impact that this critical regime has on BH growth and on the gas properties of the host galaxy, from star-forming clouds to galactic scales and explore whether a BH can sustain super-Eddington accretion when both wind and mechanical feedback work together. To this end, we perform several simulations of an individual galaxy in an isolated DM halo. We add a BH to the center of the emergent galaxy and conduct a survey on the parameter dependence regarding BH growth and overall impact on the gas inflows and outflows, varying the feedback efficiencies and modes of injection in the super-Eddington regime. This Chapter corresponds to the submitted paper Massonneau et al. (2022b).

3.1 Introduction

Over 200 quasars at high redshift, $z \geq 6$ (*i.e.* less than $\sim 1\,$Gyr after the Big Bang) have been discovered in the past decades (*e.g.* Fan et al. 2004, Mortlock et al. 2011, Wu et al. 2015, Bañados et al. 2018). These quasars host SMBHs with masses larger than $M_{\rm BH} \geq 10^9\,M_\odot$. The formation and rapid growth of these compact objects at such an early stage of the Universe are one of the most important puzzles faced by modern astrophysics.

As discussed in Section 1.4.2, several models have been suggested regarding the formation of seed BHs (*e.g.* Haiman 2013, Inayoshi et al. 2020, Volonteri et al. 2021: and references therein). There are several potential formation channels: light seeds, which are Pop III remnant BHs of $M_{\rm BH} \simeq 10$ to $10^2\,M_\odot$ (*e.g.* McKee & Tan 2008, Hosokawa et al. 2011, Hirano et al. 2014, Hirano et al. 2015, Stacy et al. 2016) formed in DM minihalos; intermediate seeds,

corresponding to intermediate mass BHs born in dense clusters from stellar or BH mergers, with $M_{\rm BH} \simeq 10^3\,{\rm M}_\odot$ (*e.g.* Devecchi & Volonteri 2009, Katz et al. 2015, Sakurai et al. 2017, 2019, Tagawa et al. 2020); heavy seeds, which emerge from the direct collapse of first halos and that leaves a seed with a large initial mass of $M_{\rm BH} \simeq 10^4$ to $10^5\,{\rm M}_\odot$ (*e.g.* Bromm & Loeb 2003, Inayoshi et al. 2014, Regan et al. 2014, Latif et al. 2016a, Wise et al. 2019). Even for massive seeds, assuming an Eddington-limited accretion, the orders of magnitude between formation mass and the observed mass of the BHs in $z \geq 6$ quasars requires a very high duty cycle of accretion close to the Eddington limit.

Massive halos can provide gas to funnel to the most central regions of high-redshift galaxies and feed BHs through direct accretion of cold cosmic streams, later on replaced by clumpy gas accretion (Bournaud et al. 2011, Di Matteo et al. 2012, Di Matteo et al. 2017, Dubois et al. 2012a). Even in the presence of large gas reservoirs, continuous accretion at Eddington levels is challenging to sustain, as feedback from gas accretion onto the BH seed can severely affect gas inflows and prevent efficient BH growth (*e.g.* Johnson & Bromm 2007, Alvarez et al. 2009, Milosavljević et al. 2009, Dubois et al. 2013). In addition, feedback from massive stars in the shallow potential well of low-mass galaxies is able to significantly suppress the availability of cold interstellar gas in the central regions of galaxies, therefore, quenching BH growth in low-mass galaxies (Dubois et al. 2015, Anglés-Alcázar et al. 2017, Bower et al. 2017, Habouzit et al. 2017, Prieto et al. 2017, Trebitsch et al. 2018, Hopkins et al. 2022). This effect, also associated to the wandering of BHs in shallow potential wells of low-mass galaxies (Bellovary et al. 2019, Pfister et al. 2019, Ma et al. 2021) might prevent BHs to grow until their host galaxy build up a massive and compact enough bulge component (Lapiner et al. 2021). Accretion rates larger than the Eddington limit could solve this timescale issue, but only if super-Eddington episodes can be sustained long or frequently enough to allow for significant mass growth (Volonteri et al. 2015, Pezzulli et al. 2017).

Breaking the Eddington limit is a natural manifestation of non-spherically symmetric accretion (Paczynski & Abramowicz 1982) and over the past decades, observational evidence supports super-Eddington accretion (see Section 1.5.1). Detections of X-ray binaries, such as SS 433 (*e.g.* Okuda 2002), or of ultra-Luminous X-ray sources that may harbor stellar-mass BHs (*e.g.* Winter et al. 2006) are considered to be signatures of accretion rates above the Eddington limit. Several observations point to the supermassive BHs in narrow-line Seyfert-1 galaxies (*e.g.* Mineshige et al. 2000, Collin & Kawaguchi 2004, Du et al. 2014, 2018, Jin et al. 2017), as well as transient sources called tidal disruption events (*e.g.* Burrows et al. 2011, Lin et al. 2017, 2022), which are also candidates for super-Eddington accretors. Several theoretical models have been developed to explain this state of accretion, such as the slim disc model (Abramowicz et al. 1988, Sądowski 2009, Abramowicz & Fragile 2013). One of the most important features of this regime is the photon trapping effect (Katz 1977, Begelman 1978), in which radiated photons are advected to the BH instead of being diffused out of the disc. As a result, the radiative efficiency drops below its typical value of $\epsilon_{\rm r} \sim 0.1$ expected in thin discs. However, there is yet no agreement on how efficient this process is, and on the exact value of the resulting radiative efficiency (*e.g.* Ohsuga et al. 2005, Jiang et al. 2014, 2019, McKinney et al. 2014, 2015, Sądowski et al. 2015). Semi-analytical models using the slim disc regime have shown that a light seed could grow from $10^2\,{\rm M}_\odot$ to a few $10^9\,{\rm M}_\odot$ (Madau et al. 2014), thanks to reduced radiative efficiency. Other numerical works in modelling the

accretion disc near the BH found that if gas inflows are funneled in the equatorial plane with the radiation and outflows escaping out from the poles, then super-Eddington accretion can be sustained (*e.g.* Inayoshi et al. 2016, Sugimura et al. 2017, Takeo et al. 2018, 2020, Toyouchi et al. 2019, 2021, Kitaki et al. 2021a).

Although numerical simulations of accretion discs are extremely detailed and cover a wide range of physical processes, such small-scale numerical experiments do not explore regions beyond the pc-scale and cannot capture the dynamics of the gas feeding the BH and the impact from super-Eddington feedback at larger galactic scales. Using sub-pc resolution hydrodynamical simulations of circum-nuclear discs with BHs releasing energy with thermal input, Lupi et al. (2016) showed that stellar-mass BHs are able to grow to $\sim 10^4\,\mathrm{M}_\odot$ within 3 Myr. This is thanks to a combination of the very high density gas clumps formed due to disc fragmentation, and the radiative inefficient accretion from this super-critical regime. Their results indicate that several events of short periods of super-Eddington accretion on light seeds can sustain enough mass growth to explain the most massive BHs powering quasars at high redshift. However, super-Eddington accretion may be accompanied (if not dominated) by powerful jets (*e.g.* Sądowski & Narayan 2015, Narayan et al. 2017), which, added to the radiation, can have an impact on BH growth. Recently, Regan et al. (2019) investigated how super-Eddington bipolar jet outflows affect gas inflows in an atomic cooling halo in a cosmological setting. They were able to reach resolutions down to the BH gravitational sphere of influence and found that jets almost entirely shut down the inflow of gas towards the BH on small scales ($\simeq 0.1$ pc) and were not able to break out of the halo. The effective accretion rate was found to be ~ 4 orders of magnitude below the Eddington limit, thus suggesting that BHs are not able to grow effectively above the limit with strong jetted outflows. On the other hand, Takeo et al. (2020) performed RHD simulations combining radiative and mechanical feedback and found that gas in the polar region was completely evacuated but gas inflows from the equatorial region maintained super-Eddington accretion rates. The outflows were able to pierce through the gas distribution without disrupting it. The discrepancy between these results may be linked to the gas geometry, however it is unclear if the axisymmetric disc configuration in Takeo et al. (2020) can be achieved assuming the turbulent nature of high-redshift galaxies.

The outline of the Chapter is as follows. We briefly describe our numerical methods in Section 3.2, including a summary of the already implemented AGN feedback models with the new application for super-Eddington accretion and feedback in `Ramses` (a detailed description is given in Chapter 2, Sections 2.3.5 to 2.4.3). In Section 3.3, we describe the set-up for our isolated DM halo simulations, in particular the initial conditions that lead to the formation of the galaxy and the addition of the BH. We then present our simulation results in Section 3.4 where we analyse the importance of the super-Eddington AGN feedback on star formation, BH growth and gas properties, varying its power and modes of injection. We discuss these results and finally conclude in Section 3.5.

3.2 Implementation of the super-Eddington regime

This Chapter showcases a number of hydrodynamical simulations of an isolated DM halo in which BHs have been evolved in the super-Eddington regime, all of them performed using

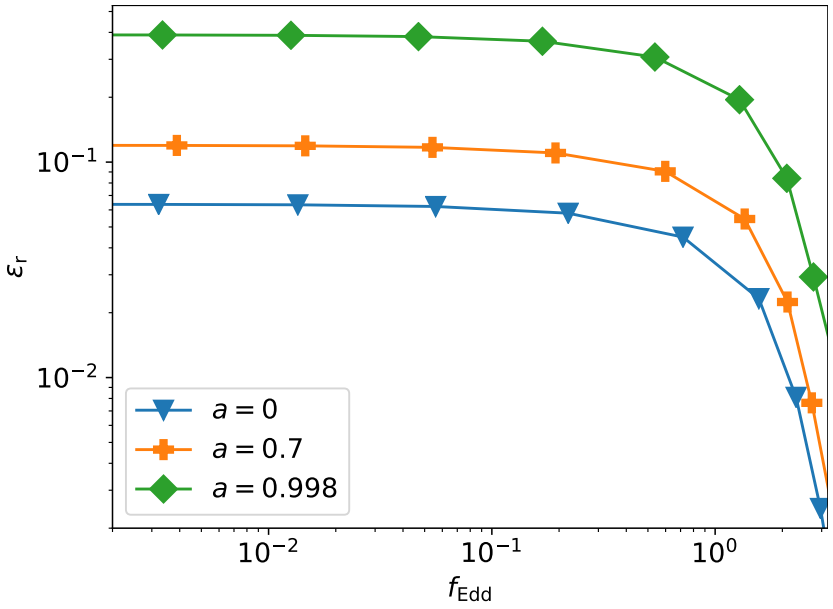

FIGURE 3.1: Radiative efficiency ϵ_r as a function of the Eddington fraction f_{Edd}. The markers showcase the different BH spin values. Photon-trapping is visible when $f_{Edd} > 1$ for all spin parameters.

the adaptive mesh refinement code `Ramses`, which was adapted to allow for accretion and feedback processes above the Eddington limit, defined as:

$$L_{Edd} \equiv \frac{4\pi G M_{BH} m_p c}{\sigma_T}, \tag{3.1}$$

where G is the gravitational constant, M_{BH} the BH mass, m_p the proton mass, c the speed of light and σ_T the Thomson cross-section. In this Section we detail how the super-Eddington regime is implemented in `Ramses`.

3.2.1 Accretion onto the BH

A BH is represented by a "sink" particle that can transfer mass, momentum and energy from and to the gas. The algorithm for gas accretion onto sink particles, first introduced by Krumholz et al. 2004 for grid codes, is described in detail in Dubois et al. 2012b for its `Ramses` implementation. We recall here the main ideas: the BH is manually placed with a given initial mass, velocity and spin, in the simulation at a certain point in time. Once set, it is able to move, following the local gravitational acceleration. At all times, we enforce the highest resolution level within a sphere of radius $4\Delta x$, where Δx is the smallest cell size, to better resolve the forces near the BH. Since we cannot resolve accretion discs around BHs, as their size is below our resolution limit, we calculate the accretion rate on the BH using the BHL formula (Hoyle & Lyttleton 1939, Bondi 1952):

$$\dot{M}_{BHL} = \frac{4\pi G^2 M_{BH}^2 \bar{\rho}}{(\bar{c}_s^2 + \bar{v}_{rel}^2)^{3/2}}, \tag{3.2}$$

where the averaged density $\bar{\rho}$, sound speed $\bar{c}_s$ and relative velocity between the BH and the gas $\bar{v}_{rel}$ are computed over a sphere of radius of $4\Delta x$ with contributions from each cell

weighted by $w \propto \exp\left(-r^2/r_{\rm K}^2\right)$ (Krumholz et al. 2004). The kernel radius $r_{\rm K}$ depends on whether the BHL radius $r_{\rm BHL} = GM_{\rm BH}/(c_{\rm s}^2 + v_{\rm rel}^2)$ is resolved or not, where $c_{\rm s}$ and $v_{\rm rel}$ are the sound speed and relative velocity in the cell where the sink lies. It is defined as follows:

$$r_{\rm K} = \begin{cases} \Delta x/4 & r_{\rm BHL} < \Delta x/4\,, \\ r_{\rm BHL} & \Delta x/4 \leq r_{\rm BHL} \leq 2\Delta x\,, \\ 2\Delta x & r_{\rm BHL} > 2\Delta x\,. \end{cases} \tag{3.3}$$

In order to prevent having cells completely depleted of gas at high accretion rates, a safety check allows for accretion of only up to 25 per cent of the total mass available in each cell at each timestep of size Δt, *i.e.* $\dot{M}_{\rm floor} = 0.25\rho\Delta x^3/\Delta t$, where ρ is the density of the cell. All the accretion rates mentioned are subject to the same weight w, applied when gas is removed from the grid and accreted onto the sink particle. The accretion rate is calculated as $\dot{M}_{\rm acc} = \min(\dot{M}_{\rm BHL}, \dot{M}_{\rm floor})$, which is always less than the mass contained in the kernel divided by the timestep. The mass contained in the kernel is used to both feed the BH and power kinetic feedback, with mass conservation enforced at all times.

To calculate the feedback energy released by the BH in the super-Eddington regime, the slim disc solution is used (Abramowicz et al. 1988, Sądowski 2009, Abramowicz & Fragile 2013). Despite having accretion rates that go well above the Eddington value, the disc emits a luminosity that is only slightly above the Eddington luminosity $L_{\rm Edd}$ (see Eq. 3.1). It has been shown in several theoretical works (Begelman 1978, Mineshige et al. 2000, Ohsuga et al. 2002, Madau et al. 2014, Inayoshi et al. 2020) that when $\dot{M}_{\rm acc} > \dot{M}_{\rm Edd}$, the luminosity $L \propto \log(\dot{M}_{\rm acc})$ which means that the radiative efficiency $\epsilon_{\rm r}$ decreases. This is due to the photon-trapping effect and it impacts the growth rate of the BH, since $\dot{M}_{\rm BH} = (1-\epsilon_{\rm r})\dot{M}_{\rm acc}$. In order to estimate $\epsilon_{\rm r}$, we use the fit from Madau et al. (2014) (who themselves use the fit from Sądowski (2009)) for the ratio of the bolometric luminosity-to-Eddington $f_{\rm Edd} \equiv L/L_{\rm Edd}$:

$$f_{\rm Edd} = A(a)\left[\frac{0.985}{1.6\dot{M}_{\rm Edd}/\dot{M}_{\rm acc} + B(a)} + \frac{0.015}{1.6\dot{M}_{\rm Edd}/\dot{M}_{\rm acc} + C(a)}\right], \tag{3.4}$$

where $\dot{M}_{\rm Edd}$ is the Eddington mass accretion rate defined as $\dot{M}_{\rm Edd} \equiv 10L_{\rm Edd}/c^2$, given an $\epsilon_{\rm r}$ of 0.1 ; a is the BH spin, and with spin-dependent functions A, B and C as:

$$A(a) = (0.9663 - 0.9292a)^{-0.5639}, \tag{3.5}$$

$$B(a) = (4.627 - 4.445a)^{-0.5524}, \tag{3.6}$$

$$C(a) = (827.3 - 718.1a)^{-0.7060}. \tag{3.7}$$

The effect of photon-trapping on the radiative efficiency is illustrated in Fig. 3.1. The different markers represent different spins, from no rotation (blue triangle) to maximum rotation, set at 0.998[1] (green diamond). We also show the BH spin $a = 0.7$ (orange cross) giving $\epsilon_{\rm r} \simeq 0.1$ for small values of $f_{\rm Edd}$. $\epsilon_{\rm r} = 0.1$ is usually adopted in cosmological simulations as a constant radiative efficiency (*e.g.* Di Matteo et al. 2008, Booth & Schaye 2009, Dubois

[1]The normalized spin $a = 0.998 < 1$, is due to the photons emitted by the accretion disc and captured by the BH (Thorne 1974).

et al. 2012b, although see Dubois et al. 2014b, 2021, Bustamante & Springel 2019 for spin-dependent radiative efficiencies). At a given accretion rate, the higher the spin, the higher the radiative efficiency. While our simulations can self-consistently evolve BH spins and, thus, associated radiative efficiencies, we prefer to simplify the problem by adopting a fixed spin value of $a = 0.7$ ($\epsilon_r = 0.1$ for $f_{\rm Edd} < 1$) throughout the rest of this Chapter. In this study, accretion is not Eddington-limited unless specified, in which case the accretion rate is limited by $\dot{M}_{\rm Edd}$.

3.2.2 Feedback in the different regimes

In `Ramses`, AGN feedback is implemented with two separate feedback modes: a kinetic mode, active at low accretion rates, which is modeled as a jet-like outflow and a thermal mode, active at high but sub-Eddington accretion rates, which heats the gas surrounding the BH by releasing thermal energy (Dubois et al. 2012b). For consistency with Madau et al. (2014) and Sądowski et al. (2016), the transition between these regimes is based on $f_{\rm Edd}$ rather than on the ratio of accretion rates.

With our current understanding of the super-Eddington regime, super-Eddington AGN feedback includes both kinetic and radiative/thermal components. We have modified `Ramses` to allow for a new super-Eddington feedback mode that injects both thermal and kinetic energy simultaneously.

Kinetic feedback

In the sub-Eddington regime, when $f_{\rm Edd} \leq 0.01$, feedback is kinetic, and modelled with jet-like outflows, called "radio" mode. At each feedback event, mass, momentum and energy are deposited in a cylinder of diameter and height equal to $2r_{\rm jet}$. The size of the jet $r_{\rm jet}$ is a user-defined parameter in units of Δx. The cylinder axis is aligned with the BH spin axis (Dubois et al. 2014b). To calculate the energy injected as kinetic energy in all the cells within the cylinder, we follow Sądowski et al. (2016), which gives a total jet feedback of

$$\dot{E}_{\rm jet} = \eta_{\rm jet} \dot{M}_{\rm BH} c^2 \,, \tag{3.8}$$

where $\eta_{\rm jet} = 1.3 a^2 f_{\rm MAD}^2$ is the efficiency factor of the kinetic feedback for a magnetically arrested disc (MAD) taken from Tchekhovskoy (2015), and $0 \leq f_{\rm MAD} \leq 1$ represents the fraction of MAD strength (magnetic field saturation).

Since jets are a relativistic phenomenon and are launched at velocities close to c on scales that cannot be resolved in our simulations (a few Schwarzschild radii), we must develop a sub-grid model to account for how the jet evolves from the launching scale to the simulation resolution. As jets traverse the interstellar medium and dense clouds, they entrain mass and slow down: the mass that loads the jet, changes its velocity such as its value at the lowest scale resolved is lower than that at the unresolved launching scale (that of the accretion disc). The mass-loading factor $\beta_{\rm jet}$ is expressed as the ratio between the mass ejection rate $\dot{M}_{\rm jet}$ in the jet and the growth rate of the BH, *i.e.* $\beta_{\rm jet} = \dot{M}_{\rm jet}/\dot{M}_{\rm BH}$. Assuming that the jet energy

is simply the kinetic energy of the jet at injection, $\dot{E}_{\rm jet} = 0.5\dot{M}_{\rm jet}v_{\rm jet}^2$, one can write the mass-loading factor as

$$\beta_{\rm jet} = 2\eta_{\rm jet}\left(\frac{v_{\rm jet}}{c}\right)^{-2}. \tag{3.9}$$

Here, we set $v_{\rm jet} = 0.1c$ in order to keep the time step of the simulation affordable, and therefore $\beta_{\rm jet} = 200\eta_{\rm jet}$.

The mass that is loaded into the jet is transferred from the same cells that were used for the accretion, *i.e.* within $4\Delta x$ of the sink particle with the same distance-weighting described previously, to all cells enclosed within the jet (Dubois et al. 2012b). In the case where insufficient mass is available to fully load the jet, the mass-loading factor is smaller than the predicted value but the jet is still launched at $v_{\rm jet} = 0.1c$. A maximum of 25 per cent of the total mass available in each cell is used to load the jet, to avoid dealing with extremely low densities and numerical instabilities.

Thermal feedback

When $0.01 < f_{\rm Edd} \leq 1$, the AGN enters the so-called "quasar" mode, which corresponds to feedback coming from disc winds and radiation. In this mode, energy is released as thermal energy in a sphere of radius $r_{\rm thm}$ around the BH. This radius, similarly to $r_{\rm jet}$, is a user-defined parameter in units of Δx.

The efficiency factor $\eta_{\rm thm}$ for this regime corresponds to the thermal wind efficiency of the disc. Following Sądowski et al. (2016), the spin-dependent thermal wind efficiency can be written as $\eta_{\rm thm} = \eta_{\rm d\to thm} \times \eta_{\rm ISCO}$, with

$$\eta_{\rm ISCO} = 1 - \sqrt{1 - \frac{2}{3R_{\rm ISCO}(a)}}, \tag{3.10}$$

where $\eta_{\rm d\to thm}$ is the fraction of energy released from the disc coupled to the gas within $r_{\rm thm}$, depending on how well the energy from the accretion disc can be absorbed by the surrounding gas. We set $\eta_{\rm d\to thm} = 0.15$, which has been calibrated to reproduce the BH-galaxy scaling relations (Dubois et al. 2012b). $R_{\rm ISCO}$ corresponds to the innermost stable circular orbit (Bardeen 1970), *i.e.*

$$R_{\rm ISCO} = \frac{GM_{\rm BH}}{c^2}\left(3 + Z_2 \mp \sqrt{(3-Z_1)(3+Z_1+2Z_2)}\right), \tag{3.11}$$

where the $\mp$ sign corresponds to respectively the positive $(-)$ and negative $(+)$ values of the BH spin, and

$$Z_1 = 1 + (1-a^2)^{1/3} \times \left((1+a)^{1/3} + (1-a)^{1/3}\right),$$
$$Z_2 = \sqrt{(3a^2 + Z_1^2)}.$$

Including this effect, the total energy deposited in the cells contained within the spherical region is thus

$$\dot{E}_{\rm thm} = \eta_{\rm thm}\dot{M}_{\rm BH}c^2. \tag{3.12}$$

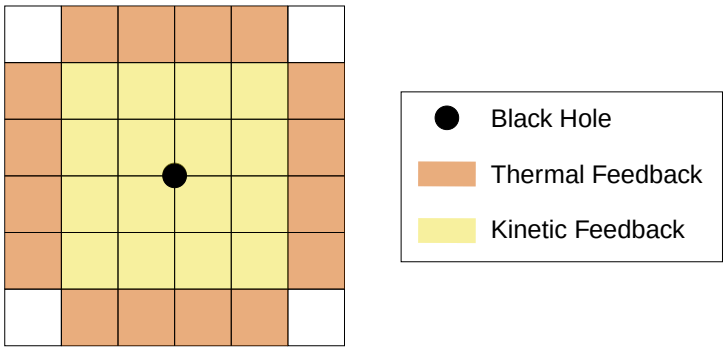

FIGURE 3.2: Schematic representation of the feedback injection in cells around the BH in `Ramses`. The region of injection of the kinetic feedback is in yellow and the thermal in vermilion. No thermal feedback is injected in the same region as the kinetic one, as the deposited energy is different for both forms.

Super-Eddington feedback

Finally, in the case when $f_{\rm Edd} > 1$, energy is injected as both thermal and kinetic energy as shown in the schematic representation in Fig. 3.2. As AGN feedback happens on scales below Δx, a small region of injection must be chosen. Dubois et al. (2012b) show that large jet sizes $r_{\rm jet}$ lead to BH masses unrealistic when compared to observations. In addition, they find that increasing $r_{\rm thm}$ would effectively lead to a weaker impact on self-regulating the growth of BHs, thus concluding that the size of injection must be close to Δx. However, to prevent having numerical issues, we cannot use a single cell for feedback injection and to ensure that both feedback forms are well-separated, we set $r_{\rm jet} = 2\Delta x$ and $r_{\rm thm} = 3\Delta x$.

All cells that are in a cylinder of radius $r_{\rm jet}$ will only contain kinetic feedback. In all other cells within $3\Delta x$ of the BH, thermal feedback will be deposited. Since the energy deposition is different for both forms, we do not allow for thermal feedback (which would impact the temperature of the gas) to be injected in the region where kinetic feedback is also acting as the kinetic feedback already changes the temperature of the gas indirectly.

Based on Sądowski et al. (2016), the total AGN feedback injected in the super-Eddington regime reads as follows:

$$\dot{E}_{\rm sEdd} = \dot{E}_{\rm jet} + \dot{E}_{\rm thm} = (\eta_{\rm jet} + 0.5\eta_{\rm thm})\dot{M}_{\rm BH}c^2. \tag{3.13}$$

3.3 Setting up the halo

3.3.1 Numerical initial conditions

Sustaining super-Eddington accretion onto the BH requires strong gas inflows, which are more likely to occur in gas-rich high-redshift galaxies. The gas distribution in a low-mass isolated halo (for instance a $10^9\,{\rm M}_\odot$ halo) at high redshift is quickly destroyed by SN feedback, with the result that star formation is shut off and that there is not sufficient cold and dense gas available for (super-Eddington) accretion on the BH (Dubois et al. 2015). In a more

$M_{\rm halo}$ (in $M_\odot$)	c_{200}	R_{200} (in kpc)	T_{200} (in K)	$Z_{\rm avg}$ (in $Z_\odot$)	$n_{\rm SF}$ (in amu cm^{-3})	M_* (in $M_\odot$)	$\epsilon_{\rm SN}$	$\Delta x_{\rm max}$ (in pc)
10^{11}	3.4	42.82	3.6×10^5	0.3	10	10^4	0.2	12

TABLE 3.1: Initial conditions for the cooling isolated halo. From left to right: halo mass ($M_{\rm halo}$), NFW concentration (c_{200}), virial radius (R_{200}), virial temperature (T_{200}), average metallicity ($Z_{\rm avg}$), density threshold for star formation ($n_{\rm SF}$), stellar mass resolution (M_*), SN feedback efficiency ($\epsilon_{\rm SN}$) and smallest cell size ($\Delta x_{\rm max}$).

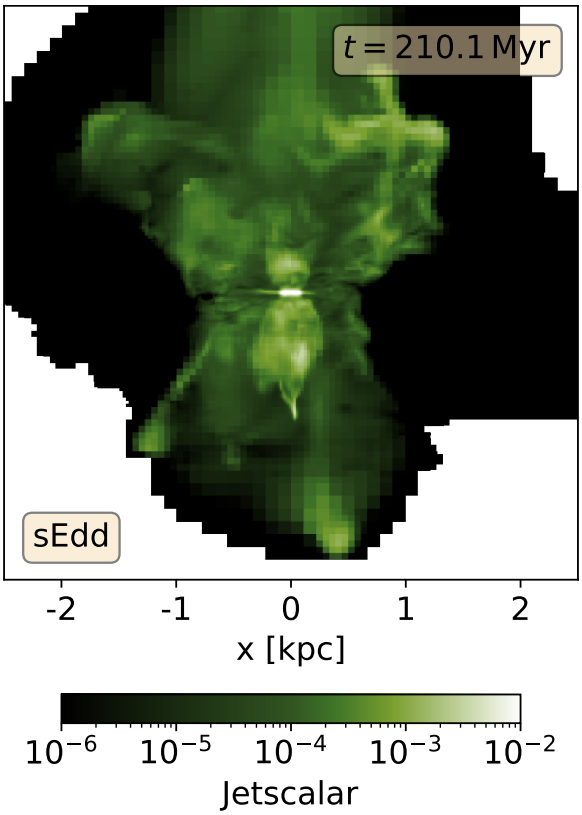

FIGURE 3.3: Passive scalar used to follow the super-Eddington jet outflows at $t = 210$ Myr for the 'sEdd' simulation.

massive halo, such as one that has $10^{11}\,M_\odot$, the evolution is less violent, since the deeper potential well limits the impact from SN. To take advantage of this, we set up our initial conditions to represent an isolated DM halo of mass $10^{11}\,M_\odot$ at redshift $z = 4$. In order to probe the progenitors of $z = 6$ SMBHs, one would need to investigate higher redshifts ($z > 6$); however SN explosions for simulations with $z > 6$ destroyed the collapsing halo without forming the galaxy and providing enough material to have even one super-Eddington episode.

The halo is modelled using a fixed DM Navarro-Frenk-White profile (NFW, Navarro et al. 1997), centerd on the box. Gas is initialised following the same density profile as the DM, with a gas fraction of $f_{\rm gas} = 0.15$. The halo is given an initial spin of 0.02 along the z-axis (Bullock et al. 2001) and turbulence is injected into the gas up to 20 per cent of the local sound speed[2]. Virial radius R_{200} and concentration parameter c_{200} are computed using the redshift-dependent relations from Dutton & Macciò 2014. Gas is initialised in hydrostatic equilibrium and allowed to cool from there as the simulation progresses. The average metallicity of

[2]This turbulence is needed to break the spherical symmetry of the initial conditions.

the gas is set to $Z_{\rm avg} = 0.3\,Z_\odot$, with $Z_\odot = 0.02$ and metal-enriched gas can cool down to 10 K, using Sutherland & Dopita (1993) cooling rates down to 10^4 K and those from Rosen & Bregman (1995) for temperatures below.

The simulations are performed in a box of size 113 kpc with a root grid of 128^3, and then adaptively refined to a maximum resolution of $\Delta x_{\rm max} = 12$ pc (corresponding to level 13) using four refinement criteria. A quasi-Lagrangian criterion forces the refinement of the mesh if cells which have a mass greater than $8 \times 10^5\,M_\odot$. In addition to that, a Jeans length based criterion is applied: a cell is refined such that its size is smaller than the local Jeans length. Thirdly, when a BH sink particle is added, the region is automatically refined to the maximum level of refinement around it up to a spherical radius of $4\Delta x_{\rm max}$. Finally, to refine the regions of interest affected by the jets in super-Eddington AGN feedback, we add a passive scalar variable in the BH super-Eddington kinetic outflows (following Beckmann et al. 2019), using a density $\rho_{\rm scalar}$ equal to the gas density $\rho_{\rm gas}$ in the region of injection. We allow for refinement if the scalar has a value above 0.01 and a variation from one cell to another greater than 0.05. This scalar follows the hydrodynamics of the gas and is able to track regions affected by the super-Eddington jets. It decays exponentially, with a decay time of $t_{\rm decay} = 3$ Myr, making sure recent super-Eddington jet episodes are refined, while avoiding refining a large fraction of the box. This value of $t_{\rm decay}$ was chosen to balance computational cost with the need to refine as much of the jet structure as reasonably possible. An example of the jet scalar distribution given in Fig. 3.3 for our fiducial simulation ('sEdd') that we will introduce later.

The BH accretion and feedback properties for all accretion regimes are described in Section 3.2.1 and Section 3.2.2 respectively. In order to help the BH particle stay bound with the galaxy, particle drag force is included (Pfister et al. 2019). We avoid applying drag force from the gas onto the BH (Dubois et al. 2013), as it sometimes causes unwanted behaviours, such as the BH to follow its own outflows, which could lead to it being ejected from the galaxy.

Stars form in cells above a gas density threshold of $n_{\rm SF}$ following the local star formation rate density from a Schmidt law $\dot{\rho}_{\rm s} = \epsilon_{\rm s}\rho/t_{\rm ff}$, where $t_{\rm ff}$ is the local gas free-fall time and $\epsilon_{\rm s}$ is the star formation efficiency. We adopt a gravo-turbulent star formation efficiency that depends on the gravitational binding energy of the cloud and on the turbulent Mach number (*e.g.* Federrath & Klessen 2012), adopting the relations and parameters as in Dubois et al. (2021). For a spatial resolution of 12 pc, the stellar mass resolution is $M_* = 10^4\,M_\odot$ (therefore star formation occurs in regions with gas densities above 181 amu cm^{-3}).

Following the energy and mechanical injection from Kimm et al. 2015, SN feedback is modelled as a total specific energy release between 3 and 50 Myr of 2×10^{49} erg/$M_\odot$, with a semi-continuous energy injection by individual SN explosions of 10^{51} erg at a time with realistic time delays Kimm et al. 2015. We set the metal yield at 10 per cent for the SN feedback.

The parameters to set up the cooling isolated halo at $z = 4$ are summarized in Table 3.1.

3.3.2 Galaxy formation

When searching for a set of initial conditions that would allow for super-Eddington accretion onto the BH, we found that efficient star formation quickly suppressed gas inflows into the center of the galaxy, which suppressed accretion rates onto the BH. The collapse of the halo triggers star formation in its center, which has densities reaching 10^3 amu cm^{-3}. The

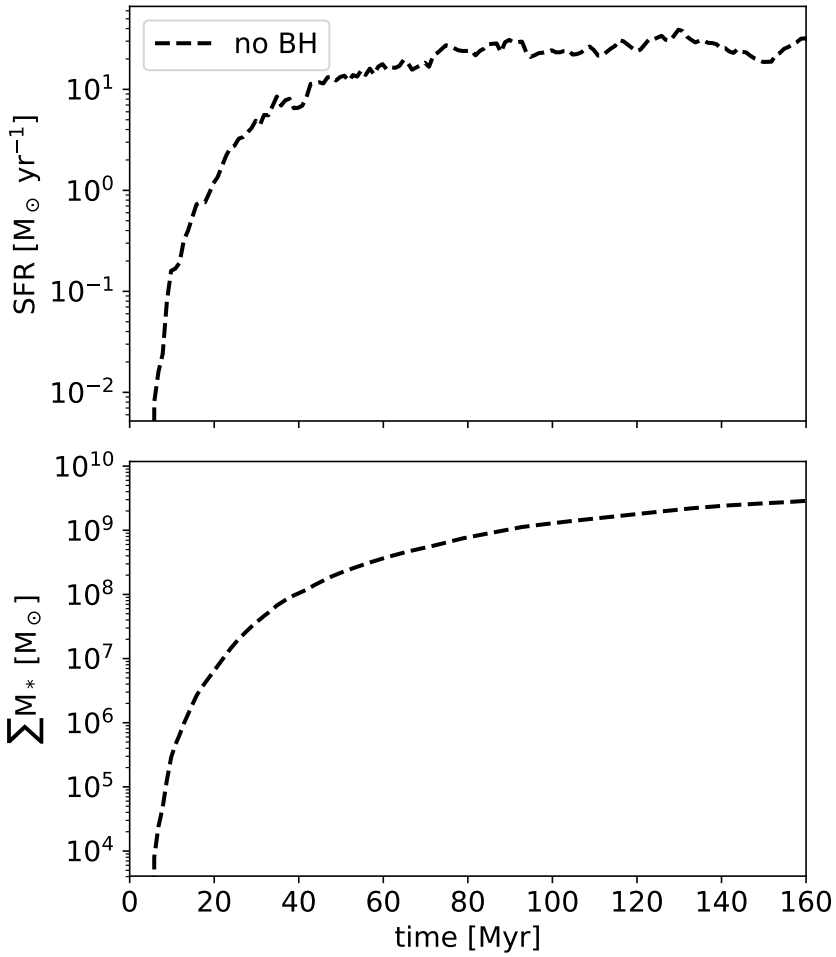

FIGURE 3.4: Evolution of the SFR (top) and total stellar mass (bottom). As the halo cools, stars start to appear as conditions for their formation are met. Over the course of 100 Myr, the SFR steadily stays above 10 $M_\odot$ yr^{-1}, allowing the galaxy to reach $M_* = 10^9$ $M_\odot$ within 160 Myr.

resulting SN explosions are strong enough to heat up the gas over several kpc, eventually breaking the integrity of the halo. Since we are looking for initial conditions that allow for super-Eddington accretion, this initial SN burst, which is a consequence of having an isolated halo rather than a fully cosmological simulation, has to be circumvented. There are various options generally used in isolated simulations, such as starting with an artificially low star formation or SN efficiency and increase it to standard values over time, or alternatively do something similar with cooling. In this Chapter we opted to suppress the SN feedback by changing the hydro solver to a more diffusive one when forming the galaxy. This eliminates the necessity of choosing the functional form of how to increase star formation, SN efficiency or cooling.

For this reason, we use a Lax-Friedrichs "llf" approximate Riemann solver for the early (BH-free phase) of the simulation, which allows for copious star formation as the halo collapses, without having SN feedback unbinding the gas. For the part of the simulation relevant for this experiment, *i.e.*, when a BH and its feedback are included, we switch to the Harten-Lax-van Leer-Contact (Toro 1999) "hllc" solver, which has a less diffusive nature and is a more accurate solver for the important part of this study.

We consider our galaxy to have reached a steady state (*i.e.* had enough cycles of star

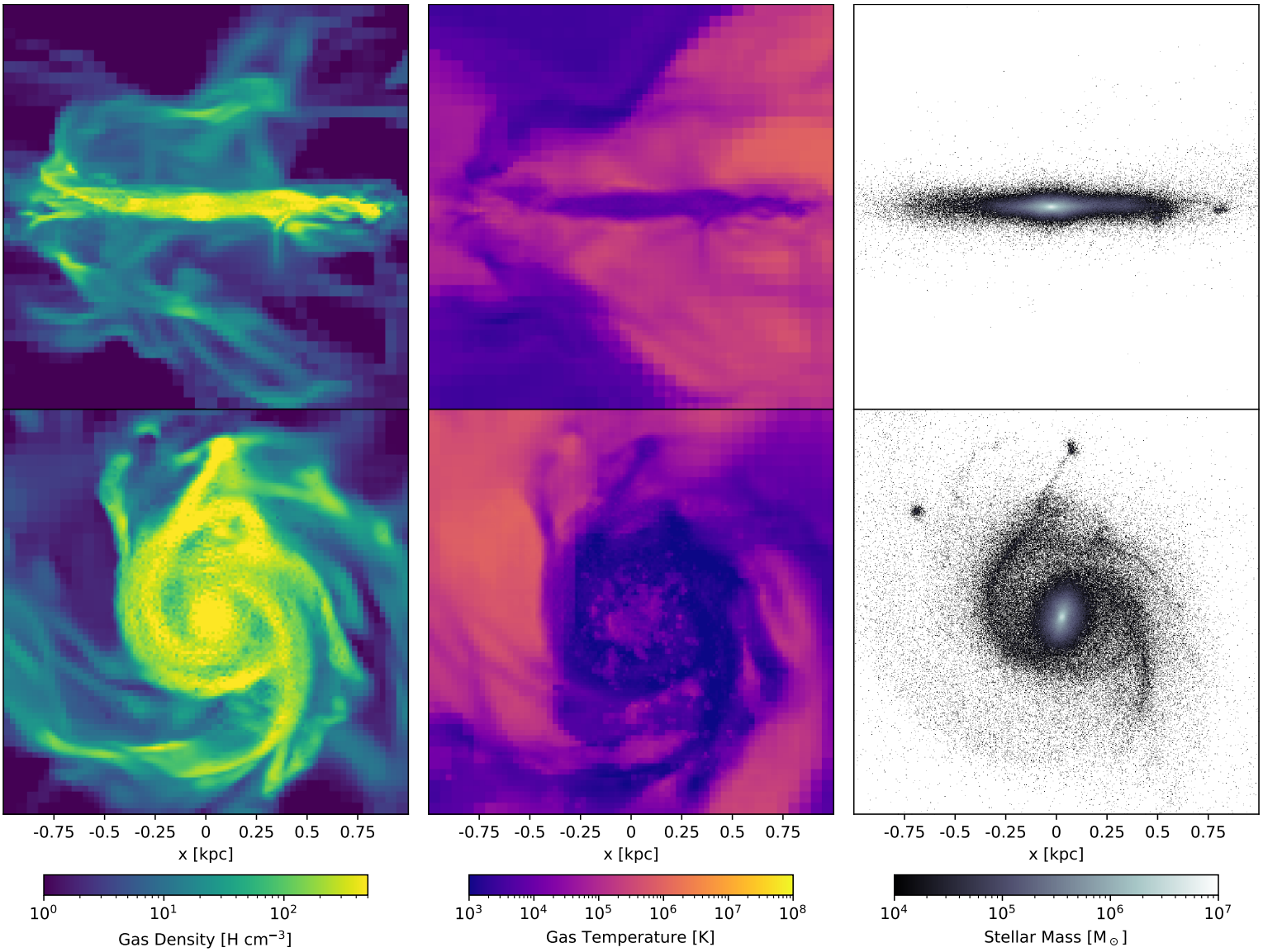

FIGURE 3.5: $1 \times 1 \times 1$kpc edge-on (top) and face-on (bottom) projections of the galaxy at the center of the DM halo at $t = 160$ Myr. The first column shows the gas density, the second column shows the gas temperature and the third column shows the stellar mass.

formation and SN feedback events) when the total stellar mass reaches the stellar-to-halo mass relationship (Moster et al. 2010): the total stellar mass for a $10^{11}\,M_\odot$ halo is about $10^8 - 10^9\,M_\odot$. As shown in Fig. 3.4, the expected total stellar mass is reached within 160 Myr, with a quasi constant SFR of a few $10\,M_\odot\,yr^{-1}$, which is also the expected order of magnitude for our target redshift $z = 4$ (Salmon et al. 2015).

We find that our galaxy is dominated by a central stellar proto-bulge, with a half-mass radius averaging ~ 110 pc at 160 Myr. The galaxy extends up to ~ 1 kpc from its center of mass, as stars continue to form in the disc. The galaxy is therefore very compact, a common trait for high-redshift galaxies (Allen et al. 2017, Shibuya et al. 2019). An edge-on (top) and face-on (bottom) projection views of the galaxy gas density, temperature and stellar mass are shown in Fig. 3.5.

Once a galaxy-like structure with clumps in its spiral arms starts to form and settles with

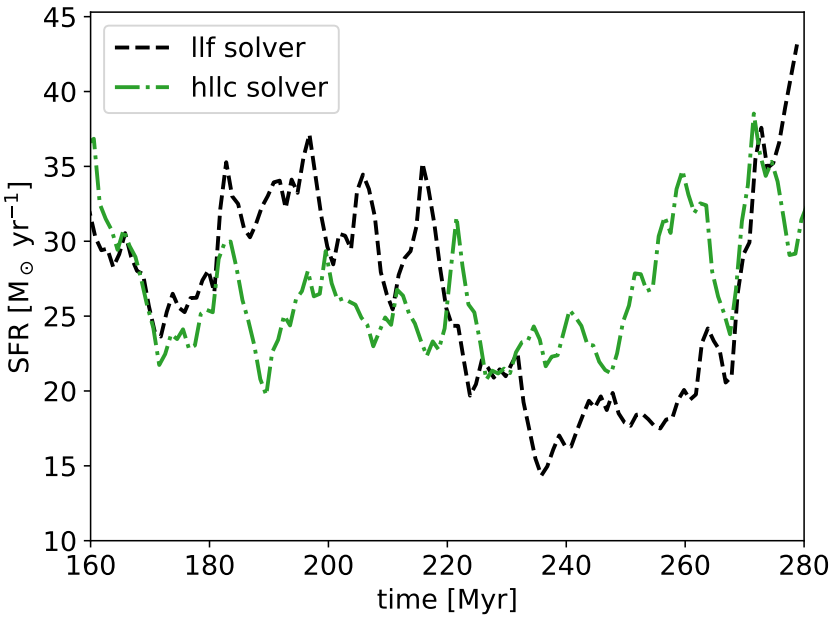

FIGURE 3.6: Comparison of the evolution of the SFR between "llf" (dashed black) and "hllc" (dash-dotted green) runs. Changing the solver to one that is less diffusive does not change the SFR drastically. The SN explosions do not disrupt the environment as effectively since the galaxy is already formed.

a realistic stellar mass and star formation rate, a BH is added in the center of the galaxy[3]. At this point, we switch to the more accurate "hllc" approximate Riemann solver.

In order to see the effect of the change of hydro solvers mid-way through the simulation, we investigate the evolution of the SFR for both solvers at late times in Fig 3.6. "hllc" (dash-dotted green) is the simulation where we swap solver at $t = 160\,\mathrm{Myr}$, and is the one used for the remainder of the work presented here, while "llf" (dashed black) continues to use the same solver throughout for comparison. In the "hllc" case the SN outflows expand further because of the less diffusive solver used. Higher diffusivity smoothes shocks, which prevents them from propagating efficiently. In a less diffusive solver, such as "hllc", the shocks are maintained and SN bubbles continue to expand due to the pressure difference inside and outside the bubble. As expected, this more efficient SN feedback somewhat decreases the SFR. This effect is notable but does not significantly impact the long-term evolution of the galaxy as the SFR is of the same order of magnitude in both cases. We therefore conclude that transitioning from an "llf" to an "hllc" solver does not produce a strong discontinuity in the evolution history of our galaxy. Changing solvers therefore allows us to have an isolated galaxy that can meet the conditions for super-Eddington accretion, while still using the most appropriate and accurate hydro solver for the part of the simulation concerned with BH accretion and feedback.

[3]The center of the proto-bulge remains close to the gas' center of mass and to the DM center of mass, centered on the box, throughout the simulation.

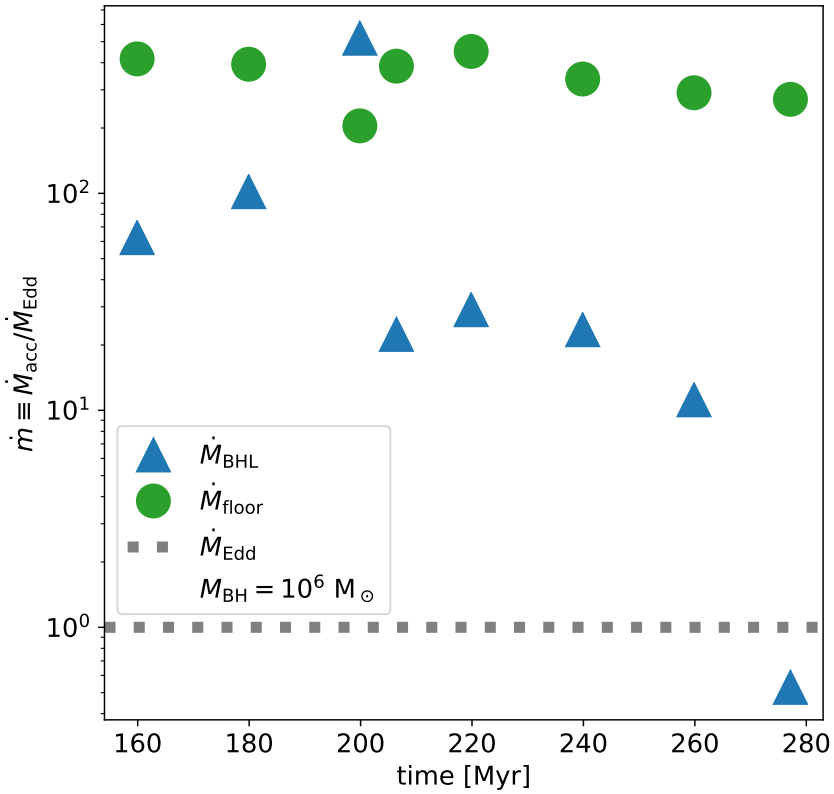

FIGURE 3.7: Evolution of the normalized accretion rate $\dot{m} \equiv \dot{M}_{acc}/\dot{M}_{Edd}$ for the isolated 10^{11} M$_\odot$ halo, assuming that a M$_{BH} = 10^6$ M$_\odot$ were present. The BHL and floor accretion rates are shown in blue and green respectively and the Eddington limit by the dotted line at 1. There is enough mass available for accretion thanks to the high density present in the central region at the start, which allows for both the BHL and floor accretion rates to be above the limit.

3.3.3 Adding the BH

The next step is to choose the properties of the BH to be inserted in the simulation. For galaxies with stellar mass in the range $10^8 - 10^{10}$ M$_\odot$, BH masses of 10^4 to 10^7 M$_\odot$ are possible, based on observations in the local Universe (Reines & Volonteri 2015). Since we need to have a setup that allows for super-Eddington accretion, and the Eddington limit is proportional to M_{BH} while the BHL accretion is proportional to M_{BH}^2, more massive BHs are favoured.

Before testing the effect of the self-consistent AGN feedback on the BH growth, we first want to test whether the galaxy setup is favorable for BH growth, and if it can produce a sustained super-Eddington accretion rate in the absence of its own feedback. Therefore, in Fig. 3.7, we estimate the accretion properties for a potential M$_{BH} = 10^6$ M$_\odot$ BH at different points of time during the evolution of our galaxy. This is done in post-processing, and, hence, it does not include the feedback from the BH. At each point in time, we assume that the BH is located at the center of mass of the galaxy, and has a velocity equal to the averaged velocity of the gas around it (see Section 3.2.1). Having the same velocity as the gas cells around the BH maximises the BHL accretion rate $\dot{M}_{BHL}$ (blue triangle). We compare this value to the available mass $\dot{M}_{floor}$ within the accretion region of the BH (green filled circle) and to the Eddington limit $\dot{M}_{Edd}$ (dotted line). We generally find an ample gas supply to sustain BHL accretion, as $\dot{M}_{BHL}$ is generally below $\dot{M}_{floor}$. The environment is also usually

Name	$M_{\rm BH}$ (in $\rm M_\odot$)	a	Accretion above Eddington	AGN Feedback above Eddington	$f_{\rm MAD}$	$\beta_{\rm jet}$	$\eta_{\rm jet}$	$\eta_{\rm thm}$	$\Delta x_{\rm max}$ (in pc)
EddLim	10^6	0.7	✗	✗	0.5	32	0.16	0.015	12
sEdd (fid.)	10^6	**0.7**	✓	**Kinetic+Thermal**	**0.5**	**32**	**0.16**	**0.015**	**12**
sEddNF	10^6	0.7	✓	✗	✗	✗	✗	✗	12
sEddThm	10^6	0.7	✓	Thermal	0.5	32	0.16	0.015	12
sEdd_0.05	10^6	0.7	✓	Kinetic+Thermal	0.05	0.32	0.0016	0.015	12
sEdd_0.1	10^6	0.7	✓	Kinetic+Thermal	0.1	1.28	0.006	0.015	12
sEdd_0.25	10^6	0.7	✓	Kinetic+Thermal	0.25	8	0.04	0.015	12
HR	10^6	0.7	✓	Kinetic+Thermal	0.5	32	0.16	0.015	6
LR	10^6	0.7	✓	Kinetic+Thermal	0.5	32	0.16	0.015	25

TABLE 3.2: Properties of the suite of simulations performed, showing from left to right: BH mass ($M_{\rm BH}$); BH spin (a); if the super-Eddington regime is allowed; the form of feedback in the super-Eddington regime; MADness fraction of the disc ($f_{\rm MAD}$); mass-loading factor ($\beta_{\rm jet}$); jet feedback efficiency ($\eta_{\rm jet}$); thermal feedback efficiency ($\eta_{\rm thm}$); and smallest cell size ($\Delta x_{\rm max}$). All simulations start with a $10^6\,\rm M_\odot$ BH with a fixed spin set to $a = 0.7$.

favorable for super-Eddington accretion, as accretion rates on average exceed $10\dot{M}_{\rm Edd}$. By contrast, a similar analysis for a $10^5\,\rm M_\odot$ BH (not shown) leads to accretion rates that are on average below the Eddington limit (and 100 times below the blue triangles in Fig. 3.7), while a significantly higher BH mass of around $10^7\,\rm M_\odot$ would lead to accretion being limited by the local gas supply ($\dot{M}_{\rm floor} < \dot{M}_{\rm BHL}$, not shown).

We therefore choose to add a $M_{\rm BH} = 10^6\,\rm M_\odot$ BH to our simulations and follow the same prescription described previously regarding its initial position and velocity. The normalized spin of the BH is fixed along the z-axis, parallel to that of the halo, and its value is set to $a = 0.7$ (which gives the canonical radiative efficiency of $\epsilon_{\rm r} = 0.1$ for the standard thin accretion disc). We chose to not evolve the spin magnitude and direction in these sets of simulations presented here to highlight only the effects of super-Eddington accretion. Studying the impact of a fully self-consistent spin evolution of the BH as in Dubois et al. (2014b) is discussed in Chapter 4.

3.4 Results

In this section, we analyse the consequences of super-Eddington accretion coupled with its AGN feedback. We study the evolution of the SFR, the accretion history of the BH and whether the feedback can have a long lasting effect on scales ranging from pc to kpc that could impact BH growth and galaxy evolution. We explore the parameter space of the jet efficiency and also perform a resolution study to understand how super-Eddington performs at different levels of resolution. We gather all the simulations performed in Table 3.2.

3.4.1 Comparison between Eddington-limited and super-Eddington accretion

In order to understand the impact of the super-Eddington regime on BH growth and galaxy evolution, we perform four simulations with different accretion and feedback regimes. The first simulation allows the BH to accrete above the Eddington limit but does not include any AGN feedback ('sEddNF'). The purpose of this simulation is to establish an upper limit to BH growth in our galaxy now in a numerically self-consistent way as opposed to

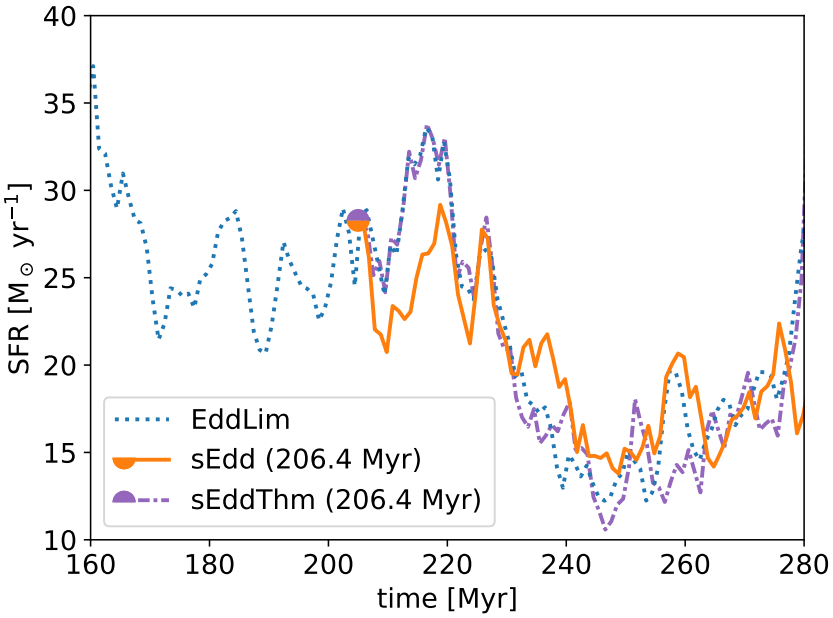

FIGURE 3.8: Evolution of the SFR after 160 Myr for the simulations with accretion capped at the Eddington limit ('EddLim' - dotted blue) and above the Eddington limit with ('sEdd' - solid orange) and without ('sEddThm' - densely dash-dotted violet) kinetic feedback starting at 206.4 Myr (orange/violet filled semi-circles). The SFR does not decrease below 10 $M_\odot$ yr^{-1} after the BH was added, even in the case of the super-Eddington feedback. The difference between the runs is small, showing that AGN feedback does not majorly impact the SFR in this particular setup.

the previous post-processing approach (section 3.3.3). The second simulation is Eddington-limited and releases AGN feedback according to its accretion rate ('EddLim'). Our fiducial simulation ('sEdd') uses the Eddington-limited accretion until $\sim$ 206.4 Myr, and allows for super-Eddington accretion and feedback processes from this point onwards. This allows for a smooth transition from the galaxy without a BH to a BH with potentially very strong feedback. If we added the BH with immediate super-Eddington feedback, the surge of accretion would produce extremely strong feedback that would sterilize the BH environment. By enforcing a few cycles of Eddington-limited feedback, the gas and BH are able to stabilize and the galaxy evolution remains more continuous. Finally, a simulation with thermal-only super-Eddington feedback (*i.e.* without the jet contribution in the super-Eddington phase) is shown ('sEddThm'). It only differs from 'sEdd' by the injection of feedback in the super-Eddington phases, which is thermal feedback released within $3\Delta x_{\rm max}$ from the BH.

Super-Eddington AGN feedback does not impact the SFR

In Fig. 3.8, we show the evolution of the SFR after the BH has been added to the simulation, for the 'EddLim', 'sEddThm' and 'sEdd' cases. In the 'sEddThm' simulation, we find that the SFR evolution is identical to the 'EddLim' simulation. Overall, adding a BH to the simulation does not strongly affect the SFR, despite the fact that the BH is able to deplete its immediate surroundings efficiently.

Over the course of $\sim$ 80 Myr, we find that AGN feedback, whether Eddington-limited or not, does not significantly influence the average SFR of the galaxy as the inflow of cold gas

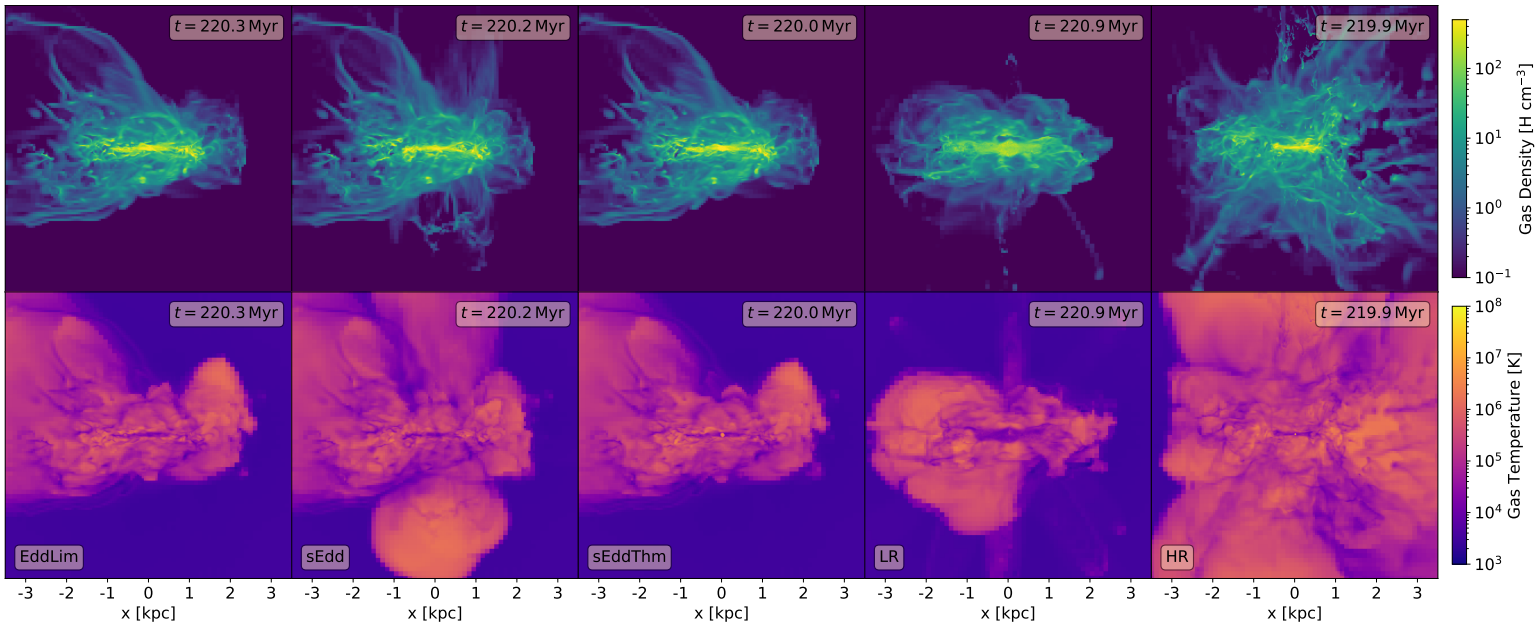

FIGURE 3.9: *Left to right:* Edge-on projection maps of the 'EddLim', 'sEdd', 'sEddThm', 'LR' and 'HR' simulations at $t = 220\,\mathrm{Myr}$. Gas density and temperature are respectively shown in the first and second row. SNe as well as super-Eddington kinetic feedback are visible on large scales.

from the cooling halo continues to drive star formation (SF). AGN feedback events are not able to counter this.

In Fig. 3.9, we plot edge-on projections maps of the gas density and temperature of the galaxy at $t = 220\,\mathrm{Myr}$. By inspecting visually these simulations, it is clear that most of the outflows correspond to SN explosions. The released SN power is $\simeq 2 \times 10^{49}\,\mathrm{erg\,M_\odot^{-1}}$ times the SFR (varying from 10 to $\simeq 40\,\mathrm{M_\odot\,yr^{-1}}$), *i.e.* $\simeq 10^{43}\,\mathrm{erg\,s^{-1}}$. They impact large scales because of the SNe occurring near the edges of the galactic disc. It is easier to warm up the cold and rarefied gas found in the outer galactic regions than ejecting gas from the galaxy center, which is very dense. The collapse of the halo is not halted despite the SN explosions expanding away from the galaxy. We find that overall, the inflow rates are larger than the outflow rates as the SN-driven outflows are hot and light and therefore do not carry away a lot of mass (but see how cosmic rays accelerated in SNe can appreciably modify the wind thermodynamics, *e.g.* Girichidis et al. 2018, Dashyan & Dubois 2020). The shallow potential of the $M_\mathrm{halo} = 10^{11}\,\mathrm{M_\odot}$ halo allows the SN-driven winds to efficiently suppress SF (*e.g.* Springel & Hernquist 2003, Dubois & Teyssier 2008, Scannapieco et al. 2008, Agertz et al. 2013, Hopkins et al. 2014). Over time, they cool down and fall back onto the galaxy, thus contributing to the inflows.

Besides SN feedback, a minor contribution to regulating SF comes from AGN feedback. As can be seen from Fig. 3.9, in the 'EddLim' run, no outflows coming from the AGN are visible at kpc-scales, as they are not powerful enough to disrupt the dense gas in the galactic center. This is not only true at the snapshot shown here but throughout the 'EddLim' simulation. By contrast, the visible super-Eddington kinetic bipolar outflows in the 'sEdd' simulation are able to reach kpc extents, with much of the energy deposited far from the galactic center. They do not affect star-forming regions directly (Dubois et al. 2013, Gabor & Bournaud 2014) and therefore have a smaller impact on SF than SNe, as AGN jets are

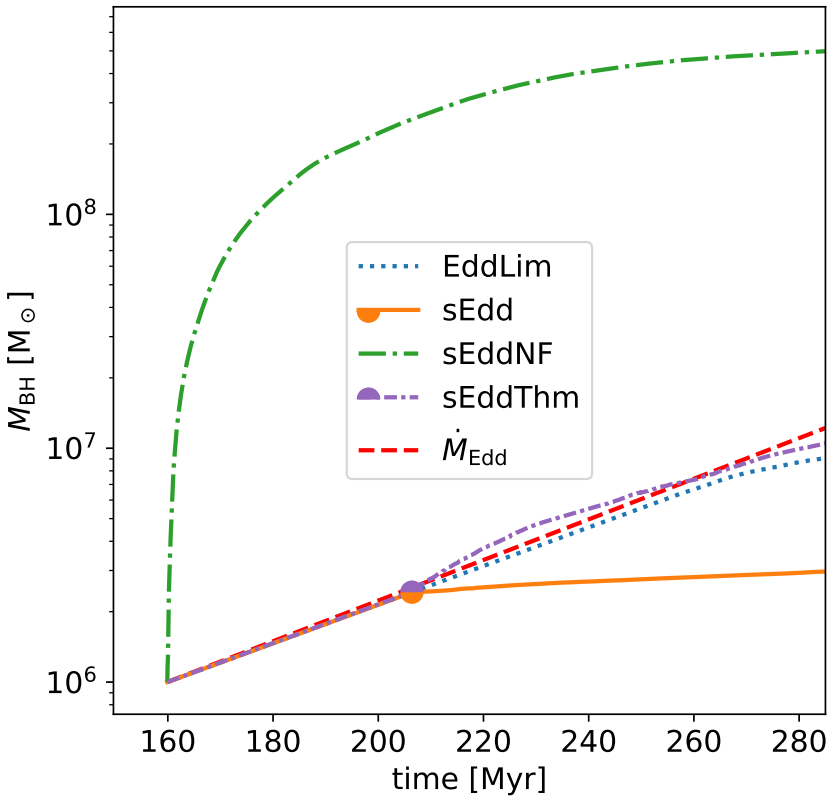

FIGURE 3.10: Evolution of the BH mass for the 'EddLim' (dotted blue), 'sEdd' (solid orange), 'sEddThm' (densely dash-dotted violet) and 'sEddNF' simulations (dash-dotted green). Both 'sEdd' and 'sEddThm' simulations start at 206.4 Myr (colored filled semi-circles). In dashed red is also added the expected evolution of a 10^6 $M_\odot$ BH if it accreted constantly at the Eddington limit. It is clear that super-Eddington accretion, coupled with feedback does not help the BH to grow. We note that without jets (*i.e.* 'sEddThm' run), BHs with super-Eddington accretion are less affected by their feedback and are able to grow above the limit for at least 60 Myr. In fact, the BH reaches a higher mass than the one in 'EddLim' (see Section 3.4.2 for more details).

more spatially concentrated and do not spread out as far as SN bubbles. In the simulations presented here, the jet is always roughly perpendicular to the galactic plane, meaning gas outside of the polar region will not be affected by the AGN over the timescale studied here. Over longer periods of time, the impact of AGN feedback will become more significant, as the AGN jet bubbles will continue to expand. Despite the fact that the jets do not contain a lot of mass, their energy is significant so they keep their regions of impact very hot because of the continuous AGN outflows in the same direction. A complete discussion of the impact of AGN feedback is given in Section 3.4.2.

In conclusion, there is little impact from the super-Eddington AGN feedback on SFR. Narrow AGN outflows cannot counter inflowing gas and most of the effect on SFR is due to SN feedback. The fact that there is no rapid quenching from AGN-driven outflows is also caused by the short timescales studied here, which do not allow us to draw firm conclusions about their long-term impact. Finally, the halo being in isolation, we cannot address the effect of feedback on the circumgalactic medium and its ability to replenish the galaxy gas supply.

Super-Eddington AGN feedback regulates BH growth

In Fig 3.10, we show the mass evolution of the BH for our different accretion regimes. In the run with super-Eddington accretion but no feedback ('sEddNF' - dash-dotted green), as expected, the BH grows rapidly in mass. This BH is able to gain more than 300 times its initial mass within 100 Myr, accumulating more mass than a BH growing constantly at the Eddington limit (dashed red). Due to its very fast growth, not enough mass is available locally to accrete at the (super-Eddington) BHL rate, and the BH is limited to $\dot{M}_{\rm floor}$. The average growth rate of this BH is almost $\sim 5\,{\rm M}_\odot\,{\rm yr}^{-1}$, which corresponds to the Eddington limit of a $10^8\,{\rm M}_\odot$ BH. When feedback from the AGN is included, the growth of the BH is hampered. In both the 'EddLim' (dotted blue) and the fiducial 'sEdd' (solid orange) cases, we find a mass growth below $\dot{M}_{\rm Edd}$. The 'EddLim' BH gains mass almost continuously at the limit, despite AGN feedback, up until ~ 260 Myr when the growth slows down, while in the 'sEdd' simulation the BH self-regulates as soon as the super-Eddington regime is turned on (at $t = 206.4$ Myr shown by the orange filled semi-circle). Overall, the BH grows more quickly in the 'EddLim' setup than in the 'sEdd' simulation, despite the fact that the BH is theoretically allowed to accrete faster in 'sEdd' than in 'EddLim'. The 'sEddThm' simulation is discussed in Section 3.4.2 below.

To better grasp what happens during the accretion phases in the simulations with AGN feedback, we compare in Fig. 3.11 the fraction of time spent by the BHs above a given AGN energy deposition rate $\dot{E}$ for both the 'EddLim' and 'sEdd' setups, using the same color code as in Fig. 3.10. This fraction of time is computed from the time when the BH is injected for the 'EddLim' simulation, or when the super-Eddington regime is turned on in the 'sEdd' and 'sEddThm' simulations, up until the end of the simulations at $t = 282$ Myr. We have added as a red patch the range of AGN feedback power for a BH (with an initial mass of $10^6\,{\rm M}_\odot$) constantly growing at the Eddington limit, *i.e.* with $\dot{E} = \eta_{\rm thm} L_{\rm Edd}$, for ~ 80 Myr. It varies between $10^{43} - 10^{44}\,{\rm erg\,s}^{-1}$ and provides an idea of how often the BH accretes close to the limit.

As can be seen, the AGN luminosity for the 'EddLim' case remains within a narrow band around $10^{43} - 10^{44}\,{\rm erg\,s}^{-1}$, close to the Eddington luminosity of the BH. Very few feedback events occur at luminosities below $10^{43}\,{\rm erg\,s}^{-1}$, with the lowest luminosity at $10^{42}\,{\rm erg\,s}^{-1}$. This means that the AGN feedback events are not strong enough to have a significant impact on the surroundings of the BH, and self-regulation is only reached towards the end of the simulation as shown in Fig. 3.10.

When allowing for super-Eddington feedback ('sEdd'), some strong feedback events occur ($\dot{E} > 10^{44}\,{\rm erg\,s}^{-1}$). These powerful episodes have a wide range of luminosities, varying from 10^{44} to $10^{46}\,{\rm erg\,s}^{-1}$. As a result of these brief super-Eddington phases, the AGN spends a significant fraction of the remaining time in a low luminosity state ($10^{36} < \dot{E}/({\rm erg\,s}^{-1}) < 10^{43}$). A small number of high luminosity events with strong feedback have overall a stronger effect than a high number of intermediate luminosity events with weaker Eddington-limited feedback. This shows that super-Eddington feedback more efficiently self-regulates BH growth than sub-Eddington feedback.

To further investigate this phenomenon, we show in Fig. 3.12 the evolution of the AGN

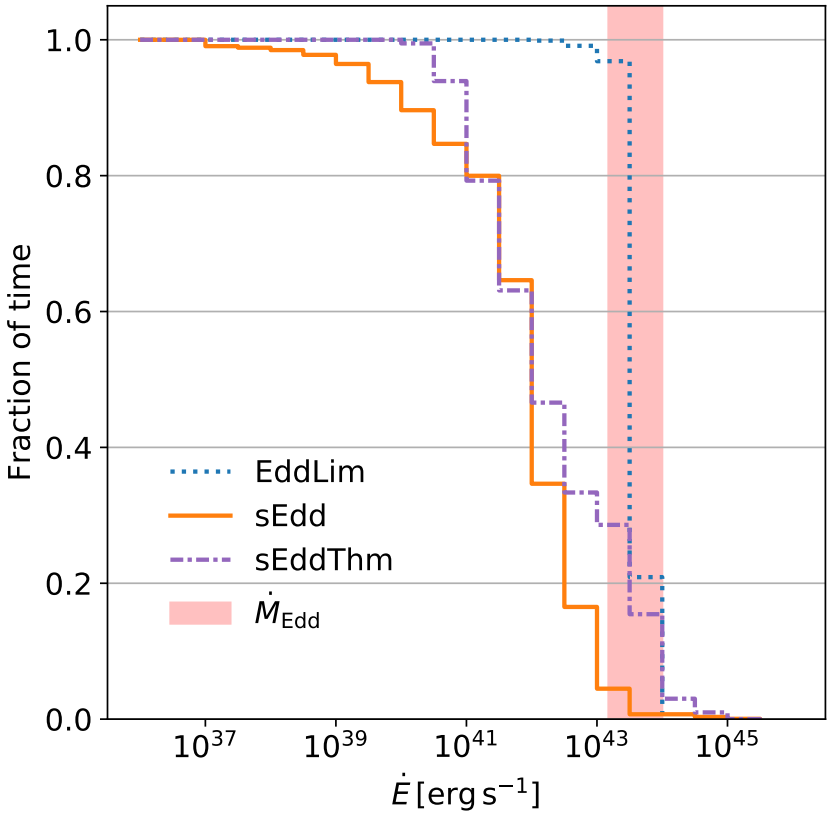

FIGURE 3.11: Fraction of time spent by the BHs above a given AGN energy injection rate $\dot{E}$ for the 'EddLim' (dotted blue), 'sEdd' (solid orange) and 'sEddThm' (densely dash-dotted violet) simulations. A red patch $\dot{M}_{\rm Edd}$ shows the AGN feedback range ($\sim 10^{43} - 10^{44}\,{\rm erg\,s^{-1}}$) of a BH between $M_{\rm BH} = 10^6 - 10^7\,{\rm M_\odot}$ at the Eddington limit. The 'EddLim' simulation has a BH constantly accreting at the limit, thanks to the ineffectiveness of the feedback. The 'sEdd' case has stronger feedback events but this results in many low luminosities feedback episodes. This regime therefore reduces the overall required AGN feedback to self-regulate the BH growth. The 'sEddThm' simulation is discussed in Section 3.4.2.

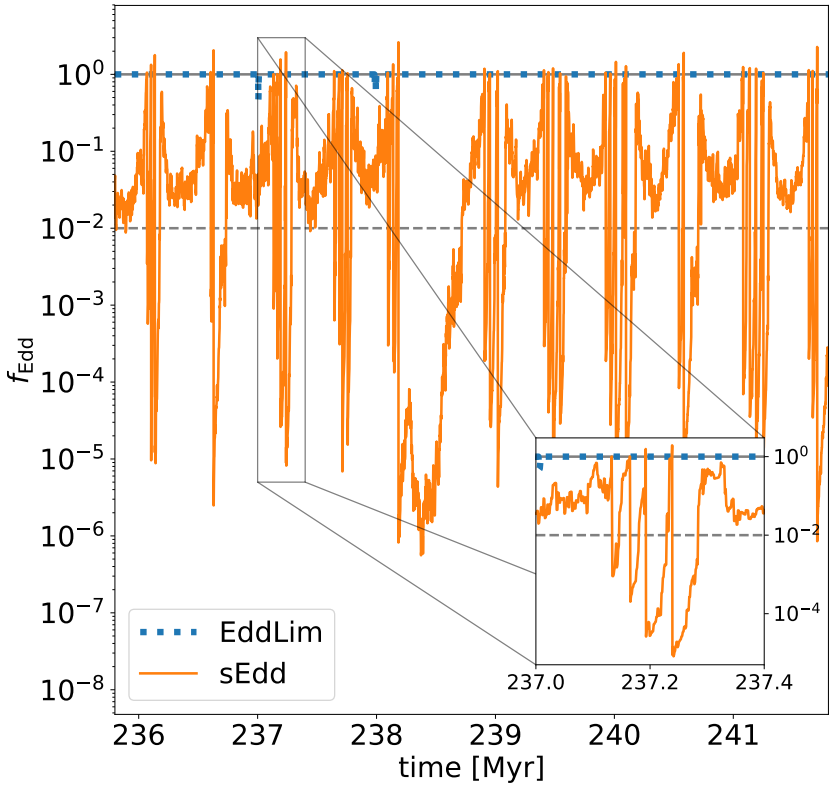

FIGURE 3.12: Evolution of the AGN Eddington fraction $f_{\rm Edd}$ for the 'EddLim' (dotted blue) and the 'sEdd' (solid orange) simulations over 8 Myr. Powerful and instantaneous super-Eddington episodes lead to sharp drops in $f_{\rm Edd}$, reducing the AGN feedback energy injected overall. Solid and dashed horizontal lines indicate $f_{\rm Edd} = 1$ and 0.01 respectively, that mark the separations between the different modes of accretion: super-Eddington, quasar, and radio modes (from high to low rates).

Eddington ratio during a short period of 8 Myr, representing a succession of typical super-Eddington episodes. We also added the 'EddLim' run for comparison. In the Eddington-limited run, although the released power keeps increasing steadily as the BH grows, the BH emits almost constantly at the Eddington luminosity, since feedback does not produce a strong effect on the BH environment. In the 'sEdd' case the Eddington ratio fluctuates rapidly, by up to five orders of magnitude. Every single super-Eddington event is followed by a sharp and instantaneous drop down to very low luminosities. At our resolution and with our set up, the slow rises and sharp drops visible in the zoomed inset are characteristic of the bursts of super-Eddington activity. Studies in RHD with more idealized set-ups but that resolve $r_{\rm BHL}$ and the associated timescales (*e.g.* Park & Ricotti 2011, Park et al. 2020) instead find sharp rises and slow drops, when the Strömgren radius is resolved. Takeo et al. 2020 find a similar oscillatory behaviour when momentum and radiation are injected in an axisymmetric two-dimensional simulation. In our simulations the unresolved $r_{\rm BHL}$ and sound-crossing time at this scale, as well as the direct deposition of feedback energy lead to our inability to resolve a possible similar oscillatory behaviour. We cannot therefore assess if slow rises and sharp drops in the accretion rate occur also in conditions characterized by a turbulent and non-smooth gas distribution in three dimensions and in the presence of relativistic jets. Nevertheless, this confirms that the balance between the high power in the short-lived super-Eddington episodes and the lower power in the longer-lived sub-Eddington phases is such that globally this type of AGN feedback is more effective at curbing BH accretion even with overall smaller energy injection.

We also notice that the succession of these super-Eddington episodes is short, with the intervals between them varying from 1 Myr down to 20 kyr. The spread in these values reflects in part the complex and multiphase structure of the interstellar medium in the galaxy, and in part the strength of the AGN feedback itself: the more powerful the super-Eddington event, the longer the time before the next super-Eddington episode. Furthermore, during a super-Eddington phase of a few 0.1 Myr (as shown in the inset), there are multiple bursts of super-Eddington accretion interleaved by ~ 10 kyr that are growing in strength until the last super-Eddington event is strong enough to quench accretion for a few 0.1 Myr. The multiple successive bursts occur when feedback is unable to evacuate the accretion region (a sphere of radius of $4\Delta x$ with weight given by Eq. 3.3). In this case the periodicity is shorter than the free-fall time at the level of one resolution element, therefore it is arguably caused by gas mixing within the accretion region. After a powerful episode where the full accretion radius is evacuated, the time to the next super-Eddington episode is of the order of the free-fall time from the edge of the evacuated region, which has an extent of several tens to hundreds of parsecs.

In conclusion, we find that the super-Eddington AGN feedback in this idealised setup does not allow the BH to grow efficiently, because each episode of super-Eddington accretion is followed by a period of very sub-Eddington accretion. This is a consequence not only of the amount of energy injected, but also of the form of injection, as we will demonstrate in Section 3.4.2.

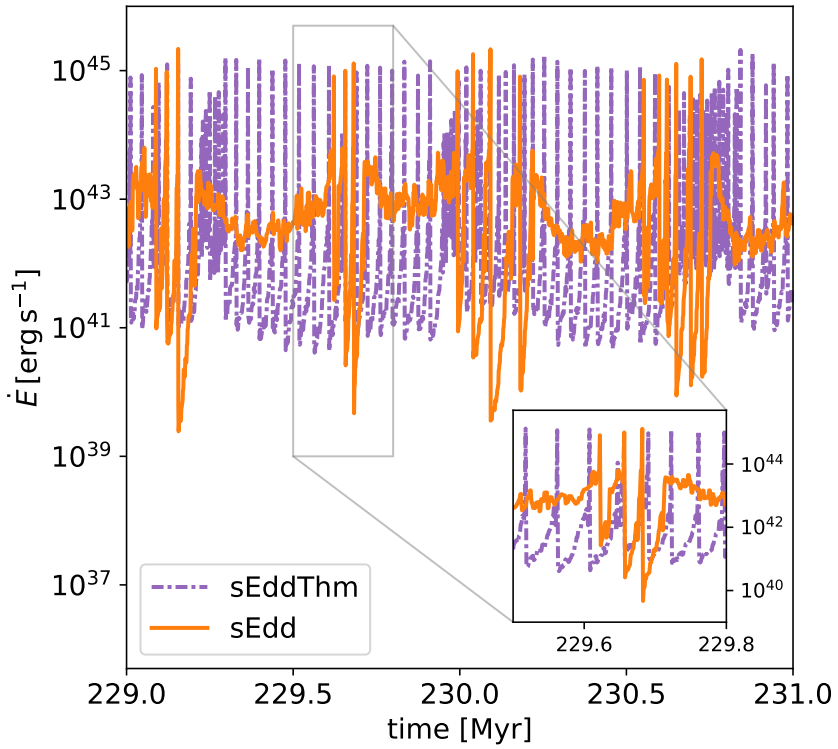

FIGURE 3.13: Comparison between the energy deposition rate $\dot{E}$ from the 'sEdd' (solid orange) and 'sEddThm' (densely dash-dotted violet) simulations, over a succession of typical super-Eddington episodes. The events deposit the same amount of energy, though in different ways, but the 'sEddThm' case seems to be more frequently in a super-Eddington regime. In addition, the drops post super-Eddington events do not fall to luminosities below 10^{40} erg s^{-1}.

3.4.2 Importance of the kinetic AGN feedback in the super-Eddington regime: impact from pc- to kpc-scales

Thermal/Kinetic AGN feedback: impact on the BH growth

Observationally, super-Eddington AGN feedback does not always produce a strong kinetic bipolar radio-like outflow, as for instance shown by the super-Eddington but radio-quiet AGN sample presented in Du et al. (2014). The lack of jet in such objects can be caused by zero or very low spins, or by unfavourable magnetic field configurations (*e.g.* Beckwith et al. 2008, McKinney et al. 2012). To explore how thermal-only super-Eddington feedback impacts BH growth, we analyse the 'sEddThm' run in comparison with our fiducial 'sEdd' run. 'sEdd' in fact has a kinetic feedback approximately 20 times more powerful than the thermal injection of energy because of the different feedback efficiencies (see Section 3.2.2 and Table 3.2).

Starting at the same time for both simulations, the BH producing only thermal feedback ('sEddThm' - densely dash-dotted violet) grows much faster than our fiducial run ('sEdd' - solid orange), as shown in Fig. 3.10. In the 'sEddThm' run, the mass of the BH immediately increases above the Eddington limit and is able to triple its mass from the first super-Eddington phase, since the inflow of cold gas is not counteracted as effectively as in the presence of kinetic feedback. We also find that thanks to this initial super-Eddington

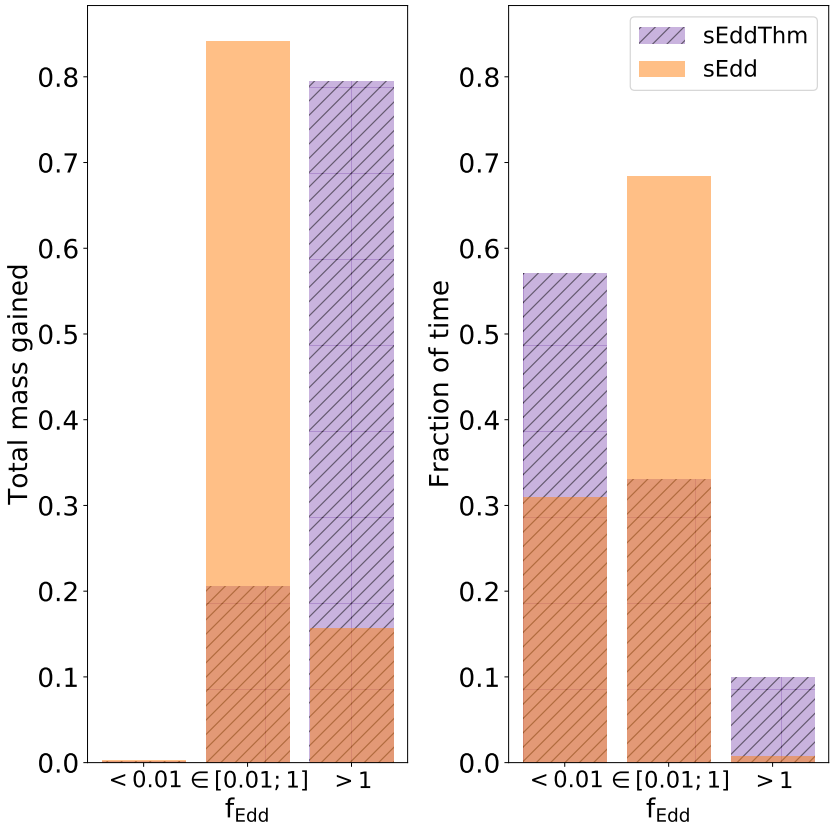

FIGURE 3.14: Fractional values of the total mass gained (left) and fraction of time spent (right) by the BH in the 'sEdd' (filled orange) and 'sEddThm' (hashed violet) runs in $f_{\rm Edd}$ bins, mirroring the three accretion/feedback regimes. Despite not spending much time in the super-Eddington regime, this mode ($f_{\rm Edd} > 1$) still contributes significantly to increasing the mass of the BH, and dominates the mass growth in the 'sEddThm' case.

mass growth, the BH is $\sim$ 15 per cent more massive than the one in the 'EddLim' run after $\sim$ 80 Myr of growth. However, BH mass growth in 'sEddThm' is not able to keep pace with the theoretical growth at the Eddington limit, whose mass gain exceeds that in 'sEddThm' after $\sim$ 60 Myr. The limiting factor that reduces the accretion rate is not the amount of available gas but its temperature.

As discussed in Section 3.4.1, in the 'EddLim' simulation, the BH is for the most part in quasar mode, which also has purely thermal energy injection, and the impact of feedback in 'EddLim' is very limited over long timescales. In 'sEddThm' the impact of feedback is stronger because the injected peak power is greater due to larger reached accretion rates in the super-Eddington regime. The feedback power reaches $\sim 10^{45}\,{\rm erg\,s^{-1}}$ during the super-Eddington phases, as shown in Fig. 3.13, over an order of magnitude above the peak luminosities in 'EddLim' and of the same order of magnitude as 'sEdd'.

There are however noticeable differences between the duty cycles of the 'sEdd' and 'sEddThm' runs, such as in the frequency at which super-Eddington episodes occur. Intervals between two episodes of the 'sEddThm' run average 40 kyr, sometimes with consecutive super-Eddington phases. This is much more frequent than in the fiducial setup, indicating a lower impact of feedback on the environment. Combining these results with Fig. 3.11, we find that the 'sEddThm' AGN feedback appears less destructive than the jetted case. This can

been seen by the fact that the 'sEddThm' simulation shows more instances of high luminosities ($\dot{E} > 10^{44}\,\mathrm{erg\,s^{-1}}$) and a higher minimum luminosity ($\dot{E} = 10^{41}\,\mathrm{erg\,s^{-1}}$). As a result, with only thermal feedback, the AGN is both more likely to be in a super-Eddington state and has a higher luminosity on average, even discounting the super-Eddington events. These events nevertheless, are less effective in impacting their environment compared to the 'sEdd' case. As a result, the BH in the 'sEddThm' run grows more efficiently above the Eddington limit.

To emphasize this change in how many super-Eddington events occur during the simulation, we show in Fig. 3.14 the total mass gained by the BH for the 'sEdd' and 'sEddThm' simulations after the super-Eddington regime is turned on, as well as the fraction of time that the BH spends in each feedback mode (radio, quasar and super-Eddington). We find that in both simulations, the strongly sub-Eddington regime (radio mode) does not contribute significantly to the mass growth of the BH ($\lesssim 0.4$ per cent), despite the BH spending a significant amount of time in this mode, as shown in the right panel.

In the 'sEdd' run, the BH gains more than 80 per cent of its mass when close to the Eddington luminosity (in quasar mode) and spends almost 70 per cent of its time in this regime. Only ~ 15 per cent of the total mass is accreted in episodes above the Eddington limit as the BH spends less than 1 per cent of its time in this regime.

In the 'sEddThm' run, the behaviour is different. The BH accretes much less of its total mass in the quasar mode, as it also spends less time in this regime with a fraction of time spent $\gtrsim 30$ per cent. Most of the mass is gained in the super-Eddington regime, whilst the time that the BH spends in this mode increases by a factor 10 in comparison to the 'sEdd' run: the BH is able to grow above the limit for a long period of time because of the weaker feedback. This factor of 10 comes from the combination of BH spending more time in the super-Eddington regime and breaking the limit more frequently.

In summary, if super-Eddington accretion is not accompanied by powerful jets, then the BH can grow up to significantly higher masses before reaching self-regulation. The BH in run 'sEddThm' is able to reach a higher mass than the one in 'EddLim', but eventually drops below the theoretical curve assuming constant accretion at the Eddington rate. Despite not spending more than 10 per cent of its time above the limit, the BH is able to accrete most of its mass above the Eddington limit. This is because thermal feedback is weaker and cannot push gas efficiently and create outflows like the kinetic feedback does in the 'sEdd' run, which we will discuss further in the following sections.

Impact of the AGN feedback on the BH environs

To understand how the gas behaves around the BH and how it is impacted by the repeated super-Eddington episodes, in this section we investigate the gas properties at tens of pc-scales for both 'sEdd' and 'sEddThm' simulations. The AGN feedback, whether kinetic or thermal, impacts the temperature of the gas surrounding the BH, with higher energy producing higher temperatures. Outflows are also to be expected to affect the gas density, so we show in Fig. 3.15 the evolution of both the gas average density $\bar{\rho}$ and temperature $\bar{T}$ around the BH, in a $4\Delta x_{\mathrm{max}} = 48$ pc radius, between 204 and 212 Myr.

Before $t = 206.4$ Myr (orange/violet filled semi-circles), the BH accretion is Eddington-limited. As discussed in Section 3.4.1, the AGN feedback released in this regime does not impact the gas in the injection region, as the gas there remains very dense (almost

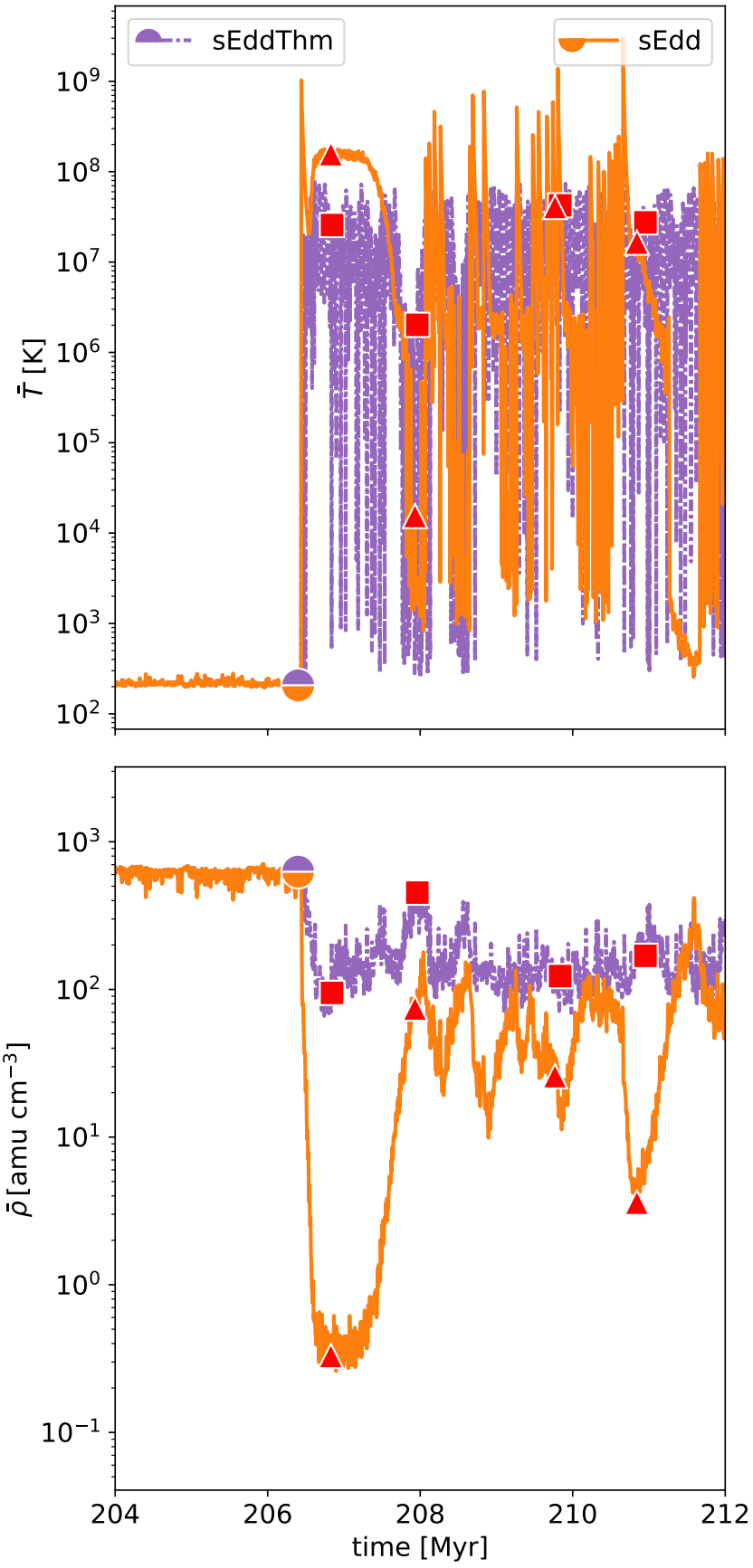

FIGURE 3.15: Evolution of the average temperature (top) and density (bottom) around the BH in the accretion region for the 'sEdd' (solid orange) and 'sEddThm' (densely dash-dotted violet) simulations. The red triangles/squares correspond to the snapshots shown in Fig. 3.16 for the 'sEdd' and 'sEddThm' simulations respectively. As soon as strong super-Eddington events occur, a peak in temperature and a drop in gas density are observed. When kinetic feedback is involved, outflows are created by the momentum carried by the jet. But thanks to the rapid gas infall and refilling of the accretion region, the BH is able to go back in a super-Eddington phase within $\leq$1 Myr.

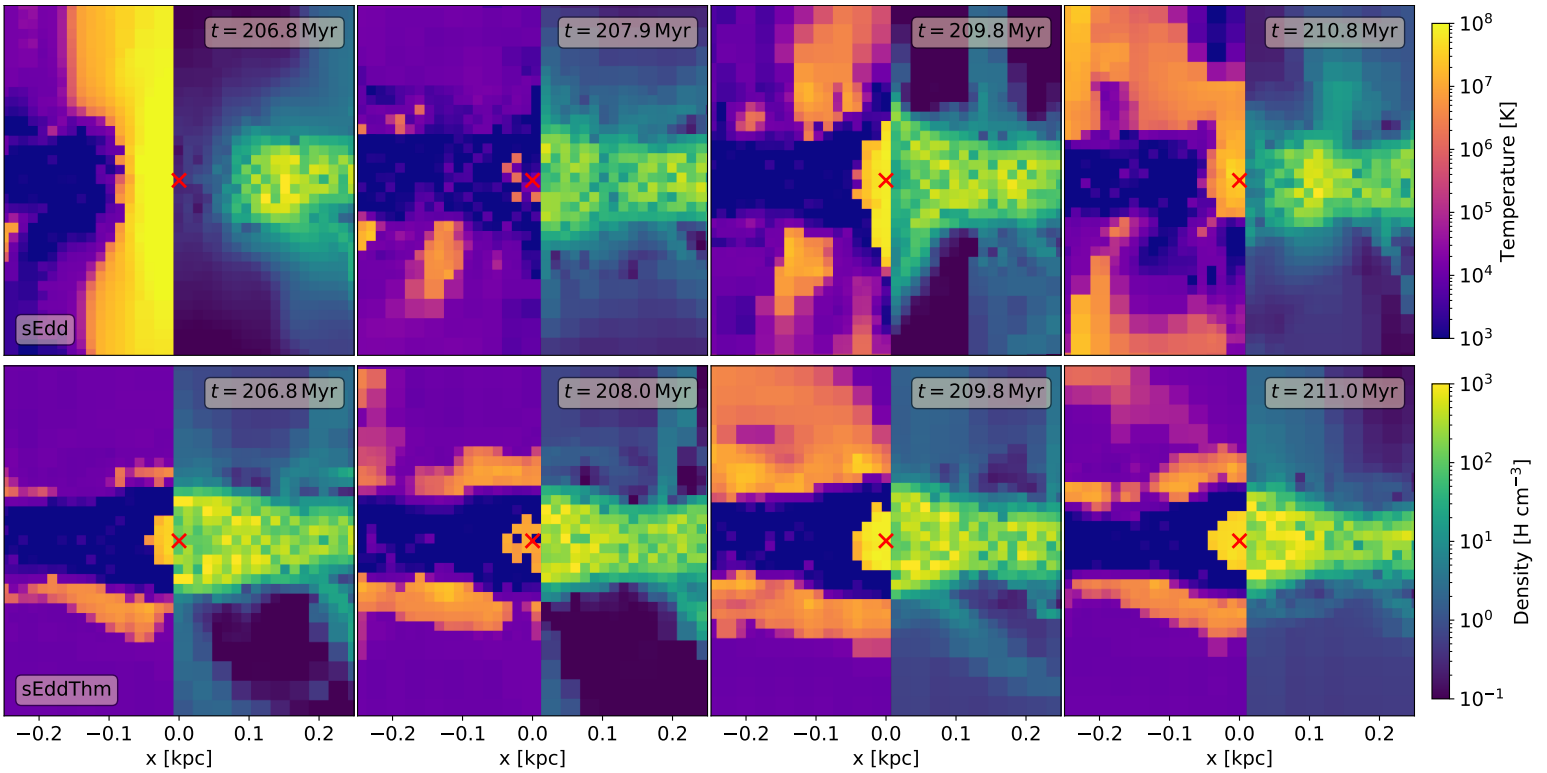

FIGURE 3.16: $0.5 \times 0.5 \times 0.5$ kpc edge-on slice maps centered on the BH (red cross) of the 'sEdd' (top) and 'sEddThm' (bottom) simulations. Each panel is split in half, with gas temperature (left) and density (right). The thermal-only super-Eddington feedback creates a "bubble" unable to push any gas to larger scale, in opposition to the kinetic feedback, strong enough to escape the vicinity of the BH.

$10^3\,\mathrm{H\,cm^{-3}}$) and cold ($\sim 10^2\,\mathrm{K}$). Looking at the temperature evolution, as soon as the BH is allowed to accrete above the Eddington limit, an instantaneous increase of > 6 orders of magnitude in temperature (from $\sim 10^2\,\mathrm{K}$ to $10^8 - 10^9\,\mathrm{K}$) is visible in both simulations. This sudden rise in temperature drastically shrinks r_{BHL} and is the main reason for the sharp drop[4] in accretion rate (see Fig. 3.12), as $\dot{M}_{\mathrm{BHL}} \propto T^{-1.5}$.

The density also varies in both simulations, but in a different way. In the fiducial 'sEdd' run, a decrease of 2 orders of magnitude in density indicates the presence of a strong outflow. The immediate increase in accretion rate suddenly drains the cells near the BH, while shortly thereafter the density drops due to the release of the powerful feedback in the super-Eddington phase. The sudden drop in density caused by this first super-Eddington outflow is clearly visible at $t = 206.8\,\mathrm{Myr}$ the gas density map, shown in Fig. 3.16. The delayed decrease in density in comparison to the sudden change in temperature is caused by the shock propagation, as it takes more time for the outflow to propagate and escape the region.

At $\sim 208\,\mathrm{Myr}$ in the 'sEdd' run, after the initial super-Eddington outflow, the density of the medium rises again to $\sim 10^2\,\mathrm{H\,cm^{-3}}$ and the temperature of the gas slowly decreases. This can indicate very rapid cooling or an inflow of new, colder gas onto the BH, or a combination of both. The dominant factor appears to be inflow of new gas, as to cool down gas at these densities/temperatures would require at least $0.1 - 1\,\mathrm{Myr}$ (assuming the maximum

[4]The erratic changes in temperature are not linked to the weighted kernel used by the accretion routines, as we checked by using a fixed kernel set to $2\Delta x_{\mathrm{max}}$ at all times. The behaviour of this test case was similar.

density of $10^3\,\mathrm{H\,cm^{-3}}$), which is much longer than the timescales over which changes in temperature are seen here. This inflow comes from galactic gas that has not been impacted by feedback from the BH: since the BH spin is fixed along the z-axis, the jet direction does not change and gas in the equatorial direction can reach the galaxy center. The constant inflows therefore provide more material for subsequent super-Eddington episodes, as visible at $t = 209.8$ and $t = 210.8\,\mathrm{Myr}$. Furthermore, as cold and dense gas slowly reaches the BH accretion region, it triggers a succession of super-Eddington episodes (see the inset in Fig. 3.12) with feedback energies unable to eject gas outside of the accretion region. Mixing with infalling gas, the super-Eddington episodes grow in strength and are able to push gas outside of this region in the equatorial direction, up to a distance determined by how powerful the last super-Eddington event is (*e.g.* Costa et al. 2014). The results of this setup are therefore in between those derived by Regan et al. (2019) and Takeo et al. (2020): in these idealized conditions, where the galaxy presents a well-defined disc and the jet is launched perpendicularly to the disc the jet's feedback affects accretion, but inflows from the equatorial plane replenish the gas reservoir.

Looking closely at the 'sEdd' run in Fig. 3.16, we see a positive effect from the super-Eddington AGN feedback on the gas density during the bursts at $t = 206.8$ and $t = 210.8\,\mathrm{Myr}$. Density is significantly larger ($10^2 - 10^3\,\mathrm{cm^{-3}}$) in the ISM at the interface with the AGN outflow, which may induce a short increase in SF (Gaibler et al. 2012, Bieri et al. 2016).

On the other hand, in the 'sEddThm' simulation, despite having a BH able to accrete above the limit which reduces the density around the BH by a factor 3, the produced feedback does not provides enough momentum to the gas to create an outflow fast enough to propagate beyond the vicinity of the BH. The feedback episodes create small local "bubbles" (visible as small pockets of a few tens of pc radius, in each panel of Fig. 3.16 for the 'sEddThm' simulation) of hot gas (which reaches up to $10^8\,\mathrm{K}$), unable to escape the dense medium around it. They quickly vanish, as cold gas swirls in to feed the BH. This situation is a more powerful re-scaled version of the processes discussed for the 'EddLim' case.

Overall, in both simulations, the infall of cold and dense gas is able to quickly replenish the surroundings of the BH, whether gas was pushed outside of the galaxy due to super-Eddington kinetic feedback events, or simply a local small bubble of gas was heated by the thermal feedback. When more low temperature gas is available, the next super-Eddington episode ensues, resulting in a sequence of super-Eddington and highly sub-Eddington events. A parallel can be drawn between the difference in total mass gained (left panel of Fig. 3.14) and the density variations: in the fiducial 'sEdd' run, density drops significantly after each super-Eddington event, because gas is displaced by the outflows driven by injected momentum injected; whereas in the 'sEddThm' simulation, gas does not participate in a large-scale outflow and remains confined in the central region. In this case, the density does not vary as significantly, leading to higher accretion rates and more frequent super-Eddington episodes.

Impact of AGN feedback on galactic scales

Despite the similar injected power, thermal feedback is less effective at disrupting the regions further away from the BH. To explore this, we set up a cylinder of height = 8 kpc and radius = 1 kpc centered on the BH and perpendicular to the galactic plane. Since the visible AGN

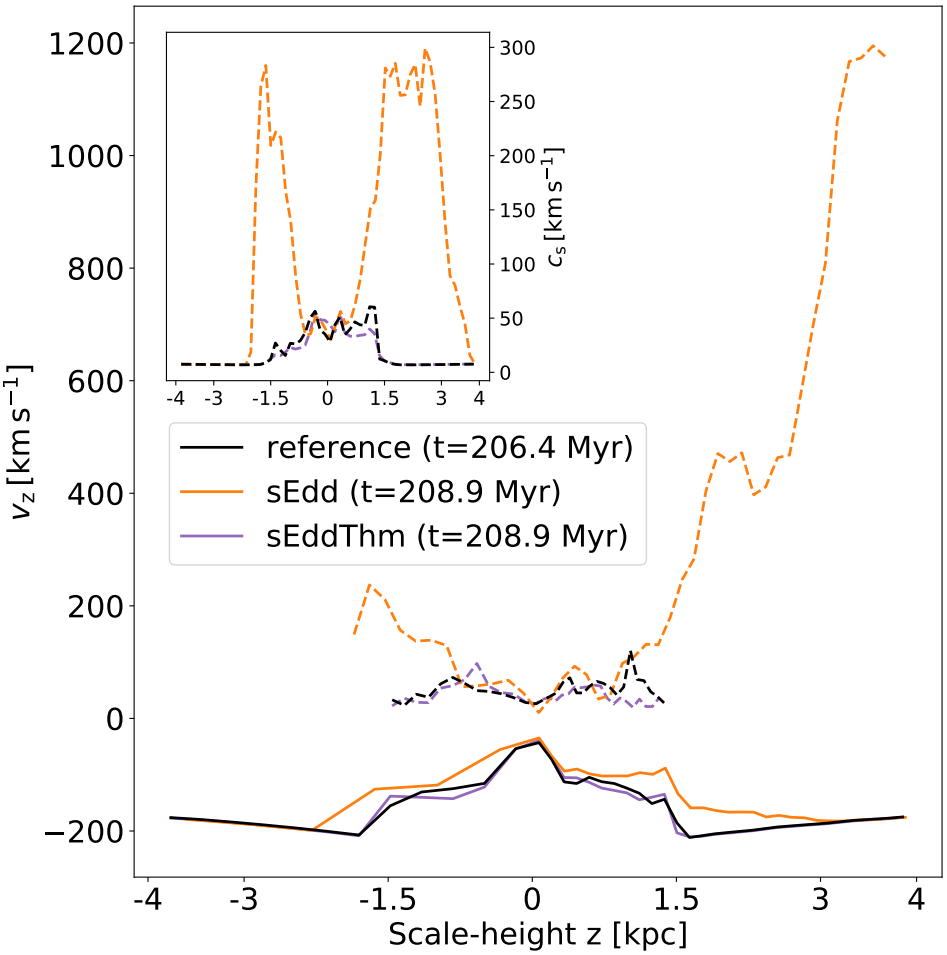

FIGURE 3.17: Evolution of the average z-velocity v_z above and below the galaxy to follow the gas outflows (dashed) and inflows (solid) for both simulations at $t = 208.9$ Myr. A "reference" curve (black) is drawn to represent the state of the gas before the first super-Eddington episode, *i.e.* at $t = 206.4$ Myr. Kinetic jets are clearly visible as they impact gas that is far away from the galactic disc, heating it up on their way out. On the other hand, thermal feedback does not have enough momentum to have said impact.

outflows (Fig 3.9, 'sEdd' run) are aligned with the z-axis of the box, we analysed the mass-weighted velocity in this direction at different heights of the cylinder, both for the inflowing (solid) and outflowing (dashed) gas in Fig. 3.17. The region above/below the galaxy plane is in the positive/negative direction of the z-axis respectively. For each inflow/outflow, we include a "reference" case corresponding to gas before the super-Eddington episodes (measured at $t = 206.4$ Myr). After 2.5 Myr, both simulations have undergone at least one super-Eddington episode, and we show the gas velocity evolution with colored curves.

The diagram can be split into three parts. The central ± 0.1 kpc of the galaxy where the BH lies corresponds to the region where feedback is injected, and has been discussed in Section 3.4.2. The SN feedback is not visible in this region, as the gas is very dense and the explosions are stifled. The gas remains cold, and only super-Eddington AGN feedback events can heat up this small region. The z-velocity of the gas in the accretion region is almost negligible, since the infalling gas coming from both above and below the disc meets in the equatorial plane.

Further away, between ± 1.5 kpc, the gas is mostly impacted by the SN explosions on the

edges of the disc which heat up and disrupt the colder gas surrounding the galaxy. Temperatures are higher than in the central region, as SN feedback propagates more easily in this lower density gas. The outflowing gas z-velocity is on average lower than the inflows as SN feedback meets with colder, infalling halo gas, which slows down the outflow and prompts them to fall back onto the galaxy. In addition, since SNe represent the dominant form of feedback in this region, we do not find significant differences regarding the outflows between the simulations. We also find that the inflowing gas z-velocity tends to increase in all simulations, from ± 0.1 to ± 1.5 kpc. There are less outflows affecting gas further away from the galaxy, and since the halo continues to collapse, the infalling z-velocity increases.

Finally, at scale heights above 1.5 kpc, we have a region where gas collapses from the halo. The inflowing gas is mostly unperturbed by feedback events, as this region has no star formation, and no SN feedback is able to reach such distances. The 'sEddThm' run shows no traces of outflows at $>$ kpc-scales (see also Fig. 3.9, 'sEddThm' run), despite having many more super-Eddington accretion episodes, as discussed in Section 3.4.2. The only feedback events that are able to propagate this far in such a short period of time (2.5 Myr), are the super-Eddington driven bipolar kinetic outflows from the 'sEdd' simulation.

The initial 'sEdd' super-Eddington episode produces an outflow powerful enough to entrain dense gas from the galaxy. It has an initial velocity close to 0.1 c but encounters dense gas when it pierces through the galaxy. This creates shocks and slows the jet down considerably, to a few $10^2 - 10^3$ km s^{-1}. Because of the different gas structures encountered on the way, the AGN outflow above and below the galaxy is not symmetric. The jet below the galaxy (negative scale heights) struggles to find its way through the dense gas. After 2.5 Myr, it reaches $\sim$ 1.5 kpc and almost stops, with $v_z \simeq 200$ km s^{-1}. It spreads out radially and mixes with the SN explosions. On the other hand, if a jet can push through this dense layer, it carves out a low-density region and creates a path for future outflows, which is what the initial outflow ejected above the galaxy does. It travels up to 4 kpc within 2.5 Myr, while keeping a steady velocity close to 10^3 km s^{-1} as it stays collimated.

In the inset, where the sound speed c_s is plotted, we find that the kinetic outflow is able to heat up the region through which it passes. In comparison to the "reference", pre-super-Eddington, and 'sEddThm' curves, which are very similar and have $c_s \leq 50$ km s^{-1} everywhere, the regions in 'sEdd' which were in contact with the jet have all heated up to high temperatures. Because of long cooling times, the gas in these regions does not have the chance to cool down, and subsequent super-Eddington outflows will prevent any long-term cooling. We also find that despite slowing down and spreading out, the kinetic outflow below the galaxy still efficiently heated up its surroundings to much higher temperatures than SN feedback alone.

Finally, we compare the galactic scale inflows for both simulations and find that they are not greatly affected by the super-Eddington kinetic feedback. More specifically, the timescales shown here are too short to see this effect. However, as time goes on, the jets start expanding outwards, and shutting down the gas inflows from the collapse. This happens, for the 'sEdd' simulation, $\sim$ 15 Myr after the first super-Eddington jet. We do not see any impact on inflows throughout the entirety of the 'sEddThm' simulation.

In summary, galactic scales outflows are only visible if there are super-Eddington jets that are able to punch through the galactic disc. The momentum given by the super-Eddington

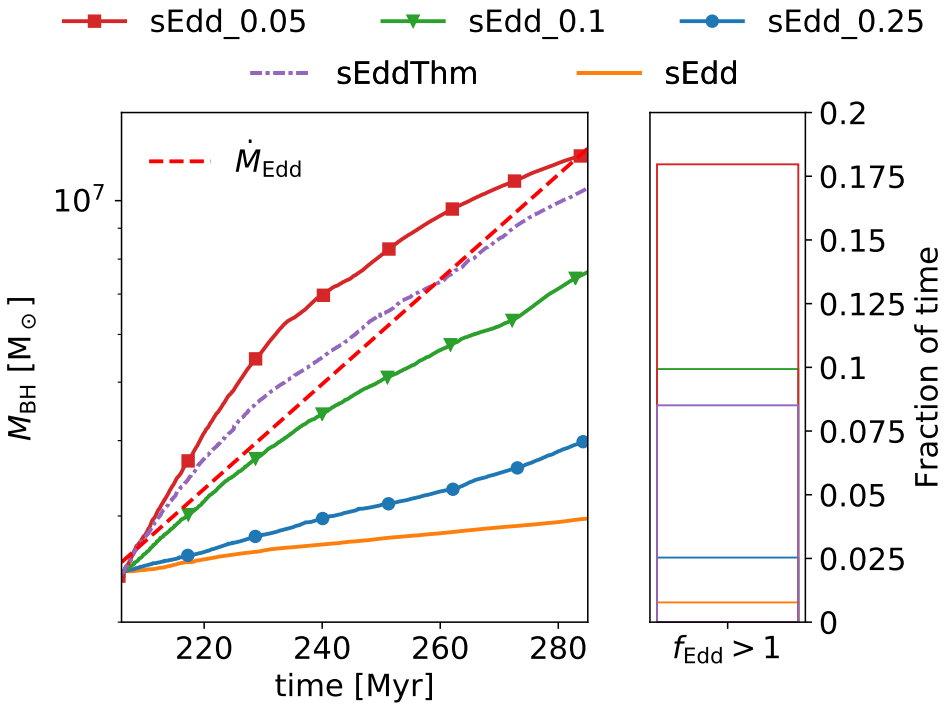

FIGURE 3.18: *Left:* Evolution of the BH mass for the 'sEdd_0.05' (red square), 'sEdd_0.1' (green triangles) and 'sEdd_0.25' (blue circle) from the moment super-Eddington was allowed ($t = 206.4$ Myr). For comparison are added 'sEdd' (solid orange) and 'sEddThm' (densely dash-dotted violet) as well as the Eddington limit $\dot{M}_{\rm Edd}$ (dashed red). *Right:* Fraction of time spent in the super-Eddington regime for the same simulations (same colors). Weaker super-Eddington kinetic feedback affects positively the BH growth and increases the fraction of time spent in the super-Eddington regime.

kinetic feedback is enough to push gas to kpc-scales within short periods of time, whilst staying fast ($\sim 10^3$ km s^{-1}) and collimated, as long as the gas met on the way is not too dense. AGN outflows heat up the gas to very high temperatures, but because of the collimated nature of the jets, it has little impact on the gas inflows.

3.4.3 Varying the AGN feedback efficiency

Our simulations showed that super-Eddington jets are very destructive, and efficiently prevent BH growth, but that the BH is able to grow above the Eddington limit, for a long periods of time, when emitting only thermal feedback. Recently, Yao et al. (2021) detected a pc-scale jet from a super-Eddington source, hinting at the fact that super-Eddington jets are not always powerful. We explore this by changing the MADness factor $f_{\rm MAD}$ for the jet efficiency $\eta_{\rm jet}$. We run three other simulations, namely 'sEdd_0.25', 'sEdd_0.1' and 'sEdd_0.05' with $f_{\rm MAD} = 0.25, 0.1$ and 0.05 respectively (with corresponding jet efficiencies $\eta_{\rm jet}$ of 0.04, 0.006, and 0.0016). The efficiency of the thermal feedback is not changed. As shown in Table 3.2, with these choices of $f_{\rm MAD}$, we are able to investigate a range of jet properties, from weak to strong ones. For this study we compare these simulations to 'sEdd' and 'sEddThm', which are the extremes (very strong and non-existent jet respectively) of the other three cases presented here. We recall here that our fiducial run 'sEdd' has $\eta_{\rm jet} = 0.16$.

The BH mass evolution is shown in the left panel of Fig. 3.18. We find that generally with

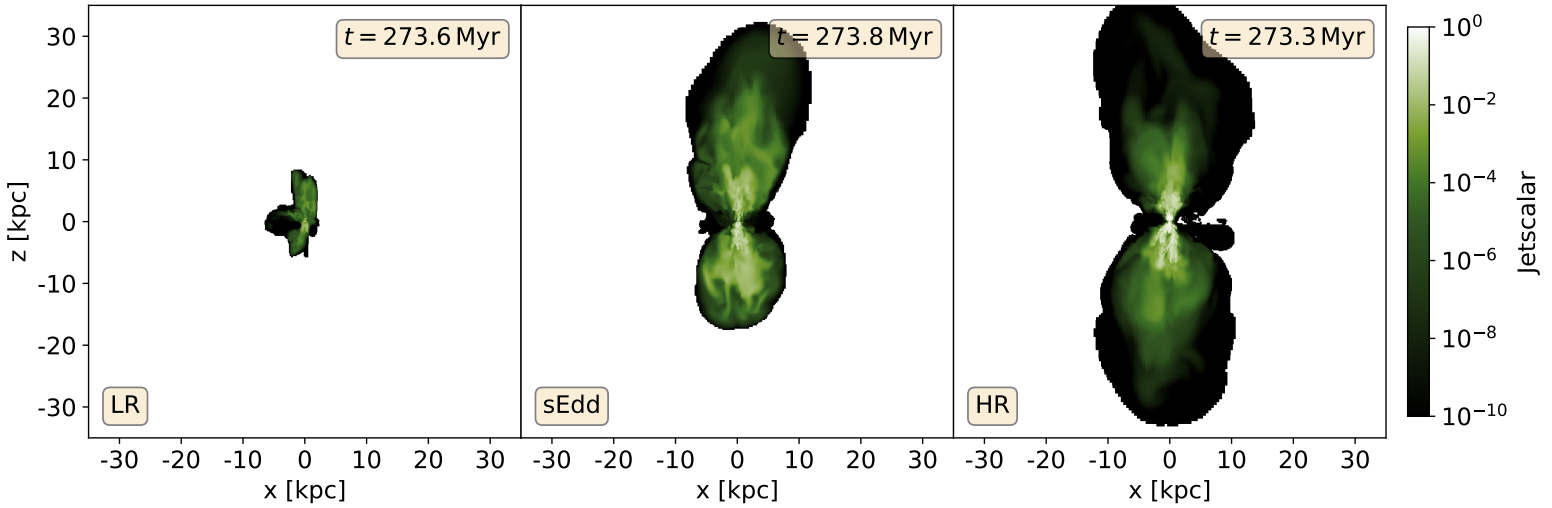

FIGURE 3.19: *Left to right:* Edge-on view at 274 Myr of the jet passive scalar for the 'LR', 'sEdd' and 'HR' runs. The jets extent tends to increase with resolution and has reached numerical convergence for spatial resolutions of order $\Delta x_{\max}$ =12 pc (*i.e.* 'sEdd').

weaker super-Eddington jets, the BH grows more efficiently. However, long-term super-Eddington mass growth is not supported even with weak jets. 'sEdd_0.25' (blue circles) and 'sEdd_0.1' (green triangles) both have BHs growing below the Eddington limit (red dashed), with their jets powerful enough to regulate their growth (Regan et al. 2019). On the other hand, 'sEdd_0.05' (red squares) has a BH growing above the limit for a long period of time, due to the much weaker jets produced. This growth is a consequence of the gas in the accretion region which is not depleted by the outflows as effectively when little momentum is injected by the kinetic feedback. The 'sEdd_0.05' BH grows somewhat more than the BH in the 'sEddThm' simulation because of slightly denser gas in the equatorial direction and less dense gas in the polar one, likely caused by the anisotropic jets. The super-Eddington episodes still create strong changes in the gas temperature, but the effect is lessened when the jet efficiency $\eta_{\rm jet}$ (or the MADness $f_{\rm MAD}$ of the disc) is lower. For instance, 'sEdd' has temperature peaks at 3×10^9 K whilst the jets in 'sEdd_0.05' only increase the temperature up to 10^8 K. This allows for more gas to be accreted and positively impacts BH growth.

In addition to the growth, we find that the fraction of time spent in the super-Eddington regime increases with decreasing disc MADness. As seen in the right panel of Fig. 3.18, the BH can spend up to 18 per cent of its time in the super-Eddington regime for the 'sEdd_0.05' run, and converges down to a few per cent with the 'sEdd_0.25' simulation. This further confirms that stronger jets decrease the frequency of super-Eddington episodes.

Galactic scale outflows are only found for 'sEdd_0.25', 'sEdd_0.1' and 'sEdd', which all have BHs growing on average below the Eddington limit. These large scale outflows are less frequent with the weaker jet feedback, as jets for lower MADness are lighter (in our algorithm) and therefore less able to punch through the dense galactic gas. We also find that weaker jets do not eject gas as far away as the more powerful ones, and tend not to stay collimated for long periods of time.

In conclusion, we show that the super-Eddington kinetic feedback, if weak, can allow for BHs to grow at a rate close to or slightly above the Eddington limit over long periods of time. Weak super-Eddington jets can be achieved by a combination of low spin a and low

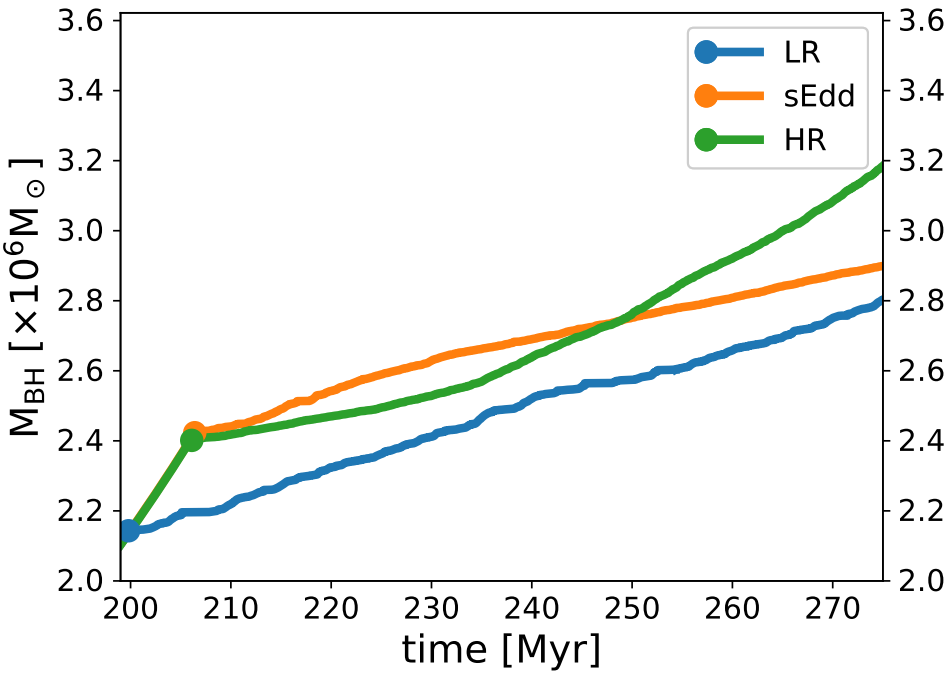

FIGURE 3.20: Evolution of the BH mass for the 'LR' (solid blue), 'sEdd' (solid orange) and 'HR' (solid green) simulations. Self-regulation is reached in the three cases in very similar fashion.

MADness factor $f_{\rm MAD}$, and in this study we focus on changing the disc MADness only. We do not see any evidence for strongly super-Eddington accretion, only mildly super-Eddington mass evolution for very low $f_{\rm MAD}$. Finally, weaker jets produce less frequently galactic scale outflows. They often mix with their surroundings and do not stay collimated for very long.

3.4.4 Effect of the resolution

In addition to the previous analysis, we perform a series of resolution studies on the same halo, with high ('HR') and low ('LR') resolutions, respectively $\Delta x_{\rm max} = 6$ & 25 pc (see Table 3.2 for more details). To make sure that the study is solely focused on resolution, we use the initial conditions detailed in Table 3.1, at 140 Myr. We then switch the resolution, either increasing or decreasing it by a refinement level, let the galaxy reach an equilibrium state for $\sim$ 20 Myr and then add a BH of 10^6 $M_\odot$. This change can be visually seen in Fig. 3.9, with the galactic disc being thinner the higher the resolution, as well as SN-driven winds expanding farther out. After an Eddington-limited growth, we allow for super-Eddington accretion at around 200 Myr. For the 'LR' run, super-Eddington is allowed at $t = 199.8$ Myr, a few Myr earlier than the 'HR' ($t = 206.1$ Myr) and the 'sEdd' ($t = 206.4$ Myr) simulations. Those different starting times of the super-Eddington regime are chosen so that the accretion rates around the BH are similar (between $20 - 50 \dot{M}_{\rm Edd}$), making the comparison possible.

We follow an analysis similar to Sections 3.4.1 and 3.4.2 and find very little differences between the three simulations. When increasing the resolution, we find that super-Eddington jets extended further and stay collimated for a longer period of time. Within $\sim$ 280 Myr, the jets reached 8 kpc in the 'LR' simulation, while converging to $\sim$ 30 kpc for the 'sEdd' and 'HR', as shown in Fig. 3.19. In fact, the smaller the area A of the jet at injection, the larger the final extent of the jet, as its velocity $v_{\rm jet} \propto A^{-1}$. Within the studied timeframe, the BH is

self-regulated due to the super-Eddington kinetic outflows. As can be seen in Fig. 3.20, the three BHs reach a similar mass, $\sim 3 \times 10^6\,\mathrm{M}_\odot$. We note that after 230 Myr, the 'HR' BH sees a sharper mass increase than the other two BHs. This is caused by the central region of the galaxy, which is denser ($\bar{\rho} \simeq 10^3\,\mathrm{cm}^{-3}$) by 1 dex than the other runs, and allows for larger mass growth. Increasing the resolution favors the creation of dense clumps inside the galaxy, which swirl in towards the BH and drive faster mass growth. However, they are insufficient to sustain average mass growth even close to the Eddington limit, as the BH reaches a mass of $3.2 \times 10^6\,\mathrm{M}_\odot$ in 70 Myr, only 10 per cent more massive than the fiducial 'sEdd' BH.

Besides these small differences, the BH produces feedback of similar luminosity and the fraction of time spent in the super-Eddington regime is less than 1 per cent in all three runs. We conclude that the behavior the BH growth with respect to the super-Eddington regime is robust against a change of resolution within the range of scales tested here, of the order of those reached in the latest high resolution cosmological simulations (*e.g.* Dubois et al. 2021). Since this isolated setup is not conducive to study spatial resolutions 0.1-1 kpc, we cannot assess whether the effect of super-Eddington AGN feedback is correctly captured at low resolution or, *e.g.*, a boost factor would be needed (Booth & Schaye 2009, DeGraf et al. 2017, Chabanier et al. 2020). We postpone such investigation to future work using cosmological simulations.

3.5 Conclusions

In this Chapter, we examine the impact of including the super-Eddington regime on BH growth and on the gas properties from 10 pc to several kpc-scales, in an isolated galaxy at $z = 4$. A BH with initial mass $M_{\mathrm{BH}} = 10^6\,\mathrm{M}_\odot$ is placed in the center of a $M_* \simeq 10^9\,\mathrm{M}_\odot$ galaxy where cold and dense gas can trigger super-Eddington episodes. To study this regime, a modification of the `Ramses` algorithm was made, to remove the cap at the Eddington limit and implement both types of feedback (kinetic and thermal) that are believed to characterise super-Eddington sources (Section 3.2). Our main findings are as follows.

- The impact of super-Eddington AGN feedback on SF is minimal due to the narrow outflows launched by the BH. (Section 3.4.1)
- With super-Eddington AGN feedback the BH reaches self-regulation within a few Myr (depending on the type of AGN feedback), even in an environment favorable for super-Eddington accretion. Sharp and instantaneous drops down to sub-Eddington regimes occur after each super-Eddington event that peak at around 2-3 times the Eddington limit. (Section 3.4.1)
- The formation of super-Eddington jets reduces the amount of time spent in the super-Eddington regime (< 1 per cent in 'sEdd', compared to $\sim$ 10 per cent in 'sEddThm' without jets) and shortens the time before self-regulation is reached. The more often a BH is in the super-Eddington regime, the more mass is accumulated in this regime (up to $\sim$ 70 per cent without jets in 'sEddThm'). Including jets in the super-Eddington regime is therefore necessary to capture its properties and effects. (Section 3.4.2)

- On small scales ($10 - 100\,\mathrm{pc}$), super-Eddington AGN feedback heats up the gas to $10^{8-9}\,\mathrm{K}$ instantaneously. The powerful jets eject most of the gas outside of the galaxy, reducing the gas density around the BH significantly; whilst the weak thermal feedback creates a hot "bubble" without sufficient momentum to launch gas further than the BH accretion region. Gas gets replenished by infalls within a few kyr, allowing for another super-Eddington episode to be triggered. (Section 3.4.2)

- On larger scales ($\sim$ kpc), super-Eddington jets do not significantly impact gas inflows. As long as the interstellar medium is not too dense, if the galaxy disc and the jets are orthogonal, the outflows escape the galaxy with a steady $\sim 10^3\,\mathrm{km\,s^{-1}}$, stay collimated and create a path for subsequent super-Eddington jets. (Section 3.4.2)

- Lower super-Eddington jet efficiencies, occurring if the BH spin is low or if the MADness state (magnetic saturation) of the accretion disc is weak, allow for more frequent super-Eddington events and for more significant BH growth, since accretion is not suppressed as often or as strongly as for powerful jets. (Section 3.4.3)

- Even with the lowest jet feedback efficiencies, there is no evidence of strong super-Eddington growth: BHs can only grow slightly above a BH that would continuously accrete at Eddington (~ 15 per cent more in BH mass). (Sections 3.4.2 and 3.4.3)

This Chapter is a first step at studying the impact on BH growth by the super-Eddington regime of AGN feedback, within a realistic galaxy environment. Our findings suggest that the right combination of BH spin and super-Eddington AGN feedback strength may lead to a window of opportunity for mildly super-Eddington mass evolution. The BH spin evolution is therefore the natural follow-up to these findings, as is developed in Chapter 4.

Chapter 4

How the super-Eddington regime affects black hole spin evolution in high-redshift galaxies

With the findings from Chapter 3, we explore one of the parameters that was set to a fixed value in all simulations explored so far: the BH spin. We use the same suite of initial conditions as described in Chapter 3, however we extend the BH spin model from Dubois et al. 2021 in `Ramses` to the super-Eddington regime. In order to follow the evolution of the spin parameter a of a BH undergoing super-Eddington phases throughout its growth, we combine super-Eddington accretion with sub-Eddington phases (quasar and radio modes). We explore the different phases of spin evolution when super-Eddington accretion is involved, as well as its impact on BH growth. We finally attempt to describe analytically the evolution in order to calculate the final value of a after a given mass is accreted. This Chapter corresponds to the submitted paper Massonneau et al. (2022a).

4.1 Introduction

Quasars are believed to be powered by SMBHs lying in the centers of galaxies, accreting gas and releasing their feedback in the form of powerful outflows. Astrophysical BHs are entirely characterised by two properties, their mass and angular momentum, as they are thought to have zero charge (Blandford & Znajek 1977). A spinning BH of mass $M_{\rm BH}$ has an angular momentum $J_{\rm BH}$ which is usually defined by its dimensionless spin parameter $a = J_{\rm BH}c/(GM_{\rm BH})$ with c the speed of light and G the gravitational constant, and is described by the Kerr metric (Kerr 1963). BH spins evolve due to gas accretion or coalescence by BHs, which relative importance vary with mass scale (Volonteri et al. 2005, Volonteri et al. 2013, Berti & Volonteri 2008, Fanidakis et al. 2011, Barausse 2012, Dubois et al. 2014b, Sesana et al. 2014, Bustamante & Springel 2019) The spin of BHs change how the feedback from the AGN proceeds and, hence, its impact on galaxy properties, as it controls the efficiency of AGN feedback, and the direction of jets in AGN (Dubois et al. 2014a, Beckmann et al. 2019, Beckmann et al. 2022a, Cenci et al. 2021, Sala et al. 2021, Talbot et al. 2021, 2022, Huško et al. 2022, Massonneau et al. 2022b).

Initial studies related to spin evolution commenced with accretion from cold discs, examining the consequences of the Kerr metric. Bardeen (1970) assumed that the angular momentum of the gas and the BH spin were always aligned, causing $a \to 1$ after a moderate

amount of mass is accreted by the compact object. In such a cold disc scenario, because of the radiation emitted from the disc at high spins, Thorne (1974) discovered that the maximum spin a BH could reach is $a \simeq 0.998$. However, not all black holes are thought to have a cold gas disc at all times, and depending on the state of the accretion disc, and associated feedback modes, the spin can evolve very differently.

How efficiently a BH accretes can be parameterised relative to the Eddington limit ($L_{\rm Edd} \equiv 4\pi G M_{\rm BH} m_{\rm p} c/\sigma_{\rm T}$, with $m_{\rm p}$ the proton mass and $\sigma_{\rm T}$ the Thomson cross-section). When accretion rates are much smaller than the Eddington limit, the accretion is radiatively inefficient (or advection dominated) and accompanied by relativistic outflows, which may be launched via the Blandford-Znajek mechanism (Blandford & Znajek 1977). The process of powering a jet leads to a loss of angular momentum, meaning that the BH would spin down, i.e. decrease its magnitude $|a|$. Early work from GRMHD simulations (e.g. Gammie et al. 2004, De Villiers et al. 2005, Komissarov et al. 2007, McKinney & Blandford 2009) opened on to many insights regarding the role of magnetic fields in accretion flows, especially related to the extraction of power from spinning BHs. Early studies predicted an equilibrium spin in the range of $a \simeq 0.9 - 0.94$ would be reached. Over the next decade, key developments in accretion theory related to the importance of magnetically-dominated accretion flows were made, which lead to the magnetically arrested disc (MADs) model (Igumenshchev et al. 2003, Narayan et al. 2003). Surrounded by such MAD discs, BHs are able to produce jets whose energy exceeds the rest mass of the accreted gas (Tchekhovskoy et al. 2011). Works such as Tchekhovskoy et al. (2012), McKinney et al. (2012), and Narayan et al. (2022) find that BHs in MAD discs may spin-down more efficiently, with an equilibrium spin $a \simeq 0.03 - 0.08$.

Accretion rates larger than the Eddington limit give a different disc structure than the typical thin disc at $L \sim L_{\rm Edd}$. Different theoretical models have been developed in the past decades (see, e.g., the comprehensive review by Mayer & Bonoli 2019) and one of the most widely adopted to explain this critical state of accretion is the slim disc model (Abramowicz et al. 1988, Sądowski 2009, Abramowicz & Fragile 2013). Gas flowing towards the BH proceeds via an optically and geometrically thick accretion disc, which traps the photons emitted from gas accretion and makes this process radiatively inefficient (e.g. Katz 1977, Begelman 1978, Ohsuga et al. 2005, Madau et al. 2014). Such super-Eddington accretion may be accompanied by powerful jets (Sądowski & Narayan 2015, Narayan et al. 2017), which may have a significant impact on BH growth (Regan et al. 2019, Massonneau et al. 2022b).

In the present study, we investigate for the first time the spin evolution of a BH undergoing both super- and sub-Eddington accretion in idealised hydrodynamical simulations of isolated galaxies, using the same suite of initial conditions as described in Chapter 3. By extending the BH spin model from Dubois et al. 2021 in `Ramses` to the super-Eddington regime, we explore the different phases of spin evolution when super-Eddington accretion is involved, as well as its impact on BH growth. We attempt to describe explicitly the evolution in order to predict the final value of a after a given mass is accreted. The structure of the Chapter is as follows: we describe the BH spin models used for different accretion rates in Section 4.2, the setup of our simulations in Section 4.3, then show and discuss our simulations results in Section 4.4 and 4.5 before presenting our conclusions in Section 4.6.

4.2 Impact of the disc structure on BH spin

Accretion from a gaseous disc orbiting a BH modifies both spin magnitude and direction. Following Shapiro (2005), we define the dimensionless spin-up parameter s,

$$s \equiv \frac{da}{dt}\frac{M_{\rm BH}}{\dot{M}_{\rm acc}} = \frac{da}{d\ln M_{\rm BH}}(1-\epsilon_{\rm r})\,, \tag{4.1}$$

where a is the spin parameter, $M_{\rm BH}$ is the BH mass, $\epsilon_{\rm r}$ is the radiative efficiency and $\dot{M}_{\rm acc}$ corresponds to the accretion rate on the accretion disc and the accretion rate on the BH is $\dot{M}_{\rm BH} = (1-\epsilon_{\rm r})\dot{M}_{\rm acc}$. Here and in the following we will use the terminology that a prograde BH has $a > 0$ and a retrograde one has $a < 0$. Furthermore, if s and a are of the same sign, then the BH spins up, i.e., it increases its magnitude $|a|$, and *vice versa*, if s and a are of the opposite sign, the BH spins down, i.e., it decreases its magnitude.

The spin-up parameter corresponding to the standard thin disc model, which we name $s_{\rm qso}$, is given by

$$s_{\rm qso} = \widetilde{L}_{\rm qso} - 2a\widetilde{E}_{\rm qso}\,, \tag{4.2}$$

where $\widetilde{E}_{\rm qso} \equiv 1-\epsilon_{\rm r}$ and $\widetilde{L}_{\rm qso}$ are respectively the energy and angular momentum of the ISCO, $r_{\rm ISCO}$. Combining and integrating Eq. 4.1 and 4.2, Bardeen (1970) obtained the following evolution law:

$$a_{\rm fin} = \frac{\sqrt{r_{\rm ISCO,ini}}}{3}\frac{M_{\rm BH,ini}}{M_{\rm BH,fin}}\left[4 - \sqrt{3r_{\rm ISCO,ini}\left(\frac{M_{\rm BH,ini}}{M_{\rm BH,fin}}\right)^2 - 2}\right] \text{ for } \frac{M_{\rm BH,fin}}{M_{\rm BH,ini}} < \sqrt{r_{\rm ISCO,ini}}\,, \tag{4.3}$$
$$= 1 \text{ otherwise.}$$

"ini" ("fin") are the initial (final) value of the quantity measured before (after) accretion respectively. This disc model has a positive spin-up parameter for all spin values up to $a = 0.998$ (Thorne 1974), meaning that counter- (co-)rotating accretion discs always spin the BH down (up).

Thick discs, or other disc models such as the advection dominated accretion flow (ADAF, Narayan & Yi 1995, Manmoto et al. 1997, Narayan et al. 1997) or slim discs have a geometry which favors relativistic jet outflows, able to collimate the jet because of the thick geometry of the discs. These jets are powered by energy extracted from the rotation of the BH, via the Blandford-Znajek mechanism, which as a consequence causes the spin magnitude $|a|$ to decrease. Recent GRMHD simulations studying spin evolution in magnetically-arrested discs (MAD, e.g. McKinney et al. 2012, Narayan et al. 2022) have been able to demonstrate this spinning-down effect. These accretion discs accumulate large-scale magnetic flux on the BH, until this flux becomes so strong that it chokes gas infall. The excess magnetic field leaves and pushes parts of the disc away: the accretion flow enters a MAD state. Although the spin-up rates provided by McKinney et al. 2012 and Narayan et al. 2022 are for the sub-Eddington regime for thick discs, since the geometry of the discs are similar, and in absence of any spin-up rate prescription in the literature for the super-Eddington regime, we assume the same spin-up rates during the super-Eddington regime. The spin-up parameter that we have adopted, which we name $s_{\rm MAD,MK12}$, is taken from McKinney et al. (2012) and can be

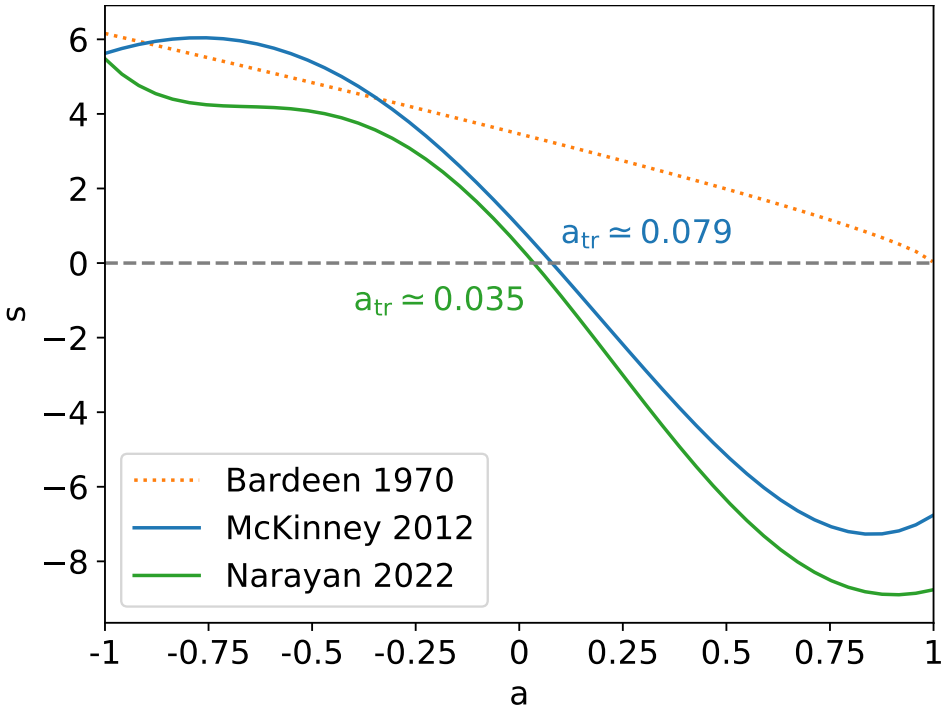

FIGURE 4.1: Spin-up parameters s for different disc models (thin disc in dotted orange, MAD in solid lines) as a function of the BH spin parameter a. Similarly to the thin disc, a MAD counter-rotating ($a < 0$) disc causes the BH to spin-down. Co-rotating ($a > 0$) thin discs will spin the BH up, unlike the MAD ones (due to loss of angular momentum to the jets). A special MAD case for very low spins ($0 \leq a < a_{\rm tr}$) shows a weak spin-up, but is less than the spin-up from thin discs.

fitted with the following fourth-order polynomial (Dubois et al. 2021):

$$s_{\rm MAD,MK12} = 0.97 - 12.00a - 4.04a^2 + 5.81a^3 + 2.50a^4\,, \tag{4.4}$$

and, for comparison, the spin-up parameter from Narayan et al. (2022) fitted with a fifth-order polynomial is:

$$s_{\rm MAD,N22} = 0.45 - 12.53a - 7.8a^2 + 9.44a^3 + 5.71a^4 - 4.03a^5\,. \tag{4.5}$$

We show in Fig. 4.1 the spin-up parameter s for the standard thin disc and the ones found for MAD, as a function of a. In both McKinney et al. (2012) and Narayan et al. (2022), the authors find that non-spinning BH ($a = 0$) experiences a mild spin-up ($s > 0$). The weak spin-up is a result of the inflowing gas having non-zero angular momentum, which spins the BH up. Therefore, for certain spins $a \in [0, a_{\rm tr}]$ with $a_{\rm tr}$ the transition from $s_{\rm MAD} > 0$ to $s_{\rm MAD} < 0$, these models predict a BH spinning up as a consequence of weak loss of angular momentum from jets, in comparison to gas accretion. Studies related to the spin-up parameter for super-Eddington discs have not yet been explored. This regime is associated with radiatively inefficient accretion, due to the photon trapping effect, meaning $\epsilon_{\rm r} \ll 1$ for higher accretion rates. Therefore, in this work, we assume that for the super-Eddington regime, Eq. 4.1 can be approximated by

$$s_{\rm sEdd} \simeq \frac{da}{d\ln M_{\rm BH}}\,. \tag{4.6}$$

4.3 Simulation setup

This Chapter presents a set of hydrodynamical simulations of an isolated galaxy in its host dark matter halo at $z = 4$, produced using the adaptive mesh refinement code `Ramses`. The addition of the accretion and feedback phases in the super-Eddington regime to `Ramses` are described in Chapter 2, however we briefly recall here their implementation, along with the spin evolution in `Ramses`. We also recall the galaxy formation and BH seeding processes to achieve super-Eddington accretion rates, however the reader may find a complete description in Chapter 3.

4.3.1 Technical details in `Ramses`

BHs in `Ramses` are represented by a 'sink' particle that can transfer mass, momentum and energy from and to the gas. In our simulations, they are manually placed with a given initial mass, velocity and spin, at a certain point in time. The mass of these BHs grows at a rate $\dot{M}_{\rm BH} = (1-\epsilon_{\rm r})\dot{M}_{\rm BHL}$ with $\dot{M}_{\rm BHL}$ the BHL accretion rate (Hoyle & Lyttleton 1939, Bondi 1952):

$$\dot{M}_{\rm BHL} = \frac{4\pi G^2 M_{\rm BH}^2 \bar{\rho}}{(\bar{c}_{\rm s}^2 + \bar{v}_{\rm rel}^2)^{3/2}}, \tag{4.7}$$

where the averaged density $\bar{\rho}$, sound speed $\bar{c}_{\rm s}$ and relative velocity between the BH and the gas $\bar{v}_{\rm rel}$ are computed within $4\Delta x$ of the BH, using mass weighting and a kernel weighting as specified in Chapter 3. The accretion rate is not capped at the Eddington limit (unless otherwise stated), only by the total mass contained in the kernel divided by the timestep. We note that there is always enough mass available for BH accretion and feedback processes, with mass conservation enforced at all times.

BH accretion is parameterised using the Eddington limit $L_{\rm Edd}$. For very low accretion rates, when $f_{\rm Edd} \equiv L/L_{\rm Edd} \leq 0.01$, accretion is radiatively inefficient and accompanied by relativistic outflows. The BH enters a so-called "radio" mode and the energy injected as kinetic energy follows Sądowski et al. (2016) giving a total jet feedback of

$$\dot{E}_{\rm jet} = \eta_{\rm jet}\dot{M}_{\rm BH}c^2, \tag{4.8}$$

where $\eta_{\rm jet} = 1.3a^2 f_{\rm MAD}^2$ is the efficiency factor of the kinetic feedback for a magnetically arrested disc (MAD) taken from Tchekhovskoy (2015), and $0 \leq f_{\rm MAD} \leq 1$ is the fraction of MAD strength (magnetic field saturation).

On the other hand, for higher but sub-Eddington accretion rates ($0.01 < f_{\rm Edd} \leq 1$), the AGN is in the "quasar" mode, corresponding to feedback coming from winds and radiation. In this regime, thermal energy is released and the total feedback deposited is

$$\dot{E}_{\rm thm} = \eta_{\rm thm}\dot{M}_{\rm BH}c^2, \tag{4.9}$$

with $\eta_{\rm thm}$ is the spin dependant thermal wind efficiency of the disc.

With our current understanding of the super-Eddington regime ($f_{\rm Edd} > 1$), super-Eddington AGN feedback includes both kinetic and radiative/thermal components. The super-Eddington implementation injects both thermal and kinetic energy simultaneously, with the total AGN

feedback in this regime based on Sądowski et al. (2016)

$$\dot{E}_{\rm sEdd} = (\eta_{\rm jet} + 0.5\eta_{\rm thm})\dot{M}_{\rm BH}c^2. \tag{4.10}$$

Dubois et al. (2021) implemented routines to follow on-the-fly the evolution of the spin parameter a. In addition to spin evolution below the Eddington limit, we now use the spin-up parameter $s_{\rm sEdd} = s_{\rm MAD,MK12}$ (Eq. 4.4) for computing the BH spin at super-critical accretion rates, since relativistic jets may be present in the super-Eddington regime.

In most general cases, misalignment between the accretion disc and the BH spin occurs. Due to the Lense-Thirring effect, it generates a torque which makes the disc precess around the axis of the BH spin. This creates a warped disc, with a certain radius which marks the transition between the equatorial inner disc aligned with the BH spin and the misaligned outer disc. Lense-Thirring precession results in the BH and disc angular momentum being aligned or anti-aligned with the total angular momentum of the BH+disc system. King et al. (2005) find a criterion for the anti-alignment of the BH with the disc:

$$\cos\theta < -\frac{J_{\rm d}}{2J_{\rm BH}}, \tag{4.11}$$

where $J_{\rm d}$ is the disc angular momentum and θ corresponds to the angle between the BH spin and disc angular momentum. For instance, if $\cos\theta \geq 0$, both angular momentum always align; while for $\cos\theta < 0$, the anti-alignment occurs for small values of $J_{\rm d}/J_{\rm BH}$. Details regarding the implementation of this process are given in Dubois et al. (2014b).

4.3.2 Galaxy and BH

Super-Eddington accretion is sustained onto the BH via strong gas inflows, which are more likely to be found in gas-rich high-redshift environments. To this end, we set up our initial conditions to represent an isolated halo of mass $10^{11}\,{\rm M}_\odot$ at redshift $z = 4$ with an NFW profile composed of 85 per cent of DM particles and 15 per cent of gas in hydrostatic equilibrium with small rotation, which gas can radiatively cool down to temperatures as low as 10K. The simulations presented here are performed in a box of size 113 kpc, adaptively refined to a maximum resolution of 12 pc. Stars form following a Schmidt law with a gravo-turbulent model for star formation efficiency, in cells above a gas density threshold of $n_{\rm SF} = 181\,{\rm H\,cm^{-3}}$, giving a stellar mass resolution of $M_* = 10^4\,{\rm M}_\odot$. Explosions from type II supernovae (SNe) are also included with release of mass (including metals), momentum, and energy (assuming $2\times10^{49}\,{\rm erg\,M_\odot^{-1}}$ of formed stars). For more details about the initial conditions and the modeled physics, we refer to Chapter 3, Section 3.3.

As the DM halo starts to collapse, our isolated galaxy begins to form. With enough cycles of star formation and SN feedback events, the galaxy comes to a steady state at $t = 160\,{\rm Myr}$ with a total stellar mass of $\sim 10^9\,{\rm M}_\odot$. It corresponds to the stellar mass expected in a $10^{11}\,{\rm M}_\odot$ dark matter halo (Moster et al. 2010). In addition, the star formation rate reaches a few $10\,{\rm M}_\odot\,{\rm yr}^{-1}$, which is also the expected order of magnitude for our target redshift $z = 4$ (Salmon et al. 2015). Despite the strong SN explosions, due to the high densities of gas available for star formation, the centre of the galaxy remains cold, dense and compact. At this point, a BH is added in the centre of the galaxy, with a given velocity similar to the gas

TABLE 4.1: Properties of the suite of simulations performed, showing from left to right: BH mass when super-Eddington is allowed ($M_{\rm BH}$); initial BH spin ($\vec{a}_{\rm ini}$); MADness fraction of the disc ($f_{\rm MAD}$, scales with the jet efficiency as $\eta_{\rm jet} \propto f_{\rm MAD}^2$)

Name	$M_{\rm BH}$ ($M_\odot$)	$\vec{a}_{\rm ini}$ (x,y,z)	$f_{\rm MAD}$
sEdd_0 (fid.)	$\mathbf{2 \times 10^6}$	**(0,0,0)**	**0.5**
sEdd_y	2×10^6	(0,0.7,0)	0.5
sEdd_-z	2×10^6	(0,0,-0.7)	0.5
sEdd_+z	2×10^6	(0,0,0.7)	0.5
sEdd_0.05_0	2×10^6	(0,0,0)	0.05
sEdd_0.05_y	2×10^6	(0,0.7,0)	0.05
sEdd_0.05_-z	2×10^6	(0,0,-0.7)	0.05
sEdd_+z_LM	10^6	(0,0,0.7)	0.5

surrounding the BH, in order to maximise the BHL rate (see Eq. 4.7). We do not allow for super-Eddington accretion as soon as the BH is added, as the very high accretion rates would produce extremely strong feedback that would sterilize the BH environment. We look for a smooth transition from a galaxy without a BH to a BH with potentially very strong feedback by enforcing a few cycles of Eddington-limited accretion, so that the evolution of the galaxy remains more continuous. After $\sim 40\,$Myr, at $t = 206.4\,$Myr, we let the BH grow at super-Eddington rates, and all our analysis starts from this time.

4.4 Results

In this work, we use the suite of initial conditions from Chapter 3 in the same halo with properties analog to a $10^{11}\,M_\odot$ dark matter halo at $z = 4$ (see Table 1 for more technical details). Similarly to the super-Eddington simulations from Chapter 3, and as described in the previous section, we add the BH in the centre of the galaxy at $t = 160\,$Myr, where it evolves under Eddington-limited accretion until $\sim 206.4\,$Myr. From this point onwards, we allow for super-Eddington accretion and feedback processes. All figures shown in this Section start when super-Eddington is allowed. We evolve both spin magnitude and direction in these new simulations to highlight the effects of the super-Eddington regime on the subsequent development of the BH spin (Section 4.4.1), its impact on BH growth (Section 4.4.2) and see how far we can predict the BH spin according to simulations and analytical modelling (Section 4.4.3). All simulations presented are summarized in Table 4.1.

4.4.1 Different phases of spin evolution

In order to study the evolution of a, we use as our fiducial simulation an initially non-spinning BH (sEdd_0). We show in Fig. 4.2 the spin evolution a against the mass gained by the BH $\Delta M_{\rm growth}$ in this simulation, after the first super-Eddington episode (at $t \sim 206.4\,$Myr). Specific snapshots are indicated by the colored markers and for each marker a zoomed-in evolution of the spin is added in the respective colored panels.

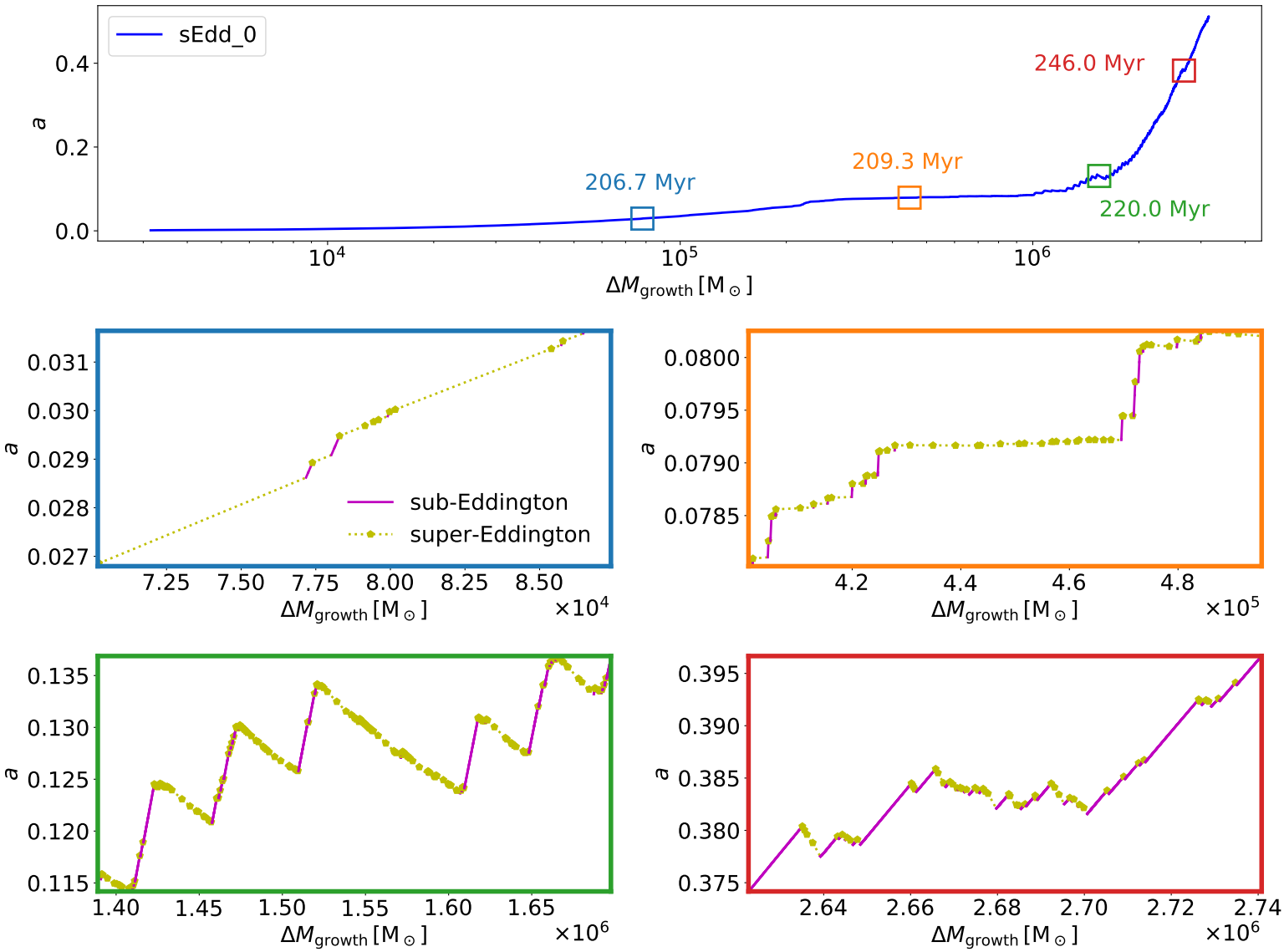

FIGURE 4.2: *Top:* Spin parameter a versus the cumulative BH mass growth $\Delta M_{\rm growth}$ for our fiducial simulation sEdd_0, after the first super-Eddington episode (at $t \sim 206.4$ Myr). Different phases of evolution are shown in the colored panels. *Middle and bottom:* Zoomed-in evolution of a at different times where each color of the plot frame corresponds to that in the top panel. Mass is either accreted above (dotted yellow) or below (solid purple) the Eddington limit. a tends to increase with more mass gained by the BH, and super-Eddington episodes are not able to effectively spin-down the BH.

Over the course of the simulation, the prograde BH spin tends to generally increase, reaching $a \simeq 0.5$ after gaining more than $3 \times 10^6\,\mathrm{M}_\odot$. As explained in Section 4.2, when $a > a_{\rm tr} = 0.079$, the quasar mode will spin-up the BH, whereas the super-Eddington and radio modes will spin-down the BH. It is important to note that mass accreted in the radio mode does not significantly contribute to BH growth and consequently to varying a throughout the entirety of the simulation. In our setup, the super-Eddington regime does not seem to be frequent enough or to last long enough to have a durable impact on the BH spin. A careful inspection of the evolution shown in the panels of Fig. 4.2 hints at the specific reasons for the spin evolution of our BH, and we detail them in the following.

Shortly after critical accretion is allowed (blue panel), the spin increases during both super- and sub-Eddington accretion phases, since $a < 0.079$ during this period, i.e. below the spin-up/spin-down transition $a_{\rm tr}$ used in our model for the MAD state. Most of the BH mass is gained via super-Eddington accretion (yellow line, inset panels of Fig. 4.2), meaning that super-Eddington accretion is the main driver of the spin evolution at this time in the simulation. There are however a few events of accretion in the quasar regime (purple line) which do not significantly impact the mass gained, but increase a at a faster rate [per unit mass]. This is caused by the spin-up parameter of the thin accretion disc being significantly larger than that of the MAD state at this low value of the BH spin (see Fig. 4.1 for small values of a).

At $t = 209.3\,\mathrm{Myr}$ in the orange panel, the picture is slightly different, as $a \sim 0.079$, and super-Eddington accretion does not have a significant impact on the BH spin evolution anymore ($s_{\rm sEdd} \approx 0$ at $a \sim a_{\rm tr}$, see Fig. 4.1). This leads to the almost flat evolution of the spin during each super-Eddington episode. Sub-Eddington accretion events lead to a continuous spin increase (with most of the mass acquired in the quasar mode), going past $a_{\rm tr}$. During this phase, the BH spin evolution is dominated by sub-Eddington accretion, while the mass growth remains dominated by the super-Eddington episodes.

From here on, the spin slowly increases with more mass accreted. Repetitive patterns, such as the ones seen in the green panel at $t = 220\,\mathrm{Myr}$, emerge: quasar accretion phases that significantly grow the BH spin are intertwined with a few super-Eddington episodes, which decrease the BH spin. Overall the mass accreted in quasar mode is larger than the mass accreted in the super-Eddington regime and the BH spin increases.

We find that, over time, the frequency of super-Eddington episodes slowly decreases, and the spin magnitude grows more steadily, as shown in the red panel at $t = 246\,\mathrm{Myr}$. Despite $|s_{\rm sEdd}| > s_{\rm qso}$ for $a \gtrsim 0.3$ (see Fig. 4.1), the scarce super-Eddington episodes cannot spin-down the BH efficiently. The more powerful spin-driven jets in the super-critical regime lead to less frequent accretion in super-Eddington, and this regime does not majorly contribute to the BH mass anymore, leading to a less effective spin-down. During this time the main role of super-Eddington episodes is to delay the overall spin-up caused by the quasar mode.

As seen in Chapter 3, more powerful super-Eddington episodes lead to very low accretion events in the radio mode ($f_{\rm Edd} < 0.01$). Due to their low accretion rates, these radio mode episodes neither significantly increase BH mass nor have any noticeable impact on the BH spin, and are therefore not visible on either panels.

If we were to compare the evolution of our BH shown here with an Eddington-limited run, the spin of our BH would generally increase more slowly at a given $\Delta M_{\rm growth}$. For

instance, using Eq. 4.3, a BH constantly accreting in the quasar mode would reach $a \simeq 0.5$ (from $a = 0$) after increasing its mass by a factor ~ 1.19 ($\Delta M_{\rm growth} \simeq 4 \times 10^5\,{\rm M}_\odot$). Our fiducial simulation has a BH reaching $a \simeq 0.5$ after accreting more than 7 times this mass.

In our analysis, we find that our BH inevitably spins up, but the super-Eddington regime is able to delay this process. For low to moderate ($a \lesssim 0.4$) spin magnitudes, AGN feedback does not significantly impact the gas surrounding the BH, leading to frequent episodes of super-Eddington accretion: the BH spin only slowly increases, showcasing the ability of super-Eddington phases to delay the spin-up process. This becomes less efficient once the spin grows to higher values, as jetted feedback becomes more powerful: the frequency of super-Eddington episodes decreases, leading to a faster increase of a from accretion at moderate sub-Eddington values. We discuss the question of predicting the BH spin when both super- and sub-Eddington regimes are involved in Section 4.4.3.

4.4.2 Evolution of the BH mass

In order to have a better understanding of the impact of the initial spin direction of the spin vector $\vec{a}_{\rm ini}$ on the super-Eddington mass evolution, we perform additional simulations, which all have $|a_{\rm ini}| = 0.7$ (as in Chapter 3) but different directions with respect to the large-scale gas distribution. We consider the following cases: in co-rotation with the galactic disc (sEdd_+z), in counter-rotation with the disc (sEdd_-z) and pointing into the disc (sEdd_y).

We show in Fig. 4.3, the evolution of the spin parameter a (top panel) and BH mass $M_{\rm BH}$ (bottom panel) for this set of simulations, as well as our fiducial simulation sEdd_0. For the same initial spin magnitudes, the BH is able to grow significantly more in mass when its spin is initially counter-rotating with the disc (sEdd_-z, solid green) than in the other configurations, as it takes $\sim 15\,$Myr to align with the angular momentum of the accreted gas. As the realignment process occurs, the magnitude of the BH spin decreases down to $|a| \simeq 0.3$, while still counter-rotating. Since AGN jet efficiency in the super-Eddington regime is $\eta_{\rm jet} \propto a^2$, feedback is weak. Super-Eddington episodes are therefore frequent and thus able to contribute to growing effectively the BH mass.

After the alignment with the disc angular momentum, the BH spin remains at moderate values ($|a| \simeq 0.3 - 0.4$) for $\sim 20\,$Myr, allowing for a short period of efficient growth. At late times, the BH spins up to higher values, unleashing more and more powerful feedback during the increasingly rarer super-Eddington episodes, which leads to decreased BH growth rates.

Both the BHs in sEdd_+z (solid red) and sEdd_y (solid orange) do not spend a lot of time in the super-Eddington regime, nor do they gain significant mass in comparison to their initial BH mass. Due to their persistently high spins, each super-Eddington event triggers powerful AGN feedback episodes and regulates BHs growth efficiently (see Chapter 3 for discussion).

By comparing the BH of the sEdd_0 run (solid blue) with the BH from the other runs discussed in this Section, it is apparent that a non-spinning BH is able to grow much faster and to higher masses than a (co- or counter-rotating) spinning BH of any other simulations presented this far. The BH that starts with $a_{\rm ini} = 0$ is at the minimum of the AGN jet feedback efficiency in the super-Eddington regime – and also at a very low value of the radiative efficiency for the AGN quasar feedback, which, although monotonically growing with the

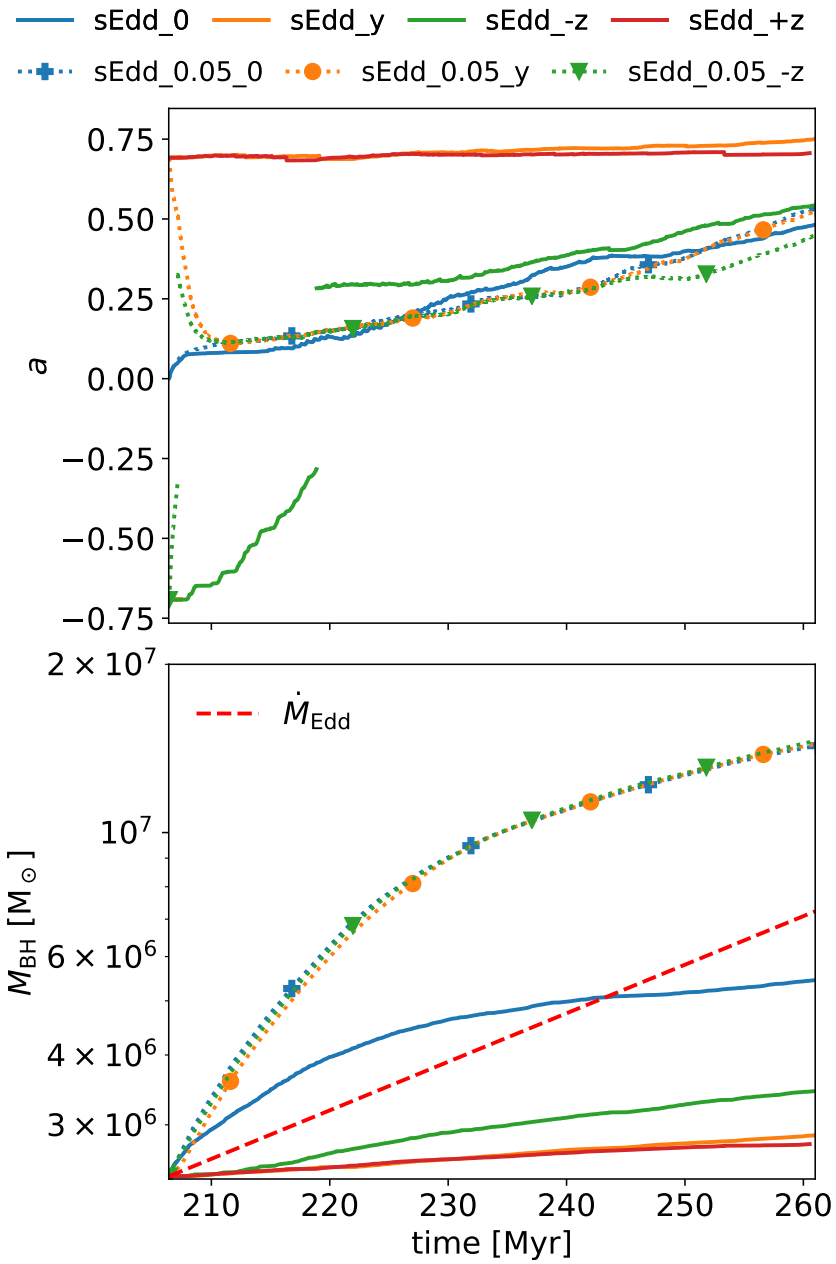

FIGURE 4.3: *Top:* Evolution of the spin parameter a for the sEdd_0 (solid blue), sEdd_y (solid orange), sEdd_-z (solid green), sEdd_+z (solid red), sEdd_0.05_0 (dotted blue), sEdd_0.05_y (dotted orange) and sEdd_0.05_-z (dotted green) simulations, from the moment super-Eddington was allowed ($t = 206.4$ Myr). *Bottom:* Evolution of the BH mass $M_{\rm BH}$ for the same simulations. For comparison is added the Eddington limit $\dot{M}_{\rm Edd}$ (dashed red). Different initial spin magnitudes and directions play a key role in the BH mass evolution, with slower BHs growing more. When the MADness factor $f_{\rm MAD}$ is low (sEdd_0.05_0, sEdd_0.05_y and sEdd_0.05_-z), the growth in spin and mass are very similar amongst the simulations.

BH spin, is nearly flat with $\epsilon_r \simeq 0.05 - 0.1$ from $a \simeq [-1, 0.7]$ until it sharply rises up to $\epsilon_r \simeq 0.4$ (see Zubovas & King 2019: for a different approach leading to similar conclusions for Eddington-limited BHs). As the BH spin slowly increases with accretion of gas, AGN feedback regulates the BH mass growth more efficiently, leading to an overall contribution to the BH mass growth dominated by the quasar mode at $t \simeq 240\,\mathrm{Myr}$ (also see Fig. 4.2, bottom right panel).

We also compare the impact of the MADness parameter f_{MAD} on the BH mass and spin evolution, with three additional simulations, namely sEdd_0.05_0 (dotted blue), sEdd_0.05_y (dotted orange) and sEdd_0.05_-z (dotted green) in Fig. 4.3. The f_{MAD} parameter has been decreased by a factor of 10, which corresponds to a 100 times lower jet feedback efficiency than the $f_{\mathrm{MAD}} = 0.5$ simulations. For all three runs, BH mass and spin evolution are nearly identical, meaning that the BH spin initial direction and magnitude cease to have a significant impact on the BH evolution when a low MADness state of the accretion disc is assumed. We find that it only takes $\lesssim 5\,\mathrm{Myr}$ for the spin to align with the angular momentum of the disc. Because of the low MADness of the disc, the energy injected in the surroundings of the BH does not make a significant difference regarding the state of the gas near the compact object, and gas can accrete on the BH almost unimpeded by the AGN feedback. Therefore, all BHs with $f_{\mathrm{MAD}} = 0.05$ evolve in almost the same environment with the same orientation after the first 5 Myr of growth required for BH realignement.

In conclusion, both MADness and spin magnitude play a key role on the BH mass growth, as hinted in Chapter 3, and on the BH spin evolution. We find that the lower the MADness factor the more massive the BH is going to grow. For low MADness states ($f_{\mathrm{MAD}} = 0.05$), for which the BH is not yet self-regulated, the growth of its mass and spin becomes independent of the initial BH spin. However, for high MADness states ($f_{\mathrm{MAD}} = 0.5$), where BH is near self-regulation, then the lower the initial BH spin magnitude $|a|$, the greater the growth. The key lies in the AGN feedback, as for lower MADness/spins, feedback is weak and will not heat up the BH surroundings as effectively, allowing for more mass gained via super-Eddington accretion.

4.4.3 Predicting the spin evolution

The understanding gained on the spin evolution in the super-Eddington regime from our simulations in the previous sections leads to the following question: is it possible to have an explicit expression of the spin a as a function of the mass accreted by the BH? First some theoretical considerations: Accretion from a thin disc of gas orbiting the BH led Bardeen (1970) to integrate the differential equation and obtain the evolution law (Eq. 4.3). A similar approach can be used for super-Eddington spin-up rate. Using Eq. 4.4, a maximally rotating BH gets spun-down by prograde accretion to $a \simeq a_{\mathrm{tr}}$ after a moderate amount of accretion in super-Eddington of $M_{\mathrm{BH,fin}} \simeq 2.64 M_{\mathrm{BH,ini}}$. A maximally rotating BH gets spun-down by retrograde accretion to $a = 0$ after $M_{\mathrm{BH,fin}} = 1.64 M_{\mathrm{BH,ini}}$.

One can combine the quasar and super-Eddington contributions to the spin evolution of the BH. For the combined case, the spin variation of the BH for a given total mass variation

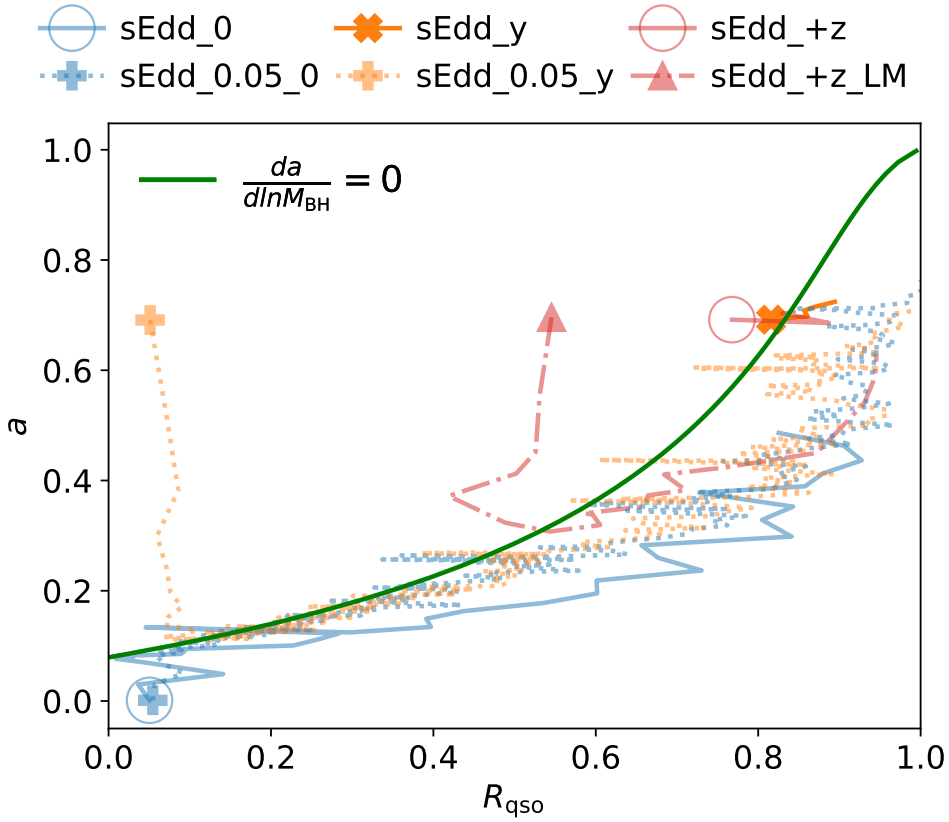

FIGURE 4.4: Evolution of the spin parameter a as a function of R_{qso} for the sEdd_0 (solid blue), sEdd_y (solid orange), sEdd_+z (solid red), sEdd_0.05_0 (dotted blue), sEdd_0.05_y (dotted orange) and sEdd_+z_LM (dashed dotted red) simulations, from the moment super-Eddington was allowed. Eq. 4.13 is shown in green. The markers show the starting a-R_{qso} for each simulation. Each step represents a mass increase of $\Delta M = 8 \times 10^4\,M_\odot$. Only BHs in corotation ($a > 0$) during the entirety of the simulation are shown here. The sEdd_y and sEdd_+z BHs have self-regulated, therefore their trajectories on the a-R_{qso} plane are very short compared to the rest of the simulations shown.

of the BH $dM_{BH} = dM_{BH,qso} + dM_{BH,sEdd}$ is

$$\frac{da}{d\ln M_{BH}} = (1 - R_{qso})s_{sEdd} + R_{qso}\frac{s_{qso}}{\widetilde{E}_{qso}}, \tag{4.12}$$

where we define $R_{qso} = dM_{BH,qso}/dM_{BH}$ to be the ratio of mass accreted in the quasar mode.

The ratio R_{qso} and BH spin a are dependent on one another: the spin variation depends directly on R_{qso} and a; and R_{qso} also depends implicitly on a because of how a changes the feedback efficiency. Thus, the exact trajectories in the $a - R_{qso}$ plane are non-trivial. Nonetheless, Eq. 4.12 can guide us to understand how the spin should naturally evolve.

Let us first consider what would happen if a BH evolves at fixed R_{qso}. In this case, its equilibrium spin value can be obtained by setting $da/d\ln M_{BH} = 0$. We only consider spin parameters $a \in [a_{tr}, 0.998]$, as the alignment process is not taken into account in Eq. 4.12. Solving Eq. 4.12 for $da/d\ln M_{BH} = 0$ leads to the following relationship:

$$R_{qso}^{-1} = 1 - \frac{s_{qso}}{\widetilde{E}_{qso}s_{sEdd}}, \tag{4.13}$$

which is shown as a green curve in Fig. 4.4. Any point on this line above $a_{\rm tr}$ and below $a = 0.998$ represents an equilibrium value, as contributions from super-Eddington phases (which decrease the spin magnitude) and quasar phases (which increase the spin magnitude) negate each other. Any BH not originally on the green curve would over time evolve towards it, and then be expected to stay at the point where it reaches the curve. For example, a BH always accreting at $R_{\rm qso} = 0.5$ would evolve to $a \simeq 0.3$ from any initial spin value and then stay there.

As any point on the line represents an equilibrium value, and $R_{\rm qso}$ is determined by the environment of the BH: a BH would not be expected to continue evolving in the $a - R_{\rm qso}$ plane once it reaches the green curve, unless significant changes in the environment force a change in $R_{\rm qso}$. Within the intricate environment of an evolving galaxy, the evolution in the $a - R_{\rm qso}$ plane is more complex, as can be seen in Fig. 4.4, which shows the evolution of a as a function of $R_{\rm qso}$ for several simulations described in Table 4.1. Each step on the figure represents a mass increase of $\Delta M = 8 \times 10^4\,{\rm M}_\odot$, and the markers show the $a - R_{\rm qso}$ after the first ΔM has been accreted for each simulation.

We exclude simulations that had $a_{\rm ini} < 0$ (i.e. sEdd_-z and sEdd_0.05_-z) from Fig. 4.4. Such simulations spin-up via gas accretion in the quasar and super-Eddington regimes, until they realign with the disc angular momentum and reach $a > 0$ (see top panel of Fig. 4.3), which is a process that is not included in Eq. 4.12. To avoid complications due to this omission, we only show simulations which have a positive spin parameter $a > 0$ for the entire duration of the run in Fig. 4.4. To investigate the role of $M_{\rm BH}$, we add a simulation, sEdd_+z_LM, which has the same properties as sEdd_+z except that the initial $M_{\rm BH}$ is half as massive.

The value of the ratio $R_{\rm qso}$ depends on the gas properties (temperature, density and gas velocity) in the BH accretion region, as well as the BH mass and the strength of the feedback. This is nicely demonstrated by the distribution of the initial coloured markers for all simulations in Fig. 4.4. We remind the reader that all[1] our simulations are variants of sEdd_0, and so the initial properties of the accretion region are identical for all BHs when they are initialised in the simulation. For this reason, one could naively expect simulations with the same $a_{\rm ini}$ to start their evolution at the same point in the $a - R_{\rm qso}$ plane in Fig. 4.4. Instead, the range of $R_{\rm qso}$ experienced by different BHs after a mass increase of only $\Delta M = 8 \times 10^4\,{\rm M}_\odot$ (coloured markers) shows the dramatic impact of feedback on the spin evolution of the BH. The highest initial $R_{\rm qso}$ (i.e. the orange cross and red circle markers) is found for sEdd_y and sEdd_+z at $R_{\rm qso} \simeq 0.8$, while the initial $R_{\rm qso}$ is lower for discs that are less MAD and BHs that have low spin values: sEdd_0.05_0, sEdd_0.05_y and sEdd_0 start with $R_{\rm qso} \lesssim 0.1$. This is also true for lower BH masses, as sEdd_+z_LM has a ratio $R_{\rm qso} \simeq 0.5$, since its feedback injection is in between the other cases already discussed (see Eq. 4.7 and Eq. 4.8). This confirms that the stronger the super-Eddington feedback, the higher $R_{\rm qso}$ becomes, i.e. the more mass is accreted at sub-Eddington rates, because super-Eddington episodes are limited by their own feedback. Weaker super-Eddington feedback occurs either with lower $\eta_{\rm jet} \propto f_{\rm MAD}^2 a^2$, so lower MADness or spin magnitude, or with less massive BHs because of the smaller growth rates $\dot{M}_{\rm BH} \propto M_{\rm BH}^2$ (see Eq. 4.7). In theory, $R_{\rm qso}$ can also change with large-scale environmental effects, for example a significant cold inflow into the galactic centre might temporarily

[1] Apart from sEdd_+z_LM which has a less massive BH.

decrease $R_{\rm qso}$ as the galaxy would feed the BH more efficiently than before.

To have a better understanding of the continued evolution of BHs in the $a - R_{\rm qso}$ plane, we separate the discussion of the BH spin evolution into three separate regions depending on the position of a BH in the $a - \mathrm{R_{qso}}$ plane: above, on and below the green curve.

For BHs above the curve, $da/d\ln M_{\rm BH} < 0$ (from Eq. 4.12) as the super-Eddington regime dominates the BH spin evolution. As the BH gains mass, the spin will therefore decrease in magnitude, which is exactly what happens for sEdd_0.05_y and sEdd_+z_LM until they reach the green curve. We note that these BH spins evolve at almost constant $R_{\rm qso}$ until they reach the green curve, due to weak AGN feedback that does not significantly change the gas properties in the vicinity of the BHs.

As mentioned before, if the BH lies on the green curve, $da/d\ln M_{\rm BH} \simeq 0$ (see Eq. 4.13) and if there are no changes to its environmental conditions it will remain at fixed $R_{\rm qso}$ and a. In the environment we have explored, super-Eddington phases become scarcer as the BH grows with time, leading to an increase of $R_{\rm qso}$. The decrease in super-Eddington phases are caused by its powerful feedback, therefore when feedback is weak, $R_{\rm qso}$ increases slowly and $da/d\ln M_{\rm BH}$ remains small; consequently, the trajectory of the BH will remain close to the curve, but with a tendency towards larger $R_{\rm qso}$. This is the case for the low MADness simulations (dotted lines): until the BHs have quadrupled their sizes (see Fig. 4.3), their spin magnitudes remain moderately small ($|a| \lesssim 0.3$) and due to their low MADness factors ($f_{\rm MAD} = 0.05$), super-Eddington feedback is not powerful enough to disturb the BHs accretion region. Cases with low spin and low MADness, limiting the strength of super-Eddington feedback, are those that tend to remain closer to the conditions under which Eq. 4.13 was derived, and can therefore be described with this equation during this period of growth.

Finally, when the BH finds itself below the green curve, $da/d\ln M_{\rm BH} > 0$ as spin-up due to accretion in the quasar mode is more important to changing the spin than the occasional spin-down during super-Eddington episodes. The quasar episodes tend to increase the spin magnitude, meaning subsequent super-Eddington episodes have a more powerful feedback which again increases $R_{\rm qso}$ and moves the BH further away from the green curve. We find that after reaching the curve, all simulations shown in Fig. 4.4 eventually fall below the curve, and then stay below due to this mechanism. From this point onward, their trajectories are mostly driven by AGN feedback, which makes Eq. 4.13 insufficient to predict spin evolution, since the effect of feedback cannot be included in a self-consistent way.

In conclusion, determining the evolution of a for a BH that undergoes both quasar and super-Eddington regimes does not lend itself to a simple expression. However, we find that with some limits (e.g. for slowly spinning BHs), the evolution can be described by Eq. 4.13. At higher spins ($|a| \gtrsim 0.3$), the evolution is mostly driven by AGN feedback so the relationship in Eq. 4.13 no longer holds. In our work, in addition to sub-Eddington accretion, we find that coherent super-Eddington accretion coupled with relativistic jets, does not spin down the BH efficiently : all of our BHs stop having super-Eddington accretion phases and, as a consequence, inevitably spin up to $a \simeq 0.998$.

For the analysis performed here, we used the super-Eddington spin-up parameter $s_{\rm sEdd}$ from McKinney et al. (2012) (Eq. 4.4). An alternative choice would have been to use the spin-up rate from Narayan et al. (2022) (Eq. 4.5), shown in Fig. 4.1, which is more efficient at spinning the BH down for low spin values in comparison to McKinney et al. (2012). If we

had used Narayan et al. (2022), the stable equilibrium curve we would find using $s_{\rm sEdd} = s_{\rm MAD,N22}$ in Eq. 4.13 would have shifted slightly below the green curve of Fig. 4.4, for all values of a. This would also lead to higher mass gained at a lower spin, i.e. more massive BH in a similar amount of time. This would impact the spin evolution over long periods of time, as can be seen using the additional simulation with $s_{\rm MAD,N22}$ discussed in Appendix B.

4.5 Discussion

An important constraint on models of SMBH growth is the observed mass-dependent spin distribution. Observationally, low-mass SMBHs tend to be rapidly spinning, suggesting growth via coherent accretion, whereas the more massive ones have modest to low spin magnitudes, indicating chaotic accretion and/or merger driven growth (e.g. Reynolds 2013, 2021, Soares & Nemmen 2020). In this paper, we study coherent super-Eddington accretion, and find that, regardless of the ability of super-Eddington feedback to spin-down BHs, it only delays their spin-up by $\lesssim 100\,$Myr. This is true for all initial BH spin magnitudes and direction probed here, so we predict that super-Eddington feedback will not have a significant impact on the global spin distribution.

Chaotic (or incoherent) accretion has been suggested to help BH seeds grow to $\gtrsim 10^8\,{\rm M}_\odot$ (e.g. King et al. 2005, 2008, Zhang & Lu 2019, Zhang et al. 2020, Zubovas & King 2021). Despite exploring only coherent accretion in this paper, we speculate that incoherent accretion may not lead to efficient super-Eddington spin-down if the BH is already rapidly spinning. For example, in Eddington-limited cosmological runs, spin-down induced by gas stripping from gas-rich mergers or counter-rotating filamentary accretion (Dubois et al. 2014b, Bustamante & Springel 2019) only decreases the spin magnitude to $|a| \sim 0.7$ (from $|a| \sim 1$), as the direction of the BH spin realigns with the gas angular momentum before the spin-down process is completed. If one of these events were to provide our BH with enough misaligned gas to reach accretion rates above the Eddington limit, the spin-down process would be less efficient than for the Eddington-limited BHs discussed before. The very powerful super-Eddington jets produced at very high spins for our BH would completely shut down accretion of the misaligned material and would leave the BH spin almost unchanged ($|a| \sim 1$). In addition to this merger-driven gas misalignment effect, coalescence between maximally spinning BHs also leads to a decrease in the spin of the BH remnant (Rezzolla et al. 2008). While this effect can be dominant for setting up the spin of BHs in the passive and most massive galaxies (Dubois et al. 2014b), it is not clear how this should affect the spin evolution when super-Eddington accretion is included.

Our model for spin-up rate assumed that the MAD state obtained by McKinney et al. 2012 (or Narayan et al. 2022, see Appendix B, which tries to capture the effect on BH growth of the uncertainties in spin-up rate) for sub-Eddington thick accretion discs can be extended to the super-Eddington regime. Although the geometry of the two discs are similar, their radiative efficiencies may differ significantly, and it remains to be tested through dedicated GRMHD simulations whether the spin-up rates in the super-Eddington regime is significantly different from the classical thick disc state.

4.6 Conclusions

In this study, we explore the evolution of the BH spin a under the conditions of critical accretion above the Eddington limit in an isolated galaxy. Understanding the conjunction of a magnetically arrested disc (MAD) in the super-Eddington regime with the thin disc for accretion comparable to the limit, as they both vary the BH spin differently, is the main focus of this paper. Our main findings are as follows.

- The super-Eddington regime does not spin the BH down effectively, as a inevitably increases towards ~ 0.998. It is only able to delay the certain spin-up of the BH from thin disc accretion. (Section 4.4.1)
- MADness and spin play a key role in BH growth: the lower the MADness the greater the growth. Similarly, the lower the spin magnitude, the greater the mass gained, thanks to weaker jets at lower spins. (Section 4.4.2)
- The combination of super-Eddington and quasar regimes does not lead to a simple expression for the spin evolution. Relatively low spins $|a| \lesssim 0.3$ are able to follow Eq. 4.13, but for higher spin magnitudes, AGN feedback makes the evolution not predictable. (Section 4.4.3)

Chapter 5

Conclusions and outlook

The main subject of this thesis revolves around the growth of supermassive black holes at high-redshift. Many groups work on this vast subject, using different techniques, providing insight on the different scenarios related to the origin of these compact objects. This thesis aims at understanding if these supermassive black holes could have grown efficiently at critical accretion, in the so-called super-Eddington regime, by answering some of the following questions. Is the super-Eddington feedback strong enough to prevent black holes from growing? Is it possible to have efficient super-Eddington growth? If so, what are the conditions related to such growth? What is the global impact that this feedback has on the gas close and far from the black hole accretion region?

The first step to study this was to implement the critical regime in the `Ramses` code (Teyssier 2002), and investigate the role that local gas properties of an isolated collapsing cloud play in the efficiency and duration of super-Eddington feedback (Chapter 2). In the process of this analysis, we noticed that a short period of super-Eddington growth allowed for the black hole to slightly increase its mass, and that less resolved simulations permit better growth. This led us to explore the impact of the resolution on the outflow properties of super-Eddington episodes, where we found that resolution in the super-Eddington jets could play a major role in heating the gas at large scales, thus impacting black hole growth altogether.

Thanks to this study, we were able to have a better understanding on the role of jetted feedback in a very idealised simulation. Applying this research to a more realistic simulation would allow the investigation of the role that super-Eddington plays in the evolution of supermassive black holes over long periods of time. This was initially studied in Chapter 3, by performing simulations of a galaxy in an isolated dark matter halo and adding a $10^6\,M_\odot$ black hole to its center. Our main findings (Massonneau et al. 2022b) suggested that due to super-Eddington feedback, the black hole reached self-regulation within a few Myr even in an environment favorable for super-Eddington accretion. The surroundings of the black hole were heated to very high temperatures ($\gtrsim 10^8$ K), preventing the compact object to accrete at high rates for $\sim$ Myr. The repeated succession of these episodes reduced the amount of time the black hole spent in the super-Eddington regime, with $\lesssim 1$ per cent of the time spent accreting at critical rates by the end of the simulations. However, black holes which had weaker super-Eddington feedback efficiencies, provided a slightly larger black hole mass evolution over ~ 80 Myr than that for a black hole constantly accreting at the Eddington limit. We concluded that there may be a window of opportunity for mildly super-Eddington mass evolution, with the right combination of black hole spin and super-Eddington feedback

efficiency.

The natural follow-up to this study was the investigation of another property of black holes: their spins. Since spin plays a key role in feedback efficiencies, we combined super-Eddington accretion with sub-Eddington phases and follow for the first time the black hole spin evolution (Chapter 4 and Massonneau et al. 2022a). Our results indicated that, due to the low frequency of super-Eddington episodes, relativistic jets in this regime were not able to decrease the magnitude of the spin effectively, as thin disc accretion in the quasar mode inevitably increased the black hole spin. Super-Eddington phases were only able to delay the spin-up of the black hole. We confirmed that black holes initially spinning slowly had significantly greater growth, due to weaker jets at lower spin magnitudes. While studying the spin evolution is essential to understand if the super-Eddington regime can efficiently contribute to black hole growth, it is also important to note that the spin-up rate in this regime has not been studied extensively in GRMHD simulations. Further constraints on this parameter in the future would be required to better assess super-Eddington growth. After investigating an other parameter that plays a role in the super-Eddington feedback efficiency, we also concluded that the lower the MADness of the disc, the greater the growth.

Whether super-Eddington accretion would be a potential solution to the issue of explaining high-redshift supermassive black holes remains a debated topic. The interest in this field of research has drastically increased in the past decades, as more discoveries of high-redshift quasars are made. The takeaway with the investigation performed in this thesis leads to the belief that unless super-Eddington feedback is weak, or that the black hole accretes gas incoherently, thus remaining more easily at a low spin magnitude; then super-Eddington episodes would hinder black hole growth. Whilst our work provides hints to the impact of super-Eddington accretion and a better understanding to the study of this critical regime in a realistic galactic environment, simulations performed were idealised, as no galaxy/black hole merger events or filamentary inflow found in cosmological setting were taken into account. The next step for such study is to launch a cosmological zoom-in simulation, and find out if super-Eddington accretion can help black holes grow up to the observed and estimated masses at $z \sim 6$. `Ramses` users who studied the high-redshift Universe have been able to find black holes accreting at the Eddington limit at $z > 6$ (*e.g.* Pfister et al. 2021), meaning that starting with the same initial conditions would provide a great tool for comparing Eddington-limited and super-Eddington growth.

Besides numerical simulations, the study of high-redshift quasars has been (and will continue to be) boosted with the recent launch of the JWST telescope. Upcoming observations with JWST will provide a unique opportunity to detect fast-accreting black hole seeds that offer an evolutionary pathway toward the very massive population of supermassive black holes at $z > 6$. Hu et al. (2022b) predict that in the most optimistic case, JWST can reveal these rapidly growing black holes up to $z \sim 17$, but it remains complex to determine the nature of the black hole seed (whether PopIII remnant or massive seed). Inayoshi et al. (2022b) focus on the observational signature at the early black holes early growth stage before reaching $M_{\rm BH} \sim 10^6\,{\rm M}_\odot$, and model their spectral energy distribution. They find that super-Eddington growth produces extremely strong Balmer lines, which could be detected in the MIRI filters.

Finally, super-Eddington studies are not limited to the high-redshift Universe, as there

are other applications to this regime in the nearby galaxies. Exploring accreting transient systems like tidal disruption events, or sources displaying sustained super-Eddington accretion like ultra luminous sources, allows the study of the properties of this extreme process and better assess its relevance for the growth of supermassive black holes.

Appendix A

Initial conditions for the isothermal sphere

In this Appendix, we describe the procedure to find a set of initial conditions for the isothermal sphere setup (see Section 2.5.1) that would lead to super-Eddington accretion as soon as the collapse of the isothermal sphere begins. The sphere has a radius of $R = 10\,\mathrm{pc}$ and a mass of $M_{\mathrm{sph}} = 2 \times 10^6\,\mathrm{M}_\odot$. As described in Section 2.5.1, several physical and numerical parameters can be played with, such as the sphere temperature T, BH mass M_{BH} and refinement level l_{max}.

Firstly, we start with investigating the accretion rate $\dot{M}_{\mathrm{acc}}$, and look for initial conditions that would allow for accretion above the limit. Fig. A.1 shows $\dot{M}_{\mathrm{acc}}$ (in units of $\dot{M}_{\mathrm{Edd}}$ to follow when the BH accretes above the limit) as a function of M_{BH} for different temperatures of the sphere $T \in [10^2\,\mathrm{K};\ 10^4\,\mathrm{K};\ 10^5\,\mathrm{K}]$ (shown in dashed, dotted and solid respectively) and different refinement levels $l_{\mathrm{max}} \in [7;\ 9;\ 11]$ (shown in green, red and blue respectively). We note that the increases/decreases are linear with respect to M_{BH}, as accretion rates are given in units of $\dot{M}_{\mathrm{Edd}}$. We have three scenarios:

- For a fixed temperature T and refinement level l_{max}, the normalised accretion rate peaks at a given M_{BH}, where $\dot{M}_{\mathrm{BHL}} \simeq \dot{M}_{\mathrm{floor}}$. Below the peak, the accretion is calculated with $\dot{M}_{\mathrm{BHL}}$; whilst above, the BH accretes at $\dot{M}_{\mathrm{floor}}$. Such setup allows to study simulations with similar accretion rates for different M_{BH}.

- For a fixed M_{BH} and l_{max}, increasing T leads to decreasing $\dot{M}_{\mathrm{BHL}}$. Therefore, a sphere with initially high values of T will tend to have BHs grow at lower accretion rates.

- Finally, if T and M_{BH} are fixed, having a more refined environment, *i.e.* increasing l_{max}, leads to increasing $\dot{M}_{\mathrm{BHL}}$, due to the higher densities in the surroundings of the BH.

Secondly, we would like to have a sphere that collapses onto the BH, while the super-Eddington feedback is visible. For example, if the binding energy of the sphere $U_{\mathrm{sph}} \gg E_{\mathrm{sEdd}}$, the sphere will completely collapse, uncountered by the AGN feedback. On the other hand, if $U_{\mathrm{sph}} \ll E_{\mathrm{sEdd}}$, the initial super-Eddington feedback episode will blow away the entire sphere of gas, which will result in no more matter infalling towards the BH, preventing the whole purpose of this simulation. We show in Fig. A.2 the ratio of the feedback energy from the first super-Eddington episode E_{sEdd} against the binding energy of the sphere U_{sph}, as a function of the BH mass M_{BH}. The colours and linestyles are the same as Fig. A.1 to simplify interpretation. The peak discussed previously now corresponds to a turnover in this Figure.

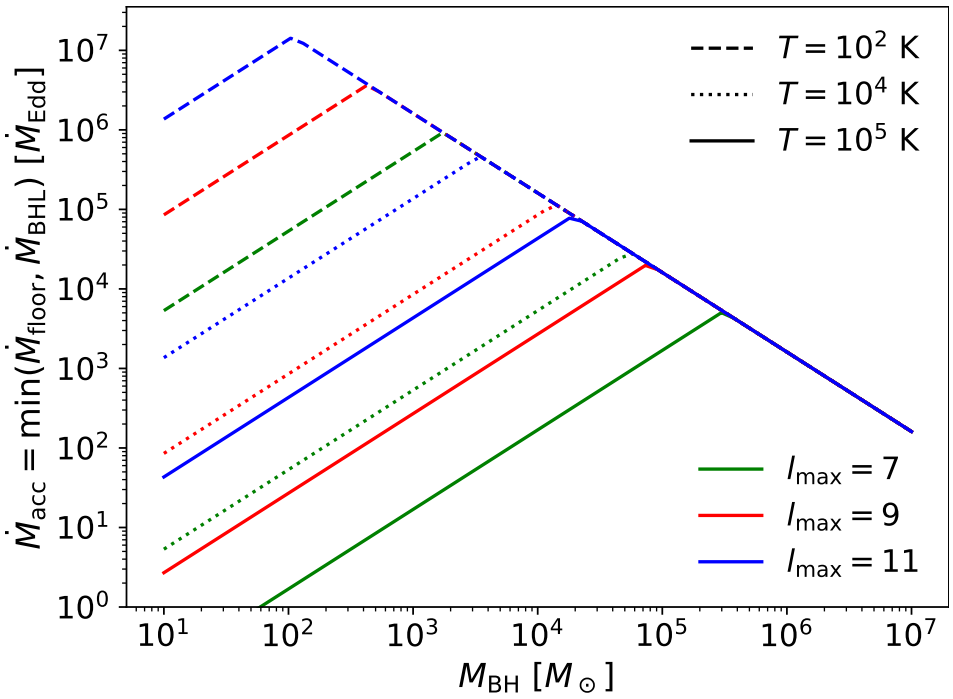

FIGURE A.1: BH accretion rate $\dot{M}_{\rm acc}$ as a function of its mass $M_{\rm BH}$. Different values of $T \in [10^2\,{\rm K};\ 10^4\,{\rm K};\ 10^5\,{\rm K}]$ (dashed, dotted and solid respectively) and refinement levels $l_{\rm max} \in [7;\ 9;\ 11]$ (green, red and blue respectively) are also shown.

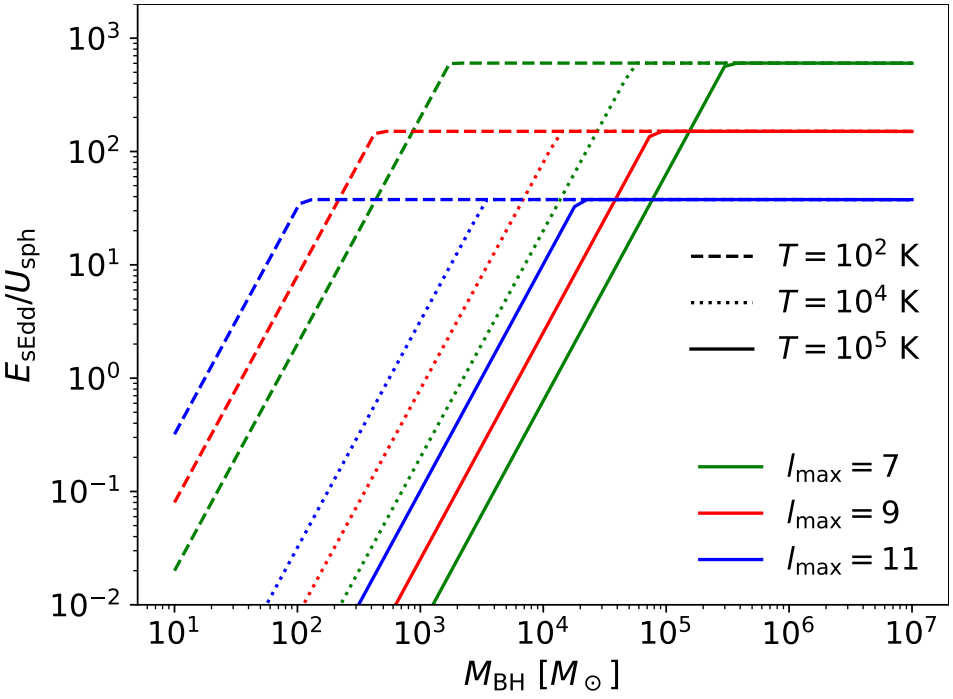

FIGURE A.2: Similar as Fig. A.1, but for the ratio of the super-Eddington feedback energy $E_{\rm sEdd}$ against the binding energy of the sphere $U_{\rm sph}$, as a function of the BH mass $M_{\rm BH}$.

Case n°	$M_{\rm BH}$ (in $\rm M_\odot$)	T (in K)	$l_{\rm max}$	$\dot{M}_{\rm acc}$ (in $\dot{M}_{\rm Edd}$)	$E_{\rm sEdd}$ (in $U_{\rm sph}$)	$r_{\rm BHL}$ resolved?
1)	10^9	10^2	11	10	10	✓
2)	10^6	10^2	11	10^3	10	✓
3)	10^3	10^4	7	10^2	10^{-1}	
4)	10	10^2	9	10^5	10^{-1}	$\sim$
5)	10^3	10^4	11	10^5	1	✓
6)	10^5	10^4	9	10^4	10^2	✓
7)	10^4	10^5	7	10^2	1	
8)	10^4	10^5	9	10^3	1	$\sim$
9)	10^4	10^5	11	10^4	10	✓

TABLE A.1: Table summarizing the different sets of parameters that will be used in the simulation of an isothermal sphere with $R_{\rm sph} = 10\,\rm pc$ and $M_{\rm sph} = 2 \times 10^6\,\rm M_\odot$. Each column, from left to right corresponds to the case number, the black hole mass $M_{\rm BH}$, the initial temperature of the sphere T, the refinement level $l_{\rm max}$, the accretion rate for the first timestep $\dot{M}_{\rm acc}$, the super-Eddington feedback energy of this first timestep $E_{\rm sEdd}$ and whether or not the BHL radius $r_{\rm BHL}$ will be resolved. *See text for explanations on the Cases.*

BHs below the turning point accrete at $\dot{M}_{\rm BHL}$, while above, they accrete at $\dot{M}_{\rm floor}$. Once again we have three scenarios:

- For a fixed T and $l_{\rm max}$, less massive BHs will produce weaker feedback, unless they already accrete at $\dot{M}_{\rm floor}$, at which point, regardless of $M_{\rm BH}$, the feedback energy $E_{\rm sEdd}$ is the same. Therefore, if a BH accretes at $\dot{M}_{\rm BHL}$, one can study a large range of feedback energies by only changing the BH mass $M_{\rm BH}$.
- Fixing $M_{\rm BH}$ and $l_{\rm max}$ has a similar effect on the feedback: when the temperature T increases, BHs will more likely accrete at $\dot{M}_{\rm BHL}$ and therefore produce less powerful feedback. Therefore, simply changing the temperature T leads to another way of studying $E_{\rm sEdd}/U_{\rm sph}$.
- Finally, in the case when both $M_{\rm BH}$ and T are fixed, varying $l_{\rm max}$ can also lead to a study of $E_{\rm sEdd}/U_{\rm sph}$. For example, if accretion is at $\dot{M}_{\rm floor}$, the higher the refinement, the lower the ratio $E_{\rm sEdd}/U_{\rm sph}$. This is the contrary for $\dot{M}_{\rm BHL}$, as the higher the refinement, the higher the ratio $E_{\rm sEdd}/U_{\rm sph}$.

With the plethora of possibilities, we have summarized in Table A.1 several sets of $M_{\rm BH}$, T and $l_{\rm max}$ to use to study super-Eddington accretion. We summarize the different options below:

- It is very difficult to find setups which have accretion rates $\dot{M}_{\rm Edd} < \dot{M}_{\rm acc} \lesssim 10\,\dot{M}_{\rm Edd}$. Either $M_{\rm BH}$ is too small and leads to very weak feedback, or the BH is very massive (even more massive than the isothermal sphere itself) and releases a too strong feedback if the simulation is not refined enough. We can only have highly resolved simulations with very massive BHs ($\gtrsim 10^8\,\rm M_\odot$) in the center of the collapsing sphere to investigate feedback processes of BHs accreting barely above the Eddington limit. This scenario corresponds to Case 1).

- For accretion rates $10\,\dot{\mathrm{M}}_{\mathrm{Edd}} < \dot{M}_{\mathrm{acc}} \lesssim 10^3\,\dot{\mathrm{M}}_{\mathrm{Edd}}$, there are more options. Still, it is not possible to probe very low M_{BH} or T as they would result in low feedback energies. However a setup where $M_{\mathrm{BH}} = 10^6\,\mathrm{M}_\odot$, $T = 10^2\,\mathrm{K}$ and $l_{\mathrm{max}} = 11$ (Case 2)) could be a good candidate for studying moderate super-Eddington accretion. With a smaller BH and lower resolution, we have Case 3) which gives a weaker feedback but allows to study $\dot{M}_{\mathrm{acc}} \simeq 10^2\,\dot{\mathrm{M}}_{\mathrm{Edd}}$.

- The highest accretion rates give the most options. To accrete at $\dot{M}_{\mathrm{acc}} > 10^3\,\dot{\mathrm{M}}_{\mathrm{Edd}}$, we need to make sure that the sphere is not completely blown off by feedback. Furthermore, gas needs to be cold $T \lesssim 10^5\,\mathrm{K}$ to reach such accretion rates. Finally, due to $\dot{M}_{\mathrm{floor}}$, we can only probe BHs with $M_{\mathrm{BH}} \lesssim 10^6\,\mathrm{M}_\odot$. With 3 additional cases (Cases 4), 5) and 6)), we have a large range of M_{BH} and $E_{\mathrm{sEdd}}/U_{\mathrm{sph}}$.

- The study of the impact of the resolution is discussed in Section 2.5.2. To investigate this, we choose a specific set of M_{BH} and T and will only vary the refinement level l_{max}. Cases 7), 8) and 9) correspond to the desired setup. The AGN feedback should not blow the sphere away and we will be able to investigate moderate super-Eddington accretion. This choice also allows to have an unresolved (Case 7)) and well resolved (Case 9)) r_{BHL}. Finally, the difference in terms of feedback energies can also be looked into.

Appendix B

Comparison of two different spin-up rates

In Section 4.2 are introduced different spin-up rates coming from McKinney et al. (2012) (Eq. 4.4) and Narayan et al. (2022) (Eq. 4.5) to compute the spin evolution of a BH producing jets. In the main body of the paper, we opt to use Eq. 4.4 from McKinney et al. (2012) in our isolated galaxy setup. We here investigate the differences between both spin-up rates, by performing a simulation similar to our fiducial run sEdd_0 (see Table 3.2), only differing in the prescription of the spin-up parameter in the super-Eddington regime $s_{\rm sEdd}$. For this run named sEdd_0_N, we used the spin-up rate of Narayan et al. 2022 (see Eq. 4.5) and we compare the BH spin and mass evolution with our fiducial simulation in Fig. B.1.

The final mass of the BH reaches almost 10^7 $M_\odot$ in the sEdd_0_N (solid green) simulation, twice as massive as sEdd_0 BH (solid blue). This faster and sustained growth is owed to much more frequent super-Eddington accretion episodes (lower $R_{\rm qso}$), triggered more often due to the low spin magnitude that stays close to (a lower) $a_{\rm tr} = 0.035$ (see Fig. 4.1, solid green) for close to 75 per cent of its evolution, driven by the corresponding lower AGN feedback efficiencies. Because of this lower AGN feedback efficiency, it requires more mass for the BH to self-regulate, and to reach a state where $R_{\rm qso}$ is sufficiently high to drive the BH spin up, and, hence, the rise of the BH spin is significantly delayed. Another way to see this is that the equilibrium curve $da/d\ln M_{\rm BH} = 0$ is lowered in the $a - R_{\rm qso}$ plane (Fig. 4.4), and, hence, the lower spin values.

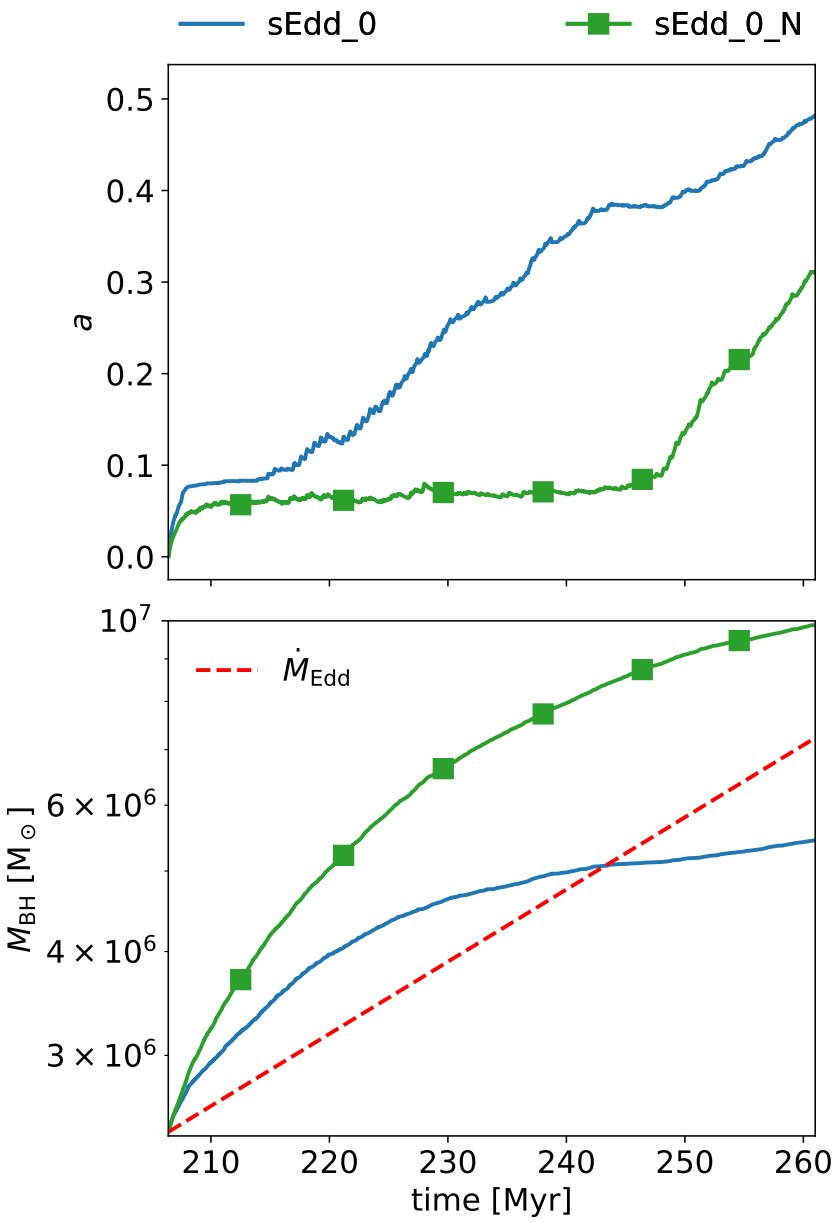

FIGURE B.1: *Top:* Evolution of the spin parameter a for the sEdd_0 (solid blue) and sEdd_0_N (solid green) simulations, from the moment super-Eddington was allowed ($t = 206.4\,\mathrm{Myr}$). *Bottom:* Evolution of the BH mass $M_{\rm BH}$ for the same simulations. For comparison is added the Eddington limit $\dot{M}_{\rm Edd}$ (dashed red).

Bibliography

Abel, T. 1995. - dissertation.

Abramowicz, M. A. et al. 1988. Slim Accretion Disks. ApJ 332. 646. https://doi.org/10.1086/166683.

Abramowicz, Marek A. & P. Chris Fragile. 2013. Foundations of Black Hole Accretion Disk Theory. *Living Reviews in Relativity* 16(1), 1. 1. https://doi.org/10.12942/lrr-2013-1.

Ackermann, M. et al. 2015. The Third Catalog of Active Galactic Nuclei Detected by the Fermi Large Area Telescope. ApJ 810(1), 14. 14. https://doi.org/10.1088/0004-637X/810/1/14.

Adams, N. J. et al. 2022. Discovery and properties of ultra-high redshift galaxies ($9 < z < 12$) in the JWST ERO SMACS 0723 Field. *arXiv e-prints*, arXiv:2207.11217. arXiv:2207.11217.

Agarwal, Bhaskar & Sadegh Khochfar. 2015. Revised rate coefficients for H_2 and H^- destruction by realistic stellar spectra. MNRAS 446(1). 160–168. https://doi.org/10.1093/mnras/stu1973.

Agarwal, Bhaskar et al. 2012. Ubiquitous seeding of supermassive black holes by direct collapse. MNRAS 425(4). 2854–2871. https://doi.org/10.1111/j.1365-2966.2012.21651.x.

Agarwal, Bhaskar et al. 2014. The First Billion Years project: birthplaces of direct collapse black holes. MNRAS 443(1). 648–657. https://doi.org/10.1093/mnras/stu1112.

Agarwal, Bhaskar et al. 2016a. Detecting direct collapse black holes: making the case for CR7. MNRAS 460(4). 4003–4010. https://doi.org/10.1093/mnras/stw1173.

Agarwal, Bhaskar et al. 2016b. New constraints on direct collapse black hole formation in the early Universe. MNRAS 459(4). 4209–4217. https://doi.org/10.1093/mnras/stw929.

Agarwal, Bhaskar et al. 2017. Metallicity evolution of direct collapse black hole hosts: CR7 as a case study. MNRAS 469(1). 231–236. https://doi.org/10.1093/mnras/stx794.

Agertz, Oscar et al. 2013. Toward a Complete Accounting of Energy and Momentum from Stellar Feedback in Galaxy Formation Simulations. ApJ 770(1), 25. 25. https://doi.org/10.1088/0004-637X/770/1/25.

Agís-González, B. et al. 2014. Black hole spin and size of the X-ray-emitting region(s) in the Seyfert 1.5 galaxy ESO 362-G18. MNRAS 443(4). 2862–2873. https://doi.org/10.1093/mnras/stu1358.

Alexander, D. M. et al. 2010. Searching for evidence of energetic feedback in distant galaxies: a galaxy wide outflow in a z ∼2 ultraluminous infrared galaxy. MNRAS 402(4). 2211–2220. https://doi.org/10.1111/j.1365-2966.2009.16046.x.

Alexander, Tal & Priyamvada Natarajan. 2014. Rapid growth of seed black holes in the early universe by supra-exponential accretion. *Science* 345(6202). 1330–1333. https://doi.org/10.1126/science.1251053.

Allen, Rebecca J. et al. 2017. The Size Evolution of Star-forming Galaxies since z $\sim$ 7 Using ZFOURGE. ApJ 834(2), L11. L11. https://doi.org/10.3847/2041-8213/834/2/L11.

Alpher, R. A., H. Bethe & G. Gamow. 1948. The Origin of Chemical Elements. *Physical Review* 73(7). 803–804. https://doi.org/10.1103/PhysRev.73.803.

Alvarez, Marcelo A., John H. Wise & Tom Abel. 2009. Accretion onto the First Stellar-Mass Black Holes. ApJ 701(2). L133–L137. https://doi.org/10.1088/0004-637X/701/2/L133.

Anglés-Alcázar, Daniel et al. 2017. Black holes on FIRE: stellar feedback limits early feeding of galactic nuclei. MNRAS 472(1). L109–L114. https://doi.org/10.1093/mnrasl/slx161.

Angus, C. R. et al. 2022. A fast rising tidal disruption event from a candidate intermediate mass black hole. *arXiv e-prints*, arXiv:2209.00018. arXiv:2209.00018.

Antonini, Fabio, Mark Gieles & Alessia Gualandris. 2019. Black hole growth through hierarchical black hole mergers in dense star clusters: implications for gravitational wave detections. MNRAS 486(4). 5008–5021. https://doi.org/10.1093/mnras/stz1149.

Antonucci, Robert. 1993. Unified models for active galactic nuclei and quasars. ARA&A 31. 473–521. https://doi.org/10.1146/annurev.aa.31.090193.002353.

Asada, Keiichi & Masanori Nakamura. 2012. The Structure of the M87 Jet: A Transition from Parabolic to Conical Streamlines. ApJ 745(2), L28. L28. https://doi.org/10.1088/2041-8205/745/2/L28.

Atek, Hakim et al. 2022. Revealing Galaxy Candidates out to $z \sim 16$ with JWST Observations of the Lensing Cluster SMACS0723. *arXiv e-prints*, arXiv:2207.12338. arXiv:2207.12338.

Bañados, E. et al. 2016. The Pan-STARRS1 Distant z > 5.6 Quasar Survey: More than 100 Quasars within the First Gyr of the Universe. ApJS 227(1), 11. 11. https://doi.org/10.3847/0067-0049/227/1/11.

Bañados, Eduardo et al. 2018. An 800-million-solar-mass black hole in a significantly neutral Universe at a redshift of 7.5. Nature 553(7689). 473–476. https://doi.org/10.1038/nature25180.

Bachetti, M. et al. 2014. An ultraluminous X-ray source powered by an accreting neutron star. Nature 514(7521). 202–204. https://doi.org/10.1038/nature13791.

Bachetti, Matteo et al. 2021. Orbital decay in M82 X-2. *arXiv e-prints*, arXiv:2112.00339. arXiv:2112.00339.

Balbus, Steven A. & John F. Hawley. 1991. A Powerful Local Shear Instability in Weakly Magnetized Disks. I. Linear Analysis. ApJ 376. 214. https://doi.org/10.1086/170270.

Baraffe, I., A. Heger & S. E. Woosley. 2001. On the Stability of Very Massive Primordial Stars. ApJ 550(2). 890–896. https://doi.org/10.1086/319808.

Barausse, Enrico. 2012. The evolution of massive black holes and their spins in their galactic hosts. MNRAS 423(3). 2533–2557. https://doi.org/10.1111/j.1365-2966.2012.21057.x.

Bardeen, James M. 1970. Kerr Metric Black Holes. Nature 226(5240). 64–65. https://doi.org/10.1038/226064a0.

Bardeen, James M. & Jacobus A. Petterson. 1975. The Lense-Thirring Effect and Accretion Disks around Kerr Black Holes. ApJ 195. L65. https://doi.org/10.1086/181711.

Barnes, Joshua E. 1988. Encounters of Disk/Halo Galaxies. ApJ 331. 699. https://doi.org/10.1086/166593.

Barrows, R. Scott, Mar Mezcua & Julia M. Comerford. 2019. A Catalog of Hyper-luminous X-Ray Sources and Intermediate-mass Black Hole Candidates out to High Redshifts. ApJ 882(2), 181. 181. https://doi.org/10.3847/1538-4357/ab338a.

Beck, Rainer. 2015. Magnetic fields in spiral galaxies. A&A Rev. 24, 4. 4. https://doi.org/10.1007/s00159-015-0084-4.

Beckmann, R. S. et al. 2019. Dense gas formation and destruction in a simulated Perseus-like galaxy cluster with spin-driven black hole feedback. A&A 631, A60. A60. https://doi.org/10.1051/0004-6361/201936188.

Beckmann, Ricarda S. et al. 2022a. AGN jets do not prevent the suppression of conduction by the heat buoyancy instability in simulated galaxy clusters. *arXiv e-prints*, arXiv:2204.12514. arXiv:2204.12514.

Beckmann, Ricarda S. et al. 2022b. Cosmic rays and thermal instability in self-regulating cooling flows of massive galaxy clusters. A&A 665, A129. A129. https://doi.org/10.1051/0004-6361/202142527.

Beckmann, Volker & Chris R. Shrader. 2012. *Active Galactic Nuclei*.

Beckwith, Kris, John F. Hawley & Julian H. Krolik. 2008. The Influence of Magnetic Field Geometry on the Evolution of Black Hole Accretion Flows: Similar Disks, Drastically Different Jets. ApJ 678(2). 1180–1199. https://doi.org/10.1086/533492.

Begelman, M. C. 1978. Black holes in radiation-dominated gas: an analogue of the Bondi accretion problem. MNRAS 184. 53–67. https://doi.org/10.1093/mnras/184.1.53.

Begelman, M. C., R. D. Blandford & M. J. Rees. 1980. Massive black hole binaries in active galactic nuclei. Nature 287(5780). 307–309. https://doi.org/10.1038/287307a0.

Begelman, Mitchell C. 2004. AGN Feedback Mechanisms. In Luis C. Ho (ed.), *Coevolution of black holes and galaxies*, 374.

Begelman, Mitchell C. 2010. Evolution of supermassive stars as a pathway to black hole formation. MNRAS 402(1). 673–681. https://doi.org/10.1111/j.1365-2966.2009.15916.x.

Begelman, Mitchell C. & Denis F. Cioffi. 1989. Overpressured Cocoons in Extragalactic Radio Sources. ApJ 345. L21. https://doi.org/10.1086/185542.

Begelman, Mitchell C., Marta Volonteri & Martin J. Rees. 2006. Formation of supermassive black holes by direct collapse in pre-galactic haloes. MNRAS 370(1). 289–298. https://doi.org/10.1111/j.1365-2966.2006.10467.x.

Bell, Eric F. & Roelof S. de Jong. 2000. The stellar populations of spiral galaxies. MNRAS 312(3). 497–520. https://doi.org/10.1046/j.1365-8711.2000.03138.x.

Bell, Eric F. et al. 2003. The Optical and Near-Infrared Properties of Galaxies. I. Luminosity and Stellar Mass Functions. ApJS 149(2). 289–312. https://doi.org/10.1086/378847.

Bellovary, Jillian M. et al. 2019. Multimessenger signatures of massive black holes in dwarf galaxies. MNRAS 482(3). 2913–2923. https://doi.org/10.1093/mnras/sty2842.

Beloborodov, A. M. 1998. Super-Eddington accretion discs around Kerr black holes. MNRAS 297(3). 739–746. https://doi.org/10.1046/j.1365-8711.1998.01530.x.

Bennett, A. S. 1962. The revised 3C catalogue of radio sources. MmRAS 68. 163.

Benson, A. J. et al. 2003. What Shapes the Luminosity Function of Galaxies? ApJ 599(1). 38–49. https://doi.org/10.1086/379160.

Benson, Andrew J. 2010. Galaxy formation theory. Phys. Rep. 495(2-3). 33–86. https://doi.org/10.1016/j.physrep.2010.06.001.

Bentz, Misty C. et al. 2009. The Lick AGN Monitoring Project: Broad-line Region Radii and Black Hole Masses from Reverberation Mapping of Hβ. ApJ 705(1). 199–217. https://doi.org/10.1088/0004-637X/705/1/199.

Berger, E. et al. 2012. Radio Monitoring of the Tidal Disruption Event Swift J164449.3+573451. I. Jet Energetics and the Pristine Parsec-scale Environment of a Supermassive Black Hole. ApJ 748(1), 36. 36. https://doi.org/10.1088/0004-637X/748/1/36.

Berger, Marsha J. & Joseph Oliger. 1984. Adaptive Mesh Refinement for Hyperbolic Partial Differential Equations. *Journal of Computational Physics* 53(3). 484–512. https://doi.org/10.1016/0021-9991(84)90073-1.

Berghea, Ciprian T. et al. 2020. Detection of a Radio Bubble around the Ultraluminous X-Ray Source Holmberg IX X-1. ApJ 896(2), 117. 117. https://doi.org/10.3847/1538-4357/ab9108.

Bernardi, M. et al. 2010. Galaxy luminosities, stellar masses, sizes, velocity dispersions as a function of morphological type. MNRAS 404(4). 2087–2122. https://doi.org/10.1111/j.1365-2966.2010.16425.x.

Berti, Emanuele & Marta Volonteri. 2008. Cosmological Black Hole Spin Evolution by Mergers and Accretion. ApJ 684(2). 822–828. https://doi.org/10.1086/590379.

Bieri, Rebekka et al. 2015. Playing with Positive Feedback: External Pressure-triggering of a Star-forming Disk Galaxy. ApJ 812(2), L36. L36. https://doi.org/10.1088/2041-8205/812/2/L36.

Bieri, Rebekka et al. 2016. External pressure-triggering of star formation in a disc galaxy: a template for positive feedback. MNRAS 455(4). 4166–4182. https://doi.org/10.1093/mnras/stv2551.

Bieri, Rebekka et al. 2017. Outflows driven by quasars in high-redshift galaxies with radiation hydrodynamics. MNRAS 464(2). 1854–1873. https://doi.org/10.1093/mnras/stw2380.

Binney, James & Scott Tremaine. 2008. *Galactic Dynamics: Second Edition*.

Blandford, R. D. & C. F. McKee. 1982. Reverberation mapping of the emission line regions of Seyfert galaxies and quasars. ApJ 255. 419–439. https://doi.org/10.1086/159843.

Blandford, R. D. & D. G. Payne. 1982. Hydromagnetic flows from accretion disks and the production of radio jets. MNRAS 199. 883–903. https://doi.org/10.1093/mnras/199.4.883.

Blandford, R. D. & R. L. Znajek. 1977. Electromagnetic extraction of energy from Kerr black holes. MNRAS 179. 433–456. https://doi.org/10.1093/mnras/179.3.433.

Blandford, Roger, David Meier & Anthony Readhead. 2019. Relativistic Jets from Active Galactic Nuclei. ARA&A 57. 467–509. https://doi.org/10.1146/annurev-astro-081817-051948.

Blanton, Michael R. & John Moustakas. 2009. Physical Properties and Environments of Nearby Galaxies. ARA&A 47(1). 159–210. https://doi.org/10.1146/annurev-astro-082708-101734.

Blondin, John M. et al. 1998. Transition to the Radiative Phase in Supernova Remnants. ApJ 500(1). 342–354. https://doi.org/10.1086/305708.

Boller, T., W. N. Brandt & H. Fink. 1996. Soft X-ray properties of narrow-line Seyfert 1 galaxies. A&A 305. 53.

Bolton, C. T. 1972. Identification of Cygnus X-1 with HDE 226868. Nature 235(5336). 271–273. https://doi.org/10.1038/235271b0.

Bondi, H. 1952. On spherically symmetrical accretion. MNRAS 112. 195. https://doi.org/10.1093/mnras/112.2.195.

Bonetti, Matteo et al. 2018. Post-Newtonian evolution of massive black hole triplets in galactic nuclei - II. Survey of the parameter space. MNRAS 477(3). 3910–3926. https://doi.org/10.1093/mnras/sty896.

Booth, C. M. & Joop Schaye. 2009. Cosmological simulations of the growth of supermassive black holes and feedback from active galactic nuclei: method and tests. MNRAS 398(1). 53–74. https://doi.org/10.1111/j.1365-2966.2009.15043.x.

Boroson, Todd A. & Richard F. Green. 1992. The Emission-Line Properties of Low-Redshift Quasi-stellar Objects. ApJS 80. 109. https://doi.org/10.1086/191661.

Bosman, Sarah E. I. 2022. *All z>5.7 quasars currently known*. Version 1.15. The continuously updated webpage is hosted at: http://www.sarahbosman.co.uk/list_of_all_quasars. https://doi.org/10.5281/zenodo.6039724. https://doi.org/10.5281/zenodo.6039724.

Botella, Ignacio et al. 2022. Structure of the super-Eddington outflow and its impact on the cosmological scale. PASJ 74(2). 384–397. https://doi.org/10.1093/pasj/psac001.

Bournaud, F., C. J. Jog & F. Combes. 2005. Galaxy mergers with various mass ratios: Properties of remnants. A&A 437(1). 69–85. https://doi.org/10.1051/0004-6361:20042036.

Bournaud, Frédéric et al. 2011. Black Hole Growth and Active Galactic Nuclei Obscuration by Instability-driven Inflows in High-redshift Disk Galaxies Fed by Cold Streams. ApJ 741(2), L33. L33. https://doi.org/10.1088/2041-8205/741/2/L33.

Bovino, S. et al. 2016. The Formation of the Primitive Star SDSS J102915+172927: Effect of the Dust Mass and the Grain-size Distribution. ApJ 832(2), 154. 154. https://doi.org/10.3847/0004-637X/832/2/154.

Bower, R. G. et al. 2006. Breaking the hierarchy of galaxy formation. MNRAS 370(2). 645–655. https://doi.org/10.1111/j.1365-2966.2006.10519.x.

Bower, Richard G. et al. 2017. The dark nemesis of galaxy formation: why hot haloes trigger black hole growth and bring star formation to an end. MNRAS 465(1). 32–44. https://doi.org/10.1093/mnras/stw2735.

Breitschwerdt, D., J. F. McKenzie & H. J. Voelk. 1991. Galactic winds. I. Cosmic ray and wave-driven winds from the galaxy. A&A 245. 79.

Brennan, Ryan et al. 2018. Momentum-driven Winds from Radiatively Efficient Black Hole Accretion and Their Impact on Galaxies. ApJ 860(1), 14. 14. https://doi.org/10.3847/1538-4357/aac2c4.

Bromm, Volker. 2013. Formation of the first stars. *Reports on Progress in Physics* 76(11), 112901. 112901. https://doi.org/10.1088/0034-4885/76/11/112901.

Bromm, Volker & Abraham Loeb. 2003. Formation of the First Supermassive Black Holes. ApJ 596(1). 34–46. https://doi.org/10.1086/377529.

Brook, C. B. et al. 2012. Hierarchical formation of bulgeless galaxies - II. Redistribution of angular momentum via galactic fountains. MNRAS 419(1). 771–779. https://doi.org/10.1111/j.1365-2966.2011.19740.x.

Brook, C. B. et al. 2014. MaGICC baryon cycle: the enrichment history of simulated disc galaxies. MNRAS 443(4). 3809–3818. https://doi.org/10.1093/mnras/stu1406.

Brüggen, M., M. Ruszkowski & E. Hallman. 2005. Active Galactic Nuclei Heating and Dissipative Processes in Galaxy Clusters. ApJ 630(2). 740–749. https://doi.org/10.1086/432112.

Brummel-Smith, Corey et al. 2019. ENZO: An Adaptive Mesh Refinement Code for Astrophysics (Version 2.6). *The Journal of Open Source Software* 4(42), 1636. 1636. https://doi.org/10.21105/joss.01636.

Bullock, J. S. et al. 2001. Profiles of dark haloes: evolution, scatter and environment. MNRAS 321(3). 559–575. https://doi.org/10.1046/j.1365-8711.2001.04068.x.

Burkert, Andreas & Scott Tremaine. 2010. A Correlation Between Central Supermassive Black Holes and the Globular Cluster Systems of Early-type Galaxies. ApJ 720(1). 516–521. https://doi.org/10.1088/0004-637X/720/1/516.

Burrows, D. N. et al. 2011. Relativistic jet activity from the tidal disruption of a star by a massive black hole. Nature 476(7361). 421–424. https://doi.org/10.1038/nature10374.

Bustamante, Sebastian & Volker Springel. 2019. Spin evolution and feedback of supermassive black holes in cosmological simulations. MNRAS 490(3). 4133–4153. https://doi.org/10.1093/mnras/stz2836.

Buta, Ronald J. 2013. Galaxy Morphology. In Terry D. Oswalt & William C. Keel (eds.), *Planets, stars and stellar systems. volume 6: extragalactic astronomy and cosmology*, vol. 6, 1. https://doi.org/10.1007/978-94-007-5609-0_1.

Bykov, A. M. et al. 2018. Cosmic Ray Production in Supernovae. Space Sci. Rev. 214(1), 41. 41. https://doi.org/10.1007/s11214-018-0479-4.

Callegari, Simone et al. 2011. Growing Massive Black Hole Pairs in Minor Mergers of Disk Galaxies. ApJ 729(2), 85. 85. https://doi.org/10.1088/0004-637X/729/2/85.

Campanelli, Manuela et al. 2007. Maximum Gravitational Recoil. Phys. Rev. Lett. 98(23), 231102. 231102. https://doi.org/10.1103/PhysRevLett.98.231102.

Capelo, Pedro R. et al. 2015. Growth and activity of black holes in galaxy mergers with varying mass ratios. MNRAS 447(3). 2123–2143. https://doi.org/10.1093/mnras/stu2500.

Carnall, A. C. et al. 2015. Two bright z > 6 quasars from VST ATLAS and a new method of optical plus mid-infrared colour selection. MNRAS 451. L16–L20. https://doi.org/10.1093/mnrasl/slv057.

Carniani, S. et al. 2016. Fast outflows and star formation quenching in quasar host galaxies. A&A 591, A28. A28. https://doi.org/10.1051/0004-6361/201528037.

Cattaneo, A. & R. Teyssier. 2007. AGN self-regulation in cooling flow clusters. MNRAS 376(4). 1547–1556. https://doi.org/10.1111/j.1365-2966.2007.11512.x.

Cenci, Elia et al. 2021. Black hole spin evolution in warped accretion discs. MNRAS 500(3). 3719–3727. https://doi.org/10.1093/mnras/staa3449.

Cenko, S. Bradley et al. 2012. Swift J2058.4+0516: Discovery of a Possible Second Relativistic Tidal Disruption Flare? ApJ 753(1), 77. 77. https://doi.org/10.1088/0004-637X/753/1/77.

Ceverino, Daniel et al. 2015. Early formation of massive, compact, spheroidal galaxies with classical profiles by violent disc instability or mergers. MNRAS 447(4). 3291–3310. https://doi.org/10.1093/mnras/stu2694.

Chabanier, Solène et al. 2020. The impact of AGN feedback on the 1D power spectra from the Ly α forest using the Horizon-AGN suite of simulations. MNRAS 495(2). 1825–1840. https://doi.org/10.1093/mnras/staa1242.

Chabrier, Gilles. 2003. Galactic Stellar and Substellar Initial Mass Function. PASP 115(809). 763–795. https://doi.org/10.1086/376392.

Chambers, K. C. et al. 2016. The Pan-STARRS1 Surveys. *arXiv e-prints*, arXiv:1612.05560. arXiv:1612.05560.

Chandrasekhar, S. 1931. The Maximum Mass of Ideal White Dwarfs. ApJ 74. 81. https://doi.org/10.1086/143324.

Chandrasekhar, S. 1943. Dynamical Friction. I. General Considerations: the Coefficient of Dynamical Friction. ApJ 97. 255. https://doi.org/10.1086/144517.

Chartas, G. et al. 2009. X-Ray Microlensing in RXJ1131-1231 and HE1104-1805. ApJ 693(1). 174–185. https://doi.org/10.1088/0004-637X/693/1/174.

Chatterjee, K. et al. 2019. Accelerating AGN jets to parsec scales using general relativistic MHD simulations. MNRAS 490(2). 2200–2218. https://doi.org/10.1093/mnras/stz2626.

Chehade, B. et al. 2018. Two more, bright, z > 6 quasars from VST ATLAS and WISE. MNRAS 478(2). 1649–1659. https://doi.org/10.1093/mnras/sty690.

Cherepashchuk, Anatol. 2021. Progress in Understanding the Nature of SS433. *Universe* 8(1). 13. https://doi.org/10.3390/universe8010013.

Chevalier, Roger A. 1974. The Evolution of Supernova Remnants. Spherically Symmetric Models. ApJ 188. 501–516. https://doi.org/10.1086/152740.

Choi, Ena et al. 2018. The Role of Black Hole Feedback on Size and Structural Evolution in Massive Galaxies. ApJ 866(2), 91. 91. https://doi.org/10.3847/1538-4357/aae076.

Choi, Jun-Hwan & Kentaro Nagamine. 2009. Effects of metal enrichment and metal cooling in galaxy growth and cosmic star formation history. MNRAS 393(4). 1595–1607. https://doi.org/10.1111/j.1365-2966.2008.14297.x.

Chon, Sunmyon & Kazuyuki Omukai. 2020. Supermassive star formation via super competitive accretion in slightly metal-enriched clouds. MNRAS 494(2). 2851–2860. https://doi.org/10.1093/mnras/staa863.

Christensen, Charlotte R. et al. 2016. In-N-Out: The Gas Cycle from Dwarfs to Spiral Galaxies. ApJ 824(1), 57. 57. https://doi.org/10.3847/0004-637X/824/1/57.

Cioffi, Denis F., Christopher F. McKee & Edmund Bertschinger. 1988. Dynamics of Radiative Supernova Remnants. ApJ 334. 252. https://doi.org/10.1086/166834.

Ciotti, Luca & Jeremiah P. Ostriker. 1997. Cooling Flows and Quasars: Different Aspects of the Same Phenomenon? I. Concepts. ApJ 487(2). L105–L108. https://doi.org/10.1086/310902.

Ciotti, Luca & Jeremiah P. Ostriker. 2001. Cooling Flows and Quasars. II. Detailed Models of Feedback-modulated Accretion Flows. ApJ 551(1). 131–152. https://doi.org/10.1086/320053.

Ciotti, Luca & Jeremiah P. Ostriker. 2007. Radiative Feedback from Massive Black Holes in Elliptical Galaxies: AGN Flaring and Central Starburst Fueled by Recycled Gas. ApJ 665(2). 1038–1056. https://doi.org/10.1086/519833.

Ciotti, Luca et al. 1991. Winds, Outflows, and Inflows in X-Ray Elliptical Galaxies. I. ApJ 376. 380. https://doi.org/10.1086/170289.

Clark, Paul C. et al. 2011. The Formation and Fragmentation of Disks Around Primordial Protostars. *Science* 331(6020). 1040. https://doi.org/10.1126/science.1198027.

Colbert, Edward J. M. & Richard F. Mushotzky. 1999. The Nature of Accreting Black Holes in Nearby Galaxy Nuclei. ApJ 519(1). 89–107. https://doi.org/10.1086/307356.

Cole, Shaun et al. 2000. Hierarchical galaxy formation. MNRAS 319(1). 168–204. https://doi.org/10.1046/j.1365-8711.2000.03879.x.

Collin, S. & T. Kawaguchi. 2004. Super-Eddington accretion rates in Narrow Line Seyfert 1 galaxies. A&A 426. 797–808. https://doi.org/10.1051/0004-6361:20040528.

Conselice, Christopher J. 2014. The Evolution of Galaxy Structure Over Cosmic Time. ARA&A 52. 291–337. https://doi.org/10.1146/annurev-astro-081913-040037.

Coriat, M. et al. 2019. The twisted jets of Circinus X-1. MNRAS 484(2). 1672–1686. https://doi.org/10.1093/mnras/stz099.

Costa, Tiago, Debora Sijacki & Martin G. Haehnelt. 2014. Feedback from active galactic nuclei: energy- versus momentum-driving. MNRAS 444(3). 2355–2376. https://doi.org/10.1093/mnras/stu1632.

Crenshaw, D. Michael, Steven B. Kraemer & Ian M. George. 2003. Mass Loss from the Nuclei of Active Galaxies. ARA&A 41. 117–167. https://doi.org/10.1146/annurev.astro.41.082801.100328.

Croton, Darren J. et al. 2006. The many lives of active galactic nuclei: cooling flows, black holes and the luminosities and colours of galaxies. MNRAS 365(1). 11–28. https://doi.org/10.1111/j.1365-2966.2005.09675.x.

Croton, Darren J. et al. 2016. Semi-Analytic Galaxy Evolution (SAGE): Model Calibration and Basic Results. ApJS 222(2), 22. 22. https://doi.org/10.3847/0067-0049/222/2/22.

Das, Arpan et al. 2021. Formation of supermassive black hole seeds in nuclear star clusters via gas accretion and runaway collisions. MNRAS 503(1). 1051–1069. https://doi.org/10.1093/mnras/stab402.

Dashyan, Gohar & Yohan Dubois. 2020. Cosmic ray feedback from supernovae in dwarf galaxies. A&A 638, A123. A123. https://doi.org/10.1051/0004-6361/201936339.

Davé, Romeel et al. 2019. SIMBA: Cosmological simulations with black hole growth and feedback. MNRAS 486(2). 2827–2849. https://doi.org/10.1093/mnras/stz937.

Davidzon, I. et al. 2017. The COSMOS2015 galaxy stellar mass function . Thirteen billion years of stellar mass assembly in ten snapshots. A&A 605, A70. A70. https://doi.org/10.1051/0004-6361/201730419.

Davies, R. I., L. J. Tacconi & R. Genzel. 2004a. The Nuclear Gas Dynamics and Star Formation of Markarian 231. ApJ 613(2). 781–793. https://doi.org/10.1086/423315.

Davies, R. I., L. J. Tacconi & R. Genzel. 2004b. The Nuclear Gasdynamics and Star Formation of NGC 7469. ApJ 602(1). 148–161. https://doi.org/10.1086/380995.

Davies, R. I. et al. 2006. The Star-forming Torus and Stellar Dynamical Black Hole Mass in the Seyfert 1 Nucleus of NGC 3227. ApJ 646(2). 754–773. https://doi.org/10.1086/504963.

Dayal, Pratika et al. 2019. The hierarchical assembly of galaxies and black holes in the first billion years: predictions for the era of gravitational wave astronomy. MNRAS 486(2). 2336–2350. https://doi.org/10.1093/mnras/stz897.

De Villiers, Jean-Pierre et al. 2005. Magnetically Driven Accretion in the Kerr Metric. III. Unbound Outflows. ApJ 620(2). 878–888. https://doi.org/10.1086/427142.

De Young, David S. 1989. Star Formation in Radio Galaxies at Large Redshift. ApJ 342. L59. https://doi.org/10.1086/185484.

DeGraf, C. et al. 2017. Black hole growth and AGN feedback under clumpy accretion. MNRAS 466(2). 1462–1476. https://doi.org/10.1093/mnras/stw2777.

Dekel, A. & J. Silk. 1986. The Origin of Dwarf Galaxies, Cold Dark Matter, and Biased Galaxy Formation. ApJ 303. 39. https://doi.org/10.1086/164050.

Delgado-Serrano, R. et al. 2010. How was the Hubble sequence 6 Gyr ago? A&A 509, A78. A78. https://doi.org/10.1051/0004-6361/200912704.

den Brok, Mark et al. 2015. Measuring the Mass of the Central Black Hole in the Bulgeless Galaxy NGC 4395 from Gas Dynamical Modeling. ApJ 809(1), 101. 101. https://doi.org/10.1088/0004-637X/809/1/101.

Devecchi, B. & M. Volonteri. 2009. Formation of the First Nuclear Clusters and Massive Black Holes at High Redshift. ApJ 694(1). 302–313. https://doi.org/10.1088/0004-637X/694/1/302.

Di Matteo, T. et al. 2012. Cold Flows and the First Quasars. ApJ 745(2), L29. L29. https://doi.org/10.1088/2041-8205/745/2/L29.

Di Matteo, Tiziana et al. 2008. Direct Cosmological Simulations of the Growth of Black Holes and Galaxies. ApJ 676(1). 33–53. https://doi.org/10.1086/524921.

Di Matteo, Tiziana et al. 2017. The origin of the most massive black holes at high-z: BlueTides and the next quasar frontier. MNRAS 467(4). 4243–4251. https://doi.org/10.1093/mnras/stx319.

Dijkstra, Mark et al. 2008. Fluctuations in the high-redshift Lyman-Werner background: close halo pairs as the origin of supermassive black holes. MNRAS 391(4). 1961–1972. https://doi.org/10.1111/j.1365-2966.2008.14031.x.

Doeleman, Sheperd S. et al. 2012. Jet-Launching Structure Resolved Near the Supermassive Black Hole in M87. *Science* 338(6105). 355. https://doi.org/10.1126/science.1224768.

D'Onofrio, Mauro, Paola Marziani & Cesare Chiosi. 2021. Past, Present and Future of the Scaling Relations of Galaxies and Active Galactic Nuclei. *Frontiers in Astronomy and Space Sciences* 8, 157. 157. https://doi.org/10.3389/fspas.2021.694554.

Dopcke, Gustavo et al. 2011. The Effect of Dust Cooling on Low-metallicity Star-forming Clouds. ApJ 729(1), L3. L3. https://doi.org/10.1088/2041-8205/729/1/L3.

Dopcke, Gustavo et al. 2013. On the Initial Mass Function of Low-metallicity Stars: The Importance of Dust Cooling. ApJ 766(2), 103. 103. https://doi.org/10.1088/0004-637X/766/2/103.

Dotti, M. et al. 2007. Supermassive black hole binaries in gaseous and stellar circumnuclear discs: orbital dynamics and gas accretion. MNRAS 379(3). 956–962. https://doi.org/10.1111/j.1365-2966.2007.12010.x.

Dotti, M. et al. 2013. On the Orientation and Magnitude of the Black Hole Spin in Galactic Nuclei. ApJ 762(2), 68. 68. https://doi.org/10.1088/0004-637X/762/2/68.

Du, Pu et al. 2014. Supermassive Black Holes with High Accretion Rates in Active Galactic Nuclei. I. First Results from a New Reverberation Mapping Campaign. ApJ 782(1), 45. 45. https://doi.org/10.1088/0004-637X/782/1/45.

Du, Pu et al. 2018. Supermassive Black Holes with High Accretion Rates in Active Galactic Nuclei. IX. 10 New Observations of Reverberation Mapping and Shortened Hβ Lags. ApJ 856(1), 6. 6. https://doi.org/10.3847/1538-4357/aaae6b.

Dubois, Y. & R. Teyssier. 2008. On the onset of galactic winds in quiescent star forming galaxies. A&A 477(1). 79–94. https://doi.org/10.1051/0004-6361:20078326.

Dubois, Yohan, Marta Volonteri & Joseph Silk. 2014a. Black hole evolution - III. Statistical properties of mass growth and spin evolution using large-scale hydrodynamical cosmological simulations. MNRAS 440(2). 1590–1606. https://doi.org/10.1093/mnras/stu373.

Dubois, Yohan et al. 2010. Jet-regulated cooling catastrophe. MNRAS 409(3). 985–1001. https://doi.org/10.1111/j.1365-2966.2010.17338.x.

Dubois, Yohan et al. 2012a. Feeding compact bulges and supermassive black holes with low angular momentum cosmic gas at high redshift. MNRAS 423(4). 3616–3630. https://doi.org/10.1111/j.1365-2966.2012.21160.x.

Dubois, Yohan et al. 2012b. Self-regulated growth of supermassive black holes by a dual jet-heating active galactic nucleus feedback mechanism: methods, tests and implications for cosmological simulations. MNRAS 420(3). 2662–2683. https://doi.org/10.1111/j.1365-2966.2011.20236.x.

Dubois, Yohan et al. 2013. Blowing cold flows away: the impact of early AGN activity on the formation of a brightest cluster galaxy progenitor. MNRAS 428(4). 2885–2900. https://doi.org/10.1093/mnras/sts224.

Dubois, Yohan et al. 2014b. Black hole evolution - II. Spinning black holes in a supernova-driven turbulent interstellar medium. MNRAS 440(3). 2333–2346. https://doi.org/10.1093/mnras/stu425.

Dubois, Yohan et al. 2015. Black hole evolution - I. Supernova-regulated black hole growth. MNRAS 452(2). 1502–1518. https://doi.org/10.1093/mnras/stv1416.

Dubois, Yohan et al. 2021. Introducing the NEWHORIZON simulation: Galaxy properties with resolved internal dynamics across cosmic time. A&A 651, A109. A109. https://doi.org/10.1051/0004-6361/202039429.

Dunn, R. J. H., A. C. Fabian & G. B. Taylor. 2005. Radio bubbles in clusters of galaxies. MNRAS 364(4). 1343–1353. https://doi.org/10.1111/j.1365-2966.2005.09673.x.

Dutton, Aaron A. & Andrea V. Macciò. 2014. Cold dark matter haloes in the Planck era: evolution of structural parameters for Einasto and NFW profiles. MNRAS 441(4). 3359–3374. https://doi.org/10.1093/mnras/stu742.

Eckart, A. & R. Genzel. 1997. Stellar proper motions in the central 0.1 PC of the Galaxy. MNRAS 284(3). 576–598. https://doi.org/10.1093/mnras/284.3.576.

Eddington, A. S. 1921. Das Strahlungsgleichgewicht der Sterne. *Zeitschrift fur Physik* 7(1). 351–397. https://doi.org/10.1007/BF01332806.

Edge, A. et al. 2013. The VISTA Kilo-degree Infrared Galaxy (VIKING) Survey: Bridging the Gap between Low and High Redshift. *The Messenger* 154. 32–34.

Ehlert, K. et al. 2018. Simulations of the dynamics of magnetized jets and cosmic rays in galaxy clusters. MNRAS 481(3). 2878–2900. https://doi.org/10.1093/mnras/sty2397.

Einstein, A. 1916. Die Grundlage der allgemeinen Relativitätstheorie. *Annalen der Physik* 354(7). 769–822. https://doi.org/10.1002/andp.19163540702.

Event Horizon Telescope Collaboration et al. 2019. First M87 Event Horizon Telescope Results. IV. Imaging the Central Supermassive Black Hole. ApJ 875(1), L4. L4. https://doi.org/10.3847/2041-8213/ab0e85.

Event Horizon Telescope Collaboration et al. 2022. First Sagittarius A* Event Horizon Telescope Results. I. The Shadow of the Supermassive Black Hole in the Center of the Milky Way. ApJ 930(2), L12. L12. https://doi.org/10.3847/2041-8213/ac6674.

Faber, S. M. & R. E. Jackson. 1976. Velocity dispersions and mass-to-light ratios for elliptical galaxies. ApJ 204. 668–683. https://doi.org/10.1086/154215.

Fabian, A. C. 2012. Observational Evidence of Active Galactic Nuclei Feedback. ARA&A 50. 455–489. https://doi.org/10.1146/annurev-astro-081811-125521.

Fabian, A. C. et al. 2006. A very deep Chandra observation of the Perseus cluster: shocks, ripples and conduction. MNRAS 366(2). 417–428. https://doi.org/10.1111/j.1365-2966.2005.09896.x.

Fabrika, S. 2004. The jets and supercritical accretion disk in SS433. Astrophys. Space Phys. Res. 12. 1–152.

Falcke, H., E. Körding & S. Markoff. 2004. A scheme to unify low-power accreting black holes. Jet-dominated accretion flows and the radio/X-ray correlation. A&A 414. 895–903. https://doi.org/10.1051/0004-6361:20031683.

Fall, S. M. 1979. Dissipation, merging and the rotation of galaxies. Nature 281(5728). 200–202. https://doi.org/10.1038/281200a0.

Fan, Xiaohui et al. 2000. The Discovery of a Luminous Z=5.80 Quasar from the Sloan Digital Sky Survey. AJ 120(3). 1167–1174. https://doi.org/10.1086/301534.

Fan, Xiaohui et al. 2001. High-Redshift Quasars Found in Sloan Digital Sky Survey Commissioning Data. IV. Luminosity Function from the Fall Equatorial Stripe Sample. AJ 121(1). 54–65. https://doi.org/10.1086/318033.

Fan, Xiaohui et al. 2003. A Survey of z>5.7 Quasars in the Sloan Digital Sky Survey. II. Discovery of Three Additional Quasars at z>6. AJ 125(4). 1649–1659. https://doi.org/10.1086/368246.

Fan, Xiaohui et al. 2004. A Survey of z>5.7 Quasars in the Sloan Digital Sky Survey. III. Discovery of Five Additional Quasars. AJ 128(2). 515–522. https://doi.org/10.1086/422434.

Fan, Xiaohui et al. 2006. A Survey of z>5.7 Quasars in the Sloan Digital Sky Survey. IV. Discovery of Seven Additional Quasars. AJ 131(3). 1203–1209. https://doi.org/10.1086/500296.

Fanidakis, N. et al. 2011. Grand unification of AGN activity in the ΛCDM cosmology. MNRAS 410(1). 53–74. https://doi.org/10.1111/j.1365-2966.2010.17427.x.

Federrath, Christoph & Ralf S. Klessen. 2012. The Star Formation Rate of Turbulent Magnetized Clouds: Comparing Theory, Simulations, and Observations. ApJ 761(2), 156. 156. https://doi.org/10.1088/0004-637X/761/2/156.

Feldmann, R. et al. 2010. The Evolution of Central Group Galaxies in Hydrodynamical Simulations. ApJ 709(1). 218–240. https://doi.org/10.1088/0004-637X/709/1/218.

Ferreras, Ignacio et al. 2009. On the formation of massive galaxies: a simultaneous study of number density, size and intrinsic colour evolution in GOODS. MNRAS 396(3). 1573–1578. https://doi.org/10.1111/j.1365-2966.2009.14828.x.

Feruglio, C. et al. 2010. Quasar feedback revealed by giant molecular outflows. A&A 518, L155. L155. https://doi.org/10.1051/0004-6361/201015164.

Fiore, F. et al. 2017. AGN wind scaling relations and the co-evolution of black holes and galaxies. A&A 601, A143. A143. https://doi.org/10.1051/0004-6361/201629478.

Forman, W. et al. 2007. Filaments, Bubbles, and Weak Shocks in the Gaseous Atmosphere of M87. ApJ 665(2). 1057–1066. https://doi.org/10.1086/519480.

Fraley, Gary S. 1968. Supernovae Explosions Induced by Pair-Production Instability. Ap&SS 2(1). 96–114. https://doi.org/10.1007/BF00651498.

Friedmann, A. 1922. Über die Krümmung des Raumes. *Zeitschrift fur Physik* 10. 377–386. https://doi.org/10.1007/BF01332580.

Fryxell, B. et al. 2000. FLASH: An Adaptive Mesh Hydrodynamics Code for Modeling Astrophysical Thermonuclear Flashes. ApJS 131(1). 273–334. https://doi.org/10.1086/317361.

Fuchs, Y., L. Koch Miramond & P. Ábrahám. 2006. SS 433: a phenomenon imitating a Wolf-Rayet star. A&A 445(3). 1041–1052. https://doi.org/10.1051/0004-6361:20042160.

Gabor, J. M. & Frédéric Bournaud. 2014. Active galactic nuclei-driven outflows without immediate quenching in simulations of high-redshift disc galaxies. MNRAS 441(2). 1615–1627. https://doi.org/10.1093/mnras/stu677.

Gaibler, V. et al. 2012. Jet-induced star formation in gas-rich galaxies. MNRAS 425(1). 438–449. https://doi.org/10.1111/j.1365-2966.2012.21479.x.

Galametz, Audrey et al. 2009. The Cosmic Evolution of Active Galactic Nuclei in Galaxy Clusters. ApJ 694(2). 1309–1316. https://doi.org/10.1088/0004-637X/694/2/1309.

Galilei, Galileo. 1610. *Sidereus nuncius magna, longeque admirabilia spectacula pandens lunae facie, fixis innumeris, lacteo circulo, stellis nebulosis, ... Galileo Galileo : nuper a se reperti beneficio sunt observata in apprime vero in quatuor planetis circa Iovis stellam disparibus intervallis, atque periodis, celeritate mirabili circumvolutis ... atque Medicea sidera nuncupandos decrevit*. https://doi.org/10.3931/e-rara-695.

Gammie, Charles F., Stuart L. Shapiro & Jonathan C. McKinney. 2004. Black Hole Spin Evolution. ApJ 602(1). 312–319. https://doi.org/10.1086/380996.

Gaspari, M., M. Ruszkowski & S. Peng Oh. 2013. Chaotic cold accretion on to black holes. MNRAS 432(4). 3401–3422. https://doi.org/10.1093/mnras/stt692.

Gaspari, M. et al. 2011. The dance of heating and cooling in galaxy clusters: three-dimensional simulations of self-regulated active galactic nuclei outflows. MNRAS 411(1). 349–372. https://doi.org/10.1111/j.1365-2966.2010.17688.x.

Gebhardt, Karl et al. 2000. A Relationship between Nuclear Black Hole Mass and Galaxy Velocity Dispersion. ApJ 539(1). L13–L16. https://doi.org/10.1086/312840.

Gebhardt, Karl et al. 2003. Axisymmetric Dynamical Models of the Central Regions of Galaxies. ApJ 583(1). 92–115. https://doi.org/10.1086/345081.

Gebhardt, Karl et al. 2011. The Black Hole Mass in M87 from Gemini/NIFS Adaptive Optics Observations. ApJ 729(2), 119. 119. https://doi.org/10.1088/0004-637X/729/2/119.

Ghez, A. M. et al. 2003. The First Measurement of Spectral Lines in a Short-Period Star Bound to the Galaxy's Central Black Hole: A Paradox of Youth. ApJ 586(2). L127–L131. https://doi.org/10.1086/374804.

Ghez, A. M. et al. 2005. Stellar Orbits around the Galactic Center Black Hole. ApJ 620(2). 744–757. https://doi.org/10.1086/427175.

Giannios, Dimitrios & Brian D. Metzger. 2011. Radio transients from stellar tidal disruption by massive black holes. MNRAS 416(3). 2102–2107. https://doi.org/10.1111/j.1365-2966.2011.19188.x.

Giersz, Mirek et al. 2015. MOCCA code for star cluster simulations - IV. A new scenario for intermediate mass black hole formation in globular clusters. MNRAS 454(3). 3150–3165. https://doi.org/10.1093/mnras/stv2162.

Girichidis, Philipp et al. 2018. Cooler and smoother - the impact of cosmic rays on the phase structure of galactic outflows. MNRAS 479(3). 3042–3067. https://doi.org/10.1093/mnras/sty1653.

Godunov, S. K. 1962. the Problem of a Generalized Solution in the Theory of Quasilinear Equations and in Gas Dynamics. *Russian Mathematical Surveys* 17(3). 145–156. https://doi.org/10.1070/RM1962v017n03ABEH004116.

Goicovic, Felipe G. et al. 2017. Infalling clouds on to supermassive black hole binaries - II. Binary evolution and the final parsec problem. MNRAS 472(1). 514–531. https://doi.org/10.1093/mnras/stx1996.

Goranskij, V. 2011. Photometric Mass Estimate for the Compact Component of SS 433: And Yet It Is a Neutron Star. *Peremennye Zvezdy* 31(5). 5.

GRAVITY Collaboration et al. 2018. Detection of the gravitational redshift in the orbit of the star S2 near the Galactic centre massive black hole. A&A 615, L15. L15. https://doi.org/10.1051/0004-6361/201833718.

GRAVITY Collaboration et al. 2020. Detection of the Schwarzschild precession in the orbit of the star S2 near the Galactic centre massive black hole. A&A 636, L5. L5. https://doi.org/10.1051/0004-6361/202037813.

Greif, Thomas H. et al. 2011. Simulations on a Moving Mesh: The Clustered Formation of Population III Protostars. ApJ 737(2), 75. 75. https://doi.org/10.1088/0004-637X/737/2/75.

Greif, Thomas H. et al. 2012. Formation and evolution of primordial protostellar systems. MNRAS 424(1). 399–415. https://doi.org/10.1111/j.1365-2966.2012.21212.x.

Grisé, F. et al. 2012. Optical Emission of the Ultraluminous X-Ray Source NGC 5408 X-1: Donor Star or Irradiated Accretion Disk? ApJ 745(2), 123. 123. https://doi.org/10.1088/0004-637X/745/2/123.

Guillet, Thomas & Romain Teyssier. 2011. A simple multigrid scheme for solving the Poisson equation with arbitrary domain boundaries. *Journal of Computational Physics* 230(12). 4756–4771. https://doi.org/10.1016/j.jcp.2011.02.044.

Guillochon, James & Enrico Ramirez-Ruiz. 2015. A Dark Year for Tidal Disruption Events. ApJ 809(2), 166. 166. https://doi.org/10.1088/0004-637X/809/2/166.

Gunn, James E. & III Gott J. Richard. 1972. On the Infall of Matter Into Clusters of Galaxies and Some Effects on Their Evolution. ApJ 176. 1. https://doi.org/10.1086/151605.

Guo, Fulai & William G. Mathews. 2010. Simulating X-ray Supercavities and Their Impact on Galaxy Clusters. ApJ 712(2). 1311–1320. https://doi.org/10.1088/0004-637X/712/2/1311.

Gúrpide, A. et al. 2021. Long-term X-ray spectral evolution of ultraluminous X-ray sources: implications on the accretion flow geometry and the nature of the accretor. A&A 649, A104. A104. https://doi.org/10.1051/0004-6361/202039572.

Guth, Alan H. 1981. Inflationary universe: A possible solution to the horizon and flatness problems. Phys. Rev. D 23(2). 347–356. https://doi.org/10.1103/PhysRevD.23.347.

Haardt, Francesco & Piero Madau. 1996. Radiative Transfer in a Clumpy Universe. II. The Ultraviolet Extragalactic Background. ApJ 461. 20. https://doi.org/10.1086/177035.

Habouzit, Mélanie, Marta Volonteri & Yohan Dubois. 2017. Blossoms from black hole seeds: properties and early growth regulated by supernova feedback. MNRAS 468(4). 3935–3948. https://doi.org/10.1093/mnras/stx666.

Habouzit, Mélanie et al. 2016. On the number density of 'direct collapse' black hole seeds. MNRAS 463(1). 529–540. https://doi.org/10.1093/mnras/stw1924.

Haehnelt, Martin G., Priyamvada Natarajan & Martin J. Rees. 1998. High-redshift galaxies, their active nuclei and central black holes. MNRAS 300(3). 817–827. https://doi.org/10.1046/j.1365-8711.1998.01951.x.

Haiman, Zoltán. 2004. Constraints from Gravitational Recoil on the Growth of Supermassive Black Holes at High Redshift. ApJ 613(1). 36–40. https://doi.org/10.1086/422910.

Haiman, Zoltán. 2013. The Formation of the First Massive Black Holes. In Tommy Wiklind, Bahram Mobasher & Volker Bromm (eds.), *The first galaxies*, vol. 396 (Astrophysics and Space Science Library), 293. https://doi.org/10.1007/978-3-642-32362-1_6.

Haiman, Zoltán, Tom Abel & Martin J. Rees. 2000. The Radiative Feedback of the First Cosmological Objects. ApJ 534(1). 11–24. https://doi.org/10.1086/308723.

Haiman, Zoltán & Abraham Loeb. 2001. What Is the Highest Plausible Redshift of Luminous Quasars? ApJ 552(2). 459–463. https://doi.org/10.1086/320586.

Haiman, Zoltan, Anne A. Thoul & Abraham Loeb. 1996. Cosmological Formation of Low-Mass Objects. ApJ 464. 523. https://doi.org/10.1086/177343.

Hammer, F. et al. 2005. Did most present-day spirals form during the last 8 Gyr?. A formation history with violent episodes revealed by panchromatic observations. A&A 430. 115–128. https://doi.org/10.1051/0004-6361:20041471.

Han, Qin & Xiang-Dong Li. 2020. On the Formation of SS433. ApJ 896(1), 34. 34. https://doi.org/10.3847/1538-4357/ab8d3d.

Harris, Gretchen L. H. & William E. Harris. 2011. The globular cluster/central black hole connection in galaxies. MNRAS 410(4). 2347–2352. https://doi.org/10.1111/j.1365-2966.2010.17606.x.

Heckman, Timothy M. & Philip N. Best. 2014. The Coevolution of Galaxies and Supermassive Black Holes: Insights from Surveys of the Contemporary Universe. ARA&A 52. 589–660. https://doi.org/10.1146/annurev-astro-081913-035722.

Heckman, Timothy M. & Todd A. Thompson. 2017. Galactic Winds and the Role Played by Massive Stars. *arXiv e-prints*, arXiv:1701.09062. arXiv:1701.09062.

Heinz, S. et al. 2006. The answer is blowing in the wind: simulating the interaction of jets with dynamic cluster atmospheres. MNRAS 373(1). L65–L69. https://doi.org/10.1111/j.1745-3933.2006.00243.x.

Hennebelle, Patrick & Gilles Chabrier. 2011. Analytical Star Formation Rate from Gravoturbulent Fragmentation. ApJ 743(2), L29. L29. https://doi.org/10.1088/2041-8205/743/2/L29.

Hernquist, Lars. 1992. Structure of Merger Remnants. I. Bulgeless Progenitors. ApJ 400. 460. https://doi.org/10.1086/172009.

Herrmann, Frank et al. 2007. Gravitational Recoil from Spinning Binary Black Hole Mergers. ApJ 661(1). 430–436. https://doi.org/10.1086/513603.

Herschel, John Frederick William. 1864. A General Catalogue of Nebulae and Clusters of Stars. *Philosophical Transactions of the Royal Society of London Series I* 154. 1–137.

Hicks, Erin K. S. & Matthew A. Malkan. 2008. Circumnuclear Gas in Seyfert 1 Galaxies: Morphology, Kinematics, and Direct Measurement of Black Hole Masses. ApJS 174(1). 31–73. https://doi.org/10.1086/521650.

Hills, J. G. 1975. Possible power source of Seyfert galaxies and QSOs. Nature 254(5498). 295–298. https://doi.org/10.1038/254295a0.

Hirano, S. et al. 2015. Primordial star formation under the influence of far ultraviolet radiation: 1540 cosmological haloes and the stellar mass distribution. MNRAS 448(1). 568–587. https://doi.org/10.1093/mnras/stv044.

Hirano, Shingo et al. 2014. One Hundred First Stars: Protostellar Evolution and the Final Masses. ApJ 781(2), 60. 60. https://doi.org/10.1088/0004-637X/781/2/60.

Hirschmann, Michaela, Gabriella De Lucia & Fabio Fontanot. 2016. Galaxy assembly, stellar feedback and metal enrichment: the view from the GAEA model. MNRAS 461(2). 1760–1785. https://doi.org/10.1093/mnras/stw1318.

Hirschmann, Michaela et al. 2012. Galaxy formation in semi-analytic models and cosmological hydrodynamic zoom simulations. MNRAS 419(4). 3200–3222. https://doi.org/10.1111/j.1365-2966.2011.19961.x.

Hirschmann, Michaela et al. 2013. The effect of metal enrichment and galactic winds on galaxy formation in cosmological zoom simulations. MNRAS 436(4). 2929–2949. https://doi.org/10.1093/mnras/stt1770.

Hirschmann, Michaela et al. 2014a. Cosmological simulations of black hole growth: AGN luminosities and downsizing. MNRAS 442(3). 2304–2324. https://doi.org/10.1093/mnras/stu1023.

Hirschmann, Michaela et al. 2014b. The influence of the environmental history on quenching star formation in a Λ cold dark matter universe. MNRAS 444(3). 2938–2959. https://doi.org/10.1093/mnras/stu1609.

Hopkins, Philip F. & Eliot Quataert. 2010. How do massive black holes get their gas? MNRAS 407(3). 1529–1564. https://doi.org/10.1111/j.1365-2966.2010.17064.x.

Hopkins, Philip F. et al. 2010. Discriminating between the physical processes that drive spheroid size evolution. MNRAS 401(2). 1099–1117. https://doi.org/10.1111/j.1365-2966.2009.15699.x.

Hopkins, Philip F. et al. 2014. Galaxies on FIRE (Feedback In Realistic Environments): stellar feedback explains cosmologically inefficient star formation. MNRAS 445(1). 581–603. https://doi.org/10.1093/mnras/stu1738.

Hopkins, Philip F. et al. 2022. Why do black holes trace bulges (& central surface densities), instead of galaxies as a whole? MNRAS 510(1). 630–638. https://doi.org/10.1093/mnras/stab3458.

Hosokawa, Takashi et al. 2011. Protostellar Feedback Halts the Growth of the First Stars in the Universe. *Science* 334(6060). 1250. https://doi.org/10.1126/science.1207433.

Hoyle, F. & R. A. Lyttleton. 1939. The effect of interstellar matter on climatic variation. *Proceedings of the Cambridge Philosophical Society* 35(3). 405. https://doi.org/10.1017/S0305004100021150.

Hu, Chen et al. 2008. A Systematic Analysis of Fe II Emission in Quasars: Evidence for Inflow to the Central Black Hole. ApJ 687(1). 78–96. https://doi.org/10.1086/591838.

Hu, Haojie et al. 2022a. Long-term Evolution of Supercritical Black Hole Accretion with Outflows: A Subgrid Feedback Model for Cosmological Simulations. ApJ 934(2), 132. 132. https://doi.org/10.3847/1538-4357/ac75d8.

Hu, Haojie et al. 2022b. Supercritical Growth Pathway to Overmassive Black Holes at Cosmic Dawn: Coevolution with Massive Quasar Hosts. ApJ 935(2), 140. 140. https://doi.org/10.3847/1538-4357/ac7daa.

Hubble, E. P. 1925. NGC 6822, a remote stellar system. ApJ 62. 409–433. https://doi.org/10.1086/142943.

Hubble, E. P. 1926. Extragalactic nebulae. ApJ 64. 321–369. https://doi.org/10.1086/143018.

Hubble, Edwin. 1929. A Relation between Distance and Radial Velocity among Extra-Galactic Nebulae. *Proceedings of the National Academy of Science* 15(3). 168–173. https://doi.org/10.1073/pnas.15.3.168.

Huško, Filip et al. 2022. Spin-driven jet feedback in idealised simulations of galaxy groups and clusters. *arXiv e-prints*, arXiv:2206.06402. arXiv:2206.06402.

Igumenshchev, Igor V., Ramesh Narayan & Marek A. Abramowicz. 2003. Three-dimensional Magnetohydrodynamic Simulations of Radiatively Inefficient Accretion Flows. ApJ 592(2). 1042–1059. https://doi.org/10.1086/375769.

Ilbert, O. et al. 2010. Galaxy Stellar Mass Assembly Between $0.2 < z < 2$ from the S-COSMOS Survey. ApJ 709(2). 644–663. https://doi.org/10.1088/0004-637X/709/2/644.

Ilbert, O. et al. 2013. Mass assembly in quiescent and star-forming galaxies since $z \simeq 4$ from UltraVISTA. A&A 556, A55. A55. https://doi.org/10.1051/0004-6361/201321100.

Imanishi, Masatoshi et al. 2011. Infrared 3-4μm Spectroscopy of Nearby PG QSOs and AGN-Nuclear Starburst Connections in High-luminosity AGN Populations. PASJ 63. 447. https://doi.org/10.1093/pasj/63.sp2.S447.

Inayoshi, K., K. Omukai & E. Tasker. 2014. Formation of an embryonic supermassive star in the first galaxy. MNRAS 445. L109–L113. https://doi.org/10.1093/mnrasl/slu151.

Inayoshi, Kohei & Zoltán Haiman. 2014. Does disc fragmentation prevent the formation of supermassive stars in protogalaxies? MNRAS 445(2). 1549–1557. https://doi.org/10.1093/mnras/stu1870.

Inayoshi, Kohei, Zoltán Haiman & Jeremiah P. Ostriker. 2016. Hyper-Eddington accretion flows on to massive black holes. MNRAS 459(4). 3738–3755. https://doi.org/10.1093/mnras/stw836.

Inayoshi, Kohei, Eli Visbal & Zoltán Haiman. 2020. The Assembly of the First Massive Black Holes. ARA&A 58. 27–97. https://doi.org/10.1146/annurev-astro-120419-014455.

Inayoshi, Kohei et al. 2018. Low-density, radiatively inefficient rotating-accretion flow on to a black hole. MNRAS 476(1). 1412–1426. https://doi.org/10.1093/mnras/sty276.

Inayoshi, Kohei et al. 2022a. Rapid Growth of Seed Black Holes during Early Bulge Formation. ApJ 927(2), 237. 237. https://doi.org/10.3847/1538-4357/ac4751.

Inayoshi, Kohei et al. 2022b. The Age of Discovery with the James Webb Space Telescope: Excavating the Spectral Signatures of the First Massive Black Holes. ApJ 931(2), L25. L25. https://doi.org/10.3847/2041-8213/ac6f01.

Irwin, M. J. et al. 1989. Photometric Variations in the Q2237+0305 System: First Detection of a Microlensing Event. AJ 98. 1989. https://doi.org/10.1086/115272.

Ishibashi, W. & A. C. Fabian. 2012. Active galactic nucleus feedback and triggering of star formation in galaxies. MNRAS 427(4). 2998–3005. https://doi.org/10.1111/j.1365-2966.2012.22074.x.

Israel, G. L. et al. 2017a. Discovery of a 0.42-s pulsar in the ultraluminous X-ray source NGC 7793 P13. MNRAS 466(1). L48–L52. https://doi.org/10.1093/mnrasl/slw218.

Israel, Gian Luca et al. 2017b. An accreting pulsar with extreme properties drives an ultraluminous x-ray source in NGC 5907. *Science* 355(6327). 817–819. https://doi.org/10.1126/science.aai8635.

Jansson, Ronnie & Glennys R. Farrar. 2012. A New Model of the Galactic Magnetic Field. ApJ 757(1), 14. 14. https://doi.org/10.1088/0004-637X/757/1/14.

Jeans, James Hopwood. 1928. *Astronomy and cosmogony*.

Jeon, Myoungwon et al. 2012. The First Galaxies: Assembly with Black Hole Feedback. ApJ 754(1), 34. 34. https://doi.org/10.1088/0004-637X/754/1/34.

Jiang, Linhua et al. 2007. Gemini Near-Infrared Spectroscopy of Luminous z ∼6 Quasars: Chemical Abundances, Black Hole Masses, and Mg II Absorption. AJ 134(3). 1150. https://doi.org/10.1086/520811.

Jiang, Yan-Fei, James M. Stone & Shane W. Davis. 2014. A Global Three-dimensional Radiation Magneto-hydrodynamic Simulation of Super-Eddington Accretion Disks. ApJ 796(2), 106. 106. https://doi.org/10.1088/0004-637X/796/2/106.

Jiang, Yan-Fei, James M. Stone & Shane W. Davis. 2019. Super-Eddington Accretion Disks around Supermassive Black Holes. ApJ 880(2), 67. 67. https://doi.org/10.3847/1538-4357/ab29ff.

Jin, Chichuan et al. 2017. Super-Eddington QSO RX J0439.6-5311 - II. Multiwavelength constraints on the global structure of the accretion flow. MNRAS 471(1). 706–721. https://doi.org/10.1093/mnras/stx1634.

Johnson, Jarrett L. & Volker Bromm. 2007. The aftermath of the first stars: massive black holes. MNRAS 374(4). 1557–1568. https://doi.org/10.1111/j.1365-2966.2006.11275.x.

Johnson, Jarrett L. et al. 2011. Accretion on to black holes formed by direct collapse. MNRAS 410(2). 919–933. https://doi.org/10.1111/j.1365-2966.2010.17491.x.

Kaaret, Philip, Hua Feng & Timothy P. Roberts. 2017. Ultraluminous X-Ray Sources. ARA&A 55(1). 303–341. https://doi.org/10.1146/annurev-astro-091916-055259.

Kant, Immanuel. 1755. *Allgemeine Naturgeschichte und Theorie des Himmels*.

Kashikawa, Nobunari et al. 2015. The Subaru High-z Quasar Survey: Discovery of Faint z ∼6 Quasars. ApJ 798(1), 28. 28. https://doi.org/10.1088/0004-637X/798/1/28.

Kashlinsky, A. & M. J. Rees. 1983. Formation of Population III stars and pregalactic evolution. MNRAS 205. 955–971. https://doi.org/10.1093/mnras/205.4.955.

Kaspi, Shai et al. 2000. Reverberation Measurements for 17 Quasars and the Size-Mass-Luminosity Relations in Active Galactic Nuclei. ApJ 533(2). 631–649. https://doi.org/10.1086/308704.

Kato, S., J. Fukue & S. Mineshige. 2008. *Black-Hole Accretion Disks — Towards a New Paradigm —*.

Katz, Harley, Debora Sijacki & Martin G. Haehnelt. 2015. Seeding high-redshift QSOs by collisional runaway in primordial star clusters. MNRAS 451(3). 2352–2369. https://doi.org/10.1093/mnras/stv1048.

Katz, J. I. 1977. X-rays from spherical accretion onto degenerate dwarfs. ApJ 215. 265–275. https://doi.org/10.1086/155355.

Kauffmann, Guinevere et al. 2003. The dependence of star formation history and internal structure on stellar mass for 10^5 low-redshift galaxies. MNRAS 341(1). 54–69. https://doi.org/10.1046/j.1365-8711.2003.06292.x.

Kaviraj, S. et al. 2009. Identifying the progenitor set of present-day early-type galaxies: a view from the standard model. A&A 503(2). 445–458. https://doi.org/10.1051/0004-6361/200810483.

Kawaguchi, Toshihiro. 2003. Comptonization in Super-Eddington Accretion Flow and Growth Timescale of Supermassive Black Holes. ApJ 593(1). 69–84. https://doi.org/10.1086/376404.

Kennicutt, Jr., Robert C. 1998. The Global Schmidt Law in Star-forming Galaxies. ApJ 498(2). 541–552. https://doi.org/10.1086/305588.

Kerr, Roy P. 1963. Gravitational Field of a Spinning Mass as an Example of Algebraically Special Metrics. Phys. Rev. Lett. 11(5). 237–238. https://doi.org/10.1103/PhysRevLett.11.237.

Khan, Fazeel Mahmood et al. 2012. Formation and Hardening of Supermassive Black Hole Binaries in Minor Mergers of Disk Galaxies. ApJ 756(1), 30. 30. https://doi.org/10.1088/0004-637X/756/1/30.

Khandai, Nishikanta et al. 2012. The formation of galaxies hosting z ∼ 6 quasars. MNRAS 423(3). 2397–2406. https://doi.org/10.1111/j.1365-2966.2012.21047.x.

Khochfar, S. & J. Silk. 2009. Dry mergers: a crucial test for galaxy formation. MNRAS 397(1). 506–510. https://doi.org/10.1111/j.1365-2966.2009.14958.x.

Khochfar, Sadegh & Joseph Silk. 2006. A Simple Model for the Size Evolution of Elliptical Galaxies. ApJ 648(1). L21–L24. https://doi.org/10.1086/507768.

Kimm, Taysun & Renyue Cen. 2014. Escape Fraction of Ionizing Photons during Reionization: Effects due to Supernova Feedback and Runaway OB Stars. ApJ 788(2), 121. 121. https://doi.org/10.1088/0004-637X/788/2/121.

Kimm, Taysun et al. 2015. Towards simulating star formation in turbulent high-z galaxies with mechanical supernova feedback. MNRAS 451(3). 2900–2921. https://doi.org/10.1093/mnras/stv1211.

Kimm, Taysun et al. 2017. Feedback-regulated star formation and escape of LyC photons from mini-haloes during reionization. MNRAS 466(4). 4826–4846. https://doi.org/10.1093/mnras/stx052.

King, A. R. 2002. The brightest black holes. MNRAS 335(1). L13–L16. https://doi.org/10.1046/j.1365-8711.2002.05745.x.

King, A. R. & J. E. Pringle. 2006. Growing supermassive black holes by chaotic accretion. MNRAS 373(1). L90–L92. https://doi.org/10.1111/j.1745-3933.2006.00249.x.

King, A. R., J. E. Pringle & J. A. Hofmann. 2008. The evolution of black hole mass and spin in active galactic nuclei. MNRAS 385(3). 1621–1627. https://doi.org/10.1111/j.1365-2966.2008.12943.x.

King, A. R. et al. 2001. Ultraluminous X-Ray Sources in External Galaxies. ApJ 552(2). L109–L112. https://doi.org/10.1086/320343.

King, A. R. et al. 2005. Aligning spinning black holes and accretion discs. MNRAS 363(1). 49–56. https://doi.org/10.1111/j.1365-2966.2005.09378.x.

King, Andrew. 2003. Black Holes, Galaxy Formation, and the M_{BH}-σ Relation. ApJ 596(1). L27–L29. https://doi.org/10.1086/379143.

King, Andrew & Ken Pounds. 2015. Powerful Outflows and Feedback from Active Galactic Nuclei. ARA&A 53. 115–154. https://doi.org/10.1146/annurev-astro-082214-122316.

Kitaki, Takaaki et al. 2021a. Outflow from super-Eddington flow: where it originates from and how much impact it gives? *arXiv e-prints*, arXiv:2101.11028. arXiv:2101.11028.

Kitaki, Takaaki et al. 2021b. The origins and impact of outflow from super-Eddington flow. PASJ 73(2). 450–466. https://doi.org/10.1093/pasj/psab011.

Klessen, Ralf S., Simon C. O. Glover & Paul C. Clark. 2012. On the formation of very metal poor stars: the case of SDSS J1029151+172927. MNRAS 421(4). 3217–3221. https://doi.org/10.1111/j.1365-2966.2012.20544.x.

Komissarov, Serguei S. et al. 2007. Magnetic acceleration of relativistic active galactic nucleus jets. MNRAS 380(1). 51–70. https://doi.org/10.1111/j.1365-2966.2007.12050.x.

Komossa, S. 2008. Narrow-line Seyfert 1 Galaxies. In *Revista mexicana de astronomia y astrofisica conference series*, vol. 32 (Revista Mexicana de Astronomia y Astrofisica Conference Series), 86–92.

Kormendy, John & Luis C. Ho. 2013. Coevolution (Or Not) of Supermassive Black Holes and Host Galaxies. ARA&A 51(1). 511–653. https://doi.org/10.1146/annurev-astro-082708-101811.

Kormendy, John & Douglas Richstone. 1995. Inward Bound—The Search For Supermassive Black Holes In Galactic Nuclei. ARA&A 33. 581. https://doi.org/10.1146/annurev.aa.33.090195.003053.

Kroupa, Pavel. 2001. On the variation of the initial mass function. MNRAS 322(2). 231–246. https://doi.org/10.1046/j.1365-8711.2001.04022.x.

Krumholz, Mark R. & Christopher F. McKee. 2005. A General Theory of Turbulence-regulated Star Formation, from Spirals to Ultraluminous Infrared Galaxies. ApJ 630(1). 250–268. https://doi.org/10.1086/431734.

Krumholz, Mark R., Christopher F. McKee & Richard I. Klein. 2004. Embedding Lagrangian Sink Particles in Eulerian Grids. ApJ 611(1). 399–412. https://doi.org/10.1086/421935.

Kuo, C. Y. et al. 2011. The Megamaser Cosmology Project. III. Accurate Masses of Seven Supermassive Black Holes in Active Galaxies with Circumnuclear Megamaser Disks. ApJ 727(1), 20. 20. https://doi.org/10.1088/0004-637X/727/1/20.

Kurk, Jaron D. et al. 2007. Black Hole Masses and Enrichment of z ∼6 SDSS Quasars. ApJ 669(1). 32–44. https://doi.org/10.1086/521596.

Lapiner, Sharon, Avishai Dekel & Yohan Dubois. 2021. Compaction-driven black hole growth. MNRAS 505(1). 172–190. https://doi.org/10.1093/mnras/stab1205.

Latif, M. A., D. R. G. Schleicher & T. Hartwig. 2016a. Witnessing the birth of a supermassive protostar. MNRAS 458(1). 233–241. https://doi.org/10.1093/mnras/stw297.

Latif, M. A. et al. 2013. Black hole formation in the early Universe. MNRAS 433(2). 1607–1618. https://doi.org/10.1093/mnras/stt834.

Latif, M. A. et al. 2014. A UV flux constraint on the formation of direct collapse black holes. MNRAS 443(3). 1979–1987. https://doi.org/10.1093/mnras/stu1230.

Latif, M. A. et al. 2016b. Impact of Dust Cooling on Direct-collapse Black Hole Formation. ApJ 823(1), 40. 40. https://doi.org/10.3847/0004-637X/823/1/40.

Latif, M. A. et al. 2022. Turbulent cold flows gave birth to the first quasars. Nature 607(7917). 48–51. https://doi.org/10.1038/s41586-022-04813-y.

Latif, Muhammad A., Sadegh Khochfar & Daniel Whalen. 2020. The Birth of Binary Direct-collapse Black Holes. ApJ 892(1), L4. L4. https://doi.org/10.3847/2041-8213/ab7c61.

Latif, Muhammad A., Marta Volonteri & John H. Wise. 2018. Early growth of typical high-redshift black holes seeded by direct collapse. MNRAS 476(4). 5016–5025. https://doi.org/10.1093/mnras/sty622.

Lawrence, A. et al. 2007. The UKIRT Infrared Deep Sky Survey (UKIDSS). MNRAS 379(4). 1599–1617. https://doi.org/10.1111/j.1365-2966.2007.12040.x.

Lemaître, G. 1927. Un Univers homogène de masse constante et de rayon croissant rendant compte de la vitesse radiale des nébuleuses extra-galactiques. *Annales de la Société Scientifique de Bruxelles* 47. 49–59.

Li, Jason, Jeremiah Ostriker & Rashid Sunyaev. 2013. Rotating Accretion Flows: From Infinity to the Black Hole. ApJ 767(2), 105. 105. https://doi.org/10.1088/0004-637X/767/2/105.

Lin, Dacheng et al. 2017. A likely decade-long sustained tidal disruption event. *Nature Astronomy* 1, 0033. 0033. https://doi.org/10.1038/s41550-016-0033.

Lin, Dacheng et al. 2022. Follow-up Observations of the Prolonged, Super-Eddington, Tidal Disruption Event Candidate 3XMM J150052.0+015452: the Slow Decline Continues. ApJ 924(2), L35. L35. https://doi.org/10.3847/2041-8213/ac4785.

Lin, Lihwai et al. 2008. The Redshift Evolution of Wet, Dry, and Mixed Galaxy Mergers from Close Galaxy Pairs in the DEEP2 Galaxy Redshift Survey. ApJ 681(1). 232–243. https://doi.org/10.1086/587928.

Linde, A. D. 1982. A new inflationary universe scenario: A possible solution of the horizon, flatness, homogeneity, isotropy and primordial monopole problems. *Physics Letters B* 108(6). 389–393. https://doi.org/10.1016/0370-2693(82)91219-9.

Liska, M. et al. 2018. Formation of precessing jets by tilted black hole discs in 3D general relativistic MHD simulations. MNRAS 474(1). L81–L85. https://doi.org/10.1093/mnrasl/slx174.

Liu, Boyuan & Volker Bromm. 2020. When did Population III star formation end? MNRAS 497(3). 2839–2854. https://doi.org/10.1093/mnras/staa2143.

Lotz, Jennifer M. et al. 2010. The effect of mass ratio on the morphology and time-scales of disc galaxy mergers. MNRAS 404(2). 575–589. https://doi.org/10.1111/j.1365-2966.2010.16268.x.

Lucchini, M. et al. 2021. Bhjet: a public multi-zone, steady state jet + thermal corona spectral model. *arXiv e-prints*, arXiv:2108.12011. arXiv:2108.12011.

Lupi, A. et al. 2014. Constraining the high-redshift formation of black hole seeds in nuclear star clusters with gas inflows. MNRAS 442(4). 3616–3626. https://doi.org/10.1093/mnras/stu1120.

Lupi, A. et al. 2016. Growing massive black holes through supercritical accretion of stellar-mass seeds. MNRAS 456(3). 2993–3003. https://doi.org/10.1093/mnras/stv2877.

Lupi, Alessandro, Francesco Haardt & Massimo Dotti. 2015. Massive black hole and gas dynamics in galaxy nuclei mergers - I. Numerical implementation. MNRAS 446(2). 1765–1774. https://doi.org/10.1093/mnras/stu2223.

Ma, Linhao et al. 2021. Seeds don't sink: even massive black hole 'seeds' cannot migrate to galaxy centres efficiently. MNRAS 508(2). 1973–1985. https://doi.org/10.1093/mnras/stab2713.

MacArthur, Lauren A. et al. 2004. Structure of Disk-dominated Galaxies. II. Color Gradients and Stellar Population Models. ApJS 152(2). 175–199. https://doi.org/10.1086/383525.

Madau, Piero, Francesco Haardt & Massimo Dotti. 2014. Super-critical Growth of Massive Black Holes from Stellar-mass Seeds. ApJ 784(2), L38. L38. https://doi.org/10.1088/2041-8205/784/2/L38.

Madau, Piero & Martin J. Rees. 2001. Massive Black Holes as Population III Remnants. ApJ 551(1). L27–L30. https://doi.org/10.1086/319848.

Magorrian, John et al. 1998. The Demography of Massive Dark Objects in Galaxy Centers. AJ 115(6). 2285–2305. https://doi.org/10.1086/300353.

Makishima, Kazuo et al. 2000. The Nature of Ultraluminous Compact X-Ray Sources in Nearby Spiral Galaxies. ApJ 535(2). 632–643. https://doi.org/10.1086/308868.

Manmoto, T., S. Mineshige & M. Kusunose. 1997. Spectrum of Optically Thin Advection-dominated Accretion Flow around a Black Hole: Application to Sagittarius A*. ApJ 489(2). 791–803. https://doi.org/10.1086/304817.

Marconi, A. et al. 2004. Local supermassive black holes, relics of active galactic nuclei and the X-ray background. MNRAS 351(1). 169–185. https://doi.org/10.1111/j.1365-2966.2004.07765.x.

Marconi, Alessandro & Leslie K. Hunt. 2003. The Relation between Black Hole Mass, Bulge Mass, and Near-Infrared Luminosity. ApJ 589(1). L21–L24. https://doi.org/10.1086/375804.

Margon, B. et al. 1984. Rapid intensity variability in the jets of SS 433. ApJ 281. 313–317. https://doi.org/10.1086/162101.

Marks, Michael et al. 2012. Evidence for top-heavy stellar initial mass functions with increasing density and decreasing metallicity. MNRAS 422(3). 2246–2254. https://doi.org/10.1111/j.1365-2966.2012.20767.x.

Marscher, Alan P. et al. 2008. The inner jet of an active galactic nucleus as revealed by a radio-to-γ-ray outburst. Nature 452(7190). 966–969. https://doi.org/10.1038/nature06895.

Massonneau, Warren et al. 2022a. How the super-Eddington regime affects black hole spin evolution in high-redshift galaxies. *arXiv e-prints*, arXiv:2209.01369. arXiv:2209.01369.

Massonneau, Warren et al. 2022b. How the super-Eddington regime regulates black hole growth in high-redshift galaxies. *arXiv e-prints*, arXiv:2201.08766. arXiv:2201.08766.

Matsuoka, Yoshiki et al. 2016. Subaru High-z Exploration of Low-luminosity Quasars (SHELLQs). I. Discovery of 15 Quasars and Bright Galaxies at 5.7 < z < 6.9. ApJ 828(1), 26. 26. https://doi.org/10.3847/0004-637X/828/1/26.

Matsuoka, Yoshiki et al. 2018. Subaru High-z Exploration of Low-Luminosity Quasars (SHELLQs). II. Discovery of 32 quasars and luminous galaxies at 5.7 < z $\leq$ 6.8. PASJ 70, S35. S35. https://doi.org/10.1093/pasj/psx046.

Matsuoka, Yoshiki et al. 2019a. Discovery of the First Low-luminosity Quasar at z > 7. ApJ 872(1), L2. L2. https://doi.org/10.3847/2041-8213/ab0216.

Matsuoka, Yoshiki et al. 2019b. Subaru High-z Exploration of Low-luminosity Quasars (SHELLQs). X. Discovery of 35 Quasars and Luminous Galaxies at 5.7 $\leq$ z $\leq$ 7.0. ApJ 883(2), 183. 183. https://doi.org/10.3847/1538-4357/ab3c60.

Matthews, Thomas A. & Allan R. Sandage. 1963. Optical Identification of 3C 48, 3C 196, and 3C 286 with Stellar Objects. ApJ 138. 30. https://doi.org/10.1086/147615.

Mayer, Lucio & Silvia Bonoli. 2019. The route to massive black hole formation via merger-driven direct collapse: a review. *Reports on Progress in Physics* 82(1), 016901. 016901. https://doi.org/10.1088/1361-6633/aad6a5.

McCarthy, I. G. et al. 2008. Ram pressure stripping the hot gaseous haloes of galaxies in groups and clusters. MNRAS 383(2). 593–605. https://doi.org/10.1111/j.1365-2966.2007.12577.x.

McConnell, Nicholas J. & Chung-Pei Ma. 2013. Revisiting the Scaling Relations of Black Hole Masses and Host Galaxy Properties. ApJ 764(2), 184. 184. https://doi.org/10.1088/0004-637X/764/2/184.

McDowell, Jonathan C. 1986. The light from Population III stars. MNRAS 223. 763–786. https://doi.org/10.1093/mnras/223.4.763.

McKee, Christopher F. & Jonathan C. Tan. 2008. The Formation of the First Stars. II. Radiative Feedback Processes and Implications for the Initial Mass Function. ApJ 681(2). 771–797. https://doi.org/10.1086/587434.

McKinney, Jonathan C. & Roger D. Blandford. 2009. Stability of relativistic jets from rotating, accreting black holes via fully three-dimensional magnetohydrodynamic simulations. MNRAS 394(1). L126–L130. https://doi.org/10.1111/j.1745-3933.2009.00625.x.

McKinney, Jonathan C., Lixin Dai & Mark J. Avara. 2015. Efficiency of super-Eddington magnetically-arrested accretion. MNRAS 454(1). L6–L10. https://doi.org/10.1093/mnrasl/slv115.

McKinney, Jonathan C., Alexander Tchekhovskoy & Roger D. Blandford. 2012. General relativistic magnetohydrodynamic simulations of magnetically choked accretion flows around black holes. MNRAS 423(4). 3083–3117. https://doi.org/10.1111/j.1365-2966.2012.21074.x.

McKinney, Jonathan C. et al. 2014. Three-dimensional general relativistic radiation magneto-hydrodynamical simulation of super-Eddington accretion, using a new code HARMRAD with M1 closure. MNRAS 441(4). 3177–3208. https://doi.org/10.1093/mnras/stu762.

McLeod, D. J. et al. 2021. The evolution of the galaxy stellar-mass function over the last 12 billion years from a combination of ground-based and HST surveys. MNRAS 503(3). 4413–4435. https://doi.org/10.1093/mnras/stab731.

McLure, R. J. et al. 2013. The sizes, masses and specific star formation rates of massive galaxies at 1.3 < z < 1.5: strong evidence in favour of evolution via minor mergers. MNRAS 428(2). 1088–1106. https://doi.org/10.1093/mnras/sts092.

McNamara, B. R. & P. E. J. Nulsen. 2007. Heating Hot Atmospheres with Active Galactic Nuclei. ARA&A 45(1). 117–175. https://doi.org/10.1146/annurev.astro.45.051806.110625.

Merloni, Andrea. 2004. The anti-hierarchical growth of supermassive black holes. MNRAS 353(4). 1035–1047. https://doi.org/10.1111/j.1365-2966.2004.08147.x.

Merloni, Andrea, Sebastian Heinz & Tiziana di Matteo. 2003. A Fundamental Plane of black hole activity. MNRAS 345(4). 1057–1076. https://doi.org/10.1046/j.1365-2966.2003.07017.x.

Messier, Charles. 1781. *Catalogue des Nébuleuses et des Amas d'Étoiles (Catalog of Nebulae and Star Clusters)*. Connoissance des Temps ou des Mouvements Célestes, for 1784, p. 227-267.

Metzger, Brian D., Dimitrios Giannios & Petar Mimica. 2012. Afterglow model for the radio emission from the jetted tidal disruption candidate Swift J1644+57. MNRAS 420(4). 3528–3537. https://doi.org/10.1111/j.1365-2966.2011.20273.x.

Migliari, S. & R. P. Fender. 2006. Jets in neutron star X-ray binaries: a comparison with black holes. MNRAS 366(1). 79–91. https://doi.org/10.1111/j.1365-2966.2005.09777.x.

Milosavljević, Miloš & David Merritt. 2003. The Final Parsec Problem. In Joan M. Centrella (ed.), *The astrophysics of gravitational wave sources*, vol. 686 (American Institute of Physics Conference Series), 201–210. https://doi.org/10.1063/1.1629432.

Milosavljević, Miloš et al. 2009. Accretion onto "Seed" Black Holes in the First Galaxies. ApJ 698(1). 766–780. https://doi.org/10.1088/0004-637X/698/1/766.

Mineshige, Shin et al. 2000. Slim-Disk Model for Soft X-Ray Excess and Variability of Narrow-Line Seyfert 1 Galaxies. PASJ 52. 499–508. https://doi.org/10.1093/pasj/52.3.499.

Miyoshi, Makoto et al. 1995. Evidence for a black hole from high rotation velocities in a sub-parsec region of NGC4258. Nature 373(6510). 127–129. https://doi.org/10.1038/373127a0.

Moe, Maxwell et al. 2009. Quasar Outflow Contribution to AGN Feedback: Observations of QSO SDSS J0838+2955. ApJ 706(1). 525–534. https://doi.org/10.1088/0004-637X/706/1/525.

Morganti, Raffaella et al. 2013. Radio Jets Clearing the Way Through a Galaxy: Watching Feedback in Action. *Science* 341(6150). 1082–1085. https://doi.org/10.1126/science.1240436.

Mortlock, Daniel J. et al. 2011. A luminous quasar at a redshift of z = 7.085. Nature 474(7353). 616–619. https://doi.org/10.1038/nature10159.

Moster, Benjamin P. et al. 2010. Constraints on the Relationship between Stellar Mass and Halo Mass at Low and High Redshift. ApJ 710(2). 903–923. https://doi.org/10.1088/0004-637X/710/2/903.

Murray, Norman, Eliot Quataert & Todd A. Thompson. 2005. On the Maximum Luminosity of Galaxies and Their Central Black Holes: Feedback from Momentum-driven Winds. ApJ 618(2). 569–585. https://doi.org/10.1086/426067.

Muzzin, Adam et al. 2013. The Evolution of the Stellar Mass Functions of Star-forming and Quiescent Galaxies to z = 4 from the COSMOS/UltraVISTA Survey. ApJ 777(1), 18. 18. https://doi.org/10.1088/0004-637X/777/1/18.

Naab, Thorsten, Andreas Burkert & Lars Hernquist. 1999. On the Formation of Boxy and Disky Elliptical Galaxies. ApJ 523(2). L133–L136. https://doi.org/10.1086/312275.

Naab, Thorsten & Jeremiah P. Ostriker. 2017. Theoretical Challenges in Galaxy Formation. ARA&A 55(1). 59–109. https://doi.org/10.1146/annurev-astro-081913-040019.

Naab, Thorsten et al. 2007. Formation of Early-Type Galaxies from Cosmological Initial Conditions. ApJ 658(2). 710–720. https://doi.org/10.1086/510841.

Narayan, Ramesh, Igor V. Igumenshchev & Marek A. Abramowicz. 2003. Magnetically Arrested Disk: an Energetically Efficient Accretion Flow. PASJ 55. L69–L72. https://doi.org/10.1093/pasj/55.6.L69.

Narayan, Ramesh, Shoji Kato & Fumio Honma. 1997. Global Structure and Dynamics of Advection-dominated Accretion Flows around Black Holes. ApJ 476(1). 49–60. https://doi.org/10.1086/303591.

Narayan, Ramesh, Aleksander SaÌ§dowski & Roberto Soria. 2017. Spectra of black hole accretion models of ultraluminous X-ray sources. MNRAS 469(3). 2997–3014. https://doi.org/10.1093/mnras/stx1027.

Narayan, Ramesh & Insu Yi. 1995. Advection-dominated Accretion: Self-Similarity and Bipolar Outflows. ApJ 444. 231. https://doi.org/10.1086/175599.

Narayan, Ramesh et al. 2022. Jets in magnetically arrested hot accretion flows: geometry, power, and black hole spin-down. MNRAS 511(3). 3795–3813. https://doi.org/10.1093/mnras/stac285.

Navarro, Julio F., Carlos S. Frenk & Simon D. M. White. 1997. A Universal Density Profile from Hierarchical Clustering. ApJ 490(2). 493–508. https://doi.org/10.1086/304888.

Nesvadba, N. P. H. et al. 2007. Compact radio sources and jet-driven AGN feedback in the early universe: constraints from integral-field spectroscopy. A&A 475(1). 145–153. https://doi.org/10.1051/0004-6361:20078175.

Novikov, I. D. & K. S. Thorne. 1973. Astrophysics of black holes. In *Black holes (les astres occlus)*, 343–450.

Oh, S. Peng & Zoltán Haiman. 2002. Second-Generation Objects in the Universe: Radiative Cooling and Collapse of Halos with Virial Temperatures above 10^4 K. ApJ 569(2). 558–572. https://doi.org/10.1086/339393.

Ohsuga, K. & S. Mineshige. 2007. Why Is Supercritical Disk Accretion Feasible? ApJ 670(2). 1283–1290. https://doi.org/10.1086/522324.

Ohsuga, Ken & Shin Mineshige. 2011. Global Structure of Three Distinct Accretion Flows and Outflows around Black Holes from Two-dimensional Radiation-magnetohydrodynamic Simulations. ApJ 736(1), 2. 2. https://doi.org/10.1088/0004-637X/736/1/2.

Ohsuga, Ken et al. 2002. Does the Slim-Disk Model Correctly Consider Photon-trapping Effects? ApJ 574(1). 315–324. https://doi.org/10.1086/340798.

Ohsuga, Ken et al. 2005. Supercritical Accretion Flows around Black Holes: Two-dimensional, Radiation Pressure-dominated Disks with Photon Trapping. ApJ 628(1). 368–381. https://doi.org/10.1086/430728.

Ohsuga, Ken et al. 2009. Global Radiation-Magnetohydrodynamic Simulations of Black-Hole Accretion Flow and Outflow: Unified Model of Three States. PASJ 61(3). L7–L11. https://doi.org/10.1093/pasj/61.3.L7.

Okuda, Toru. 2002. Super-Eddington Black-Hole Models for SS 433. PASJ 54. 253–266. https://doi.org/10.1093/pasj/54.2.253.

Olivares, V. et al. 2019. Ubiquitous cold and massive filaments in cool core clusters. A&A 631, A22. A22. https://doi.org/10.1051/0004-6361/201935350.

Omma, Henrik et al. 2004. Heating cooling flows with jets. MNRAS 348(4). 1105–1119. https://doi.org/10.1111/j.1365-2966.2004.07382.x.

Omukai, K., R. Schneider & Z. Haiman. 2008. Can Supermassive Black Holes Form in Metal-enriched High-Redshift Protogalaxies? ApJ 686(2). 801–814. https://doi.org/10.1086/591636.

Omukai, Kazuyuki. 2001. Primordial Star Formation under Far-Ultraviolet Radiation. ApJ 546(2). 635–651. https://doi.org/10.1086/318296.

Omukai, Kazuyuki & Francesco Palla. 2003. Formation of the First Stars by Accretion. ApJ 589(2). 677–687. https://doi.org/10.1086/374810.

Onken, Christopher A. et al. 2007. The Black Hole Mass of NGC 4151: Comparison of Reverberation Mapping and Stellar Dynamical Measurements. ApJ 670(1). 105–115. https://doi.org/10.1086/522220.

Oppenheimer, Benjamin D. & Romeel Davé. 2008. Mass, metal, and energy feedback in cosmological simulations. MNRAS 387(2). 577–600. https://doi.org/10.1111/j.1365-2966.2008.13280.x.

Oser, Ludwig et al. 2010. The Two Phases of Galaxy Formation. ApJ 725(2). 2312–2323. https://doi.org/10.1088/0004-637X/725/2/2312.

Ostriker, Eve C. 1999. Dynamical Friction in a Gaseous Medium. ApJ 513(1). 252–258. https://doi.org/10.1086/306858.

Ostriker, Jeremiah P. et al. 2010. Momentum Driving: Which Physical Processes Dominate Active Galactic Nucleus Feedback? ApJ 722(1). 642–652. https://doi.org/10.1088/0004-637X/722/1/642.

Pacucci, Fabio & Andrea Ferrara. 2015. Simulating the growth of Intermediate Mass Black Holes. MNRAS 448(1). 104–118. https://doi.org/10.1093/mnras/stv018.

Paczynski, B. 1986. Gravitational Microlensing by the Galactic Halo. ApJ 304. 1. https://doi.org/10.1086/164140.

Paczynski, B. & M. A. Abramowicz. 1982. A model of a thick disk with equatorial accretion. ApJ 253. 897–907. https://doi.org/10.1086/159689.

Padoan, Paolo & Åke Nordlund. 2011. The Star Formation Rate of Supersonic Magnetohydrodynamic Turbulence. ApJ 730(1), 40. 40. https://doi.org/10.1088/0004-637X/730/1/40.

Pakull, Manfred W. & Laurent Mirioni. 2002. Optical Counterparts of Ultraluminous X-Ray Sources. *arXiv e-prints*, astro-ph/0202488. astro–ph/0202488.

Park, KwangHo & Massimo Ricotti. 2011. Accretion onto Intermediate-mass Black Holes Regulated by Radiative Feedback. I. Parametric Study for Spherically Symmetric Accretion. ApJ 739(1), 2. 2. https://doi.org/10.1088/0004-637X/739/1/2.

Park, KwangHo et al. 2020. Biconical-dominated Accretion Flow onto Seed Black Holes in a Hyperaccretion Regime. ApJ 905(2), 92. 92. https://doi.org/10.3847/1538-4357/abc336.

Penzias, A. A. & R. W. Wilson. 1965. A Measurement of Excess Antenna Temperature at 4080 Mc/s. ApJ 142. 419–421. https://doi.org/10.1086/148307.

Pérez-González, Pablo G. et al. 2008. The Stellar Mass Assembly of Galaxies from z = 0 to z = 4: Analysis of a Sample Selected in the Rest-Frame Near-Infrared with Spitzer. ApJ 675(1). 234–261. https://doi.org/10.1086/523690.

Peterson, B. M. et al. 2004. Central Masses and Broad-Line Region Sizes of Active Galactic Nuclei. II. A Homogeneous Analysis of a Large Reverberation-Mapping Database. ApJ 613(2). 682–699. https://doi.org/10.1086/423269.

Peterson, Bradley M. 1993. Reverberation Mapping of Active Galactic Nuclei. PASP 105. 247. https://doi.org/10.1086/133140.

Peterson, J. R. et al. 2003. High-Resolution X-Ray Spectroscopic Constraints on Cooling-Flow Models for Clusters of Galaxies. ApJ 590(1). 207–224. https://doi.org/10.1086/374830.

Petri, A., A. Ferrara & R. Salvaterra. 2012. Supermassive black hole ancestors. MNRAS 422(2). 1690–1699. https://doi.org/10.1111/j.1365-2966.2012.20743.x.

Pezzulli, Edwige, Rosa Valiante & Raffaella Schneider. 2016. Super-Eddington growth of the first black holes. MNRAS 458(3). 3047–3059. https://doi.org/10.1093/mnras/stw505.

Pezzulli, Edwige et al. 2017. The sustainable growth of the first black holes. MNRAS 471(1). 589–595. https://doi.org/10.1093/mnras/stx1640.

Pfister, Hugo et al. 2019. The erratic dynamical life of black hole seeds in high-redshift galaxies. MNRAS 486(1). 101–111. https://doi.org/10.1093/mnras/stz822.

Pfister, Hugo et al. 2021. Tidal disruption events in the first billion years of a galaxy. MNRAS 500(3). 3944–3956. https://doi.org/10.1093/mnras/staa3471.

Pichon, C. et al. 2011. Rigging dark haloes: why is hierarchical galaxy formation consistent with the inside-out build-up of thin discs? MNRAS 418(4). 2493–2507. https://doi.org/10.1111/j.1365-2966.2011.19640.x.

Pillepich, Annalisa et al. 2018. First results from the IllustrisTNG simulations: the stellar mass content of groups and clusters of galaxies. MNRAS 475(1). 648–675. https://doi.org/10.1093/mnras/stx3112.

Planck Collaboration et al. 2020. Planck 2018 results. VI. Cosmological parameters. A&A 641, A6. A6. https://doi.org/10.1051/0004-6361/201833910.

Pognan, Quentin et al. 2020. Searching for super-Eddington quasars using a photon trapping accretion disc model. MNRAS 492(3). 4058–4079. https://doi.org/10.1093/mnras/staa078.

Potter, William J. & Garret Cotter. 2015. New constraints on the structure and dynamics of black hole jets. MNRAS 453(4). 4070–4088. https://doi.org/10.1093/mnras/stv1657.

Poutanen, Juri et al. 2007. Supercritically accreting stellar mass black holes as ultraluminous X-ray sources. MNRAS 377(3). 1187–1194. https://doi.org/10.1111/j.1365-2966.2007.11668.x.

Prieto, Joaquin et al. 2017. How AGN and SN Feedback Affect Mass Transport and Black Hole Growth in High-redshift Galaxies. ApJ 836(2), 216. 216. https://doi.org/10.3847/1538-4357/aa5be5.

Quinlan, Gerald D. 1996. The dynamical evolution of massive black hole binaries I. Hardening in a fixed stellar background. New A 1(1). 35–56. https://doi.org/10.1016/S1384-1076(96)00003-6.

Quintin, E. et al. 2021. A new candidate pulsating ULX in NGC 7793. MNRAS 503(4). 5485–5494. https://doi.org/10.1093/mnras/stab814.

Rafferty, D. A. et al. 2006. The Feedback-regulated Growth of Black Holes and Bulges through Gas Accretion and Starbursts in Cluster Central Dominant Galaxies. ApJ 652(1). 216–231. https://doi.org/10.1086/507672.

Rasera, Y. & R. Teyssier. 2006. The history of the baryon budget. Cosmic logistics in a hierarchical universe. A&A 445(1). 1–27. https://doi.org/10.1051/0004-6361:20053116.

Reed, S. L. et al. 2017. Eight new luminous z $\geq$ 6 quasars discovered via SED model fitting of VISTA, WISE and Dark Energy Survey Year 1 observations. MNRAS 468(4). 4702–4718. https://doi.org/10.1093/mnras/stx728.

Rees, Martin J. 1984. Black Hole Models for Active Galactic Nuclei. ARA&A 22. 471–506. https://doi.org/10.1146/annurev.aa.22.090184.002351.

Rees, Martin J. 1989. The radio/optical alignment of high-z radio galaxies : triggering of star formation in radio lobes. MNRAS 239. 1P–4. https://doi.org/10.1093/mnras/239.1.1P.

Regan, John A., Peter H. Johansson & Martin G. Haehnelt. 2014. Numerical resolution effects on simulations of massive black hole seeds. MNRAS 439(1). 1160–1175. https://doi.org/10.1093/mnras/stu068.

Regan, John A. et al. 2019. Super-Eddington accretion and feedback from the first massive seed black holes. MNRAS 486(3). 3892–3906. https://doi.org/10.1093/mnras/stz1045.

Regan, John A. et al. 2020. Massive Star Formation in Metal-Enriched Haloes at High Redshift. *J. Astrophys.* 3. 2020. https://doi.org/10.21105/astro.2006.14625.

Reines, Amy E. & Marta Volonteri. 2015. Relations between Central Black Hole Mass and Total Galaxy Stellar Mass in the Local Universe. ApJ 813(2), 82. 82. https://doi.org/10.1088/0004-637X/813/2/82.

Reynolds, Christopher S. 2013. The spin of supermassive black holes. *Classical and Quantum Gravity* 30(24), 244004. 244004. https://doi.org/10.1088/0264-9381/30/24/244004.

Reynolds, Christopher S. 2021. Observational Constraints on Black Hole Spin. ARA&A 59. 117–154. https://doi.org/10.1146/annurev-astro-112420-035022.

Reynolds, Christopher S. & Michael A. Nowak. 2003. Fluorescent iron lines as a probe of astrophysical black hole systems. Phys. Rep. 377(6). 389–466. https://doi.org/10.1016/S0370-1573(02)00584-7.

Rezzolla, Luciano et al. 2008. Final spin from the coalescence of two black holes. Phys. Rev. D 78(4), 044002. 044002. https://doi.org/10.1103/PhysRevD.78.044002.

Richards, Gordon T. et al. 2004. Microlensing of the Broad Emission Line Region in the Quadruple Lens SDSS J1004+4112. ApJ 610(2). 679–685. https://doi.org/10.1086/421868.

Ritter, Jeremy S. et al. 2012. Confined Population III Enrichment and the Prospects for Prompt Second-generation Star Formation. ApJ 761(1), 56. 56. https://doi.org/10.1088/0004-637X/761/1/56.

Rodriguez, C. et al. 2006. A Compact Supermassive Binary Black Hole System. ApJ 646(1). 49–60. https://doi.org/10.1086/504825.

Rodriguez-Gomez, Vicente et al. 2016. The stellar mass assembly of galaxies in the Illustris simulation: growth by mergers and the spatial distribution of accreted stars. MNRAS 458(3). 2371–2390. https://doi.org/10.1093/mnras/stw456.

Rosdahl, J. et al. 2013. RAMSES-RT: radiation hydrodynamics in the cosmological context. MNRAS 436(3). 2188–2231. https://doi.org/10.1093/mnras/stt1722.

Rosen, Alexander & Joel N. Bregman. 1995. Global Models of the Interstellar Medium in Disk Galaxies. ApJ 440. 634. https://doi.org/10.1086/175303.

Sakurai, Y. et al. 2016a. Supermassive star formation via episodic accretion: protostellar disc instability and radiative feedback efficiency. MNRAS 459(2). 1137–1145. https://doi.org/10.1093/mnras/stw637.

Sakurai, Yuya, Kohei Inayoshi & Zoltán Haiman. 2016b. Hyper-Eddington mass accretion on to a black hole with super-Eddington luminosity. MNRAS 461(4). 4496–4504. https://doi.org/10.1093/mnras/stw1652.

Sakurai, Yuya, Naoki Yoshida & Michiko S. Fujii. 2019. Growth of intermediate mass black holes by tidal disruption events in the first star clusters. MNRAS 484(4). 4665–4677. https://doi.org/10.1093/mnras/stz315.

Sakurai, Yuya et al. 2017. Formation of intermediate-mass black holes through runaway collisions in the first star clusters. MNRAS 472(2). 1677–1684. https://doi.org/10.1093/mnras/stx2044.

Sala, Luca et al. 2021. Non-isotropic feedback from accreting spinning black holes. MNRAS 500(4). 4788–4800. https://doi.org/10.1093/mnras/staa3552.

Salmon, Brett et al. 2015. The Relation between Star Formation Rate and Stellar Mass for Galaxies at 3.5 <= z <= 6.5 in CANDELS. ApJ 799(2), 183. 183. https://doi.org/10.1088/0004-637X/799/2/183.

Salpeter, Edwin E. 1955. The Luminosity Function and Stellar Evolution. ApJ 121. 161. https://doi.org/10.1086/145971.

Sánchez-Blázquez, P. et al. 2014. Stellar population gradients in galaxy discs from the CALIFA survey. The influence of bars. A&A 570, A6. A6. https://doi.org/10.1051/0004-6361/201423635.

Santini, P. et al. 2012. Enhanced star formation rates in AGN hosts with respect to inactive galaxies from PEP-Herschel observations. A&A 540, A109. A109. https://doi.org/10.1051/0004-6361/201118266.

Sassano, Federica et al. 2022. Super-critical accretion of medium-weight seed black holes in gaseous proto-galactic nuclei. *arXiv e-prints*, arXiv:2204.10330. arXiv:2204.10330.

Scannapieco, Cecilia et al. 2008. Effects of supernova feedback on the formation of galaxy discs. MNRAS 389(3). 1137–1149. https://doi.org/10.1111/j.1365-2966.2008.13678.x.

Scharwächter, J. et al. 2013. Kinematics and excitation of the molecular hydrogen accretion disc in NGC 1275. MNRAS 429(3). 2315–2332. https://doi.org/10.1093/mnras/sts502.

Schaye, Joop et al. 2015. The EAGLE project: simulating the evolution and assembly of galaxies and their environments. MNRAS 446(1). 521–554. https://doi.org/10.1093/mnras/stu2058.

Schindler, Jan-Torge et al. 2020. The X-SHOOTER/ALMA Sample of Quasars in the Epoch of Reionization. I. NIR Spectral Modeling, Iron Enrichment, and Broad Emission Line Properties. ApJ 905(1), 51. 51. https://doi.org/10.3847/1538-4357/abc2d7.

Schmidt, M. 1963. 3C 273 : A Star-Like Object with Large Red-Shift. Nature 197(4872). 1040. https://doi.org/10.1038/1971040a0.

Schmidt, Maarten. 1959. The Rate of Star Formation. ApJ 129. 243. https://doi.org/10.1086/146614.

Schneider, R. et al. 2003. Low-mass relics of early star formation. Nature 422(6934). 869–871. https://doi.org/10.1038/nature01579.

Schneider, Raffaella, Dafne Guetta & Andrea Ferrara. 2002. Gamma-ray bursts from the first stars: neutrino signals. MNRAS 334(1). 173–181. https://doi.org/10.1046/j.1365-8711.2002.05511.x.

Schneider, Raffaella et al. 2006a. Constraints on the initial mass function of the first stars. MNRAS 369(2). 825–834. https://doi.org/10.1111/j.1365-2966.2006.10331.x.

Schneider, Raffaella et al. 2006b. Fragmentation of star-forming clouds enriched with the first dust. MNRAS 369(3). 1437–1444. https://doi.org/10.1111/j.1365-2966.2006.10391.x.

Schneider, Raffaella et al. 2012. The first low-mass stars: critical metallicity or dust-to-gas ratio? MNRAS 419(2). 1566–1575. https://doi.org/10.1111/j.1365-2966.2011.19818.x.

Schödel, R. et al. 2003. Stellar Dynamics in the Central Arcsecond of Our Galaxy. ApJ 596(2). 1015–1034. https://doi.org/10.1086/378122.

Schwarzschild, Karl. 1916. Über das Gravitationsfeld eines Massenpunktes nach der Einsteinschen Theorie. *Sitzungsberichte der Königlich Preußischen Akademie der Wissenschaften (Berlin*. 189–196.

Schwarzschild, M. & L. Spitzer. 1953. On the evolution of stars and chemical elements in the early phases of a galaxy. *The Observatory* 73. 77–79.

Sesana, A. et al. 2014. Linking the Spin Evolution of Massive Black Holes to Galaxy Kinematics. ApJ 794(2), 104. 104. https://doi.org/10.1088/0004-637X/794/2/104.

Sesana, Alberto, Marta Volonteri & Francesco Haardt. 2007. The imprint of massive black hole formation models on the LISA data stream. MNRAS 377(4). 1711–1716. https://doi.org/10.1111/j.1365-2966.2007.11734.x.

Seyfert, Carl K. 1943. Nuclear Emission in Spiral Nebulae. ApJ 97. 28. https://doi.org/10.1086/144488.

Shakura, N. I. & R. A. Sunyaev. 1973. Black holes in binary systems. Observational appearance. A&A 24. 337–355.

Shang, Cien, Greg L. Bryan & Z. Haiman. 2010. Supermassive black hole formation by direct collapse: keeping protogalactic gas H_2 free in dark matter haloes with virial temperatures T_{vir} > rsim 10^4 K. MNRAS 402(2). 1249–1262. https://doi.org/10.1111/j.1365-2966.2009.15960.x.

Shankar, Francesco, David H. Weinberg & Jordi Miralda-Escudé. 2009. Self-Consistent Models of the AGN and Black Hole Populations: Duty Cycles, Accretion Rates, and the Mean Radiative Efficiency. ApJ 690(1). 20–41. https://doi.org/10.1088/0004-637X/690/1/20.

Shapiro, Stuart L. 2005. Spin, Accretion, and the Cosmological Growth of Supermassive Black Holes. ApJ 620(1). 59–68. https://doi.org/10.1086/427065.

Shapiro, Stuart L. & Saul A. Teukolsky. 1983. *Black holes, white dwarfs, and neutron stars : the physics of compact objects*.

Shen, Yue. 2013. The mass of quasars. *Bulletin of the Astronomical Society of India* 41(1). 61–115.

Shibata, Masaru & Stuart L. Shapiro. 2002. Collapse of a Rotating Supermassive Star to a Supermassive Black Hole: Fully Relativistic Simulations. ApJ 572(1). L39–L43. https://doi.org/10.1086/341516.

Shibuya, Takatoshi et al. 2019. Morphologies of ∼190,000 Galaxies at z = 0-10 Revealed with HST Legacy Data. III. Continuum Profile and Size Evolution of Lyα Emitters. ApJ 871(2), 164. 164. https://doi.org/10.3847/1538-4357/aaf64b.

Silk, Joseph. 2005. Ultraluminous starbursts from supermassive black hole-induced outflows. MNRAS 364(4). 1337–1342. https://doi.org/10.1111/j.1365-2966.2005.09672.x.

Silk, Joseph. 2013. Unleashing Positive Feedback: Linking the Rates of Star Formation, Supermassive Black Hole Accretion, and Outflows in Distant Galaxies. ApJ 772(2), 112. 112. https://doi.org/10.1088/0004-637X/772/2/112.

Silk, Joseph & Martin J. Rees. 1998. Quasars and galaxy formation. A&A 331. L1–L4.

Sądowski, Aleksander. 2009. Slim Disks Around Kerr Black Holes Revisited. ApJS 183(2). 171–178. https://doi.org/10.1088/0067-0049/183/2/171.

Sądowski, Aleksander & Ramesh Narayan. 2015. Powerful radiative jets in supercritical accretion discs around non-spinning black holes. MNRAS 453(3). 3213–3221. https://doi.org/10.1093/mnras/stv1802.

Sądowski, Aleksander et al. 2014. Numerical simulations of super-critical black hole accretion flows in general relativity. MNRAS 439(1). 503–520. https://doi.org/10.1093/mnras/stt2479.

Sądowski, Aleksander et al. 2015. Global simulations of axisymmetric radiative black hole accretion discs in general relativity with a mean-field magnetic dynamo. MNRAS 447(1). 49–71. https://doi.org/10.1093/mnras/stu2387.

Sądowski, Aleksander et al. 2016. Energy flows in thick accretion discs and their consequences for black hole feedback. MNRAS 456(4). 3915–3928. https://doi.org/10.1093/mnras/stv2854.

Slipher, V. M. 1913. The radial velocity of the Andromeda Nebula. *Lowell Observatory Bulletin* 2(8). 56–57.

Sluse, D. et al. 2011. Zooming into the broad line region of the gravitationally lensed quasar QSO 2237 + 0305 ≡ the Einstein Cross. III. Determination of the size and structure of

the C iv and C iii] emitting regions using microlensing. A&A 528, A100. A100. https://doi.org/10.1051/0004-6361/201016110.

Sluse, D. et al. 2012. Microlensing of the broad line region in 17 lensed quasars. A&A 544, A62. A62. https://doi.org/10.1051/0004-6361/201219125.

Smith, Britton D. et al. 2009. Three Modes of Metal-Enriched Star Formation in the Early Universe. ApJ 691(1). 441–451. https://doi.org/10.1088/0004-637X/691/1/441.

Smith, Britton D. et al. 2018. The growth of black holes from Population III remnants in the Renaissance simulations. MNRAS 480(3). 3762–3773. https://doi.org/10.1093/mnras/sty2103.

Smith, Rowan J. et al. 2012. Weakly Interacting Massive Particle Dark Matter and First Stars: Suppression of Fragmentation in Primordial Star Formation. ApJ 761(2), 154. 154. https://doi.org/10.1088/0004-637X/761/2/154.

Soares, Gustavo & Rodrigo Nemmen. 2020. Jet efficiencies and black hole spins in jetted quasars. MNRAS 495(1). 981–991. https://doi.org/10.1093/mnras/staa1241.

Sokasian, Aaron et al. 2004. Cosmic reionization by stellar sources: population III stars. MNRAS 350(1). 47–65. https://doi.org/10.1111/j.1365-2966.2004.07636.x.

Somerville, Rachel S. & Romeel Davé. 2015. Physical Models of Galaxy Formation in a Cosmological Framework. ARA&A 53. 51–113. https://doi.org/10.1146/annurev-astro-082812-140951.

Somerville, Rachel S. et al. 2008. A semi-analytic model for the co-evolution of galaxies, black holes and active galactic nuclei. MNRAS 391(2). 481–506. https://doi.org/10.1111/j.1365-2966.2008.13805.x.

Soria, R. et al. 2021. The ultraluminous X-ray source bubble in NGC 5585. MNRAS 501(2). 1644–1662. https://doi.org/10.1093/mnras/staa3784.

Spinoso, Daniele et al. 2022. Multi-flavour SMBH seeding and evolution in cosmological environments. *arXiv e-prints*, arXiv:2203.13846. arXiv:2203.13846.

Springel, Volker, Tiziana Di Matteo & Lars Hernquist. 2005. Modelling feedback from stars and black holes in galaxy mergers. MNRAS 361(3). 776–794. https://doi.org/10.1111/j.1365-2966.2005.09238.x.

Springel, Volker & Lars Hernquist. 2003. Cosmological smoothed particle hydrodynamics simulations: a hybrid multiphase model for star formation. MNRAS 339(2). 289–311. https://doi.org/10.1046/j.1365-8711.2003.06206.x.

Springel, Volker et al. 2021. Simulating cosmic structure formation with the GADGET-4 code. MNRAS 506(2). 2871–2949. https://doi.org/10.1093/mnras/stab1855.

Stacy, Athena, Volker Bromm & Aaron T. Lee. 2016. Building up the Population III initial mass function from cosmological initial conditions. MNRAS 462(2). 1307–1328. https://doi.org/10.1093/mnras/stw1728.

Starobinsky, A. A. 1982. Dynamics of phase transition in the new inflationary universe scenario and generation of perturbations. *Physics Letters B* 117(3-4). 175–178. https://doi.org/10.1016/0370-2693(82)90541-X.

Stephenson, C. B. & N. Sanduleak. 1977. New H-alpha emission stars in the Milky Way. ApJS 33. 459–469. https://doi.org/10.1086/190437.

Stone, Nicholas C., Andreas H. W. Küpper & Jeremiah P. Ostriker. 2017. Formation of massive black holes in galactic nuclei: runaway tidal encounters. MNRAS 467(4). 4180–4199. https://doi.org/10.1093/mnras/stx097.

Sugimura, Kazuyuki et al. 2017. Rapid black hole growth under anisotropic radiation feedback. MNRAS 469(1). 62–79. https://doi.org/10.1093/mnras/stx769.

Sutherland, Ralph S. & M. A. Dopita. 1993. Cooling Functions for Low-Density Astrophysical Plasmas. ApJS 88. 253. https://doi.org/10.1086/191823.

Tadhunter, Clive. 2008. An introduction to active galactic nuclei: Classification and unification. New A Rev. 52(6). 227–239. https://doi.org/10.1016/j.newar.2008.06.004.

Tagawa, Hiromichi, Zoltan Haiman & Bence Kocsis. 2020. Making a Supermassive Star by Stellar Bombardment. ApJ 892(1), 36. 36. https://doi.org/10.3847/1538-4357/ab7922.

Takeo, Eishun, Kohei Inayoshi & Shin Mineshige. 2020. Hyper-Eddington accretion flows on to black holes accompanied by powerful outflows. MNRAS 497(1). 302–317. https://doi.org/10.1093/mnras/staa1906.

Takeo, Eishun et al. 2018. Rapid growth of black holes accompanied with hot or warm outflows exposed to anisotropic super-Eddington radiation. MNRAS 476(1). 673–682. https://doi.org/10.1093/mnras/sty264.

Talbot, Rosie Y., Martin A. Bourne & Debora Sijacki. 2021. Blandford-Znajek jets in galaxy formation simulations: method and implementation. MNRAS 504(3). 3619–3650. https://doi.org/10.1093/mnras/stab804.

Talbot, Rosie Y., Debora Sijacki & Martin A. Bourne. 2022. Blandford-Znajek jets in galaxy formation simulations: exploring the diversity of outflows produced by spin-driven AGN jets in Seyfert galaxies. MNRAS 514(3). 4535–4559. https://doi.org/10.1093/mnras/stac1566.

Tanaka, Takamitsu & Zoltán Haiman. 2009. The Assembly of Supermassive Black Holes at High Redshifts. ApJ 696(2). 1798–1822. https://doi.org/10.1088/0004-637X/696/2/1798.

Tanaka, Takamitsu L. 2014. Driving the growth of the earliest supermassive black holes with major mergers of host galaxies. *Classical and Quantum Gravity* 31(24), 244005. 244005. https://doi.org/10.1088/0264-9381/31/24/244005.

Tang, Ji-Jia et al. 2017. A quasar discovered at redshift 6.6 from Pan-STARRS1. MNRAS 466(4). 4568–4572. https://doi.org/10.1093/mnras/stw3287.

Tchekhovskoy, Alexander. 2015. Launching of Active Galactic Nuclei Jets. In Ioannis Contopoulos, Denise Gabuzda & Nikolaos Kylafis (eds.), *The formation and disruption of black hole jets*, vol. 414 (Astrophysics and Space Science Library), 45. https://doi.org/10.1007/978-3-319-10356-3_3.

Tchekhovskoy, Alexander, Jonathan C. McKinney & Ramesh Narayan. 2012. General Relativistic Modeling of Magnetized Jets from Accreting Black Holes. In *Journal of physics conference series*, vol. 372 (Journal of Physics Conference Series), 012040. https://doi.org/10.1088/1742-6596/372/1/012040.

Tchekhovskoy, Alexander, Ramesh Narayan & Jonathan C. McKinney. 2011. Efficient generation of jets from magnetically arrested accretion on a rapidly spinning black hole. MNRAS 418(1). L79–L83. https://doi.org/10.1111/j.1745-3933.2011.01147.x.

Tchekhovskoy, Alexander et al. 2014. Swift J1644+57 gone MAD: the case for dynamically important magnetic flux threading the black hole in a jetted tidal disruption event. MNRAS 437(3). 2744–2760. https://doi.org/10.1093/mnras/stt2085.

Tegmark, Max et al. 1997. How Small Were the First Cosmological Objects? ApJ 474. 1. https://doi.org/10.1086/303434.

Teyssier, R. 2002. Cosmological hydrodynamics with adaptive mesh refinement. A new high resolution code called RAMSES. A&A 385. 337–364. https://doi.org/10.1051/0004-6361:20011817.

Thorne, Kip S. 1974. Disk-Accretion onto a Black Hole. II. Evolution of the Hole. ApJ 191. 507–520. https://doi.org/10.1086/152991.

Tomczak, Adam R. et al. 2014. Galaxy Stellar Mass Functions from ZFOURGE/CANDELS: An Excess of Low-mass Galaxies since z = 2 and the Rapid Buildup of Quiescent Galaxies. ApJ 783(2), 85. 85. https://doi.org/10.1088/0004-637X/783/2/85.

Toomre, Alar. 1977. Mergers and Some Consequences. In Beatrice M. Tinsley & D. Campbell Larson Richard B. Gehret (eds.), *Evolution of galaxies and stellar populations*, 401.

Toro, E. 1999. *Riemann Solvers and Numerical Methods for Fluid Dynamics*. Springer-Verlag.

Toyouchi, Daisuke et al. 2019. Super-Eddington accretion of dusty gas on to seed black holes: metallicity-dependent efficiency of mass growth. MNRAS 483(2). 2031–2043. https://doi.org/10.1093/mnras/sty3012.

Toyouchi, Daisuke et al. 2021. Super-Eddington Mass Growth of Intermediate-mass Black Holes Embedded in Dusty Circumnuclear Disks. ApJ 907(2), 74. 74. https://doi.org/10.3847/1538-4357/abcfc2.

Trebitsch, Maxime et al. 2017. Fluctuating feedback-regulated escape fraction of ionizing radiation in low-mass, high-redshift galaxies. MNRAS 470(1). 224–239. https://doi.org/10.1093/mnras/stx1060.

Trebitsch, Maxime et al. 2018. Escape of ionizing radiation from high-redshift dwarf galaxies: role of AGN feedback. MNRAS 478(4). 5607–5625. https://doi.org/10.1093/mnras/sty1406.

Trebitsch, Maxime et al. 2021. The OBELISK simulation: Galaxies contribute more than AGN to H I reionization of protoclusters. A&A 653, A154. A154. https://doi.org/10.1051/0004-6361/202037698.

Tremaine, Scott et al. 2002. The Slope of the Black Hole Mass versus Velocity Dispersion Correlation. ApJ 574(2). 740–753. https://doi.org/10.1086/341002.

Tremonti, Christy A., John Moustakas & Aleksandar M. Diamond-Stanic. 2007. The Discovery of 1000 km s^{-1} Outflows in Massive Poststarburst Galaxies at z=0.6. ApJ 663(2). L77–L80. https://doi.org/10.1086/520083.

Tully, R. B. & J. R. Fisher. 1977. A new method of determining distances to galaxies. A&A 54. 661–673.

Turk, Matthew J., Tom Abel & Brian O'Shea. 2009. The Formation of Population III Binaries from Cosmological Initial Conditions. *Science* 325(5940). 601. https://doi.org/10.1126/science.1173540.

Turner, Edwin L. 1991. Quasars and Galaxy Formation. I. The Z > 4 Objects. AJ 101. 5. https://doi.org/10.1086/115663.

Übler, Hannah et al. 2014. Why stellar feedback promotes disc formation in simulated galaxies. MNRAS 443(3). 2092–2111. https://doi.org/10.1093/mnras/stu1275.

Urry, M. 2003. The AGN Paradigm for Radio-Loud Objects. In Suzy Collin, Francoise Combes & Isaac Shlosman (eds.), *Active galactic nuclei: from central engine to host galaxy*, vol. 290 (Astronomical Society of the Pacific Conference Series), 3.

Valiante, Rosa et al. 2016. From the first stars to the first black holes. MNRAS 457(3). 3356–3371. https://doi.org/10.1093/mnras/stw225.

Valiante, Rosa et al. 2021. Unveiling early black hole growth with multifrequency gravitational wave observations. MNRAS 500(3). 4095–4109. https://doi.org/10.1093/mnras/staa3395.

van der Marel, R. P. 1994. Velocity profiles of galaxies with claimed black holes - III. Observations and models for M 87. MNRAS 270. 271–297. https://doi.org/10.1093/mnras/270.2.271.

van Dokkum, Pieter G. & Marijn Franx. 2001. Morphological Evolution and the Ages of Early-Type Galaxies in Clusters. ApJ 553(1). 90–102. https://doi.org/10.1086/320645.

Veilleux, Sylvain, Gerald Cecil & Joss Bland-Hawthorn. 2005. Galactic Winds. ARA&A 43(1). 769–826. https://doi.org/10.1146/annurev.astro.43.072103.150610.

Venemans, B. P. et al. 2013. Discovery of Three z > 6.5 Quasars in the VISTA Kilo-Degree Infrared Galaxy (VIKING) Survey. ApJ 779(1), 24. 24. https://doi.org/10.1088/0004-637X/779/1/24.

Vestergaard, M. 2002. Determining Central Black Hole Masses in Distant Active Galaxies. ApJ 571(2). 733–752. https://doi.org/10.1086/340045.

Vestergaard, M. & Patrick S. Osmer. 2009. Mass Functions of the Active Black Holes in Distant Quasars from the Large Bright Quasar Survey, the Bright Quasar Survey, and the Color-selected Sample of the SDSS Fall Equatorial Stripe. ApJ 699(1). 800–816. https://doi.org/10.1088/0004-637X/699/1/800.

Visbal, Eli, Zoltán Haiman & Greg L. Bryan. 2014. Direct collapse black hole formation from synchronized pairs of atomic cooling haloes. MNRAS 445(1). 1056–1063. https://doi.org/10.1093/mnras/stu1794.

Vogelsberger, Mark et al. 2014. Introducing the Illustris Project: simulating the coevolution of dark and visible matter in the Universe. MNRAS 444(2). 1518–1547. https://doi.org/10.1093/mnras/stu1536.

Volonteri, M. et al. 2013. The Evolution of Active Galactic Nuclei and their Spins. ApJ 775(2), 94. 94. https://doi.org/10.1088/0004-637X/775/2/94.

Volonteri, Marta. 2010. Formation of supermassive black holes. A&A Rev. 18(3). 279–315. https://doi.org/10.1007/s00159-010-0029-x.

Volonteri, Marta & Mitchell C. Begelman. 2010. Quasi-stars and the cosmic evolution of massive black holes. MNRAS 409(3). 1022–1032. https://doi.org/10.1111/j.1365-2966.2010.17359.x.

Volonteri, Marta, Francesco Haardt & Piero Madau. 2003. The Assembly and Merging History of Supermassive Black Holes in Hierarchical Models of Galaxy Formation. ApJ 582(2). 559–573. https://doi.org/10.1086/344675.

Volonteri, Marta, Mélanie Habouzit & Monica Colpi. 2021. The origins of massive black holes. *Nature Reviews Physics* 3(11). 732–743. https://doi.org/10.1038/s42254-021-00364-9.

Volonteri, Marta & Martin J. Rees. 2005. Rapid Growth of High-Redshift Black Holes. ApJ 633(2). 624–629. https://doi.org/10.1086/466521.

Volonteri, Marta & Martin J. Rees. 2006. Quasars at z=6: The Survival of the Fittest. ApJ 650(2). 669–678. https://doi.org/10.1086/507444.

Volonteri, Marta, Joseph Silk & Guillaume Dubus. 2015. The Case for Supercritical Accretion onto Massive Black Holes at High Redshift. ApJ 804(2), 148. 148. https://doi.org/10.1088/0004-637X/804/2/148.

Volonteri, Marta et al. 2005. The Distribution and Cosmic Evolution of Massive Black Hole Spins. ApJ 620(1). 69–77. https://doi.org/10.1086/426858.

Wadsley, James W., Benjamin W. Keller & Thomas R. Quinn. 2017. Gasoline2: a modern smoothed particle hydrodynamics code. MNRAS 471(2). 2357–2369. https://doi.org/10.1093/mnras/stx1643.

Wang, Feige et al. 2018. The Discovery of a Luminous Broad Absorption Line Quasar at a Redshift of 7.02. ApJ 869(1), L9. L9. https://doi.org/10.3847/2041-8213/aaf1d2.

Wang, Feige et al. 2019. Exploring Reionization-era Quasars. III. Discovery of 16 Quasars at $6.4 \lesssim z \lesssim 6.9$ with DESI Legacy Imaging Surveys and the UKIRT Hemisphere Survey and Quasar Luminosity Function at $z \sim 6.7$. ApJ 884(1), 30. 30. https://doi.org/10.3847/1538-4357/ab2be5.

Wang, Feige et al. 2021. A Luminous Quasar at Redshift 7.642. ApJ 907(1), L1. L1. https://doi.org/10.3847/2041-8213/abd8c6.

Wang, J. M. & H. Netzer. 2003. Extreme slim accretion disks and narrow line Seyfert 1 galaxies: The nature of the soft X-ray hump. A&A 398. 927–936. https://doi.org/10.1051/0004-6361:20021511.

Watarai, Ken-ya et al. 2000. Galactic Black-Hole Candidates Shining at the Eddington Luminosity. PASJ 52. 133. https://doi.org/10.1093/pasj/52.1.133.

Webster, B. Louise & Paul Murdin. 1972. Cygnus X-1-a Spectroscopic Binary with a Heavy Companion ? Nature 235(5332). 37–38. https://doi.org/10.1038/235037a0.

Weil, M. L., V. R. Eke & G. Efstathiou. 1998. The formation of disc galaxies. MNRAS 300(3). 773–789. https://doi.org/10.1046/j.1365-8711.1998.01931.x.

Whalen, Daniel, Tom Abel & Michael L. Norman. 2004. Radiation Hydrodynamic Evolution of Primordial H II Regions. ApJ 610(1). 14–22. https://doi.org/10.1086/421548.

Whalen, Daniel et al. 2008. The Destruction of Cosmological Minihalos by Primordial Supernovae. ApJ 682(1). 49–67. https://doi.org/10.1086/589643.

Whalen, Daniel J. et al. 2020. Finding Direct-collapse Black Holes at Birth. ApJ 897(1), L16. L16. https://doi.org/10.3847/2041-8213/ab9d29.

White, S. D. M. & M. J. Rees. 1978. Core condensation in heavy halos: a two-stage theory for galaxy formation and clustering. MNRAS 183. 341–358. https://doi.org/10.1093/mnras/183.3.341.

Wiersema, K. et al. 2012. Polarimetry of the transient relativistic jet of GRB 110328/Swift J164449.3+573451. MNRAS 421(3). 1942–1948. https://doi.org/10.1111/j.1365-2966.2011.20379.x.

Willott, Chris J. et al. 2007. Four Quasars above Redshift 6 Discovered by the Canada-France High-z Quasar Survey. AJ 134(6). 2435–2450. https://doi.org/10.1086/522962.

Willott, Chris J. et al. 2009. Six More Quasars at Redshift 6 Discovered by the Canada-France High-z Quasar Survey. AJ 137(3). 3541–3547. https://doi.org/10.1088/0004-6256/137/3/3541.

Willott, Chris J. et al. 2010. The Canada-France High-z Quasar Survey: Nine New Quasars and the Luminosity Function at Redshift 6. AJ 139(3). 906–918. https://doi.org/10.1088/0004-6256/139/3/906.

Winter, Lisa M., Richard F. Mushotzky & Christopher S. Reynolds. 2006. XMM-Newton Archival Study of the Ultraluminous X-Ray Population in Nearby Galaxies. ApJ 649(2). 730–752. https://doi.org/10.1086/506579.

Wise, John H. et al. 2019. Formation of massive black holes in rapidly growing pre-galactic gas clouds. Nature 566(7742). 85–88. https://doi.org/10.1038/s41586-019-0873-4.

Wright, Thomas. 1750. *An original theory or new hypothesis of the universe : founded upon general phaenomena of the visible creation; and particularly the Via the laws of nature, and solving by mathematical principles : the Lactea ...compris'd in nine familiar letters from the author to his friendand : illustrated with upward of thirty graven and mezzotinto plates ...* https://doi.org/10.3931/e-rara-28672.

Wu, Xue-Bing et al. 2015. An ultraluminous quasar with a twelve-billion-solar-mass black hole at redshift 6.30. Nature 518(7540). 512–515. https://doi.org/10.1038/nature14241.

Yajima, Hidenobu & Sadegh Khochfar. 2016. The role of stellar relaxation in the formation and evolution of the first massive black holes. MNRAS 457(3). 2423–2432. https://doi.org/10.1093/mnras/stw058.

Yang, Jinyi et al. 2019. Exploring Reionization-era Quasars. IV. Discovery of Six New $z \gtrsim 6.5$ Quasars with DES, VHS, and unWISE Photometry. AJ 157(6), 236. 236. https://doi.org/10.3847/1538-3881/ab1be1.

Yang, Jinyi et al. 2020. Pōniuā'ena: A Luminous z = 7.5 Quasar Hosting a 1.5 Billion Solar Mass Black Hole. ApJ 897(1), L14. L14. https://doi.org/10.3847/2041-8213/ab9c26.

Yang, Jinyi et al. 2021. Probing Early Supermassive Black Hole Growth and Quasar Evolution with Near-infrared Spectroscopy of 37 Reionization-era Quasars at $6.3 < z \leq 7.64$. ApJ 923(2), 262. 262. https://doi.org/10.3847/1538-4357/ac2b32.

Yao, Su et al. 2021. Detection of a parsec-scale jet in a radio-quiet narrow-line Seyfert 1 galaxy with highly accreting supermassive black hole. MNRAS 508(1). 1305–1313. https://doi.org/10.1093/mnras/stab2651.

Yoshioka, Shogo et al. 2022. Large-scale outflow structure and radiation properties of super-Eddington flow: Dependence on the accretion rates. *arXiv e-prints*, arXiv:2209.01427. arXiv:2209.01427.

Zauderer, B. A. et al. 2011. Birth of a relativistic outflow in the unusual γ-ray transient Swift J164449.3+573451. Nature 476(7361). 425–428. https://doi.org/10.1038/nature10366.

Zauderer, B. A. et al. 2013. Radio Monitoring of the Tidal Disruption Event Swift J164449.3+573451. II. The Relativistic Jet Shuts Off and a Transition to Forward Shock X-Ray/Radio Emission. ApJ 767(2), 152. 152. https://doi.org/10.1088/0004-637X/767/2/152.

Zhang, Dong. 2018. A Review of the Theory of Galactic Winds Driven by Stellar Feedback. *Galaxies* 6(4). 114. https://doi.org/10.3390/galaxies6040114.

Zhang, Xiaoxia & Youjun Lu. 2019. On Constraining the Growth History of Massive Black Holes via Their Distribution on the Spin-Mass Plane. ApJ 873(2), 101. 101. https://doi.org/10.3847/1538-4357/ab06c6.

Zhang, Xiaoxia, Youjun Lu & Taotao Fang. 2020. Effects of Spin on Constraining the Seeds and Growth of $\gtrsim 10^9 M_\odot$ Supermassive Black Holes in z > 6.5 Quasars. ApJ 903(1), L18. L18. https://doi.org/10.3847/2041-8213/abc077.

Zhu, Qirong et al. 2022. The formation of the first quasars: the black hole seeds, accretion, and feedback models. MNRAS 514(4). 5583–5606. https://doi.org/10.1093/mnras/stac1556.

Zinn, P. C. et al. 2013. Active Galactic Nucleus Feedback Works Both Ways. ApJ 774(1), 66. 66. https://doi.org/10.1088/0004-637X/774/1/66.

Zubovas, Kastytis & Andrew King. 2019. Slow and massive: low-spin SMBHs can grow more. MNRAS 489(1). 1373–1378. https://doi.org/10.1093/mnras/stz2235.

Zubovas, Kastytis & Andrew King. 2021. High-redshift SMBHs can grow from stellar-mass seeds via chaotic accretion. MNRAS 501(3). 4289–4297. https://doi.org/10.1093/mnras/stab004.

Zubovas, Kastytis et al. 2013. AGN outflows trigger starbursts in gas-rich galaxies. MNRAS 433(4). 3079–3090. https://doi.org/10.1093/mnras/stt952.